10-1-2018

Analysis of the SET/FTY720 complex by NMR reveals a unique mechanism for the activation of PP2A

Ryan M. De Palma
Medical University of South Carolina

Analysis of the SET/FTY720 complex by NMR reveals a unique mechanism for the activation of PP2A

By

Ryan M. De Palma

A Dissertation submitted to the Medical University of South Carolina in partial fulfillment of the requirements for the degree of Doctor of Philosophy in the College of Graduate Studies.

Department of Biochemistry and Molecular Biology

October 2018

Approved by,

Advisory Committee

Besim Ogretmen, Ph.D.

Christopher Davies, Ph.D.

Steven Rosenzweig, Ph.D.

L. Ashley Cowart, Ph.D.

Dennis Watson, Ph.D.

TABLE OF CONTENTS

Acknowledgements

First and foremost, I would like to thank my advisor, Dr. Besim Ogretmen. He was interested and patient enough to let me tackle a very tough project in a way that had not been done before, while always steering me back to the important questions, when my focus drifted to the minutia. I learned a lot over the years from his approach to scientific questions, his experience, and his leadership skills. Thank you to my advisory committee members: Dr. Davies, Dr. Cowart, Dr. Watson, and Dr. Rosenzweig. I appreciate your time and candor.

I would like to thank my wife, Heather, for her support and saint-like patience. I know you were pretending to listen when I would talk about science. I appreciate the attempt to feign interest. None of this would be possible without your support and love. I need to thank my mom and dad for hanging in there with me. I know you thought I would be a student forever to avoid getting a "real job". I could always count on you to know when I needed a distraction despite my denial and objections.

A special thank you is needed for Dr. Stuart Parnham. Your help and guidance with the NMR studies was invaluable. You were always keen to remind me that a Ph.D. is a philosophical journey; and that sympathy can be found "between shit and syphilis in the dictionary." I genuinely appreciate your friendship. Thank you Dr. Yuri Peterson for your time and great conversations during the final stretch of my project. I thoroughly enjoyed our weekly meetings to go over/redo the binding models again and again and again…

Ogretmen Lab members past and present deserve recognition. We are a diverse, extended family and very close friends. We share the good days and the bad days. I don't

think anyone could ask for a friendlier work environment. Thank you all for your help, guidance, and friendship: Shanmugam Panneer Selvam, Mohammed Dany, Rose Nganga, Raquela Thomas, Salih Gencer, Natalia Oleinik, Josh Oaks, Suriyan Ponnusamy, Can Senkal, Jisun Kim, Silvia Vaena-Alvaros, Kyla Baron and Braden Roth.

Abbreviations

AC: Acid ceramidase

AKT: serine/threonine kinase also known as protein kinase B (or PKB)

ANOVA: analysis of variance

AML: Acute myeloid leukemia

ASMase: Acid sphingomyelinase

BSA: Bovine serum albumin

B56γ: PPP2R5C regulatory subunit of Protein Phosphatase 2A

B56δ: PPP2R5D regulatory subunit of Protein Phosphatase 2A

C1P: Ceramide-1-phosphate

C6P: D-*erythro*-C6 pyridinium ceramide

CERK: Ceramide kinase

CERS: (dihydro) ceramide synthase

CERT: Ceramide transfer protein

CD: circular dichroism

CML: Chronic myeloid leukemia

COSY: Correlational Spectroscopy

D-e-C18: D-*erythro*-C18 ceramide

DES: Dihydro-ceramide desaturase

DMEM: Dulbecco's Modified Eagle Medium

DOSY: Diffusion Ordered Spectroscopy

eNOS: endothelial nitric oxide sunthase

ER: Endoplasmic reticulum

FTY720: Fingolimod, Gleevec

FPLC: Fast Protein Liquid Chromatography

HDAC: Histone deacetylase

GA: Glutaraldehyde

GCS: Glucosylceramide synthase

I2PP2A/SET: Inhibitor 2 of PP2A

INHAT: inhibitor of histone acetyltransferases

ITC: Isothermal Titration Calorimetry

L-e-C18: L-*erythro*-C18 ceramide

MOE: Molecular Operating Environment

NMR: Nuclear Magnetic Resonance

NOESY: Nuclear Overhauser Enhancement Spectroscopy

NSMase: Neutral sphingomyelinase

PCR: Polymerase Chain Reaction

PDI: Protein disulfide isomerase

PLA: Proximity Ligation Assay

PMSF: phenylmethane sulfonyl fluoride

PAGE: Polyacrylamide gel electrophoresis

PP2A: Protein Phosphatase 2A

PP2AA: Scaffold A subunit of Protein Phosphatase 2A

PP2AC: Catalytic subunit of Protein Phosphatase 2A

RCI: Random Coil Index

S1P: Sphingosine-1-phosphate

SCR: scramble sequence

SDS: Sodium Dodecyl Sulfate

SET: Su(var), Enhancer-of-zeste, Trithorax

SILAC: Stable isotope labeling of cells in culture

shRNA: Short hairpin ribonucleic acid

SK1: Sphingosine kinase 1

SK2: Sphingosine kinase 2

SPL: Sphingosine-1-phosphate lyase

SPR: surface plasmon resonance

SPT: Serine palmitoyltransferase

STD-NMR: Saturation Transfer Difference Nuclear Magnetic Resonance

TOCSY: Total Correlational Spectroscopy

TROSY: Transverse Relaxation Optimized Spectroscopy

LIST OF TABLES

LIST OF FIGURES

Abstract

Protein phosphatase 2A (PP2A) is a major serine/threonine phosphatase with tumor suppressor function. PP2A holoenzyme contains numerous combinations of its various isoforms of scaffolding (A), regulatory (B), and catalytic (C) subunits. In many cancer types, an endogenous PP2A inhibitor, inhibitor 2 of PP2A (SET) oncoprotein, is overexpressed, resulting in PP2A inhibition, leading to enhanced cell growth, and attenuation of cell death. It is known that targeting SET with bioactive sphingolipid ceramide or sphingolipid analogue drug FTY720 leads to the reactivation of PP2A, leading to necroptosis. However, structural details of the interaction between SET and FTY720 (or ceramide) with regards to mechanism of the PP2A activation have been unknown. Here, we report the first in solution examination of SET-sphingolipid complex by NMR spectroscopy. Data revealed that FTY720 binding may result in a structural shift in the N-terminal region of SET, which prevents its oligomerization. This then leads to the release of SET from the catalytic subunit of a specific PP2A holoenzyme, which comprises PP2AAβ, PP2A-B56γ, and PP2ACα subunits, for increased PP2A activity, while SET remains associated with the PP2A-B56γ. The activation of this specific PP2A holoenzyme by SET-FTY720 complex then regulates a number of downstream effector proteins involved in various biological functions, such as tumor suppressor non-muscle myosin IIA. Attenuation of FTY720-SET association by point mutations enhances SET-PP2A inhibitory complex, leading to resistance to PP2A activation, which is recapitulated by R71A and E111A SET mutations.

Chapter 1: Introduction and Review of Literature

Sphingolipids and Cancer

Sphingolipids are a class of lipids responsible for the fluidity and creation of sub-domains in lipid bilayers. Research over the last two decades established sphingolipids as bioactive molecules with roles in a variety of cell signaling processes. Ceramide and sphingosine-1-phosphate (S1P), are the best characterized sphingolipids with roles in cancer pathogenesis. They function in cell death, cell migration, cell proliferation, inflammation, and senescence.

Ceramide is the central molecule of sphingolipid metabolism (Fig. 1). It is composed of a sphingosine backbone that is esterified to a fatty acyl chain by an amide bond to carbon 3 of the sphingosine base[1–3]. A hallmark of biologically active ceramide, is the trans-double bond between carbons 4 and 5 on the sphingosine backbone[2,4,5]. Failure to produce or loss of this double bond results in the formation of dihydro-ceramide. There is great variety in fatty acyl chain length (C_{14}-C_{26}), resulting in many different species of ceramide, each with specific cellular roles[6–8].

Ceramide can be produced through 1) *de novo* synthesis from the condensation of serine and palmitoyl-CoA, 2) the hydrolysis of sphingomyelin, or 3) the acetylation of sphingosine (Fig. 1). It is a potent lipid-messenger involved in regulating apoptosis, cancer-cell growth, senescence, and cell differentiation [6–8]. Ceramide is also the building block for other complex sphingolipids such as sphingomyelin, glycosphingolipids, and gangliosides. Sphingosine-1-phosphate is another important sphingolipid in cancer pathophysiology.

S1P is catalyzed by sphingosine kinases 1 (SK1) and 2 (SK2). The substrate sphingosine is generated by the catabolism of ceramide by acid ceramidase (AC), where

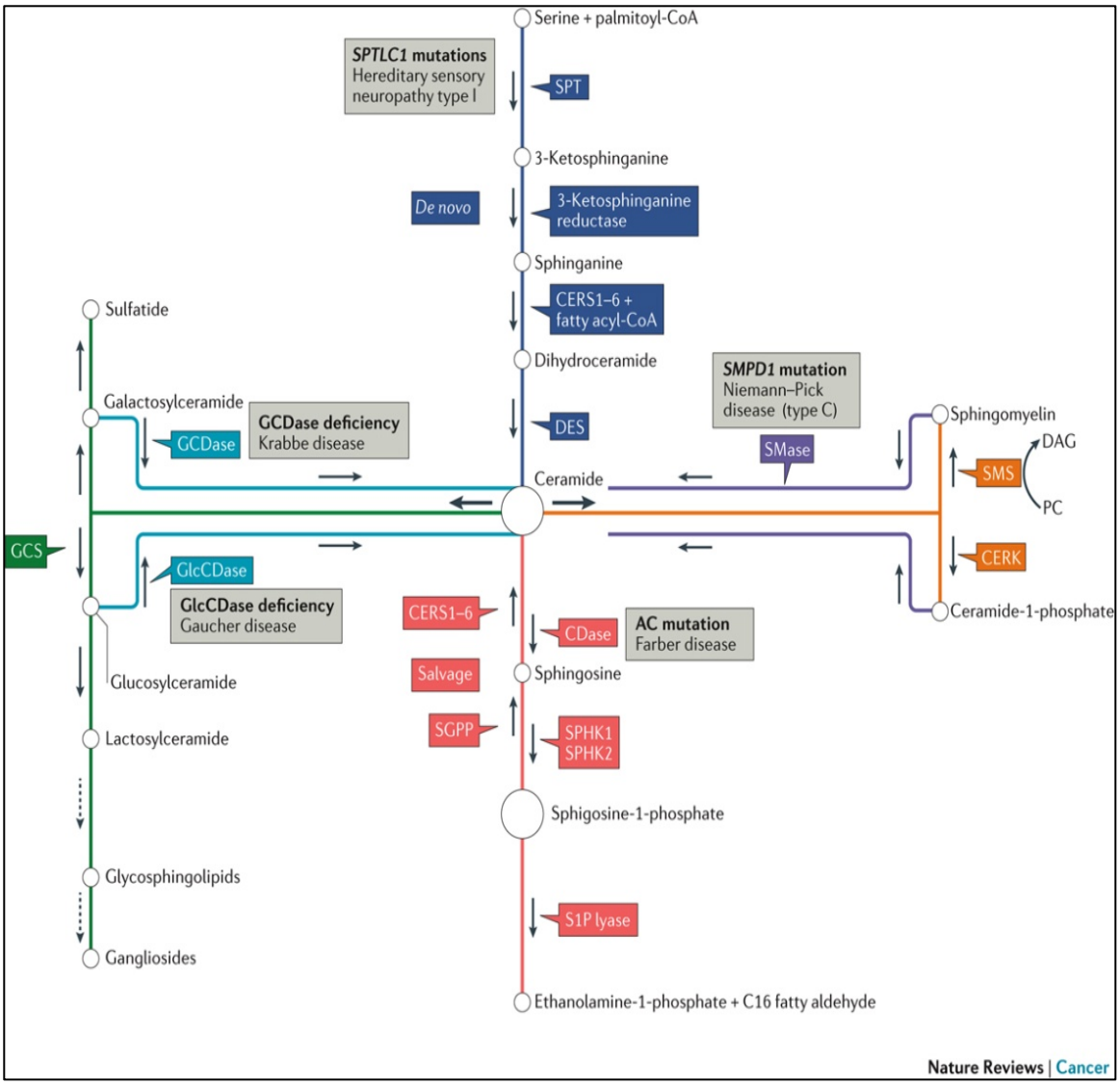

Figure 1| Schematic of known sphingolipid metabolism

Sphingolipids are built with three main groups: a sphingosine backbone, a fatty acyl chain, and a polar head group. Changes to either the head group or acyl chain length drive sub-cellular localization and function. Cells tightly regulate these pathways to maintain the balance between pro-proliferative sphingosine-1-phosphate and the cell death-mediating ceramide. (Figure taken from: Ogretmen. Nature Reviews. 2017)

the fatty acyl chain is removed. SK1 and SK2 then add a phosphate group to the α-hydroxyl of sphingosine. S1P is then secreted from cells where it can engage S1P receptors to initiate various signaling pathways in a paracrine or autocrine fashion. S1P receptors (1-5) are a family of G-protein-coupled receptors. Sphingosine-1-phosphate is considered a pro-survival lipid because of its involvement in inflammation, vasculorogenesis, metastasis, and its ability to counter apoptosis[10,11].

Most of the enzymes in the sphingolipid metabolic system have been cloned and characterized. Comprehensive research has defined their roles in either tumor suppression or pro-survival signaling. As ceramide and S1P are the central bioactive molecules of the sphingolipid world, dysregulation of their respective enzymatic pathways usually result in an imbalance of one or the other, and contributes to malignant pathologies accordingly.

Sphingosine-1-Phosphate and Cancer

Enzymes relating to the production and destruction of S1P have well defined roles in cancer. While S1P is a known pro-survival signaling molecule, the breakdown of S1P by sphingosine-1-phosphate lyase (SPL) leads to an accumulation of ceramide and subsequent cell death in colon cancer cells[1–3]. Cytosolic S1P, generated by SK1, initiates pro-survival signaling and metastasis in lung, bladder, and melanoma cell lines and mouse models via a number of signaling cascades[12]. Nuclear S1P, generated by SK2, can cause drug resistance by stabilizing telomerase, thus extending telomere length and cell survival in lung cancer cells[13]. It can also inhibit HDAC1 and 2 to epigenetically promote pro-survival signaling in breast cancer cell lines[13].

S1P can act in both receptor-dependent and receptor-independent manners, although the receptor-dependent signaling is the first that comes to mind. It seems that the effects of S1PR signaling are receptor and cell type dependent. For example, S1PR signaling is anti-proliferative in B cell and T lymphoblastic lymphomas[14,15], while S1PR2 signaling supports increased cancer cell proliferation, motility, and metastasis in AML, bladder, and melanoma models[16–18]. Interestingly, host/systemic S1P plays a role in tumor progression and metastasis by manipulating both immune cell and cancer cell functions[3,16,19–21]. Microfluidics chamber experiments and FACS cell sorting demonstrated that T-cells follow an S1P gradient for thymic egress[22,23]. There is evidence that S1PR3 signaling promotes stem cell-like characteristics in cancer cells; although the mechanism still remains rather ambiguous. Intriguingly, SMAD3, an important component in the TGFβ signaling family, has been shown to activate S1PR3 in a metastatic lung cancer mouse model[24]. S1PR4 promotes cell growth of estrogen receptor (ER)-negative breast cancer cells by preventing nuclear translocation of S1PR2 by an unknown mechanism[25]. Expression of S1PR4 was also associated with lower survival rates in ER-negative breast cancer patients[26]. A recent study showed that S1P-S1PR5 stimulated mitosis through a PI3K-AKT-PLK1 signaling cascade resulting in defects in chromosomal segregation[27]. Antagonism of S1P receptors 1-5 signaling could hinder cancer growth and metastasis, dependent upon matching the correct receptor to the correct cancer type.

S1P is able to regulate cancer cell signaling by binding directly to protein targets other than the S1P receptors. SK1-generated S1P has been shown to interact with TRAF2 and PPARγ, initiating NF-κB signaling and PPARγ-dependent gene expression

responsible for angiogenesis and metastasis[28–30]. Nuclear-localized S1P generated by SK2 was found to directly bind HDAC1 and HDAC2 by mass spectrometry lipidomics analysis, promoting the expression of both p21 and the proto-oncogene FOS[13]. Furthermore, S1P localized to the nuclear envelope binds to and stabilizes hTERT, the catalytic subunit of telomerase, by mimicking phosphorylation at Ser[921 12]. This prevents ubiquitylation by MKRN1 and degradation of hTERT, leading to preservation of telomere integrity and senescence, both of which are hallmarks of cancer. Intriguingly, SK2 has been reported in mitochondria where S1P directly interacts with PHB2 to enhance Complex IV activity and overall mitochondrial respiration[31] as measured by oxygen consumption rate.

Ceramide and Cancer

Ceramide is considered the bioactive lipid mediator of cell death. Many studies show that changes in the endogenous levels of ceramide in response to chemotherapeutic agents is a trigger for apoptosis[32–36], necroptosis, endoplasmic reticulum (ER) stress/cell cycle arrest, and lethal mitophagy[37–39] (Fig. 2). There is also evidence for roles in pro-proliferative signaling. Each of these pathways for cell death is dependent upon tissue, subcellular localization of the sphingolipids, and target availability. The *de novo* synthesis of ceramide in the ER by the serine palmitoyltransferases 1-3 (SPTs) and their auxiliary subunits[40] increases as a response to chemotherapeutic agents and radiation therapy in breast cancer cells[41,42]. Additionally, the increased production of dihydro-ceramides, ceramide precursors, by (dihydro) Ceramide Synthases (CERS) 1 and 6 induces cell death in an acyl chain-dependent and tissue-dependent manner. The

synthesis of C18 ceramide by CERS1 causes lethal mitophagy in both AML and head and neck cancer cell lines[38,39,43,44]. CERS6, generates C16 ceramide, activating caspase-dependent cell death in lung cancer cells. Elevated levels of CERS6 have been shown to be beneficial in head and neck, breast, colon, leukemia, and glioblastoma cell lines and mouse models[45–51]. To the contrary, there is also a report that describes C16 ceramide as having pro-survival functions[45]. CERS6/C16-ceramide expression protected against ER stress by activating the ATF6/CHOP unfolded protein response pathway. Genetic knockdown of CERS6/C16-ceramide resulted in ER stress and apoptotic cell death in head and neck squamous cell carcinomas[45]. Dihydro-ceramide desaturase (DES) produces mature ceramide by desaturating the bond between carbons 4 and 5 on the sphinganine backbone[52]. The resulting accumulation of ceramide causes cell cycle arrest in neuroblastoma cells. These enzymes are all part of the biosynthetic pathway of ceramide generation.

Ceramide can also be generated by the catabolism of more complex sphingolipids or used as a substrate to make more complex sphingolipids. Neutral sphingomyelinase (NSMase) generates ceramide by the hydrolysis of sphingomyelin. This activity has been linked with cell-cycle arrest and exosome release in breast cancer cells[53–55]. Acid sphingomyelinase (ASMase) also generates ceramide by the hydrolysis of sphingomyelin, but research has shown dual, opposing functions such as induction of apoptosis in lymphoblasts, while promoting metastasis of hematogenous tumors in some mouse models[32,56,57].

Other ceramide-related enzymes have roles in pro-proliferative signaling. Ceramide transfer protein (CERT) transports ceramide from the ER to Golgi for

packaging and transport to the plasma membrane where the ceramide can be converted to sphingomyelin[58,59]. An increase in CERT activity can drain the bioavailability of ceramide and inhibit ceramide-mediated apoptotic signals in breast cancer cells and mouse models[60–62]. Acid ceramidase (AC) removes the fatty acyl chain, producing sphingosine as a byproduct. This has a two-pronged effect: First, it lowers the bioavailability of ceramide. Then the increase in sphingosine creates an increase in S1P as well, resulting in an imbalance between the anti- and pro-proliferative lipids[63–66].

Increased ceramide kinase (CERK) activity is able to promote cancer cell survival in mouse models by converting ceramide to ceramide-1-phosphate (C1P)[67–69]. Glucosylceramide synthase (GCS) activity stimulates drug resistance in patients with oral cancers and in mouse models of breast cancer[70–74]. Both enzymes discussed above work by reducing ceramide levels and its anti-proliferative signaling capabilities by converting ceramide to a more complex sphingolipid. Similar to S1P, nuclear ceramide can also regulate hTERT. The repressor function of the SP3-HDAC1 complex is enhanced by ceramide along with the prevention of glyceraldehyde-3-phosphate dehydrogenase (GAPDH) nuclear localization, which is known to protect telomeres[75,76].

Ceramide is able to bind directly to specific proteins targets to regulate tumor growth[77]. Ceramide activates the mitogen-activated protein kinase (MAPK) signaling cascade by binding to both c-Raf and kinase suppressor of RAS (KSR)[34,78,79]. Likewise, ceramide binds to and activates PKC-ζ, which is a kinase well known to be involved in cell survival. However, the lipid-protein complex is then targeted to stress-activated protein kinase (SAPK), resulting in tumor suppression[80]. Cathepsin D contributes to metastasis and tumor growth by degrading extracellular matrix proteins. When bound by

ceramide, cathepsin D induces self-proteolysis and apoptosis[81]. Another major ceramide-binding protein is Inhibitor 2 of Protein Phosphatase 2A (I2PP2A or SET), which will be discussed later in the chapter.

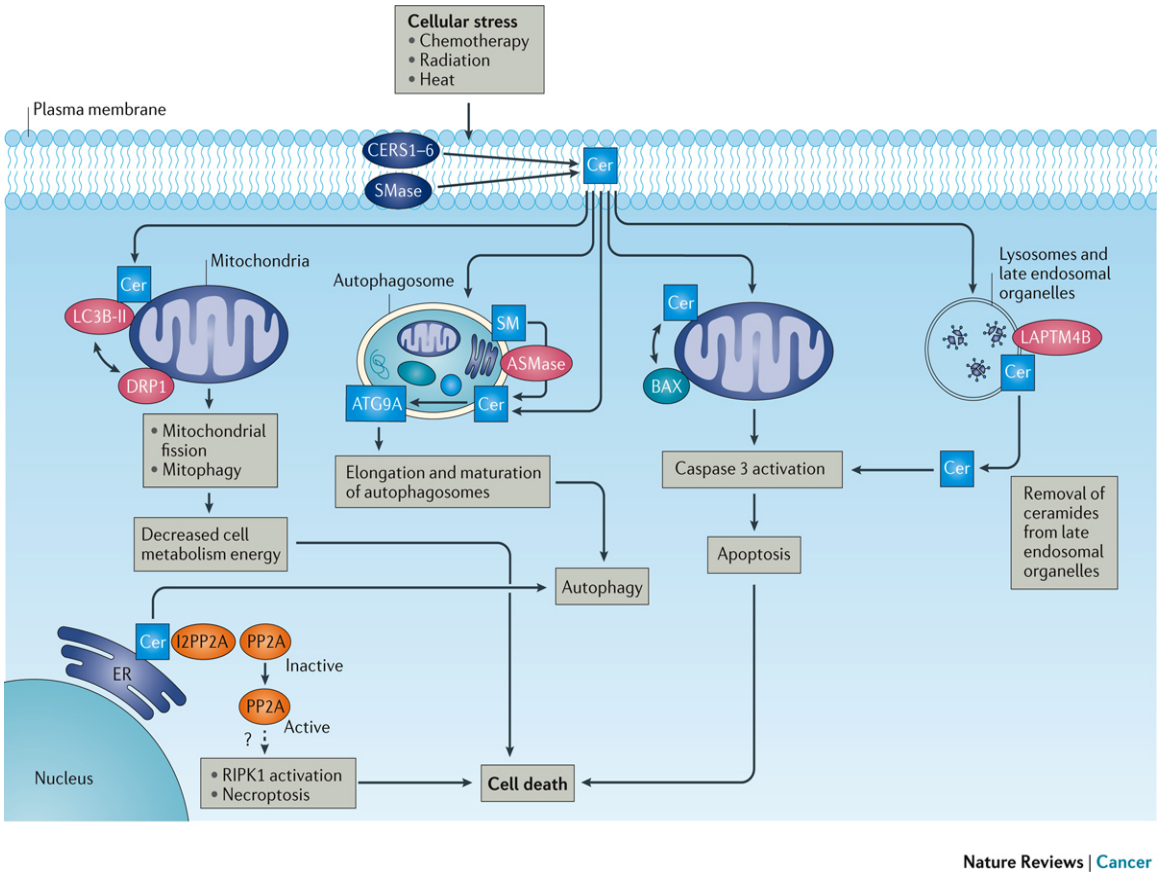

Figure 2| Ceramide signaling and cancer cell death pathways

Ceramide accumulates in response to various stressors, such as chemotherapies and radiation, to trigger cell death through direct and indirect targets. The ceramide is generated *de novo*, by the hydrolysis of sphingomyelin, or scavenged and transported from late endosomal organelles. Ultimately the localization and fatty acyl chain length dictate the manner of cell death. C16 or C18 ceramides localized to the mitochondria initiate apoptosis or mitophagy, respectively. C18 ceramide generated in the ER can activate tumor PP2A through direct binding to SET to initiate necroptosis or can accumulate in the ER and trigger autophagy or apoptosis depending on the cancer cell type. (Figure taken from: Ogretmen. Nature Reviews. 2017)

Sphingolipids as Cancer Therapies

In the previous section, we discussed roles for sphingolipids and their enzymes in cancer progression and tumor suppression. Dysregulation of these enzymes within the sphingolipid biosynthetic pathway can cause an imbalance between anti-proliferative ceramide and pro-proliferative S1P, leading to cancer pathologies (Fig. 3). Sphingolipid-based therapeutics are designed to shift the balance in favor of ceramide to induce a variety of cell death mechanisms. Table 1 lists anti-cancer drugs that target sphingolipid metabolism. These potential therapeutics can be divided into two main categories: Ceramide analogs/producers or inhibitors of S1P signaling/production.

Ceramide analogs are an interesting therapeutic avenue. The problem of delivery has always been an issue due to solubility problems with the long fatty acyl chains of ceramides. Pyridinium-conjugated ceramides have circumvented this problem by increasing water solubility and membrane permeability of long chain ceramide analogs. Interestingly, the positive charge of the pyridinium ring cause the ceramides to accumulate in the mitochondria of cancer cells, inducing lethal mitophagy[37–39,82]. Other cationic, short-chain ceramides have been very effective at inducing apoptosis in a variety of drug-resistant breast cancer cell lines[83,84]. Ceramide delivery via nanoliposomes has been very effective in the preclinical stages and is now advancing to Phase I clinical trials for the treatment of patients with advanced stage solid tumors[85–88].

Halting the generation of S1P by targeting sphingosine kinase 1 and 2 is also being pursued as an anti-cancer strategy. SK1-I is a competitive inhibitor of SK1 and has shown promise in cell lines and xenograft models of glioblastoma[89].

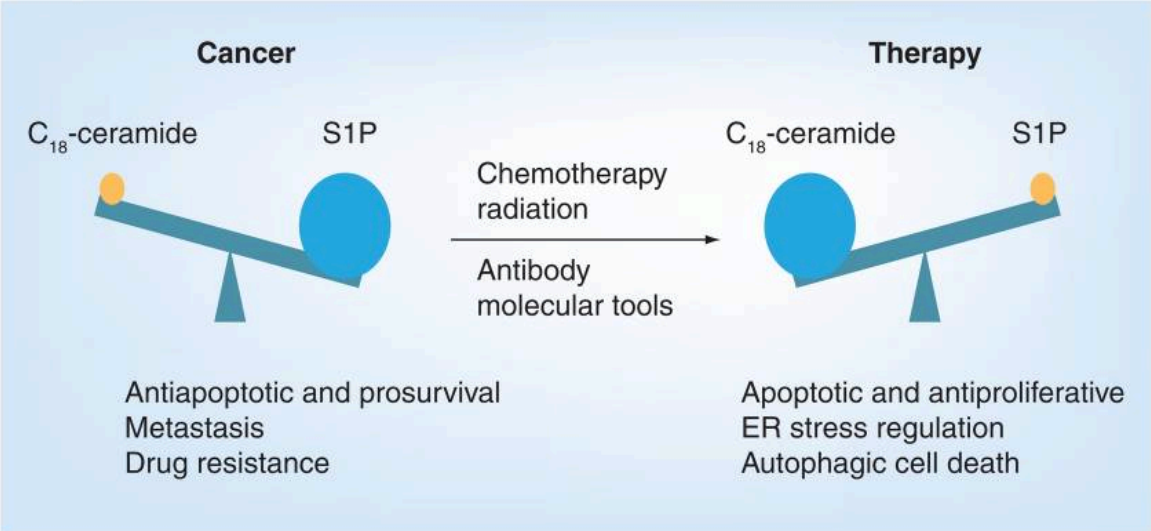

Figure 3| Balance of Ceramide and Sphingosine-1-phosphate in cancer pathology.

In many cancers a decrease in ceramide is observed along with a corresponding increase with S1P. This results in an imbalance that favors cell proliferation, metastasis, and drug resistance. Sphingolipid-based therapeutics are designed to shift the balance in favor of ceramide to induce a variety of cell death mechanisms. (Taken from Ponnusamy et al. Future Oncology. 2010)

PF-543 is another SK1 inhibitor in development. Initially thought to be ineffective, further studies have shown inhibition of cell propagation in colorectal cancer and triple negative breast cancer cell lines and mouse models[90–92]. There is also an inhibitor for SK2, ABC294640, which has is currently in a number of Phase I and Ib clinical trials[93,94]. It has completed a Phase I trial against solid tumors and is now in a Phase II clinical trial for patients with hepatocellular carcinoma.

TABLE 1: Drugs that Target Sphingolipid Metabolism

Name	Function/Target	Stage of development	References
C8-CPC	Dihydro-ceramide desaturase	Preclinical	52
CHC	CERT/inhibits ceramide transport essential for sphingomyelin synthesis	Preclinical	62
NVP-231	Ceramide kinase	Preclinical	68
LCL521 and LCL204	Acid ceramidase	Preclinical	64–66
Pyridinium ceramide (LCL-461 and LCL29)	Mitophagy/targets cancer mitochondria	Preclinical	95,96
Nanoliposomal ceramide	Survivin	Preclinical	85
FTY720 (fingolimod, Gleevec)	S1PR1; I2PP2A/SET	FDA approved for M.S. (Multiple Sclerosis)	97–101
JTE013	S1PR2	Preclinical	16
AB1	S1PR2	Preclinical	102
SK1-I	SK1	Preclinical	89
PF543	SK1	Preclinical	90–92
VPC03090	S1PR1;S1PR3	Preclinical	103
Sphingomab (sonepcizumab)	S1P	Phase II	104
ABC294640	SK2; DES	Phase Ib and II	93,94,105–110

Table adapted from *Ogretmen. Nature Reviews. 2017

There is also an anti-S1P antibody[20], Sphingomab, which recently completed a Phase II clinical trial against renal clear cell carcinoma[104]. The efficacy was weak, however, suggesting that the antibody alone may not be enough. Perhaps in concert with an SK1 or SK2 inhibitor, patients may respond better. More studies are needed to understand the potential synergy between the two types of therapies.

Protein Phosphatase 2A

Protein Phosphatase 2A (PP2A) is a member of the protein phosphatase family (PPP) and the serine/threonine phosphatase super family. A major regulator in both cell division and apoptosis [111–113], the PP2A holoenzyme consists of three unique subunits. The 'Core Enzyme' is comprised of a 36 kDa catalytic 'C' subunit (PP2AC) and a 65 kDa scaffolding 'A' subunit (PP2AA). The third subunit is a regulatory 'B' subunit (PP2AB). There are 18 known B subunit isomers, each conferring unique substrate and tissue specificity to PP2A, accounting for its variety of functions in multiple cellular processes. This heterogeneity has led to the mapping of trimeric holoenzyme PP2A complexes to almost 300 protein targets ranging across myriad biological functions [114]. Table 2 gives a full listing of PP2A subunits and their subcellular localization. Given the number of subunits, there are 72 unique PP2A holoenzymes, each with its own set of substrates guided by subcellular localization.

TABLE *2*: PP2A Subunit Names and Subcellular Localization

Subunit	Gene Name	Isoforms	Aliases	Subcellular Localization
A	PPP2R1A PPP2R1B	Aα Aβ	PR65α PR65β	Cytoplasm Cytoplasm
B	PPP2R2A PPP2R2B PPP2R2C PPP2R2D	Bα Bβ Bγ Bδ	PR55α, B55α PR55β, B55β PR55γ, B55γ PR55δ, B55δ	Everywhere Cytoplasm Cytoskeletal fraction Cytoplasm
B'	PPP2R5A PPP2R5B PPP2R5C PPP2R5D PPP2R5E	B'α B'β B'1γ, B'2γ, B'3γ B'δ B'ε	PR61α, B56α PR61β, B56β, R61β2 PR61γ1, B56γ1, B'α3 PR61γ2, B56γ2, B'α2 B56γ3, B'α1 PR61δ, B56δ PR61ε, B56ε	Cytoplasm Cytoplasm Cytoplasm, nucleus, focal adhesions Cytoplasm, nucleus, mitochondria Cytoplasm
B"	PPP2R3A PPP2R3B PPP2R3C	B"α1, B"α2 B"β1, B"β2 B"γ	PR130, PR72 PR48, PR59 G5PR	Centrosome and Golgi
B"'	STRN STRN 3	None	PR110, PR93 PR112, PR102, PR94	Membrane and Cytoplasm Nucleus
C	PPP2AC PPP2AB	Cα Cβ	PP2Aα PP2Aβ	Cytoplasm and nucleus

*****Adapted from Chen et al. Gastroenterology Research and Practice 2013.

The catalytic PP2AC has two forms (α and β) that are encoded by two separate genes with 97% DNA sequence similarity. PP2ACα is the predominant catalytic subunit in cells. Despite their similarity, one subunit cannot compensate for the other because of their differences in expression. The scaffolding A-subunit is the platform for the assembly of the holoenzyme. It binds to the C-subunit with its N-terminus and to the B-subunit with its C-terminus via tandem-repeat regions known as HEAT (huntingtin/elongation/A subunit/TOR) motifs (Fig 4). The HEAT repeats create a horseshoe-shaped structure that orients the C and B subunits to the same side of the A subunit [115] (Fig. 4). This precise orientation is essential for substrate recognition and activity. The A subunit also has two forms (α and β), with 87% DNA sequence similarity. Aα is ubiquitously expressed, but Aβ expression varies by tissue. Similar to the C subunit, the A subunits are unique and one cannot compensate for the loss of the other [116]. Mutations in either Aα or Aβ, found in some cancers at low frequencies, cause a disruption in the assembly of the PP2A holoenzyme and compromise PP2A-mediated tumor suppression [117–120].

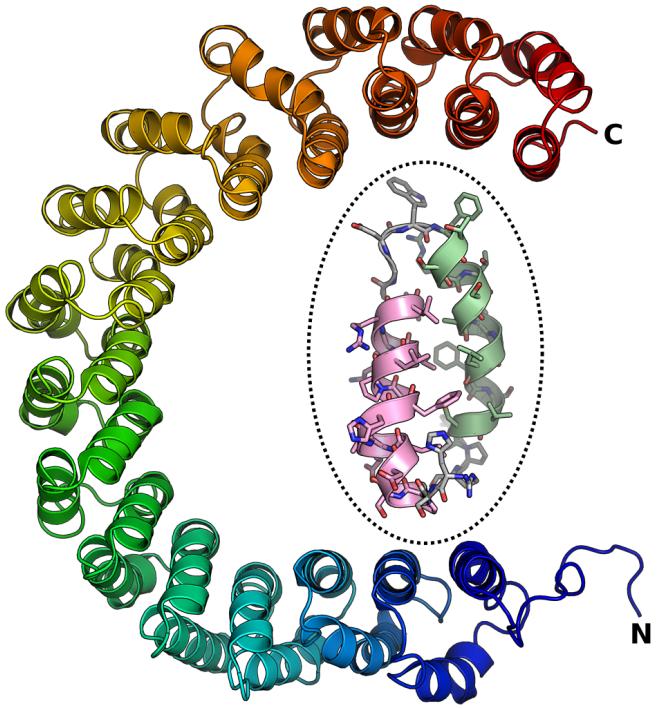

Figure 4| Assembly of the PP2A holoenzyme onto the A subunit.

The HEAT repeats of the A subunit create a horseshoe-shaped structure that orients the C and B subunits to the same side of the A subunit. The bottom panel details a single helix-turn-helix repeat is shown in the center, with the outer helix in pink, the inner helix in green, and the turn in white**. (PDB ID 2IAE. Cho US, Xu W. Crystal structure of a protein phosphatase 2A heterotrimeric holoenzyme. (2007). Nature 445, 53-57. DOI 10.1038/nature05351)**

The regulatory B subunits are the most varied, comprising of four unique gene families: B, B', B", and B"'. Each member of the four families has minimal overall sequence similarity [111]. This variety in the B-subunits accounts for the functional specificity of PP2A [121–128]. The B family is made up of four isoforms: α, β, γ, and δ. The

α and δ isoforms are ubiquitously expressed, while γ and β are predominantly expressed in the brain [111]. The B' family is comprised of five isoforms: α,β,γ, δ, and ε, each with multiple splice variants. Their expression also varies by tissue and subcellular localization. All B' family members contain a centrally conserved region that is required for A and C subunit interaction. They are dissimilar in both the N- and C-termini, possibly conferring different functions and substrate specificities [121]. B'56γ in particular has been found to be important in tumor suppression, and various mutations or changes in expression can disrupt this function [129–131]. The B" family also has five isoforms; they differ from the other families in that they are splice variants of the same gene. The B"' family is the most recently discovered and has been found predominantly in neuronal cells [132]. Alterations in some B subunits have been found in certain cancers [132–135].

Post-translational modifications are a major regulator of the phosphatase activity of the catalytic subunit. PP2AC activity is strictly controlled by phosphorylation at threonine (Thr) 304 and tyrosine (Tyr) 307. Autophosphorylation-activated protein kinase phosphorylates at Thr^{304} [136,137]. Tyr^{307} can be phosphorylated by various receptor and non-receptor tyrosine kinases and is typically a sign of reduced activity [138,139]. Methylation at leucine 309 is thought to be a precursor to assembly of the holoenzyme and activation [138]. Interestingly, some reports show that C18-ceramide can enhance methylation *in vitro* through an unknown mechanism [140,141]. In addition to post-translational modifications, there are endogenous protein inhibitors of PP2A activity.

Ceramide and FTY720

The balancing act between the lipid-messengers ceramide and sphingosine-1-phosphate in cancer progression provide an appealing area for drug development. Great strides have been made in developing some promising anti-cancer therapies, as discussed in the previous section. An area of drug development where little is currently being done, but with huge potential, is the activation of tumor suppressive Protein Phosphatase 2A. Ceramide (Fig. 5) has long been known to activate PP2A [142]. Ceramide is also a known ligand of PP1A, leading to the dephosphorylation of RB and growth arrest in cancer cells[143,144]. The generation of proapoptotic variants of caspase 9 and Bcl-x in lung cancer cells is also PP1A-ceramide dependent[143]. However, whether ceramide actually activates PP1A is still unclear. Similarly to ceramide, it was shown that pro-drug FTY720 (Fig. 5) activated PP2A, resulting in cell cycle arrest, apoptosis, or necroptosis [97,145]. FY720 (fingolimod, Gleevec) is a sphingosine analog approved by the FDA for the treatment of multiple sclerosis[146]. This pro-drug is phosphorylated by sphingosine kinase 2, and exported from the cell, where it targets the sphingosine-1-phosphate receptor 1 in an autocrine/paracrine manner[147]. The subsequent internalization and degradation of the receptor leads to immune suppression. Since then, many groups have reported that ceramide and FTY720

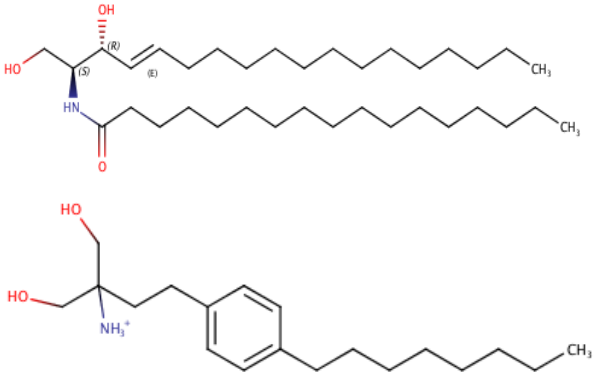

Figure 5| Chemical structures of D-*e*-C18 ceramide and FTY720

Both molecules have polar head group consisting of two hydroxyls and an amine. Both also have long saturated hydrocarbon tails. FTY720 has an aromatic ring instead of a fatty acyl chain.

activate PP2A [97,148–150] by targeting an endogenous protein inhibitor, and that the reactivation of PP2A, in general, has potent tumor suppressive powers.

Inhibitor 1 of PP2A

I1PP2A (also known as acidic leucine-rich phosphoprotein 32 A or ANP32A or PHAP1 -Putative HLA-DR-associated protein 1) is a sphingosine/dimethyl sphingosine-sensitive PP2A inhibitor found in human umbilical vein endothelial cells (HUVEC)[151,152]. Sphingosine binding to I1PP2A increases PP2A activity and leads to the expression of COX2, a major mediator of inflammation[152]. I1PP2A also plays a role in the histone acetyltransferase INHAT complex. Another member of the ANP32 family, ANP32e, is a PP2A inhibitor with a role in neuronal development[153,154]. Its role in cancer progression is defined by the type of cancer being studied. In non-small cell lung, breast and pancreatic cancers, I1PP2A has been described as a tumor suppressor[154–156]. However, I1PP2A expression in glioma, prostate, colorectal, hepatocellular carcinoma, and oral squamous cell carcinoma promotes cancer cell progression[157–162]. Interestingly, I1PP2A may have a more important role in neurodegenerative disorders such as Alzheimer's Disease. Deficiency in PP2A activity leads to a hyperphosphorylation of tau protein, a component neurofibrillary plaques, and cognitive impairment in rat models[163–165].

Cancerous Inhibitor of PP2A

CIP2A is a 90 kDa protein with no significant homology to any protein with a known function. It does, however, have a number of protein binding domains[166–168]. It is

known as the c-Myc protector, by preventing the dephosphorylation of S62 and promoting c-Myc stability[169]. In addition to c-Myc, CIP2A protects other PP2A-targeted proteins such as E2F1, Akt, DAPK1 (death-associated protein kinase 1), and Plk1 (polo-like kinase 1)[170]. CIP2A was first detected in a leukemia patient and has subsequently been described to have both proto-oncogenic and prognostic value in cancers[171]. Expression is localized primarily to the cytoplasm of cancer cells, whereas expression is non-existent in non-transformed cells[172]. Interestingly, CIP2A-negative tumors respond better to treatment than CIP2A positive tumors[173]. Because of this, CIP2A overexpression can be associated with tumor stage and as a prognostic marker for survival[174]. There are a number of potential therapeutics in the preclinical stages of development being tested in many cancer types. Only Celastrol has progressed beyond the preclinical stages[175]. Celastrol enhances CIP2A/CHIP interaction, leading to ubiquitination and degradation. Specificity and overall toxicity have been issues in drug development because of CIP2A direct regulation of oncogenic transcription factors such as E2F1 and c-Myc. Targeting CIP2A could be a promising avenue for cancer therapy, but is there a better option to reactivate tumor suppressive PP2A?

Inhibitor 2 of PP2A

One of the most studied and still enigmatic endogenous PP2A inhibitors is Inhibitor 2 of PP2A (I2PP2A/SET also known as TAF-1β). SET belongs to a family of SET domain-containing acidic proteins that tend to be nuclear. First identified in *Dosophila melanogaster*, SET (Su(var), Enhancer-of-zeste, Trithorax) domain-containing proteins play a role in gene transcription and histone methylation[176]. SET was originally

observed as a chimeric protein in a single acute lymphocytic leukemia (ALL) patient sample [177,178] by a fusion between full length SET with the C-terminal end of CAN nuclear pore protein. SET is predominantly nuclear, with functions in the histone acetyltransferase regulatory INHAT complex[151] in addition to its inhibitory role of PP2A regulation. SET can also form an inhibitory complex with nm23-H1 to mute metastasis [179]. Structurally, SET (37kDa) has several domains, each with specific functions. A region between residues 36-124 near the N-terminus is critical for PP2A inhibition[180]. The C-terminal end has a highly acidic stretch of glutamic and aspartic acids, which is crucial for histone binding[181]. The coil-coiled domain (E25-Q65) controls SET dimerization, which partially controls the nuclear functions of SET[182]. It is thought that SET directly inhibits PP2A by binding the C-subunit, but details on the interaction between SET and PP2A have not been described.

Along with being a potent PP2A inhibitor, SET is also a well-described proto-oncoprotein. Chromosomal mutations of the SET gene have been associated with acute myelogenous leukemia[183]. SET is involved in a variety of cancers through phosphorylation changes [98,184–187], overexpression [184,188–190], and loss of inhibitory ceramide [191]. There has been some *in vitro* evidence showing ceramide directly activates PP2AC [149,150], but the predominant mechanism of ceramide-induced activation of PP2A is through direct binding of ceramide to SET [97,148,192,193]. Previous research identified SET as a binding partner with ceramide [148]. SET has a high affinity for D-*erythro*-C18-ceramide [97,148], with only minimal specificity for other acyl chain length ceramides. Subsequent studies showed that FTY720 and not P-FTY720 binds to SET with a comparable affinity to C18-ceramide[97].

Structural modeling of FTY720 and C18-ceramide binding was completed using a partial SET crystal structure. Sequence alignment suggests that SET has a hydrophobic binding pocket similar to that of the ceramide-binding domain of CERT, a ceramide transport protein [97]. The current *in silico* model supports the presence of this hydrophobic pocket in SET containing lysine 209 and tyrosine 122. We believe these residues create a gating mechanism with their side chains. In this potential mechanism, the cationic ε-amino group of lysine would participate in hydrogen bonding with the π-system of the aromatic ring of tyrosine. Mutation of lysine 209 to aspartic acid would "close" the gate and reduce SET/ceramide binding compared to wild type (WT), while a tyrosine 122 to cysteine mutation would enhance SET/ceramide binding by "opening" the lipid- binding gate.

SET-Targeted PP2A Activation in Cancer Treatment

The tumor suppressive function of PP2A was first noted almost 30 years ago when known carcinogen okadaic acid was found to specifically inhibit PP2A [194–196]. Since then, PP2A activity has been found to be inhibited in multiple cancers [97,98,188,197], and the reactivation of PP2A induces cell death in these cancer cells. Overexpression of various endogenous protein inhibitors such as SET inhibits the tumor suppressive activity of PP2A. Furthermore, chromosomal mutations of the SET gene are associated with AML[183]. The interplay between SET and PP2A has not been defined, despite increasing

incidence of overexpression in many cancers, resulting in poor clinical outcomes[198,207].

The therapeutic value of targeting SET to reactivate tumor suppressor PP2A has been shown in many cancer cells. Genetically targeting SET in Chronic Myeloid Leukemia (CML) cell lines resulted in reduced BCR/ABL activity and apoptosis [188]. Targeting SET with shRNA or the synthetic peptide inhibitor OP449 [208] reactivates PP2A and induces cell death in B-Cell Chronic Lymphocytic Leukemia cells (B-CLL) [202,209]. Recently, targeting SET with OP449 was shown to sensitize drug-resistant myeloid leukemia cells (AML and CML) to tyrosine kinase inhibitors (TKIs) [201,209]. In addition, targeting SET demonstrated curtailed tumor growth in breast cancer cell lines, resulting in PP2A activation and reduced c-MYC stability/activity [206]. Recently, it was shown that FTY720 causes a significant increase in ceramide levels in the M2 subtype of acute myeloid leukemia (AML-M2). The resulting activation of PP2A is thought to be through SET inhibition and subsequent apoptosis [199]. It is interesting to note that the pro-drug FTY720 and not phospho-FTY720, have the SET-targeting anti-cancer functions. Lipidomics analysis showed that pro-drug FTY720 accumulated predominantly in lung tumor tissues, while phospho-FTY720 was found in serum of mice after treatment[97].

TABLE 1: Types of Cancer with SET Overexpression

Cancer Type	Reference
AML AML-M2	98,198–200
CML	188,201
B-CLL	202
Lung adenocarcinoma	97,148
Wilms' tumor	125,189
Non-Hodgkin's lymphoma	202
Prostate	192
Pancreatic	203,204
Hepatocellular carcinoma	205
Breast cancer	206
Colorectal cancer	207

Project Objectives

Although the therapeutic value of targeting SET to reactivate PP2A is well documented in many cancer types, little is known about its interactions with the tumor suppressor PP2A. The structural details of the interaction between SET and FTY720 (or ceramide) with regards to mechanism of the PP2A activation are also unknown. In this study, we seek to define the interplay between SET and PP2A, with particular attention to its regulation by ceramide and FTY720. The structural information obtained concerning the lipid-binding pocket of SET will provide the foundation for the development of FTY720/ceramide analogs as novel SET inhibitors to reactivate tumor suppressor PP2A with improved specificity and anti-cancer function, without immune suppression and other deleterious toxicities.

Chapter 2: Materials and Methods

Protein Purification

The various SET genes were cloned into pET-22b (+), pET-28b (+), or pHGK vectors. BL21 pLys cells were transformed and grown in four liters of Luria-Bertani (LB) media at 37°C with 100μg/ml ampicillin or kanamycin. Protein expression was induced with 0.05 mM IPTG for three hours, with shaking at 225rpm. The cells were collected, lysed by sonication, and the lysate was then clarified by centrifugation. The protein was loaded onto a sepharose Fast Flow HisTrap column (GE Healthcare) and eluted with 200 mM imidazole. The elution fractions were then pooled and loaded onto a HiLoad 16/60 Superdex 200 prep grade column. The pooled fractions were then dialyzed overnight at 4°C into phosphate buffer (20 mM phosphate buffer, 50 mM NaCl pH 8.0).

(*Detailed protocols of purification and recipes for isotopically-labeled proteins can be found in Appendix I).

Backbone Assignment of SET by NMR

The backbone of $^{13}C/^{15}N/^{2}H$-labeled Nd-SET was assigned using standard triple resonance experiments [210–217]. Experiments were acquired in 20 mM phosphate buffer, 50 mM sodium chloride pH 8.0 and 1% D20 at 310K on a Bruker Ascend 850 MHz spectrometer using a 5mm cryogenically cooled triple resonance z-gradient probe. Data were processed in TopSpin (Bruker BioSpin) and spectral analysis was done in CCPnmr2.2.2[218]. (BMRB accession number: 27482).

TABLE 2: Three-Dimensional NMR Experiments

Experiment	Nuclei	Number of Points F1	Number of Points F2	Number of Points F3	Literature References
TRHNCACB	^{13}C-^{15}N-^{2}H	**128**	**128**	**2048**	214,217
TRCBCACONH	^{13}C-^{15}N-^{2}H	**128**	**128**	**2048**	212
TRHNCA	^{13}C-^{15}N-^{2}H	**200**	**256**	**4096**	219
TRHNCOCA	^{13}C-^{15}N-^{2}H	**256**	**256**	**256**	210
TRNHCO	^{13}C-^{15}N-^{2}H	**256**	**128**	**4096**	211,213,216
TRHNCACO	^{13}C-^{15}N-^{2}H	**256**	**128**	**4096**	220,221

NMR Titrations

Experiments were acquired in 20 mM phosphate buffer, 50 mM sodium chloride pH 8.0 and 5% D20 at 310K on a Bruker Ascend 850 MHz spectrometer using a 5mm cryogenically cooled triple resonance z-gradient probe. For the NMR titration analysis, Nd-Cd SET was incubated with 0.5 μM-10.0 μM FTY720, D-*e*-C18 ceramide, or L-*e*-C18 ceramide in 0.5 μM increments. Chemical shift perturbations were monitored using BEST-TROSY experiment [222–224]. Data were processed in TopSpin (Bruker BioSpin) and spectral analysis was done in CCPnmr2.2.2[218]. Chemical shift perturbations were normalized and calculated using the following equation[225]:

$$d = \sqrt{\frac{1}{2}[\delta_H^2 + (\alpha \cdot \delta_N^2)]}$$

Structural Identification of FTY720 and D-e-C6-pyridinium ceramide protons

The following two-dimensional experiments were collected on a Bruker Avance II 600MHz spectrometer using a 5mm cryogenically cooled quadruple resonance QCI probe at a temperature of 298K.

TABLE 3: Two-Dimensional NMR Experiments

Experiment	Nuclei	Number of Points F1	Number of Points F2	Number of Scans	Mixing Time(s)	Literature Reference
Dq-COSY	^{1}H-^{1}H	512	2048	16	none	[226]
HSQC	^{1}H-^{13}C	256	2048	16	none	[227]
HMBC	^{1}H-^{13}C	256	2048	16	none	[228]
NOESY	^{1}H-^{1}H	256	2048	16	0.5s, 0.3s	[229]

Saturation Transfer Difference NMR

All STD-NMR experiments were carried out on a Bruker Avance II 600MHz spectrometer using a 5mm cryogenically cooled quadruple resonance QCI probe at a temperature of 298K. A pseudo-2D version of the STD NMR sequence was used for the acquisition of on- and off-resonance spectra [230–232]. For selective saturation, cascades of Gaussian pulses were used with a pulse length of 50 ms and 41.9 dB. The on-resonance frequency was set to 0.034 ppm to saturate methyl resonances [233] and the off-resonance frequency was set to -25.0 ppm for all experiments. To obtain the STD buildup curves saturation times were 0.1, 0.25, 0.5, 0.75, 1.0, 1.5, 2.0, 2.5, 3.0, 3.5, 4.0, 4.5, 5.0, 5.5, and 6.0 seconds. Eight scans were used with each experiment. LCL29 titration concentrations were 0.1, 0.2, 0.3, 0.4 and 0.5 mM with the protein concentration of 50 μM. For each titration, a STD buildup curve was recorded. For analysis a STD amplification factor

(STD-AF) is used to assess the absolute magnitude of the saturation transfer difference [234]. This factor is the partial saturation of a specific proton multiplied by the excess concentration of ligand. It is calculated as: STD-AF= $(\boldsymbol{I_o - I_{sat}})/ I_o$ • [ligand excess] where $\boldsymbol{I_o}$ is the reference spectrum and $\boldsymbol{I_{sat}}$ is the saturation spectrum.

Diffusion-Ordered Spectroscopy (DOSY)

Experiments were performed on a 400MHz Oxford spectrometer with a broadband probe at 295K. 32 scans were collected through a linear gradient with a 1.25s delay (D1), Δ = 0.1s, and δ =2500 μs.

Molecular Modeling of SET with Ceramide or FTY720

Modeling and simulations were performed using MOE 2018 (Chemical Computing Group, Inc). Structural PDB was SET:pdb2E50 (PMID 17360516)[235]. Before simulations the monomer was isolated and protonated at T=310K, pH 7.3, salt at 200mM using GB/VI electrostatics. Docking simulations used induced fit for the receptor and flexed the ligand. For each docking simulation, initial placement calculated 50 poses using triangle matching with London ΔG scoring, then the top 30 poses were refined using forcefield (Amber10: ETH) and Affinity ΔG scoring (Escore2). The top 10 poses from these simulations were analyzed and the top scoring pose is presented. For FTY720 we used the final model generated from our previous paper (PMID 23180565)[97] but allowed induced fit of the receptor. For C18 ceramide, we performed two iterative induced fit docking simulations. The first simulation allowed access to the entire protein; the second

round used the top pose from the first round and used the ligand atoms as the site to be probed.

Cell lines and Reagents

A549 human lung adenocarcinoma cells were grown in Dulbecco's Modified Eagle Medium (DMEM) (Corning) containing 10% FBS (Atlanta Biologicals) and 5% penicillin/streptomycin (Corning) at 37°C and 5% CO_2. Overexpression vectors of WT, S9A, S9E, S24A, S25E, S93A, S93E, Y133F, Y133E, S171A, S171E Flag-SET were generated in pCDH plasmid. SET was originally cloned into MigR1 at Ecor1 and Hpa1. It was removed using Ecor1 and Xho1 and sub-cloned into pCDH-CMV-MCS-EF1-copGFP (CD511B-1) via blunting the Xho1 site of FLAG-SET. The Xba1 site of pCDH was cut and blunted, followed by sticky-end ligation of ECOR1 sites. All stable knockdowns are shRNA to coding sequence unless otherwise noted: shSET/PLKO (3'UTR), shPP2ACα/PLKO, shPP2ACβ/PLKO, shPP2A B56δ/PLKO, shPP2A B56γ/PLKO (shRNA sequences can be found in Appendix I). All cell lines were established in A549 cells. Cells were treated with FTY720 (Cayman Chemical Company), D-*e*-C18 ceramide, L-*e*-C18 ceramide, D-*e*-C6-pyridinium ceramide (Lipidomics Shared Resource Facility, MUSC), and OP449 for experiments.

Proximity Ligation Assay

A549 cells were plated in each chamber of a glass four-well chamber slide and incubated overnight in DMEM, at 37°C, and 5% CO2. Cells were then treated with 5 μM FTY720 or DMSO for 3 hours, washed in cold PBS, and fixed using 4% paraformaldehyde. The

proximity ligation assay protocol was followed as outlined by Olink Biosciecnces® (Sigma). Images were collected as Z-stacks on an Olympus VF10i laser scanning confocal microscope.

Preparation and Assembly of PP2A Holoenzyme

All constructs and point mutations were generated using a standard PCR-based cloning strategy. B56ɣ1 was overexpressed in E. coli as a fusion protein with glutathione S transferase (GST) and purified as described [236]. The PP2A core enzyme, involving the full-length Ca (residues 1–309) and Aa (residues 8–589), was assembled as described [236]. The PP2A core enzyme was methylated by a PP2A-specific leucine carboxyl methyltransferase (LCMT). Following complete methylation, the fully methylated PP2A core enzyme was incubated with a stoichiometric amount of B56ɣ1. The PP2A holoenzyme was purified to homogeneity by gel-filtration chromatography. In addition, the purified full length Ca was used to generate a carboxy-terminally truncated variant (residues 1–294) through trypsin digestion.

GST-Mediated *in vitro* pull-down assays

Approximately 20 μg of GST-holoenzyme, GST-core enzyme (PP2AA and PP2AC), or GST- B56ɣ1[237] were immobilized onto glutathione resin (GS4B). 10 μM SET was pre-incubated with different concentrations of FTY720 for 30 min. SET and the holoenzyme were then mixed and incubated for 15-30 minutes. The resin was then washed two times with 1X TBST. The remaining protein and resin were mixed with 30 μl of loading buffer, heated for five minutes at 98°C, and applied to SDS-PAGE for electrophoresis. The results were visualized by Coomassie staining of the SDS-PAGE.

Stable Isotope Labeling of Cells in Culture (SILAC)

A549 cells stably overexpressing HA-tagged PP2ACα were grown in heavy (15N-arginine labeled) and light (normal) DMEM media. After three weeks of growing cells, the 'heavy cells' were treated with a high dose (20 μM) of FTY720 for 2 hours, washed, collected, and lysed. PP2ACα was immuno-precipitated by the HA-tag in both treated and control cells. The elution of control and treated samples were mixed and run on SDS-PAGE. The gel was then Coomassie stained for analysis by mass spectrometry. The ratio of ^{15}N:^{14}N was analyzed for changes in protein levels as result of exposure to FTY720.

Isothermal Titration Calorimetry

To determine the K_D value of C6-pyridinium-ceramide binding to N22d-SET, 0.05 mM C6-D-e-pyridinium-ceramide was injected in 1.5μl increments at 20°C into a 300 μl detection cell volume of 0.021 mM protein for 33 injections. As a control 0.05 mM C6-D-e-pyridinium-ceramide was injected in 1.5μl increments at 20°C into a 300 μl detection cell containing 20 mM phosphate buffer, 50 mM NaCl pH 8.0. This data set was then used to subtract background heat changes as a result of ligand dilution.

PP2A Activity Assay

Protein lysate (100μg) was used for PP2AC immunoprecipitation with a phosphatase kit (Millipore), as described by the manufacturer with the exception of using purified rabbit non-muscle Myosin IIa as a substrate.

Statistical analysis

All data are presented as means ± S.D. or S.E.M, and group comparisons were performed with a two-tailed Student's t test. For comparison among groups with one or more characteristics, one-way or two-way ANOVA followed by Tukey multiple comparison *post-hoc* test was used. Analyses were performed using GraphPad Prism 7 software and $p < 0.05$ was considered statistically significant.

Chapter 3: NMR Backbone Assignments of SET nuclear proto-oncogene

To analyze the effect of lipid binding on SET structure, we first had to assign the backbone amide resonances of SET. In order to do this, it, was necessary to purify isotopically labeled protein with NMR active nuclei such as ^{13}C, ^{15}N, and ^{2}H. NMR active nuclei possess a property called 'spin', meaning a charged nucleus spins about an axis to generate its own dipole moment. This property is necessary for NMR experiments because it allows nuclei to align to an external magnetic field and absorb radiofrequency radiation. ^{13}C NMR active nucleus allows us to monitor the couplings between the ^{H}N, N, and C^{α}. The incorporation of ^{13}C and ^{15}N means that most of the NMR active nuclei within a given protein are separated by a single bond coupling. The [^{1}H-^{15}N] bond coupling is present in every peptide bond (except proline) and is therefore the starting point for heteronuclear NMR analysis (Fig. 6). Additionally, substitution of protons with deuterons plays an important role in the backbone assignment of large proteins. Large proteins (>25 kDa) are less NMR compatible due to their slower tumbling, which leads to unfavorable (fast) relaxation properties and deterioration of spectral quality. By removing the side chain protons and replacing them with deuterons, hydrogen exchange between protein and buffer is limited, which, in turn, improves relaxation properties and spectral quality[238] .

These nuclei also possess a property known as relaxation, which can pose a problem when collecting data on large proteins. In general, relaxation refers to the weakening of signal over time. This is a result of magnetized, or excited nuclei, returning to an equilibrium state within the external field of the spectrometer (commonly oriented along the *z* axis)[238]. The restoration of magnetic moments back to the bulk magnetization

or z-magnetization can be described by two separate processes that govern NMR signal decay.

The overall process of the z-magnetization returning to equilibrium is referred to longitudinal or T_1 relaxation. T_1 relaxation is responsible for the loss of signal intensity. In order to acquire data these spins need to be energized by radio frequency pulses to rotate them 90° away from the z-magnetization and into the transverse plane. In order to for the z-magnetization to return to equilibrium energy needs to be lost. This loss is characterized by the flow of energy between localized fields and molecular motion, which causes these fields to clash. This process is referred to as spin-lattice relaxation, where 'lattice' refers to neighboring molecules of the solution and the wall of the NMR tube itself[238]. Similarly, the process by which transverse-magnetization returns to equilibrium is called transverse relaxation or T_2 relaxation. Radio frequency pulses to rotate NMR active nuclei 90° away from the z-magnetization and into the transverse plane. A small proportion of spins are bunched together in phase, a phenomenon known as phase coherence. As a function of time, the nuclear spins that are bunched together will lose their phase coherence and 'fan out'. This can be thought of as a process of entropy and results in the broadening of signal[238,240].

The equilibrium state, or bulk magnetization of the sample, is dependent upon the number of spins, their gyromagnetic ratios, and the strength of the applied field. Each proton can be thought of as a bar magnet (dipole) with its own magnetic moment. The spinning of electrons about a nucleus as a result of a strong external field creates a localized magnetic field. An additional mechanism of relaxation is to as a dipole-dipole mechanism. Simply, there are two spins (dipoles): one generates a field and the other

experiences it. This mechanism is typically experienced over short distances (< 5 Å), but it is important to note, especially for proteins, that local fields can be contributed by multiple spins; therefore relaxation can be influenced by a single spin nearby or by many spins farther away[240].

To combat deleterious relaxation properties we engineered a double truncation SET construct (NdCd SET) where 52 C-terminal residues (consisting of a long unstructured acidic tail) were deleted in addition to the 22 N-terminal residues (Fig. 7). The size of the protein is more amenable to NMR spectroscopy, while still containing the putative lipid-binding pocket[97]. Additionally, NdCd SET was triple labeled with [^{2}H-^{13}C-^{15}H] by perdeuteration (See Appendix I for details on isotopic labeling and purification) to further enhance signal to noise. In order to assign the backbone of NdCd SET, the protein was triple labeled with [^{2}H-^{13}C-^{15}H].). Substitution of protons with deuterons plays an important role in the backbone assignments of large proteins.

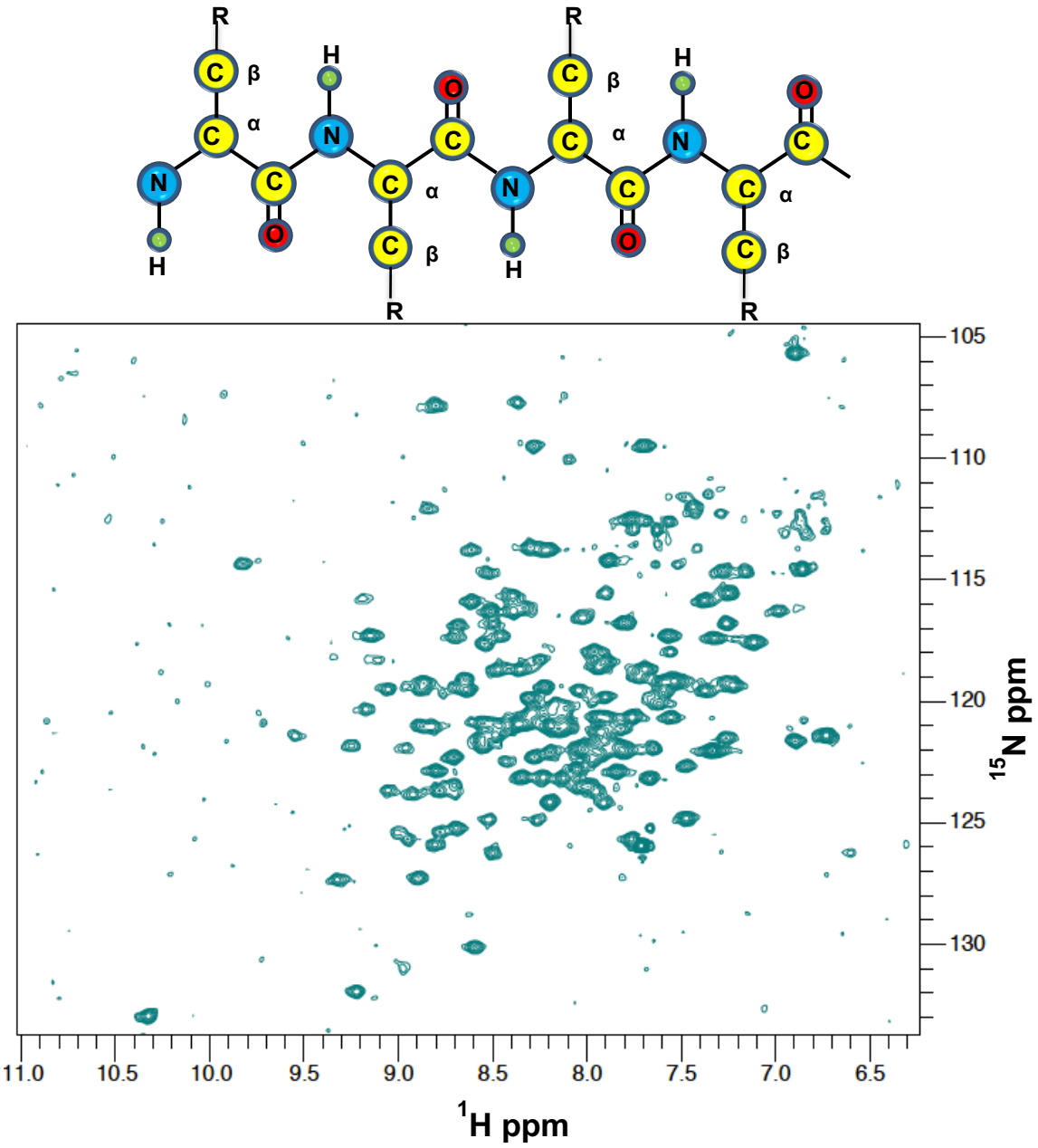

Figure 6| [1H-15N] TROSY of NdCd SET

A Transverse Relaxation Optimized Spectroscopy shows the [^{1}H-^{15}N] correlation for the backbone amides of NdCd SET. Each peak corresponds to an amino acid, providing a 'blueprint' for the protein.

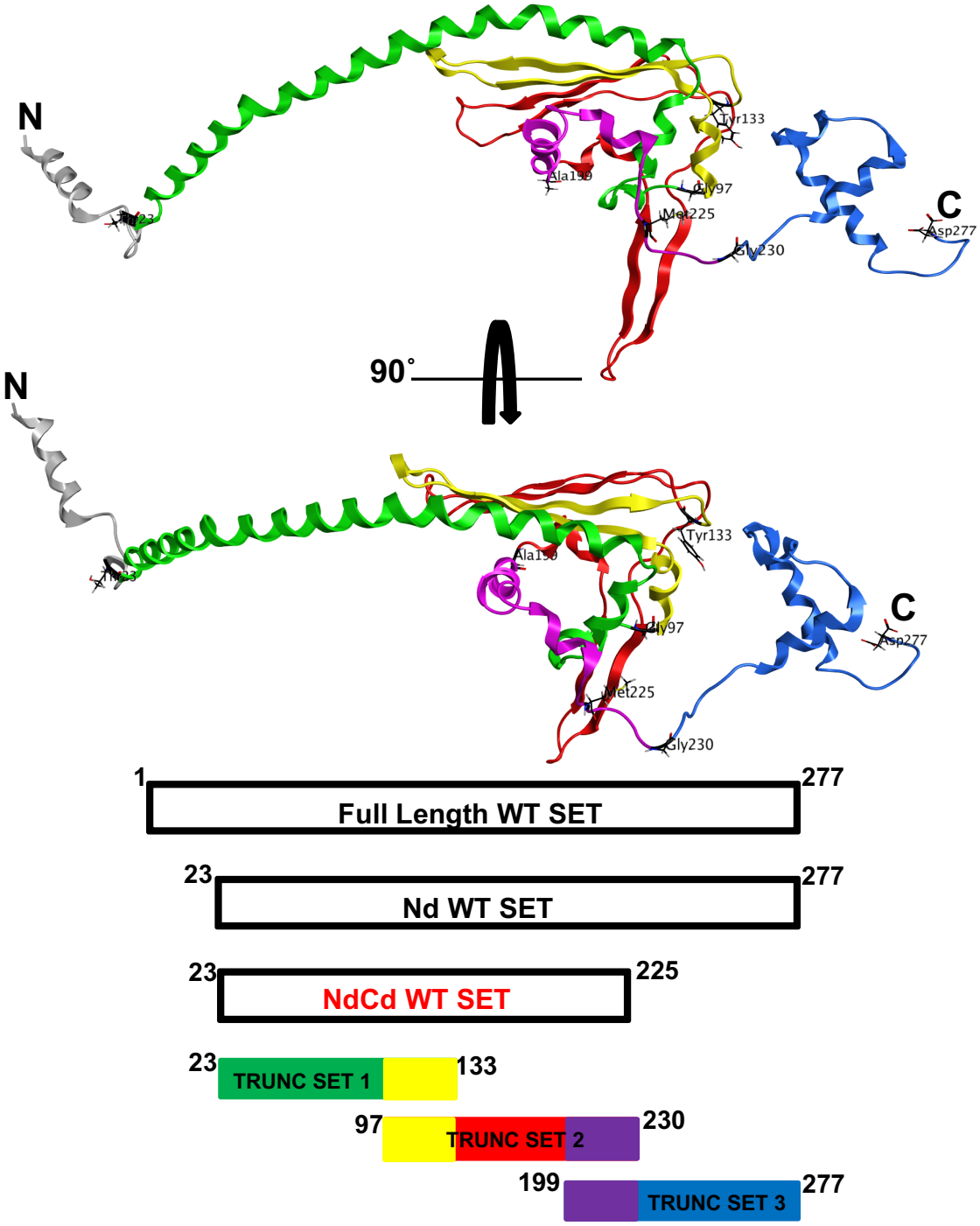

Figure 7| Schematic showing different truncated SET constructs used during backbone assignments

Each truncated SET was designed to overlap by 30-40 amino acids. The truncation sites (in green) were designed to fall within regions of random coil, so as to preserve secondary structure. The highly acid tail of SET, residues 231-277, was built onto the crystal structure (PDB 2e50) to show a complete representation of how SET was truncated to preserve secondary structure.

Large proteins (>25 kDa) are less NMR compatible due to slower tumbling that causes unfavorable relaxation properties and deterioration of spectral quality. By removing most of the side chain protons, hydrogen exchange between protein and buffer is limited, which improves relaxation properties of the protein[239]. Additionally, The ^{13}C NMR active nucleus allows us to monitor the couplings between the H^N, N and C^α of a single residue via triple resonance experiments. This essentially makes the entire protein a connected spin system. The incorporation of both ^{13}C and ^{15}N means that almost all of the NMR active nuclei in the protein are separated by a single bond coupling. The [^{1}H-^{15}N] bond coupling is present in every peptide bond (except prolines) and is therefore the starting point for heteronuclear NMR analysis (Fig. 7). A series of triple resonance experiments were then performed to assign the amide backbone of SET.

Triple resonance experiments record the couplings between ^{H}N, N, and C^α or C^β The HNCACB experiment records ^{15}N, C^α, and C^β couplings in one residue (*i*). It is paired with the CBCA(CO)NH, which records ^{15}N, C^α, and C^β couplings in one residue (*i*) and the ^{13}C- C^α and C^β of the preceding residue (*i-1*). The spectra are overlaid and the chemical shifts that superimpose are from the preceding '*i-1*' residue. That residue can then be found as an '*i*' by navigating to identical chemical shifts in the HNCACB. Sequential assignments can be connected (black lines) working from C-terminus to N-terminus (Fig. 8). For example, in strip 1 of figure 8, the HNCACB (red and blue peaks) has 4 peaks in total (two red and two blue). Two peaks (one red and one blue) overlay with the green peaks of the CBCA(CO)NH, these are the '*i-1*'. The remaining red and blue peaks are the C^α and C^β of the '*i*' residue, respectively. The C^α (blue) has a chemical shift around 59 ppm and C^β (red) has a chemical shift around 30 ppm, indicating the '*i*' as

a valine. Navigating to strip 2 using the chemical shifts of the green peaks of the CBCA(CO)NH (these are the '*i-1')* from strip 1 allows us to identify the next residue. The C^{α} (green overlaid on blue peak) has a chemical shift around 53.5 ppm and C^{β} (green overlaid on red peak) has a chemical shift around 27.5 ppm indicating a glutamate in strip two. The process is repeated until a unique sequence can be identified. This resulted in a partially assigned NdCd SET because there is still a lack of peak dispersion in the area between 7.8 - 8.5 ^{1}H ppm and 120 -125 ^{15}N ppm due to similar chemical shifts, which confers a degree of ambiguity, making assignments difficult (Fig. 9). An alternative approach would be necessary to resolve peak overlap and increase the number of assignments.

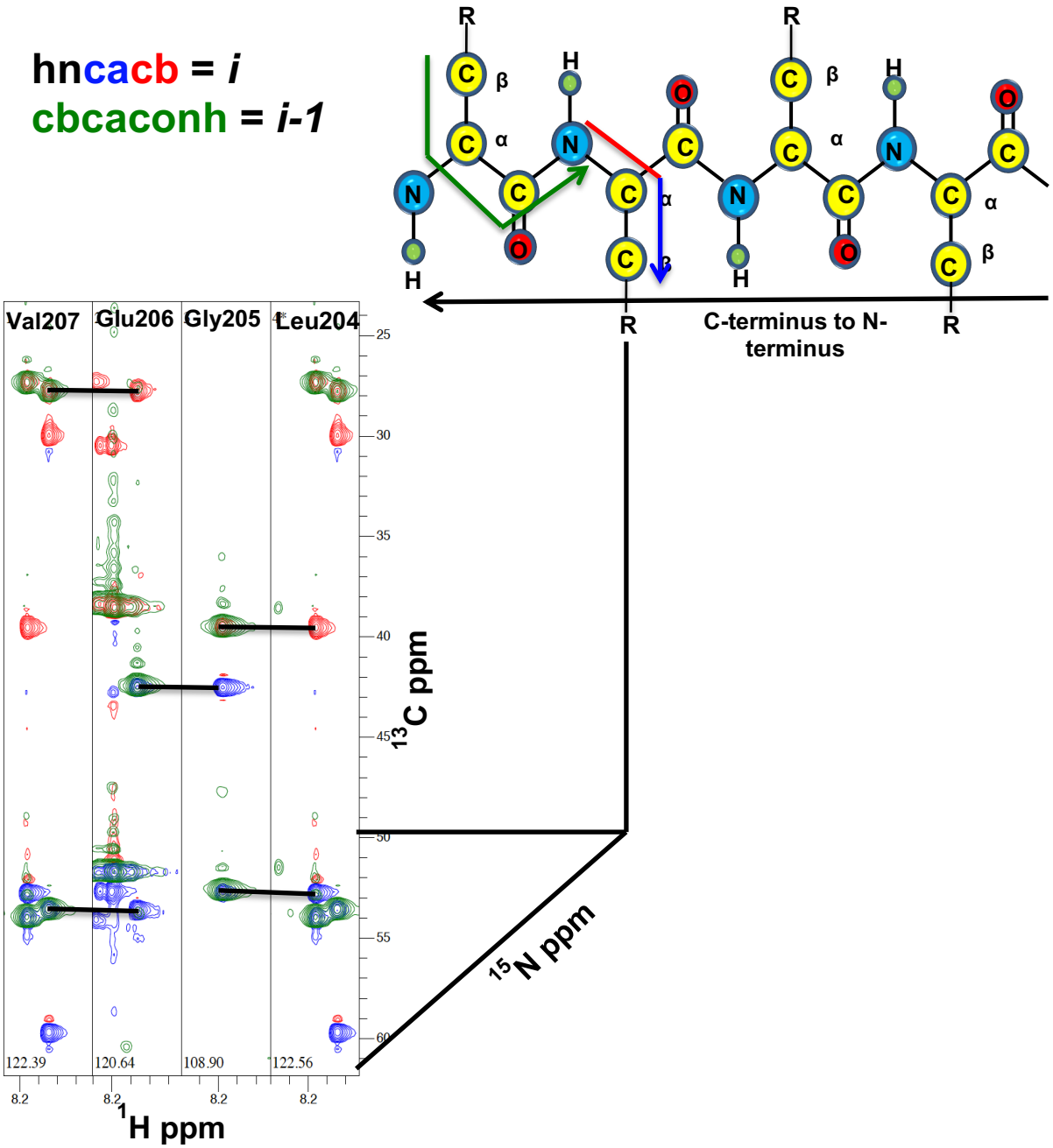

Figure 8| Triple resonance example demonstrating the 'i' and 'i-1' concept.

[^{1}H-^{15}N-^{13}C] HNCACB (red and blue) and CBCACONH (green) experiments overlaid for backbone assignments of NdCd SET. Data collected on 1mM protein. Red peaks represent Cβ while blue peaks represent Cα of the '*i*' and '*i*-1'residues. The green peaks represent the Cα and Cβ of the *'i-1'* residue. The spectra are overlaid and peaks in the HNCACB that superimpose with peaks in the CBCACONH correspond to the preceding '*i-1*' residue. That residue can then be found as an '*i*' by navigating to identical chemical shifts in the HNCACB. Sequential assignments can be connected (black lines) working from C-terminus to N-terminus by using the unique chemical shifts for each amino acid.

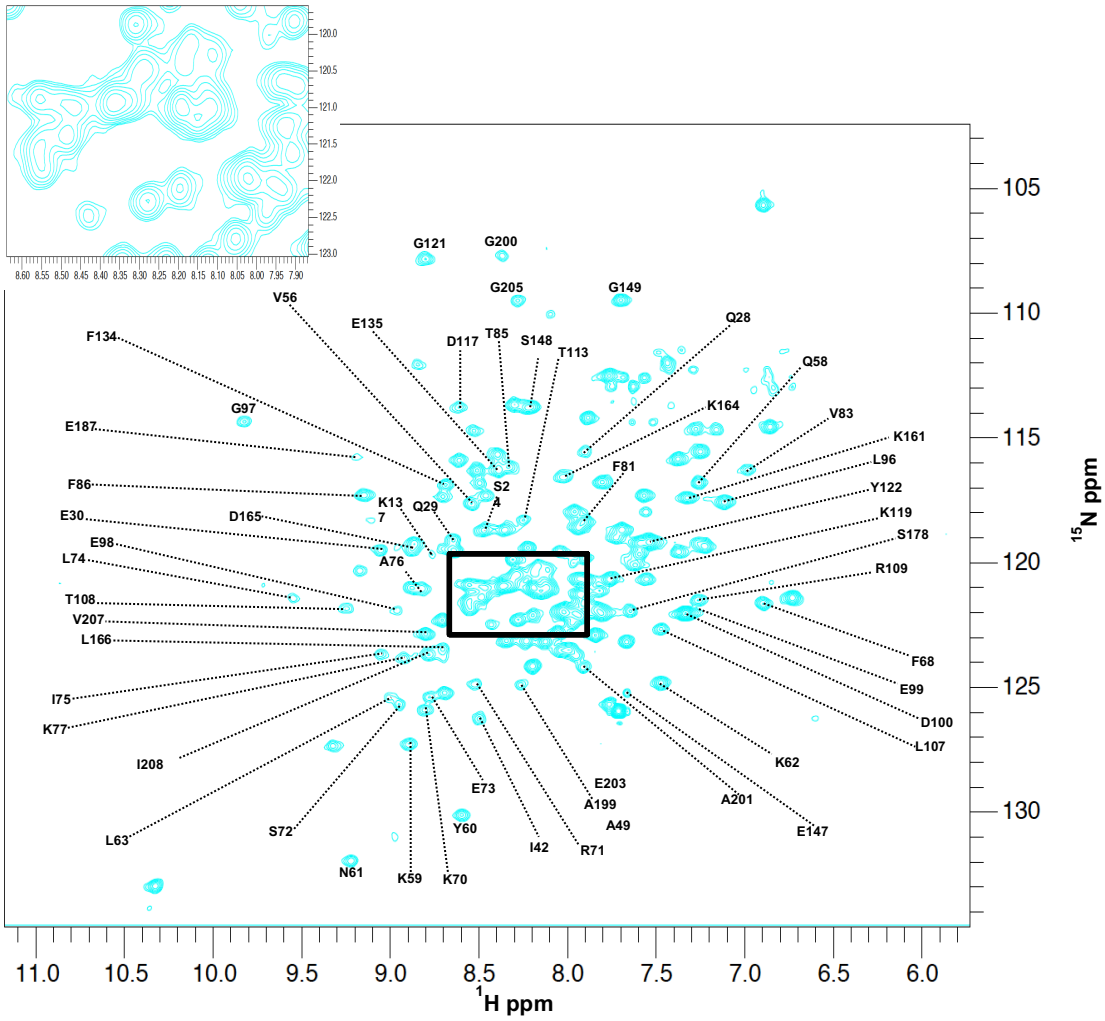

Figure 9| Partially assigned NdCd SET after [2H-13C-15H] triple resonance experiments.

The region between 7.8 - 8.5 ^{1}H ppm and 120 -125 ^{15}N ppm, magnified in the blowout, has significant signal overlap and a high degree of ambiguity caused by repeating residues and residues with similar chemical shifts.

Therefore, Nd SET was divided into three separate constructs, each overlapping by 30-40 amino acids (Fig. 6, lower panel). There is the risk of losing secondary structure by truncating the protein. However, secondary structure is not necessary for backbone assignments of proteins. Regardless, due diligence was executed by comparing the crystal structure with multiple secondary structure predications, the truncation sites were designed to fall within regions of random coil, so as to preserve secondary structure (Fig. 7, upper panel). A 'divide-and-conquer' methodology will help deconvolute regions of spectral overlap by allowing smaller fractions of these residues to be extracted for assignment. Figure 8 shows the two dimensional experiments for each of the truncated SET proteins except for TRUNC SET 1, which aggregates during the purification process and could not be used for an NMR spectroscopic experiments. These two-dimensional experiments establish a fingerprint for the protein where each peak corresponds to an amino acid of the protein being examined. The black arrows show common peaks between constructs, indicating residues in the regions designed to overlap (Fig. 10). As shown in Figure 10a-b, truncated SET constructs demonstrated significantly improved peak resolution. This shows that the 'divide-and-conquer' methodology will help with additional assignments. Identical triple resonance experiments were then performed on [^{1}H-^{13}C-^{15}N]-labeled TRUNC SET 2 (55% assigned) and TRUNC SET 3 (57% assigned). Each spectra was then be overlaid and assignments transferred onto larger and larger spectra. The final assignments were transferred to a NdCd SET [^{1}H-^{15}N] TROSY (Fig. 11) resulting in 54% total assignment of NdCd SET.

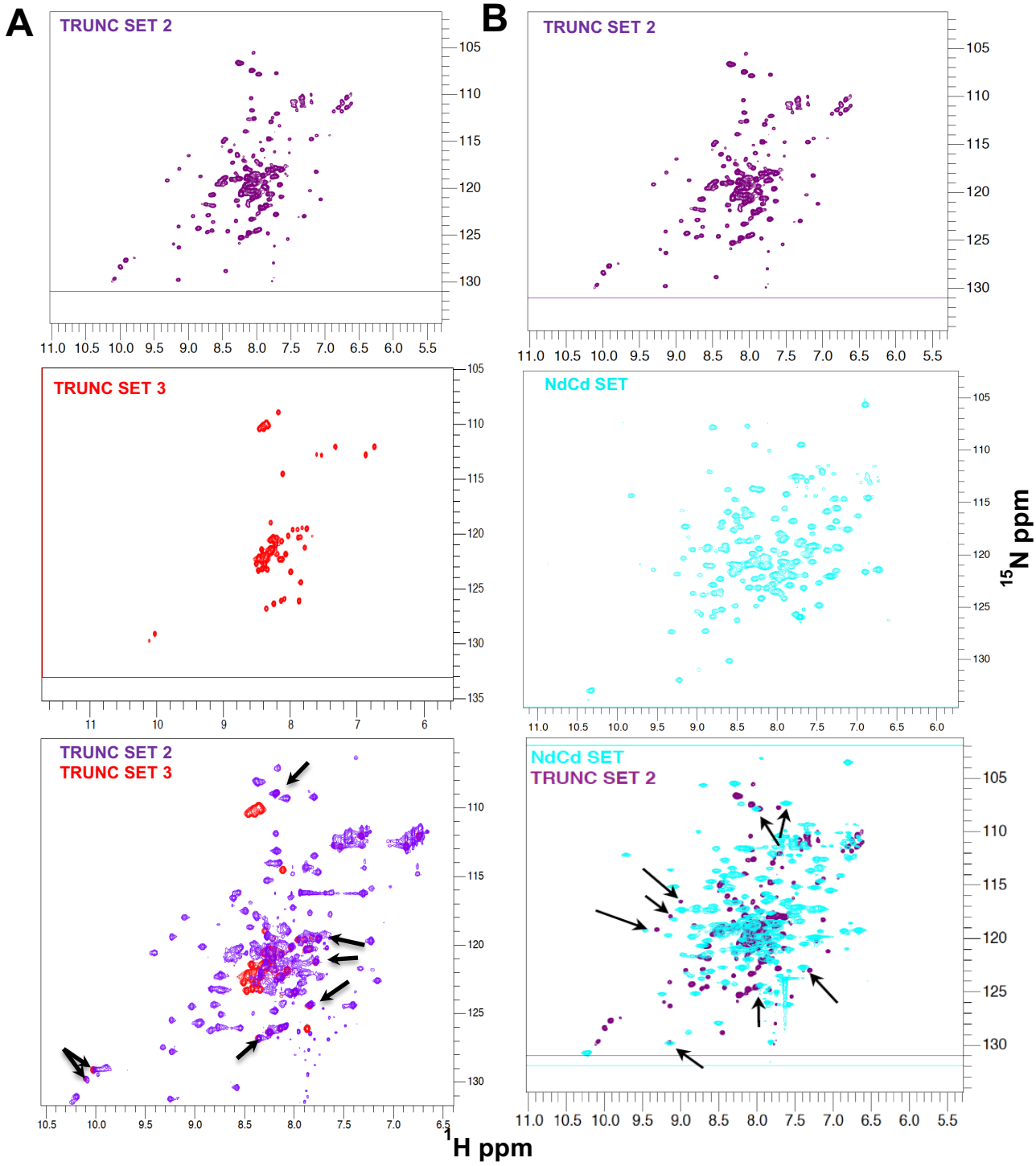

Figure 10| [1H-15N] HSQC of TRUNC SET 2 and 3.

(a) [^{1}H-^{15}N] HSQC spectra of TRUNC SET 2 **(b)** [^{1}H-^{15}N] HSQC spectra of TRUNC SET 3. **(c)** Overlaid [^{1}H-^{15}N] HSQC spectra of TRUNC SET 2 and TRUNC SET 3. Arrows indicate identical peaks used as reference points. **(d)** Overlaid [^{1}H-^{15}N] HSQC spectra of TRUNC SET 2 and NdCd SET. Arrows indicate identical peaks used as reference points.

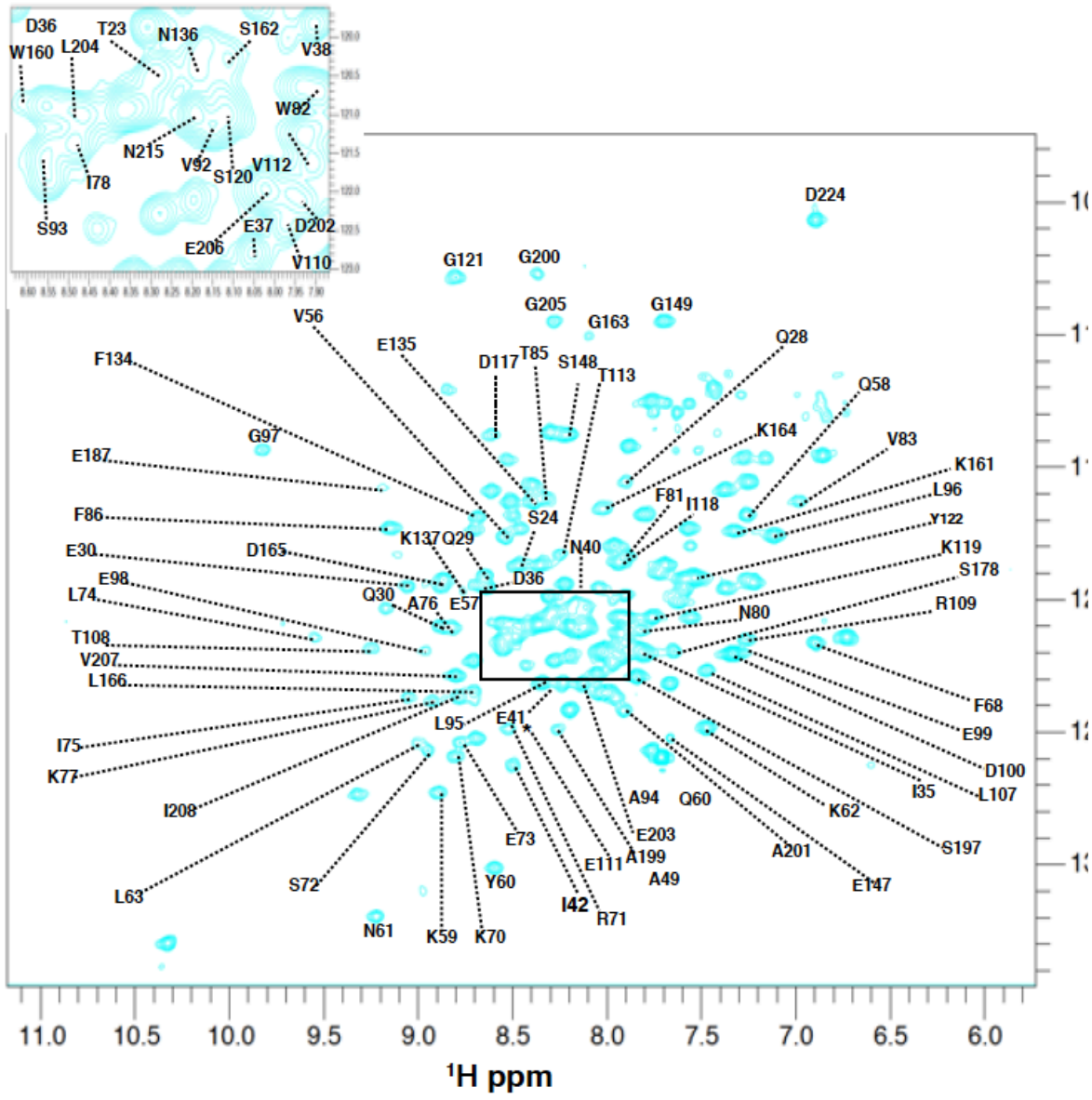

Figure 11| Assigned [^{1}H-^{15}N] TROSY spectra of NdCd SET.

Backbone assignments compiled from NdCd SET and TRUNC SET 2. Residues and assignments from TRUNC SET 3 are not present in the engineered NdCd SET construct. *denotes peak observable at a higher contour level than what is shown.

Summary

The backbone assignment of NdCd SET proved to be very difficult. Firstly, NdCd SET, although only 24 kDa, behaves like a much larger protein due to its propensity to form dimers (48 kDa) and tetramers (72k kDa) (this will be discussed in more detail in the next chapter). This resulted in a high degree of peak overlap and poor signal to noise cause by unfavorable relaxation properties. The resultant signal degeneracy made connecting related spin systems in long stretches extremely difficult. We alleviated the unfavorable relaxation properties to some extent by deuterating the sample and employing a divide-and-conquer approach. However, it was not enough to complete a full backbone assignment and collect the additional data necessary to solve an NMR solution structure. Ultimately resulting in 54% total assignment of NdCd SET. Dedicated, full-time NMR analysis could potentially increase the backbone assignment percentage, but it would take extensive protein engineering and time due to trial and error. Perdeuteration of the TRUNC SET constructs may help generate additional assignments by reducing unfavorable relaxation properties. Alternatively, If a construct of SET that preferred a monomeric state could be designed, while maintaining native secondary structure it may be possible to complete backbone assignments and solve an NMR solution structure. This would entail making a series of mutations within the dimerization domain of SET (E25-Q65) where charge swaps would repel each other and prevent dimerization.

Chapter 4: Structural examination of SET's lipid-binding capabilities

Extended conformation of D-*erythro*-C6-pyridinium ceramide is favored, stabilized upon binding to Nd SET

To uncover the molecular details of ceramide binding to SET, we first set out to determine lipid-binding from the perspective of ceramide. Previous data suggested that ceramide binds to SET in an "extended" conformation[97], in which the sphingosine backbone and fatty acyl chains are extended away from each other to form a long, almost linear chain. In the "compact" conformation, sphingosine backbone and fatty acyl chain run parallel to each other on the same side of the molecule (Fig. 12). We decided to use D-*erythro*-C6-pyridinium ceramide (C6P) to test whether SET binding requires an "extended" versus "compact" conformation. C6P is an established substrate for SET[148,192], and the structure of the pyridine ring can act as a molecular probe during nuclear magnetic resonance (NMR) studies due to its unique chemical shift signature. To begin, we utilized a construct with an N-terminal deletion (Nd) of 22 amino acids[241] (Fig. 13a). We purified both Nd-SET^{WT} and Nd-SET^{K209D}, a mutation that largely decreases ceramide-binding[97], and confirmed their intact secondary structures using circular dichroism (Fig. 13a-c). The loss of 22 N-terminal residues did not affect ceramide binding, whereas K209D conversion causes a threefold reduction of ceramide-SET binding, as shown by isothermal titration calorimetry (Fig. 14a-c).

The peaks of the raw data were integrated to create a Wiseman plot. An independent model was chosen to fit the isotherms. The stoichiometry is calculated as the *x*-axis value at the inflection point of an ITC sigmoidal curve. We assumed a 1:1 stoichiometry. Interestingly, the stoichiometry for both SET constructs is approximately 1:2 (n= ~0.5). Generally, knowledge of the reactant concentrations are the major source

of error in determining stoichiometry. This could be caused by the protein concentration being lower than we thought as a result of error in the measurement technique. The ligand concentration in the syringe could also be higher than originally calculated. More likely, it may allude to data showing SET as largely dimeric, which is consistent with the early work on SET characterization[180,182,242].

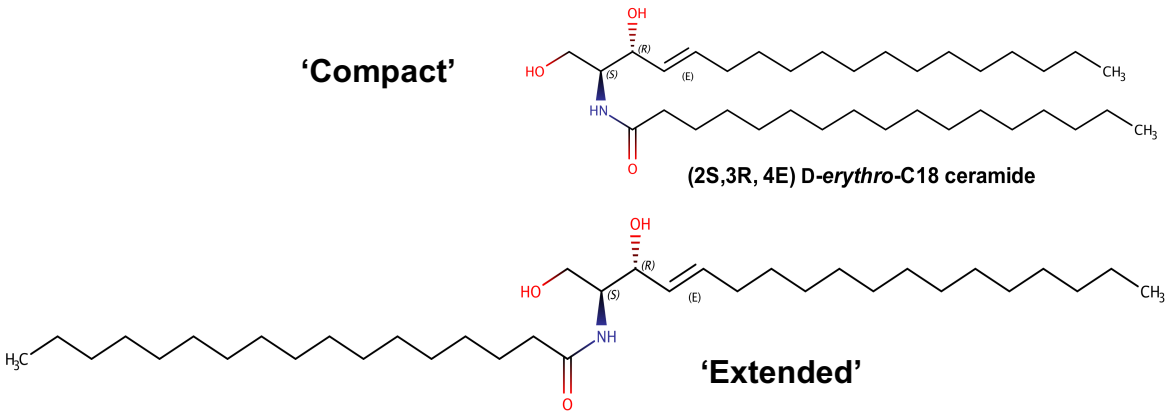

Figure 12| Comparison of 'compact' vs. 'extended' ceramide conformations.

In the "extended" conformation[97], the sphingosine backbone and fatty acyl chains are extended away from each other to form a long almost linear chain. In the "compact" conformation, sphingosine backbone and fatty acyl chain run parallel to each other on the same side of the molecule

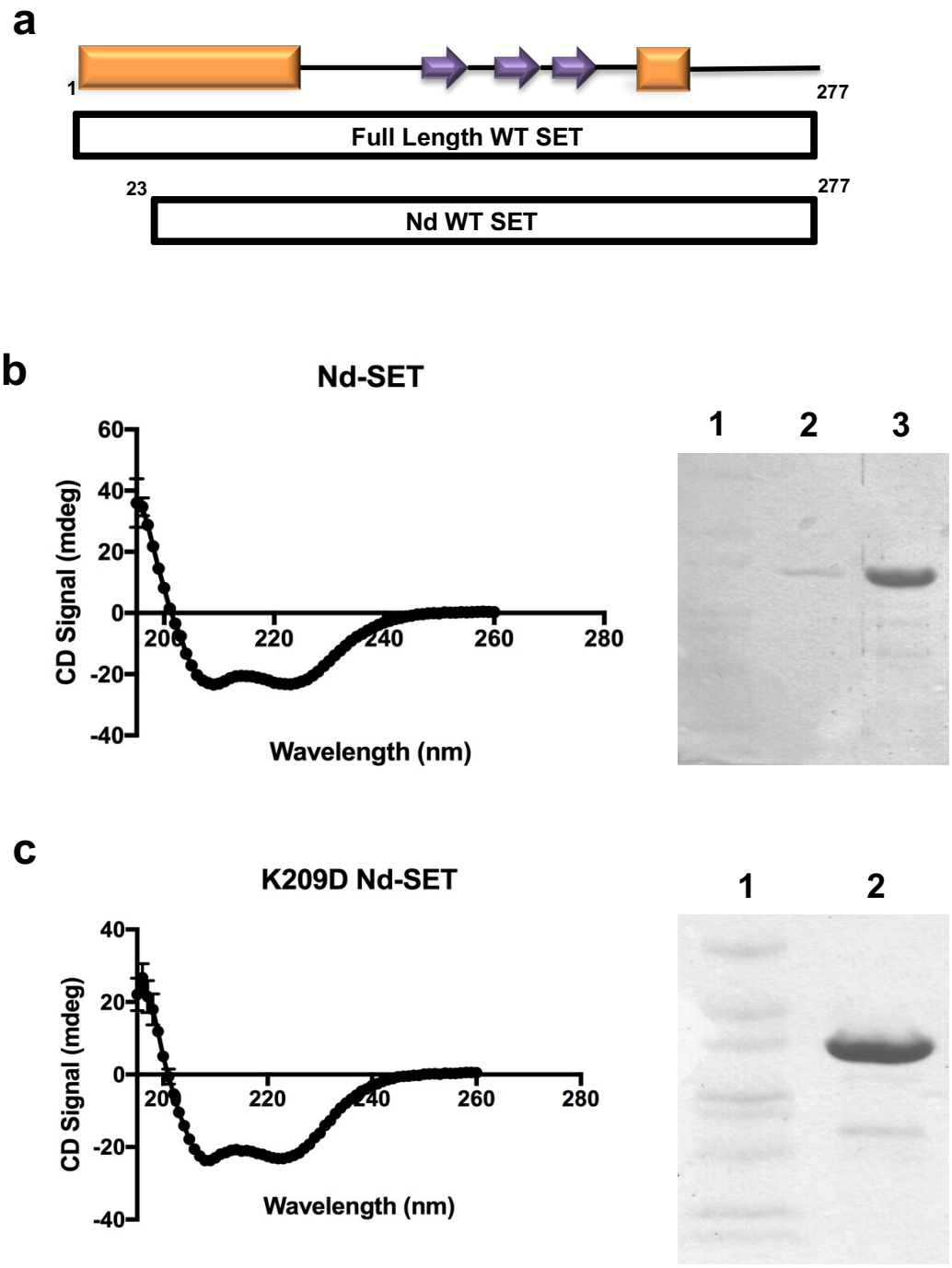

Figure 13| Expression of recombinant Nd SET constructs.

(a) Schematic representation of SET truncation. **(b)** CD spectra and Coomassie stained Nd-SET^{WT}. Lane 1: Marker. Lane 2: 50mM Imidazole wash. Lane 3: Purified Nd-SET after gel filtration. **(c)** CD spectra and Coomassie stained Nd-SET^{K209D}. Lane 1: Marker. Lane 2: Purified Nd-SET^{K209D} after gel filtration. All CD scans were in triplicate, averaged, and from 195-260 nm wavelength range at 20°C.

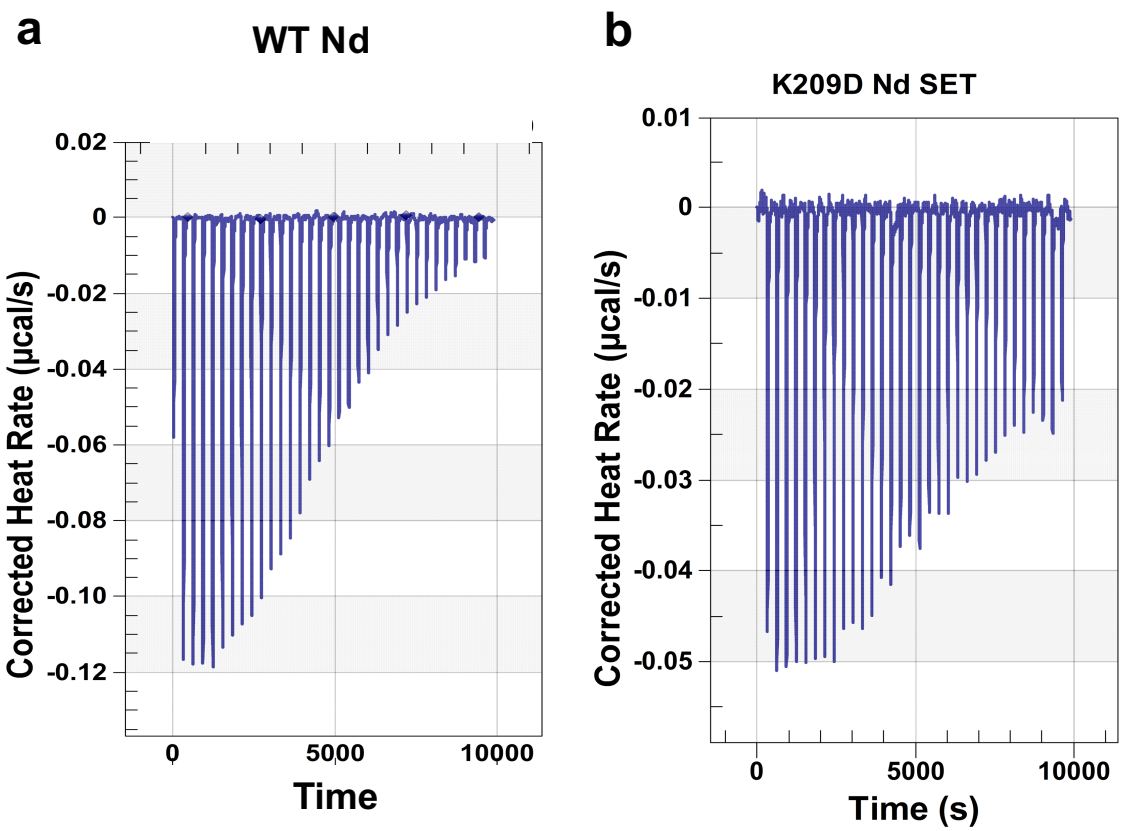

c

	K_D(nm)	n
Nd-SET^{WT}	281.4 ± 89.2	0.43 ± 0.01
Nd-SET^{K209D}	725.4 ± 68.6	0.42 ± 0.01

Figure 14| Isothermal titration calorimetry of D-*erythro*-C6-pyridinium ceramide and Nd SET.

(a) Corrected heat rate per injection as a function of time for Nd-SET^{WT}. **(b)** Corrected heat rate per injection as a function of time for Nd-SET^{K209D}. **(c)** Compiled ITC data presented as mean of n =3 individual experiments ± SEM. For all experiments 0.05mM C6P was titrated into 300µL of 0.021mM Nd-SET^{WT} or Nd-SET^{K209D}, respectively, at a 20˚C temperature lock.

Then, the two-dimensional (NOESY) NMR data were collected on C6P in order to identify which protons make contact with or are in close proximity to the binding pocket of Nd-SET^{WT}, and therefore obtain transferred magnetization. The 2D Nuclear Overhauser Enhancement Spectroscopy (NOESY) (Fig. 15a) provides information relating to distance between ^{1}H spin systems in space. The insert of Figure 15a shows an expanded region of interest, the pyridine ring, and how the proton resonances are coupled within 3-4 bonds. Focusing on the aromatic region, the diagonal peak H26 at 8.15 ppm (black arrow) has two cross peaks at 8.62 (H36-H25) and 9.0 (H26-H27) ppm indicating that it is in close proximity to both of these protons, whereas the two remaining diagonal peaks, at 8.62 (H25) and 9.0 (H27) ppm, only associate with the proton at 8.15 ppm, and not with each other (Fig. 15b). These data tell us that the peak at 8.15 ppm is located between the protons corresponding to peaks 8.62 and 9.0 ppm on the pyridinium ring. The full spectrum (Fig. 15a showed that the diagonal peak H27 (green arrow) has weak aliphatic cross peaks at 2.06 ppm and 1.43 ppm indicating that this proton is closest to lipid backbone. There is also a weak cross peak H27-H1O1(at 4.65 ppm), suggesting this proton associates with a hydroxyl group of the polar head group. These weak cross peaks indicate transient NOEs, suggesting that the acyl chain is rotating around the amide bond, exhibiting a rotation between “extended” and “compact” conformation of C6P (Fig. 15b). The missing proton resonances are due to signal overlap, exchange, and shielding effects of the lipid chain protons.

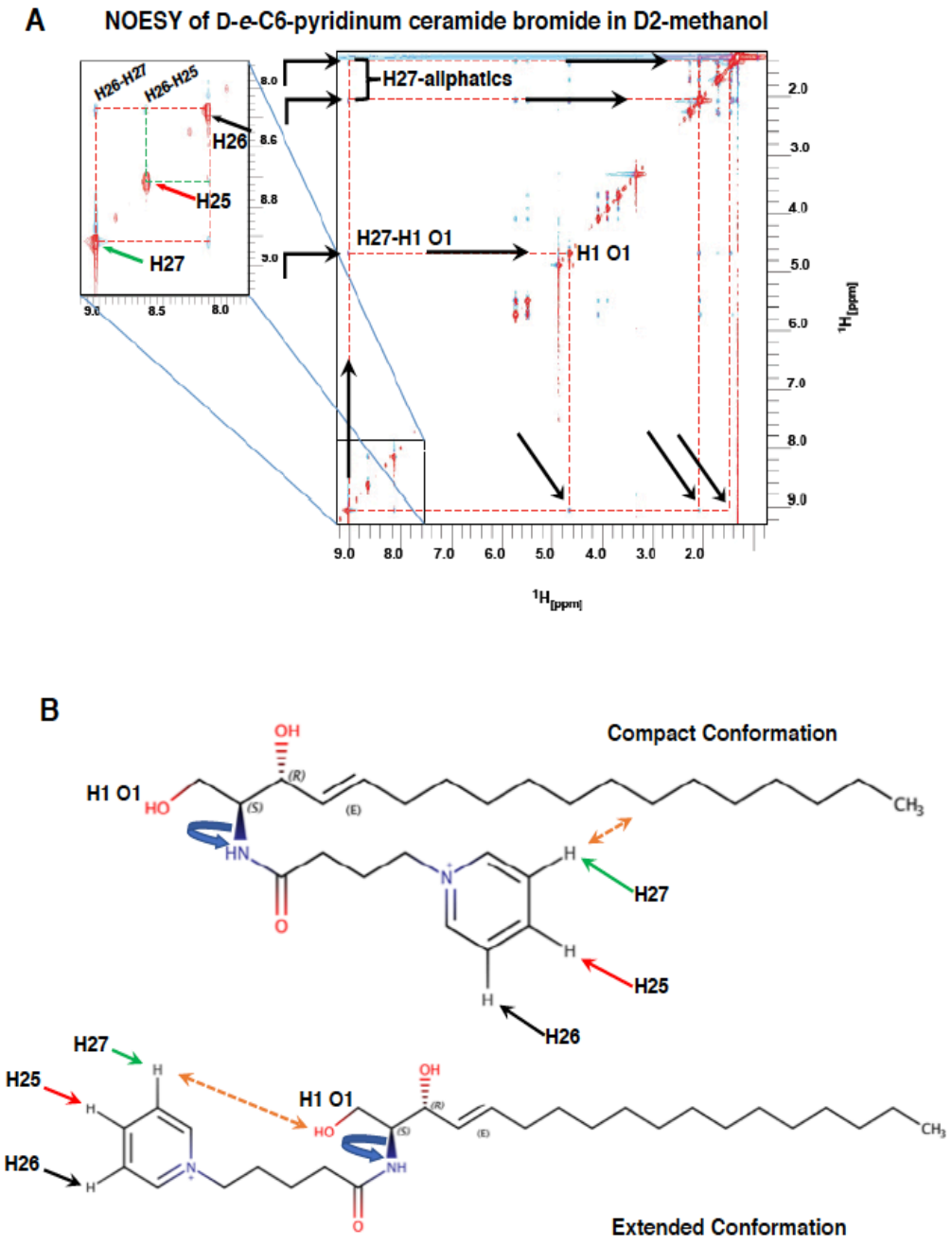

Figure 15| Nuclear Overhauser Enhancement spectroscopy of C6-D-e-pyridinium-ceramide bromide.

(a) [^{1}H-^{1}H] NOESY spectra of 0.5mM C6-pyridinium-ceramide. Data collected on C6-pyridinium-ceramide with 16 scans, 2048 points in the direct dimension, 256 points in the indirect dimension, and 500 ms NOE mix time. Black arrows indicate NOE signals between the pyridinium ring and other regions of the ceramide. **(b)** Green, red, and black arrows correspond to proton assignments on the aromatic ring. The orange double arrows indicates protons with weak NOEs between the sphingosine backbone and the pyridinium ring.

Saturation Transfer Difference NMR was performed to map and assign protons on the C6-pyridinium-ceramide involved in SET binding[243,244]. STD-NMR takes the difference between 'on-resonance and off-resonance' experiments. On-resonance experiments selectively saturate proton magnetization of the protein by a series of Gaussian pulses targeting methyl groups [233]. The saturation disseminates to other protons through intramolecular ^{1}H- ^{1}H cross relaxation pathways [245]. This saturation is then transferred to bound ligand, where it persists even after ligand dissociation with the protein. Off-resonance experiments are used to generate a reference spectrum. The difference between the two yields only resonances that have undergone saturation transfer. Due to the lower concentration of protein and much faster T_1 relaxation time its resonances are not usually visible.

As a positive control we tested the STD-NMR on a known binding system of BSA and tryptophan, using sucrose as an internal negative control [246]. The overlaid spectra show that tryptophan resonances (7-8 ppm) are present with increasing intensity as saturation times increase, while there are no sucrose resonances (3-4 ppm) present (Fig. 16a). As a negative binding control we ran STD experiments described below on 0.5 mM C6P in the presence of BSA. In the aromatic region between 7.5- 9 ppm we see no resonance buildup, and this is the region in which we see the greatest buildup during STD experiments with BSA (Fig. 16b).

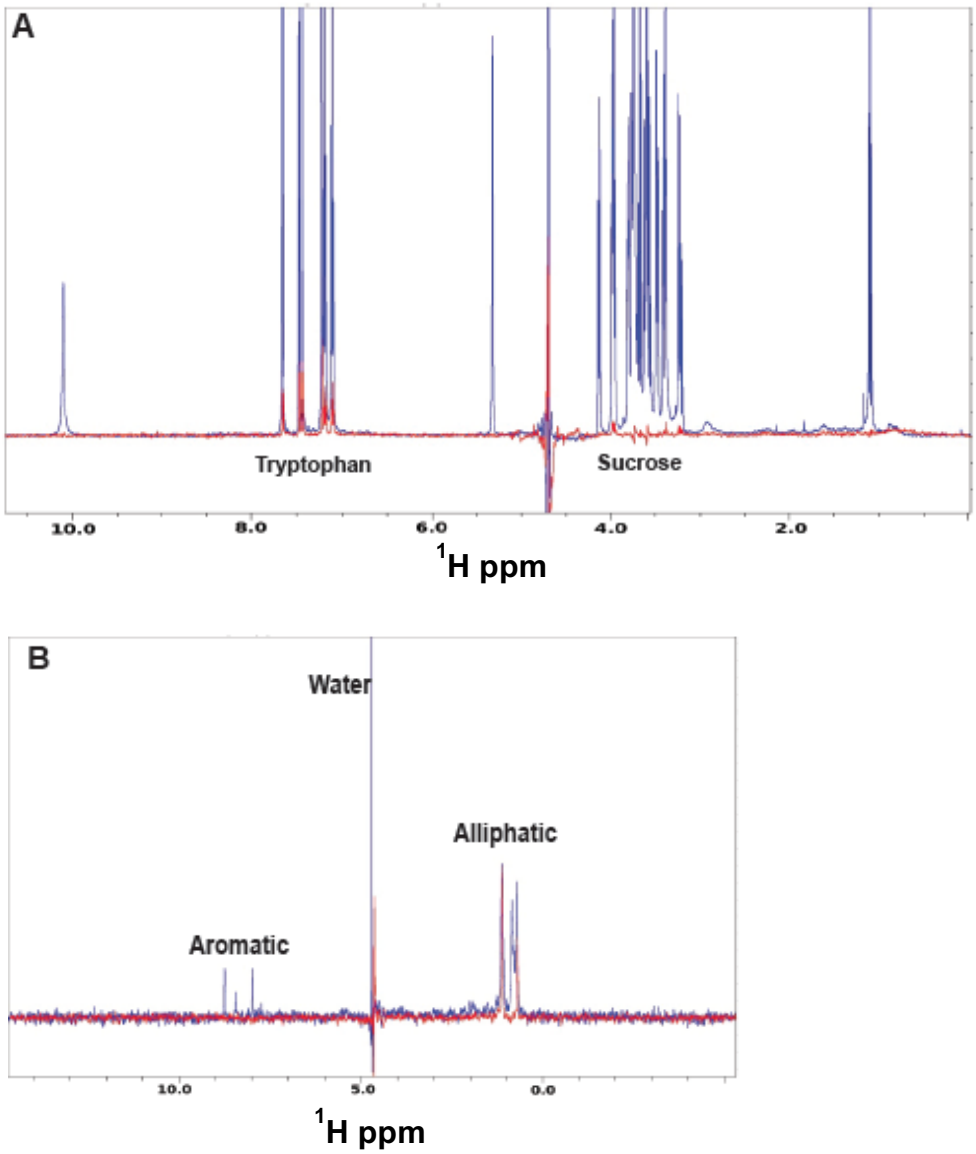

Figure 16| Positive and negative controls for Saturation Transfer Difference experiments.

(a) Tryptophan binding to BSA with a sucrose non-binding control to show pulse sequence works. The blue reference spectrum shows the hydrogen atoms of tryptophan and sucrose. The red spectrum shows an STD experiment where Trp is binding to BSA but not sucrose**. (b)** Negative binding control of C6-pyridinium-ceramide. The blue spectrum is 0.5 mM C6-pyridinium-ceramide, 6.0 s saturation, in the presence of BSA. The red spectrum is 0.5 mM C6-pyridinium-ceramide, 6.0 s saturation without protein.

The Saturation Transfer Difference (STD) experiments on Nd-SET^{WT} showed 3 distinct resonances in the aromatic region of the STD-difference spectra that corresponded to the three resonances of the pyridine ring identified in Figure 15a-b. There are also three distinct resonances in the aliphatic region of the STD-difference spectra. The resonances were seen to grow with intensity over the course of the saturation buildup until they reach a plateau (~4.0 seconds), where the "free pool" of ligand is saturated with magnetization (Fig. 17a). An STD amplification factor (STD-AF) was determined in the form of STD-diff= (Io-I_{sat})/Io, where the difference (STD-diff) was normalized by dividing each signal intensity by the strongest signal in the reference spectrum [234] (Fig. 17b). The difference spectrum was calculated using STD-diff= Io-I_{sat}, where Io is the reference spectrum, and I_{sat} is the saturation spectrum. The difference spectrum shows only ligand resonances that are bound to the receptor protein, or any protein signals which are further removed using a spin-lock filter.

The STD-AF was used to assess the absolute magnitude of the saturation transfer difference effect of a given proton. We detected maximal saturation around 4 s for each of the 3 aromatic peaks with H25 (7.98 ppm) peak acquiring the most magnetization followed by H27 (8.75 ppm) and H26 (8.43 ppm peaks). Proton signals detected within the aliphatic region of C6P, specifically 1.90 and 1.55 ppm, suggest the lipid backbone may also play a role in binding. However, degeneracy of aliphatic proton signals in two-dimensional spectra made specific assignments impossible. It is important to note that the chemical shifts reported here are different from those noted for the structural assignment of C6-pyridinium-ceramide. This difference is due to the fact that the structural assignment experiments were performed in methanol while all STD experiments were

carried out in PBS. Interestingly, data revealed that the conformation of C6P changes upon binding to SET. The proton at 8.75 ppm on the pyridine ring had strong interaction with SET (76% magnetization compared to the proton H25). These data suggested that C6-pyridinium-ceramide adopts an 'extended' lipid conformation, which exposes this proton to the lipid-binding pocket of SET (Fig. 17c). Otherwise, the proton H27 (8.75 ppm) on the pyridine ring would not gain magnetization in a "compact" conformation due to shielding by the sphingosine backbone. Thus, these data suggest that C6P binds SET in an "extended" confirmation, as predicted by the previous molecular modeling for ceramide-SET complex[97].

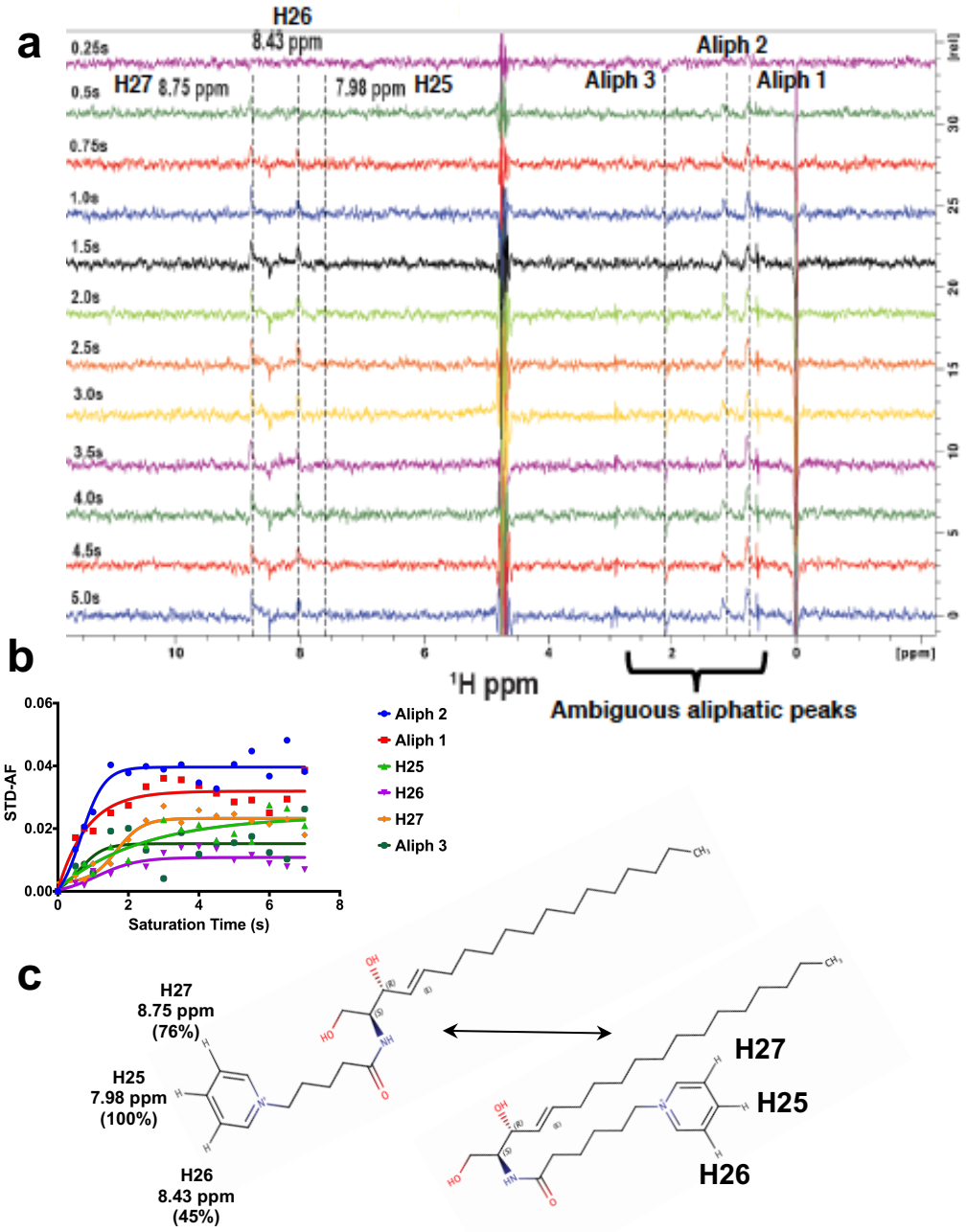

Figure 17| Analysis of D-*erythro*-C6-pyridinium ceramide binding to SET by STD-NMR.

(a) STD-NMR saturation build-up of 0.5mM C6P from 0.25s to 5.0s. **(b)** STD-NMR build-up curves were calculated using STD-Amplification Factor Isotherm. **(c)** Proposed model of ceramides binding in an 'extended' conformation.

D-*erythro*-C18 ceramide, but not its enantiomer L-*erythro*-C18 ceramide, binds SET

To continue the analysis of ceramide-SET binding we performed an *in silico* prediction using Molecular Operating Environment (MOE) to look at 'hot spots' or sites with a potential or propensity to bind lipid. This analysis tool calculates the relative positions and accessibility of the receptor atoms using the amino acid composition, such as hydrogen and hydrophobic interaction potentials[247]. The ligand binding prediction model shows three possible regions for lipid binding, **1:** at the interface between the N-terminal helix and globular domain, **3:** the cleft created by two anti-parallel beta sheet stabilized loops and an alpha helix, and **2:** at the base of the globular domain (Fig. 18). However, the interface between the N-terminal helix and globular domain predicts as the most likely area on SET to engage a ligand (Fig. 18). That region is marked as an area to monitor closely in subsequent binding experiments.

To analyze the effect of lipid-binding on SET, we engineered a double truncation SET construct (NdCd-SET) where 52 C-terminal residues (consisting of a long unstructured acidic tail) were deleted in addition to the 22 N-terminal residues (Fig. 19a). The size of the protein would be more amenable to NMR spectroscopy, while still containing the putative lipid-binding pocket[9]. NdCd-SET was purified to >95% purity, and we confirmed its native secondary structure using circular dichroism (Fig. 19b-c). We then performed titrations of D-*e*-C18-ceramide and L-*e*-C18-ceramide (Fig. 20) against ^{15}N-labeled NdCd-SET and monitored chemical shift perturbations (CSP) via [^{1}H-^{15}N] Transverse Relaxation Optimized Spectroscopy (TROSY). Ceramides were added to 0.9 mM ^{15}N-labeled NdCd-SET in 0.5 μM increments at 0.5-10 μM. The CSP

calculations showed that D-*e*-C18-ceramide, but not L-*e*-C18-ceramide, binds SET (Fig. 21a-c). The perturbations exhibited organized and confined clusters with increasing amounts of ceramide.

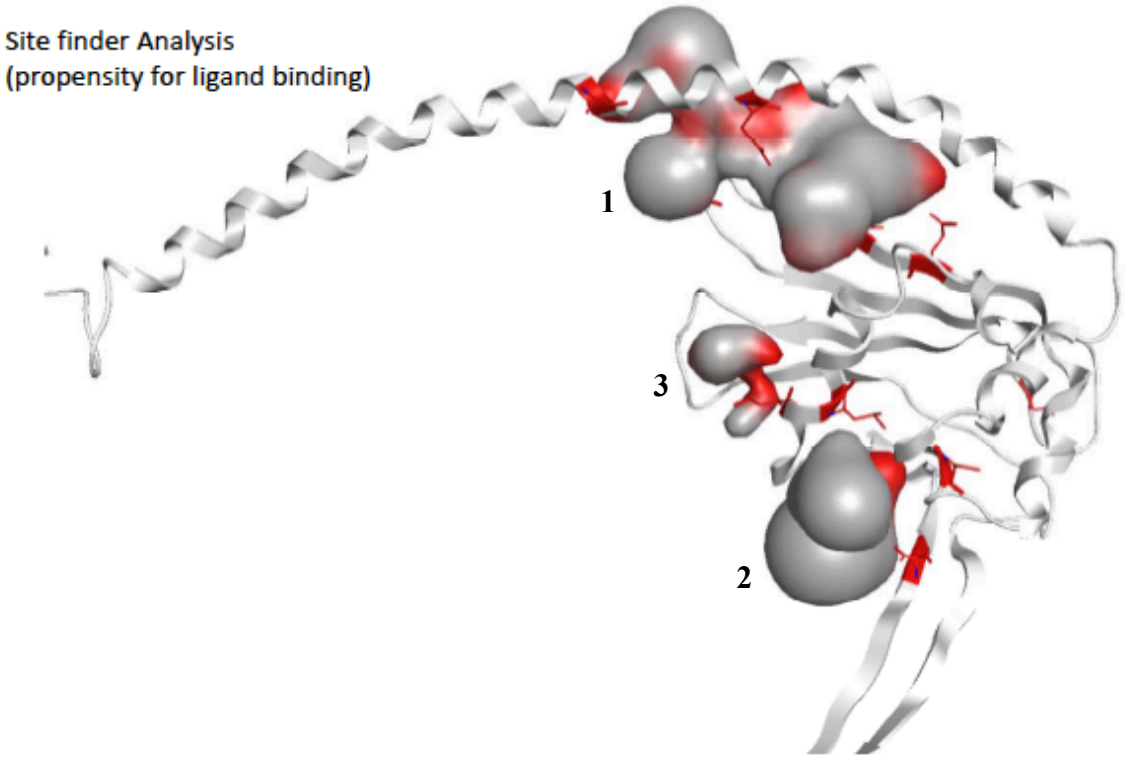

Figure 18| *In silico* prediction of ligand binding 'hot spots' on SET.

The propensity of ligand binding prediction model run in MOE shows three, labeled as 1,2, and 3, possible regions for lipid binding (in grey). The area between the N-terminal helix and globular domain projects as the most likely area on SET to engage a ligand.

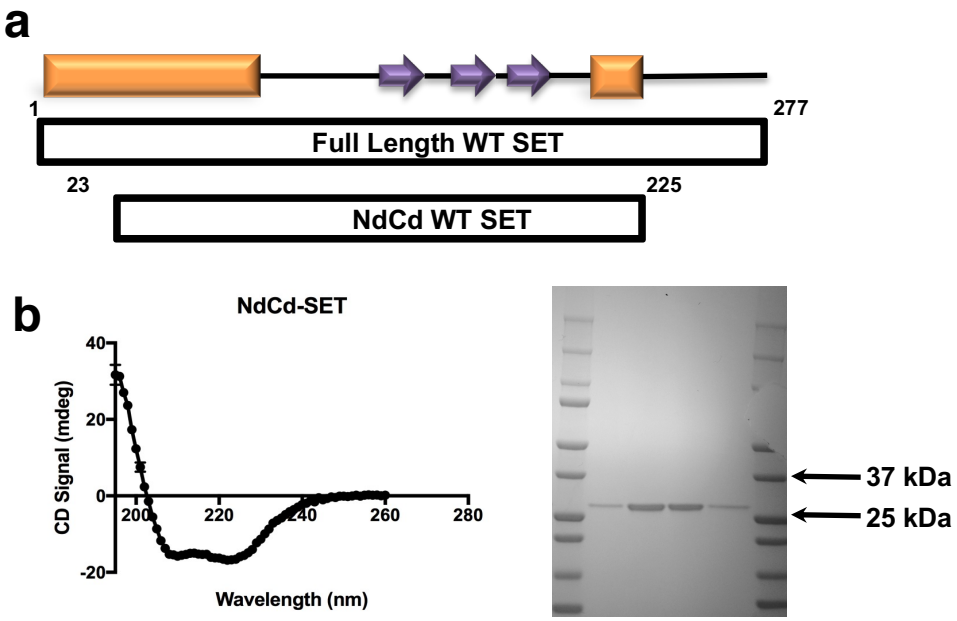

Figure 19| NMR compatible NdCd SET construction for expression.

(a) Graphic representation on recombinant SET proteins used in this study. **(b)** CD spectra and Coomassie stained NdCd SET demonstrating folded protein at >95% purity.

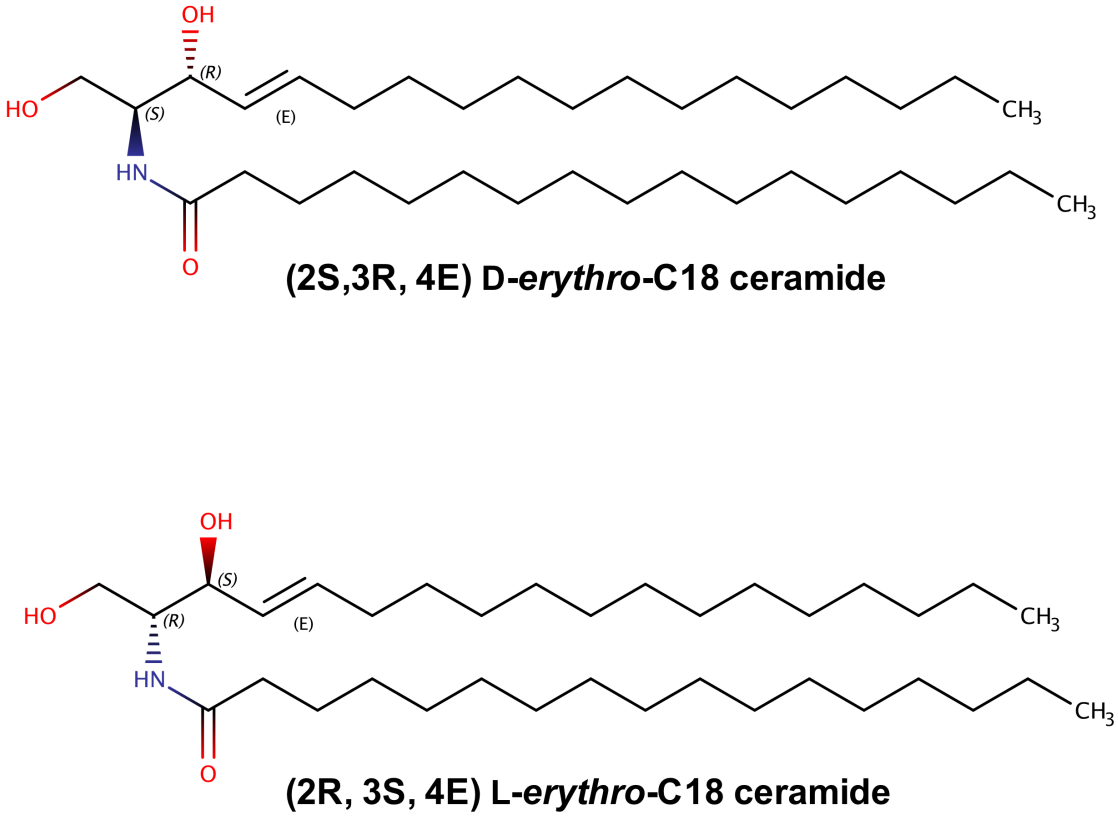

Figure 20| D-*erythro* vs. L-*erythro* stereochemistry.

The stereochemistry of ceramides is derived from the substitutions on carbons 2 and 3 of the sphingosine backbone. D-*erythro* is the naturally dominant conformation, making its enantiomeric partner L-*erythro* the ideal negative binding control.

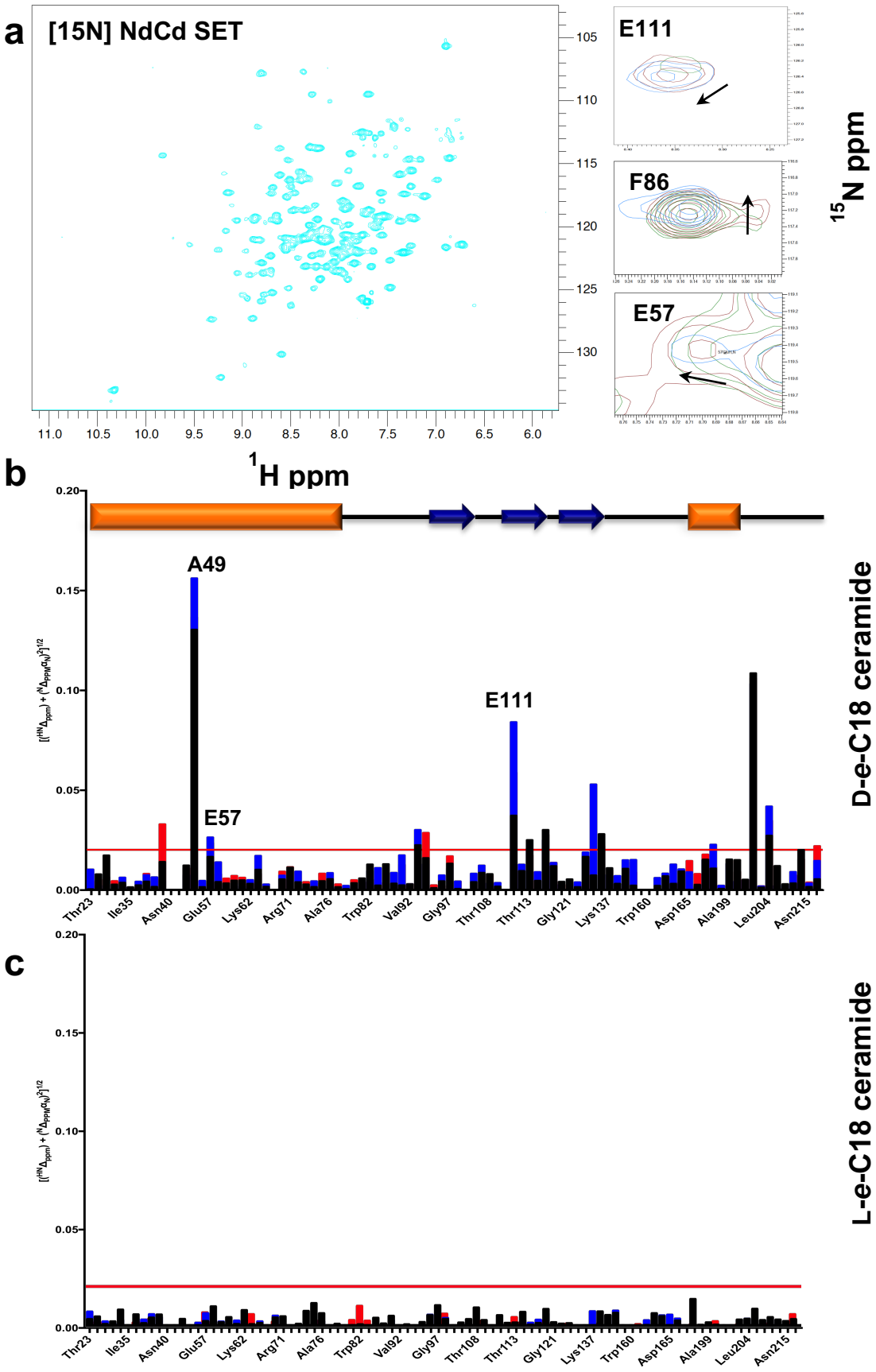
a
[15N] NdCd SET
E111
F86
E57
^{15}N ppm
^{1}H ppm
b
A49
E111
E57
D-e-C18 ceramide
c
L-e-C18 ceramide
Thr23
Ile35
Asn40
Glu57
Lys62
Arg71
Ala76
Trp82
Val92
Gly97
Thr108
Thr113
Gly121
Lys137
Trp160
Asp165
Ala199
Leu204
Asn215

Figure 21| Chemical shift perturbations of D-*erythro* and L-*erythro*-C18 ceramides.

(a) [^{1}H-^{15}N] TROSY spectra of 0.9 mM NdCd SET. Expansion of spectral regions showing specific residues perturbed upon binding with D-*e*-C18-ceramide. **(b)** CSP of NdCd SET induced by 3 μM (black bars), 7 μM (red bars), and 10 μM D-e-C18-ceramide (blue bars) as a function of assigned residue. **(c)** CSP of NdCd SET induced by 3 μM (black bars), 7 μM (red bars), and 10 μM L-*e*-C18 ceramide (blue bars) as a function of assigned residue. All CSP titrations were performed in triplicate. Red line is calculated as 3σ, and any value greater than 3σ is considered a significant shift.

The modeling and simulations were performed using Molecular Operating Environment (MOE 2018, Chemical Computing Group, Inc). Prior to simulations the monomer was isolated for the SET structure (pdb2E50: PMID 17360516) and protonated at T=310K, pH 7.3, salt at 200mM using GB/VI electrostatics[248]. We defined the ligand binding site using the chemical shift data as area constraints. We performed two iterative induced fit docking simulations. The first simulation allowed access to the entire protein; the second round used the top pose from the first round and used the ligand atoms as the site to be probed. The docking simulations used induced fit for the receptor and flexed the ligand. For each docking simulation the initial placement calculated 50 poses using triangle matching with London ΔG scoring, then the top 20 poses were refined using forcefield (Amber10:ETH) and Affinity ΔG scoring (Escore2). The affinity ΔG score is a linear function that estimates the enthalpic contribution to the free energy of binding. It was chosen due to an explicit hydrophobicity term, whereas most common scoring schemes use Van der Waals as a surrogate. The top 10 poses from these simulations were analyzed, and the final best pose was chosen based on being in concordance with the both CSP and ligand-observed NMR data followed by best E_score2 (Fig 22).

The final ceramide-SET model determined using the CSP data as constraints showed ceramide in an 'extended' conformation oriented along the interface between the helix of the dimerization domain and beta sheets in the globular region (Fig. 23). The polar head group of ceramide is stabilized by E111 and V112 (Fig. 24). The sphingosine backbone may be stabilized by hydrophobic interactions with Y127 (Figs. 23 and 24). The acyl chain appeared to be free to intercalate a cleft created by two anti-parallel beta sheet stabilized loops and an alpha helix (Figs. 23 and 25). Chemical shifts occurring

away, some highlighted in blue (Fig. 23), from the binding pocket were suspected to be the result of slight structural changes as the protein structure tightens around the lipid. Thus, these data suggest that ceramide binding results in site specific conformational changes in SET structure.

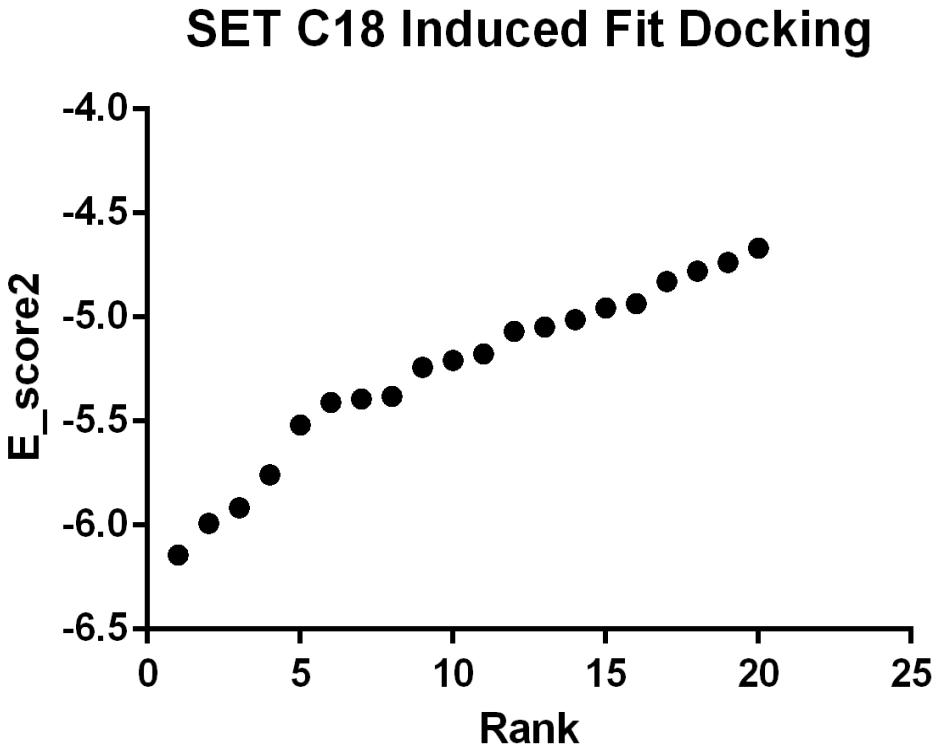

$$\Delta G = C_{\mathrm{hb}} f_{\mathrm{hb}} + C_{\mathrm{ion}} f_{\mathrm{ion}} + C_{\mathrm{mlig}} f_{\mathrm{mlig}} + \underline{C_{\mathrm{hh}} f_{\mathrm{hh}} + C_{\mathrm{hp}} f_{\mathrm{hp}}} + C_{\mathrm{aa}} f_{\mathrm{aa}}$$

Figure 22| Ranking of the top 20 Affinity scores for SET D-*erythro*-C18 ceramide modeling

Affinity ΔG (E_score2) rank for the top 20 poses. The lower the score, the more favorable the pose. Mathematical representation of Affinity ΔG (E_score2), where the hydrophobicity term is underlined. '*hh'* represents hydrophobic interactions, for example, interactions between alkanes. *'hp'* represents interactions between hydrophobics and polar atoms.

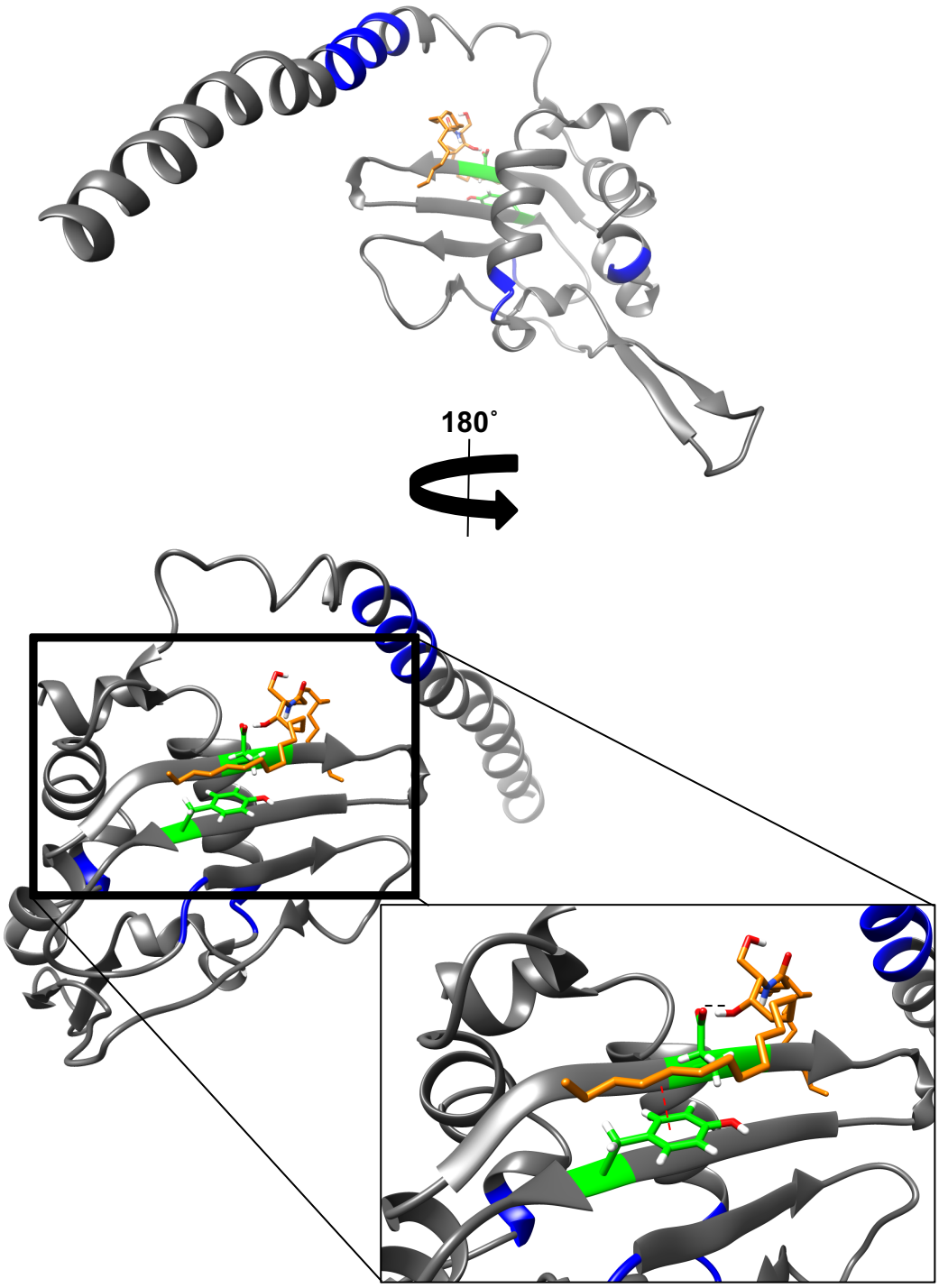

Figure 23| Pose of D-*erythro*-C18 ceramide-bound SET.

Model of D-*e*-C18-ceramide-bound SET. Residues colored blue and green underwent a significant chemical shift during NMR titration analysis.

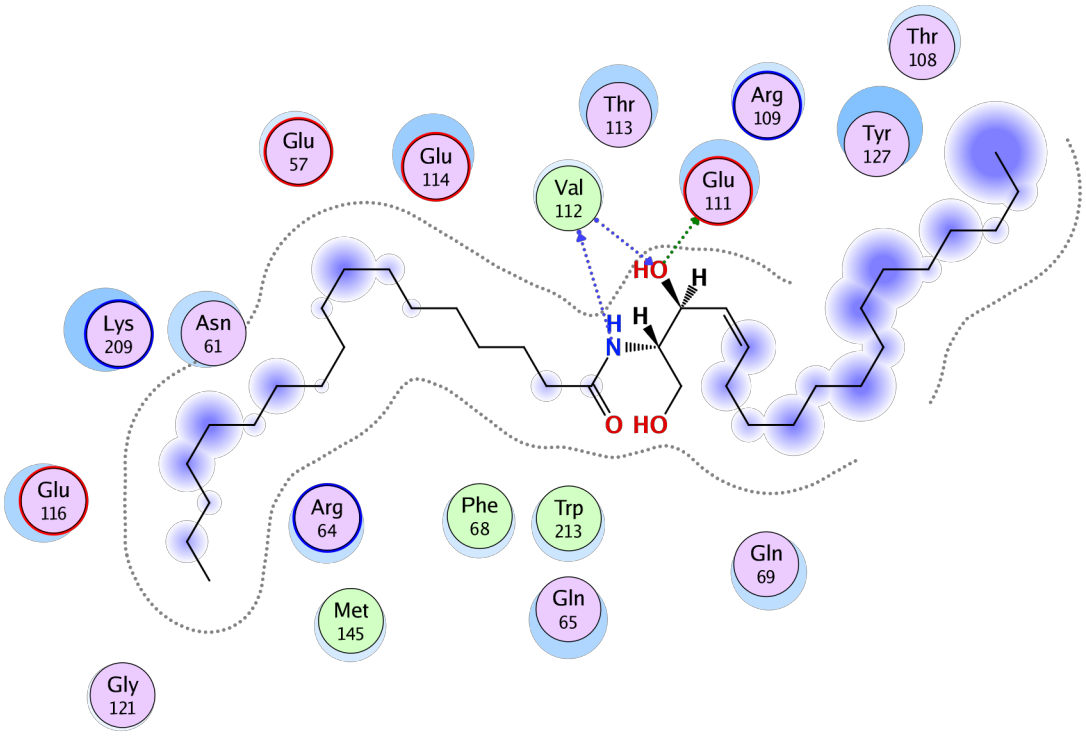

Figure 24| Interaction diagram of SET and D-e-C18 ceramide binding

Interaction diagram of D-*e*-C18-ceramide binding suggests that one of the prominent binding sites includes the E111, V112, and Y127.

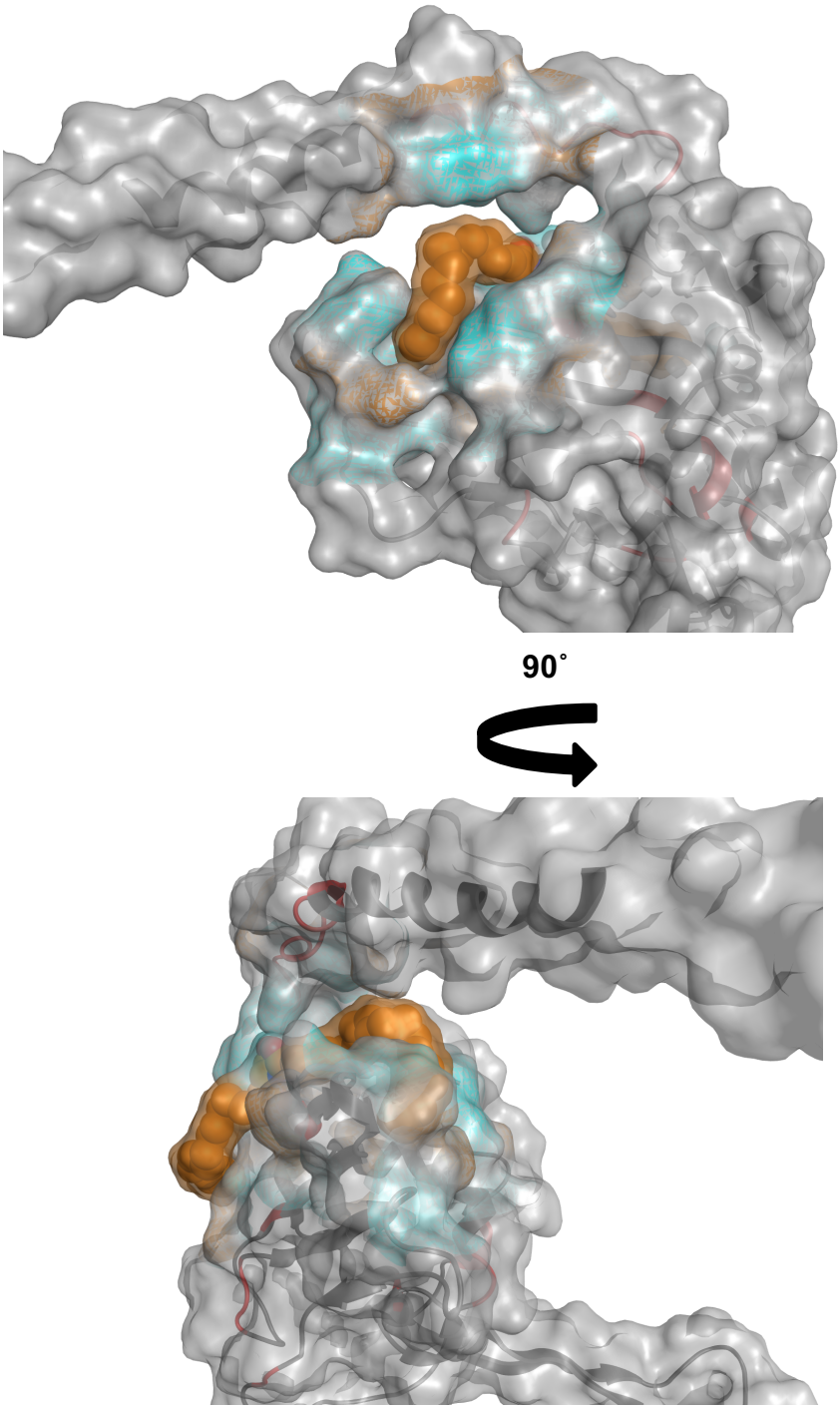

Figure 25| Molecular Surface-filled model of D-e-C18 ceramide and SET binding

The fill model applies a 'skin' to both the lipid and protein by covering the Van der Waals surface of the molecule while filling in solvent inaccessible gaps. The grey surface represents Van der Waals, and the orange surface shows lipid hydrophobic surface.

N-terminal helix is necessary for SET-FTY720 or SET-ceramide binding

In order to define the precise nature of the SET-FTY720 complex, we again employed a ligand-observed NMR strategy. 1D and 2D NMR spectra were collected on FTY720 in the presence and absence of SET protein. It was found that FTY720 was incompatible with STD-NMR experiments due to false positive signals generated during control experiments. As an alternative, we employed 2D [^{1}H-^{1}H]-TOtal Correlational SpectroscopY (TOCSY) in which we monitored FTY720 as a function of Nd-SET concentration. One drawback to this approach is that signals arising from protein aliphatic protons obscure aliphatic FY720 peaks, therefore preventing their use in binding quantification. To overcome this limitation, we instead focused on FTY720 peaks found in the less-crowded aromatic/amide region (7.0-8.0 ppm), specifically N1-H1, C5,C3-H1, and C2,C6/C3C5-H1 cross peaks. As expected, we observed peak broadening coincidental with increasing Nd-SET concentration (Fig. 26).

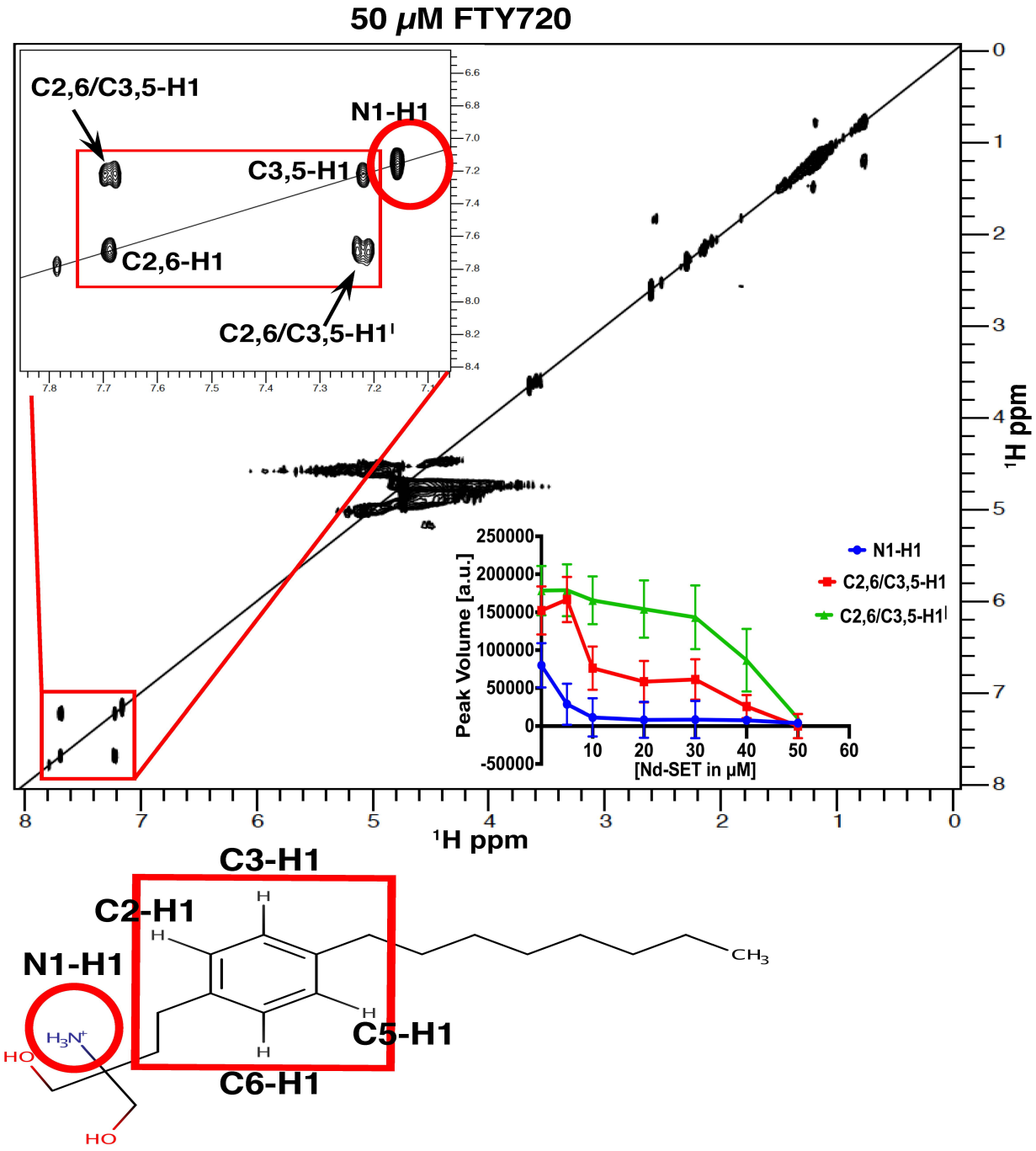

Figure 26| Aromatic and amine groups of FTY720 are important for binding to SET.

[^{1}H-^{1}H] TOCSY spectra of FTY720. Quantitation of line broadening as a function of peak volume and increasing concentration of Nd SET^{WT} (0-50 μM). Chemical structure of functional groups on FTY720 affected by the addition of Nd SET.

Next, we titrated FTY720 against ^{15}N-labeled NdCd-SET, and monitored CSP by [^{1}H-^{15}N] TROSY spectra (Fig. 27a-b). The modeling and simulations were performed using MOE 2018 (Chemical Computing Group, Inc). The same methodology was used with as outlined on page 62. The top 10 poses from these simulations were analyzed, and the final best pose was chosen based on being in concordance with the both CSP and ligand-based NMR data followed by best E_score2 (Fig 28).

Similar to D-*e*-C18-ceramide, the perturbations resulted in confined binding clusters with increasing amounts of FTY720 (0.5-10 μM) (Fig. 29). The final pose for FTY720 in complex with NdCd-SET was strikingly similar to the C18-ceramide/NdCd-SET model, highlighting an overlapping set of protein residues that define the lipid-binding pocket. These include R64, Q65, F68 and R69 of the helical dimerization domain, and residues E111, V112, and W213 found in the globular region (Figs. 29 and 30). Interestingly, with both FTY720 and C18-ceramide poses, a similar conformational transition from alpha-helix to random coil in the N-terminal helix was predicted by molecular modeling and simulations (Figs. 25 and 29). Based on these data, E111 appears to play an important role in stabilizing the head groups of ceramide and FTY720 (Figure 30). Data also indicate that R71 may be a key mediator of the FTY720-SET interaction, while D-*e*-C18 ceramide did not show any association with R71 (Fig. 26 and 30). This interaction between FTY720 and R71 of SET seemed to be driven by an electrostatic cation/π-arene mechanism (Fig. 30). The structural data also suggested that FTY720 is more buried in the cleft created by two anti-parallel beta sheet stabilized loops and an alpha helix than ceramide (Fig. 31). To account for protein specificity, FTY720 was

titrated against Immunoglobulin 1. The CSP was calculated, and showed no significant shifts (Fig. 32e).

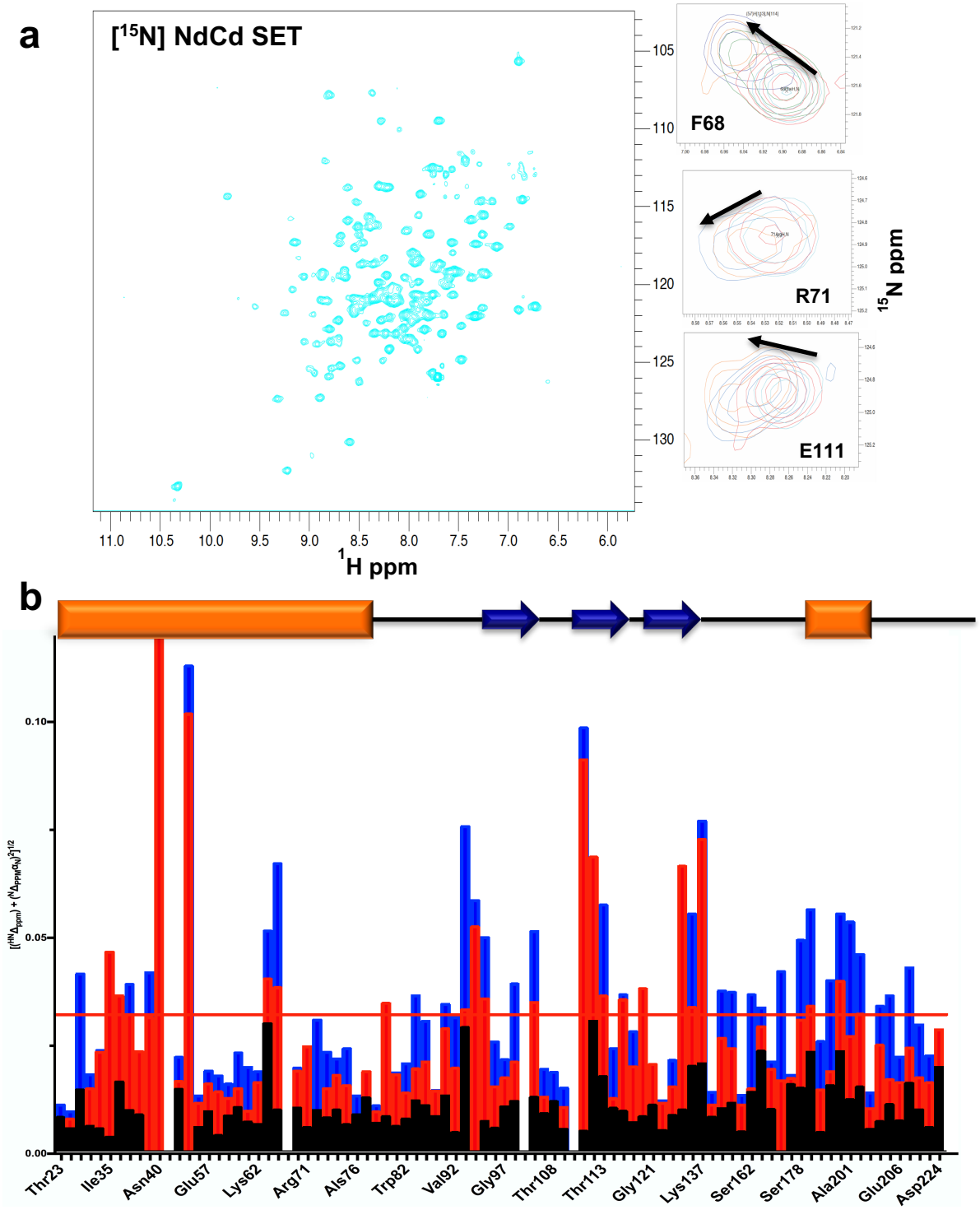

Figure 27| Chemical shift perturbations caused by the addition of FTY720.

(a) [^{1}H-^{15}N] TROSY of NdCd SET. Expansion of spectral regions shows specific shifts upon FTY720 binding. **(b)** CSP of NdCd SET induced by 3μM (black bars), 7μM (red bars), and 10μM FTY720 (blue bars) as a function of assigned residue of n= 3 trials. Red line is calculated as 3σ, and any value greater than 3σ is considered a significant shift.

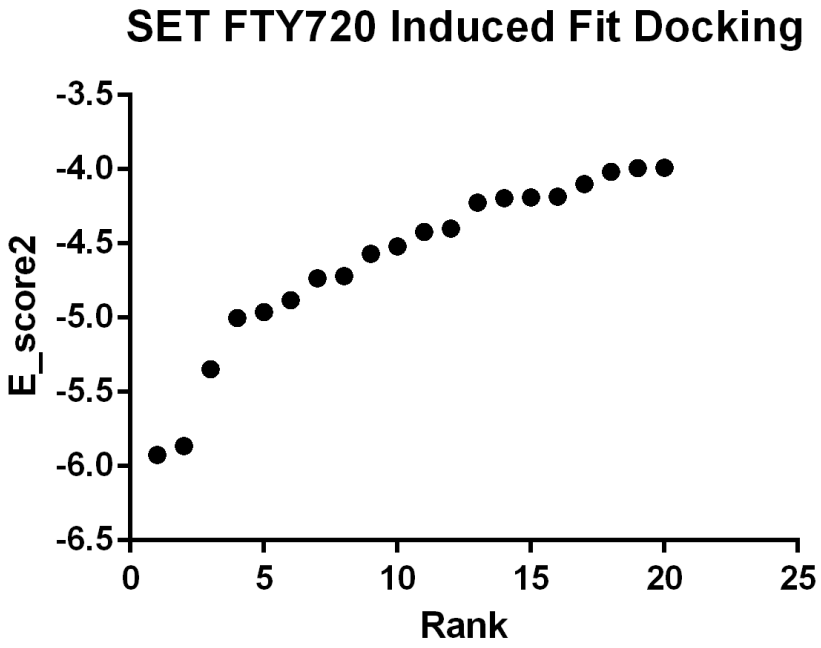

$$\Delta G = C_{\mathrm{hb}} f_{\mathrm{hb}} + C_{\mathrm{ion}} f_{\mathrm{ion}} + C_{\mathrm{mlig}} f_{\mathrm{mlig}} + \underline{C_{\mathrm{hh}} f_{\mathrm{hh}} + C_{\mathrm{hp}} f_{\mathrm{hp}}} + C_{\mathrm{aa}} f_{\mathrm{aa}}$$

Figure 28| Ranking of the top 20 Affinity score for FTY720/SET binding

Affinity ΔG (E_score2) rank for the top 20 poses. The lower the score, the more favorable the pose. Mathematical representation of Affinity ΔG (E_score2), where the hydrophobicity term is underlined. '*hh'* represents hydrophobic interactions, for example, interactions between alkanes. *'hp'* represents interactions between hydrophobics and polar atoms.

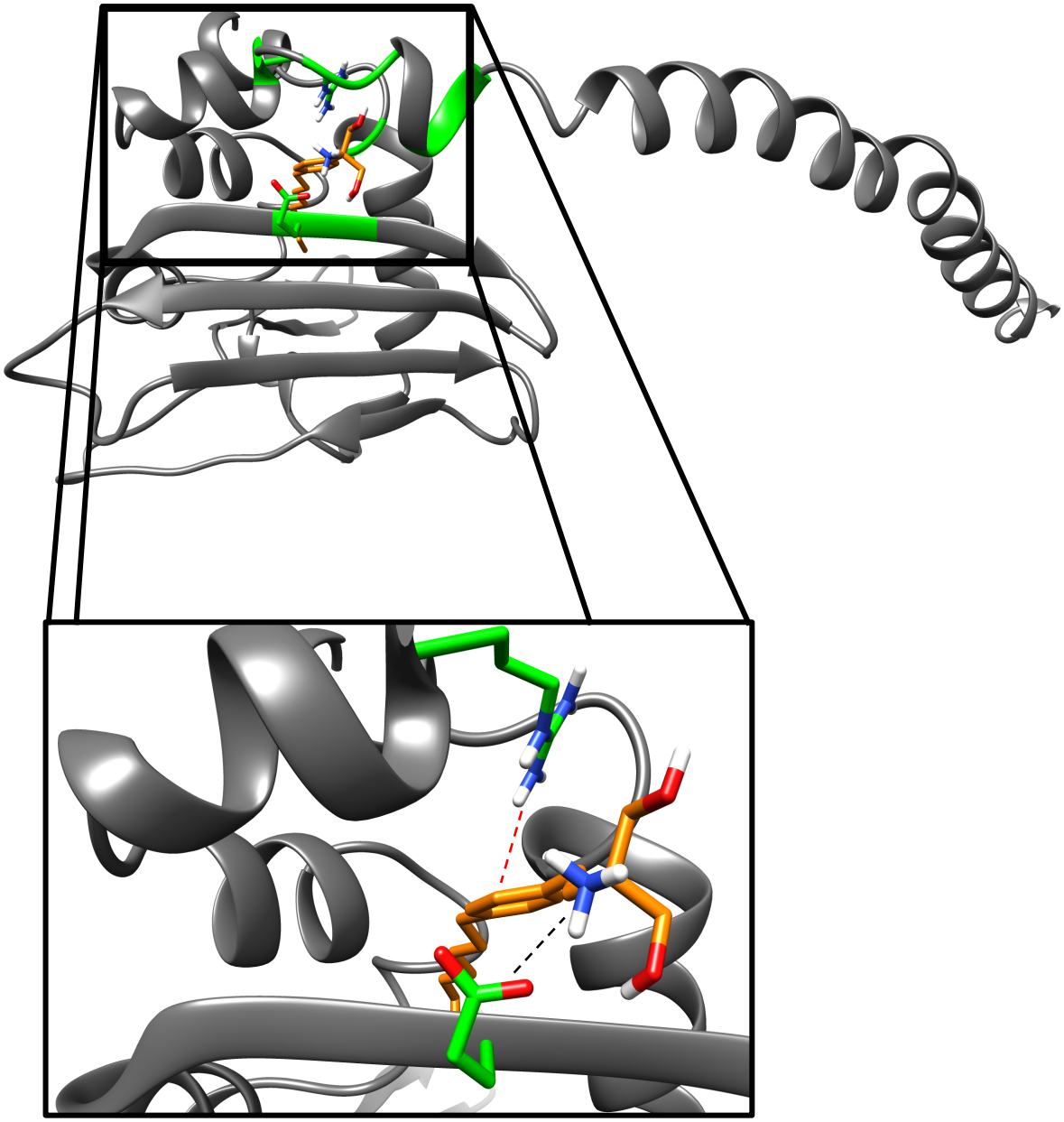

Figure 29| Model of FTY720-bounnd SET.

Residues colored green underwent a significant chemical shift during NMR titration analysis.

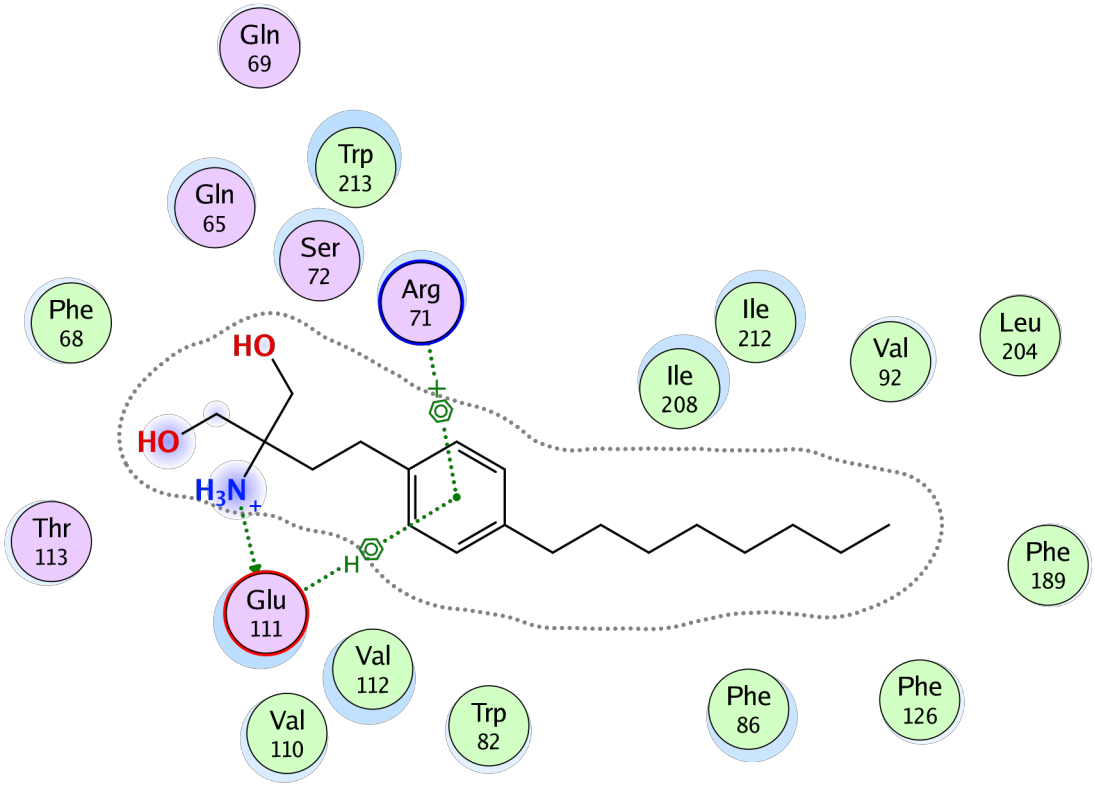

Figure 30| Interaction diagram of SET and FTY720 binding

Interaction diagram FTY720-SET binding generated using MOE suggests that one of the prominent binding sites includes the E111 and R71 residues, which electrostatically interact with the amide group and the π electrons of the phenyl ring, respectively.

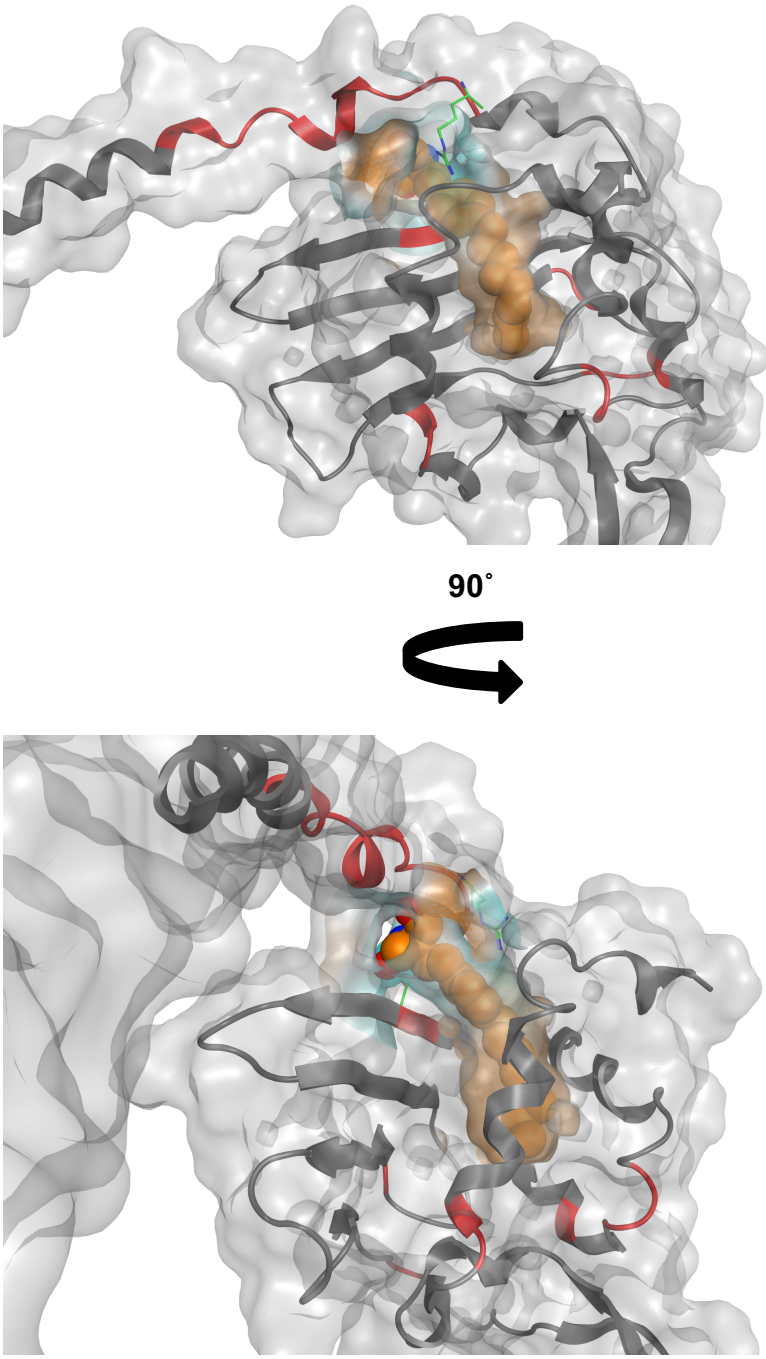

Figure 31| Molecular Surface-filled model of FTY720 ceramide and SET binding

The fill model applies a 'skin' to both the lipid and protein by covering the Van der Waals surface of the molecule while filling in solvent inaccessible gaps. The grey surface represents Van der Waals, and the orange surface shows lipid hydrophobicity. FTY720 fully intercalates into the core of SET.

The N-terminal helix containing the dimerization domain of SET seems to be important in both FTY720 and D-*e*-C18 ceramide binding. To test this, we used the TRUNC-SET-2 recombinant protein (Fig. 30a-c), which lacks the entire N-terminal helix in a titration against FY720 while monitoring CSP by [^{1}H-^{15}N] TROSY spectra. There were no chemical shifts detected on TRUNC-SET-2 with FTY720 (Fig. 30d). Thus, these data suggest that the N-terminal helix is necessary for SET-FTY720 (and SET-ceramide) binding.

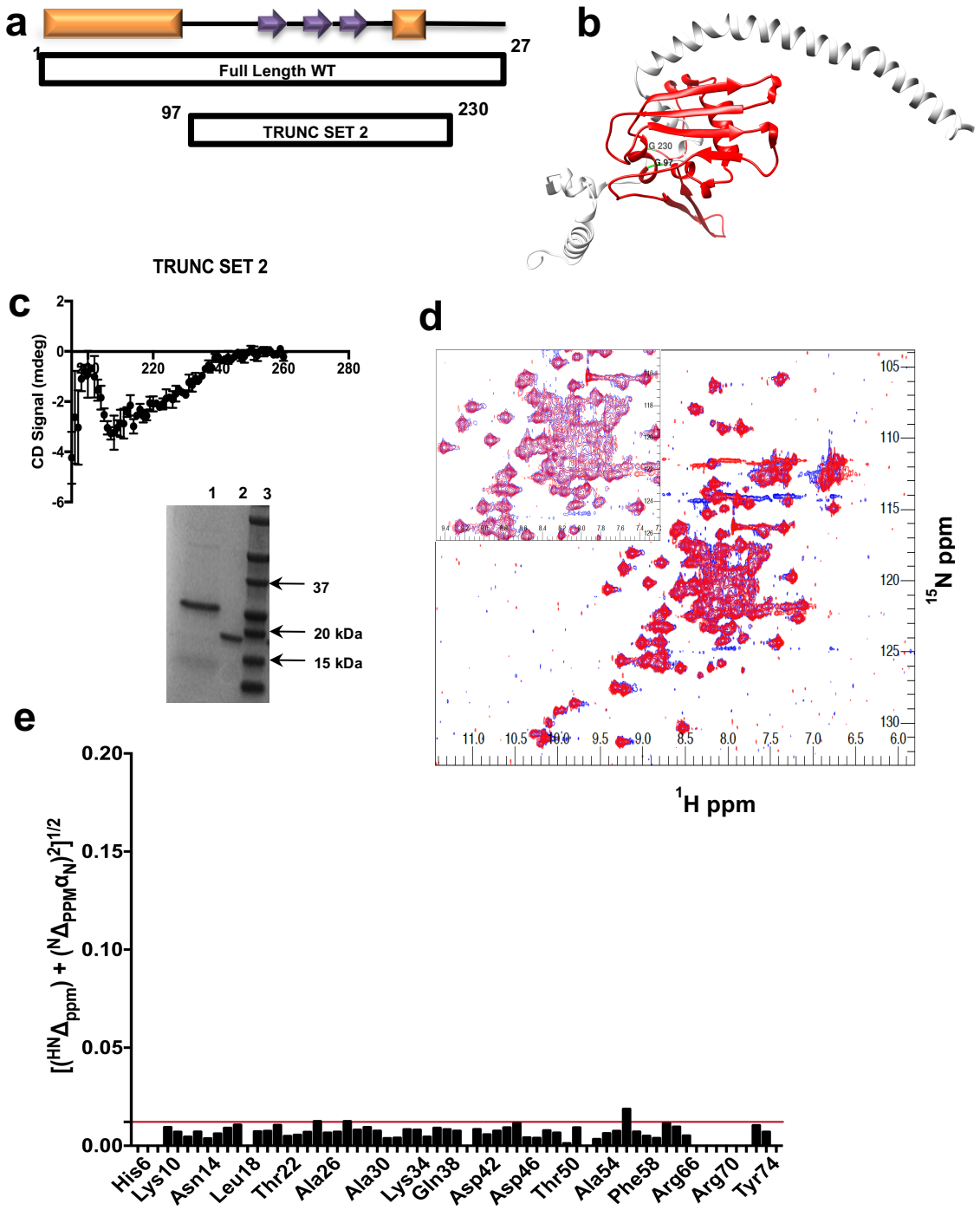
a
1
27
Full Length WT
97
230
TRUNC SET 2
b
G 230
G 97
TRUNC SET 2
c
CD Signal (mdeg)
2
0
-2
-4
-6
220
240
260
280
1 2 3
37
20 kDa
15 kDa
d
105
110
115
120
125
130
11.0
10.5
10.0
9.5
9.0
8.5
8.0
7.5
7.0
6.5
6.0
15N ppm
1H ppm
e
[(HNΔppm) + (NΔPPMσN)2]1/2
0.20
0.15
0.10
0.05
0.00
His6
Lys10
Asn14
Leu18
Thr22
Ala26
Ala30
Lys34
Gln38
Asp42
Asp46
Thr50
Ala54
Phe58
Arg66
Arg70
Tyr74

Figure 32| N-terminal helix containing the dimerization domain is essential for lipid-binding.

(a) schematic representation of recombinant SET used in this study. **(b)** model of SET truncation, illustrating the loss of the N-terminal helix. **(c)** Coomassie stained gel and CD spectra showing folded protein with a high percentage of random coil and β-sheets. **(d)** [^{1}H-^{15}N] TROSY spectra overlay of TRUNC SET 2 with and without 10μM FTY720, demonstrating no chemical shifts. **(e)** CSP of Immunoglobulin 1 (GB1) and 10μM FTY720. Lack of significant CSP indicates protein specificity. CSP titrations were performed in triplicate. Red line is calculated as 3σ, and any value greater than 3σ is considered a significant shift.

To validate residues of SET that may be important for ligand binding, identified by both NMR and pose data, we generated two SET mutants, SET^{E111A} and SET^{R71A} that should attenuate FTY720 binding. Circular dichroism showed the mutants retain intact secondary structure when compared to SET^{WT} (Fig. 33 and 34d-g). Proximity ligation assays (PLA) were performed to measure the association of PP2A-C and FLAG-SET^{WT}, FLAG-SET^{R71A}, or FLAG-SET^{E111A} (Fig. 34a-b) in A549 cells using anti-PP2AC and anti-FLAG antibodies with and without FTY720 (5 μM for 3 h). This treatment regime did not affect cell growth (Fig. 34c). Data showed that FTY720 reduced the association between PP2A-C and FLAG-SET^{WT}. However, mutants of SET with R71A and E111A conversions showed no reduction in FLAG-SET-PP2AC association in response to FTY720, supporting that R71 and E111 play key roles in FTY720 binding, as suggested by the NMR structure of the FTY720-SET complex (Fig. 34a-b).

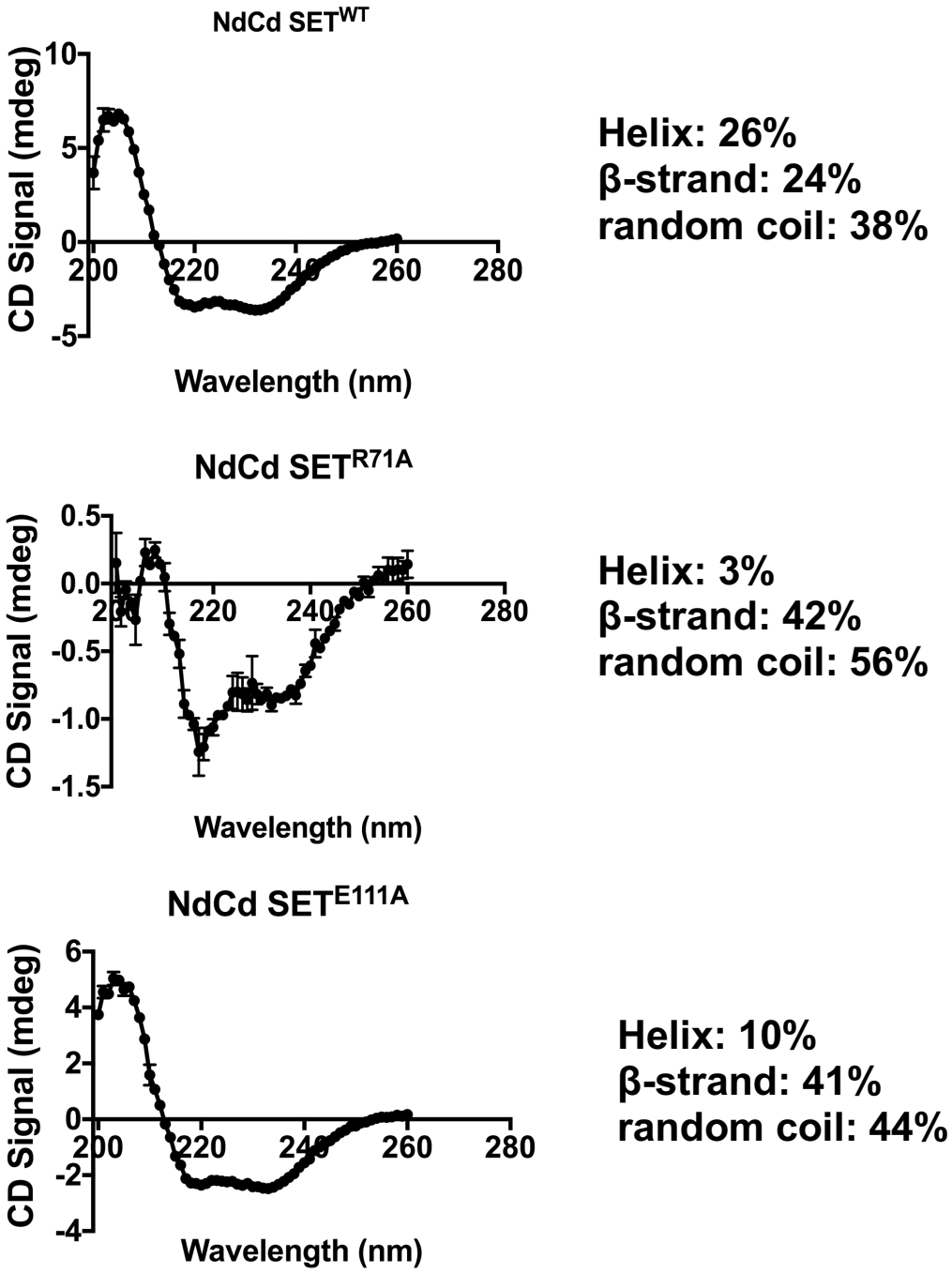

Figure 33| R71A and E111A mutations do not cause protein unfolding

Circular dichroism shows similar secondary structure between SET^{WT}, SET^{R71A}, and SET^{E111A} indicating no major changes in overall protein structure as a result of mutations.

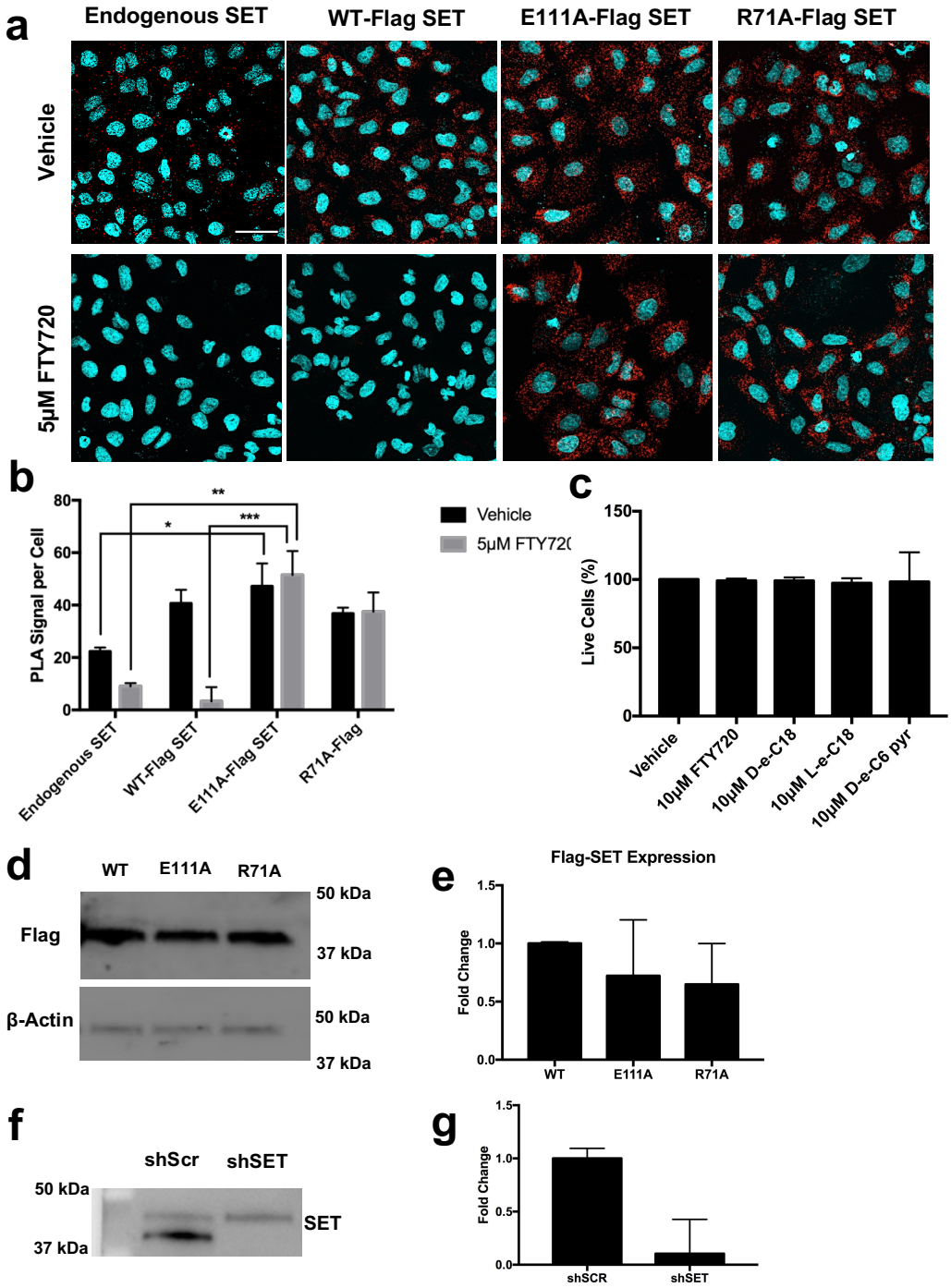

Figure 34| Arg[71] and Glu[111] play key roles in FTY720 binding.

(a) association between endogenous SET, Flag-SET^{WT}, Flag-SET^{E111A}, and Flag-SET^{R71A} mutants and PP2AC ± 5 μM FTY720 was monitored by PLA using antibodies against SET, Flag, or PP2AC. SET mutants were generated from CSP and modeling. Representative images of n ≥ 3 independent experiments per group. Scale bars represent 100 μm. **(b)** quantitation of PLA for SET mutants designed to limit response to FTY720 treatment. Data are means ± S.E.M. of n ≥ 3 independent experiments per group,

analyzed by two-way ANOVA with Tukey's post hoc test (*p = 0.0391, **p = 0.0259, ***p = 0.0083). **(c)** Trypan blue counts of FTY720, D-*e*-C18, L-*e*-C18, and D-*e*-C6-pyr-ceramides at twice the concentrations used in experiments to show changes in SET oligomerization are not a result of cell death. Error bars represent the SD of mean from triplicate experiments. **(d)** expression of R71A and E111A Flag-SET constructs. **(e)** quantitation of E111A and R71A Flag-SET normalized to actin. **(f)** SET expression knocked down with shRNA to the 3'UTR. **(g)** quantitation of SET knock down normalized to β-actin. Error bars are SEM of n=2 independent experiments.

FTY720-binding unravels SET dimerization domain

Early characterization showed SET to exist primarily as a dimer and tetramer both *in vitro* and in HeLa cells via a combination of chemical cross-linking and analytical gel filtration[182,235,242,249]. Recombinant Nd SET was also observed as both dimer and tetramer[241]. A region between residues 36-124 near the N-terminus is critical for PP2A inhibition[180]. Additionally, this region contains a coil-coiled domain (E25-Q65), which controls SET dimerization[182]. Together these data suggest SET dimerization or even oligomerization may be necessary for PP2A inhibition.

NMR titration data, and the associated lipid-binding simulation models generated with MOE, suggest that FTY720 or ceramide binding may modulate secondary structure within the N-terminal alpha helix between Gln29-Lys77. Interestingly, TROSY peaks corresponding to these residues appeared to undergo line broadening upon the addition of FTY720 during NMR titrations (Fig. 35a-c). This region encompasses SET's dimerization domain and may coincide with the disruption of the dimerization interface, which subsequently could prevent SET from forming dimers and/or higher order oligomers. In order to rule out protein degradation as a major contributor to this phenomenon, [^{1}H-^{1}H] 1D spectra were collected before each [^{1}H-^{15}N] TROSY. Hallmarks of degraded protein shows peaks sharpening and collapsing back to the baseline, especially in the amide region, and the methyl peaks, located between 0 ppm and -1 ppm disappear as a result of protein degradation. [^{1}H-^{1}H] 1D spectra indicate there were no major changes to indicate protein degradation, with or without 10 μM FTY720 (Fig. 36). This could indicate that lipid binding results in structural changes in the N-terminal alpha helix between Gln29-Lys77, which subsequently would prevent SET from

forming dimers/oligomers, which are active forms of SET[182,242]. More work will need to be done to provide further details on the potential mechanism a site-specific conformational transition.

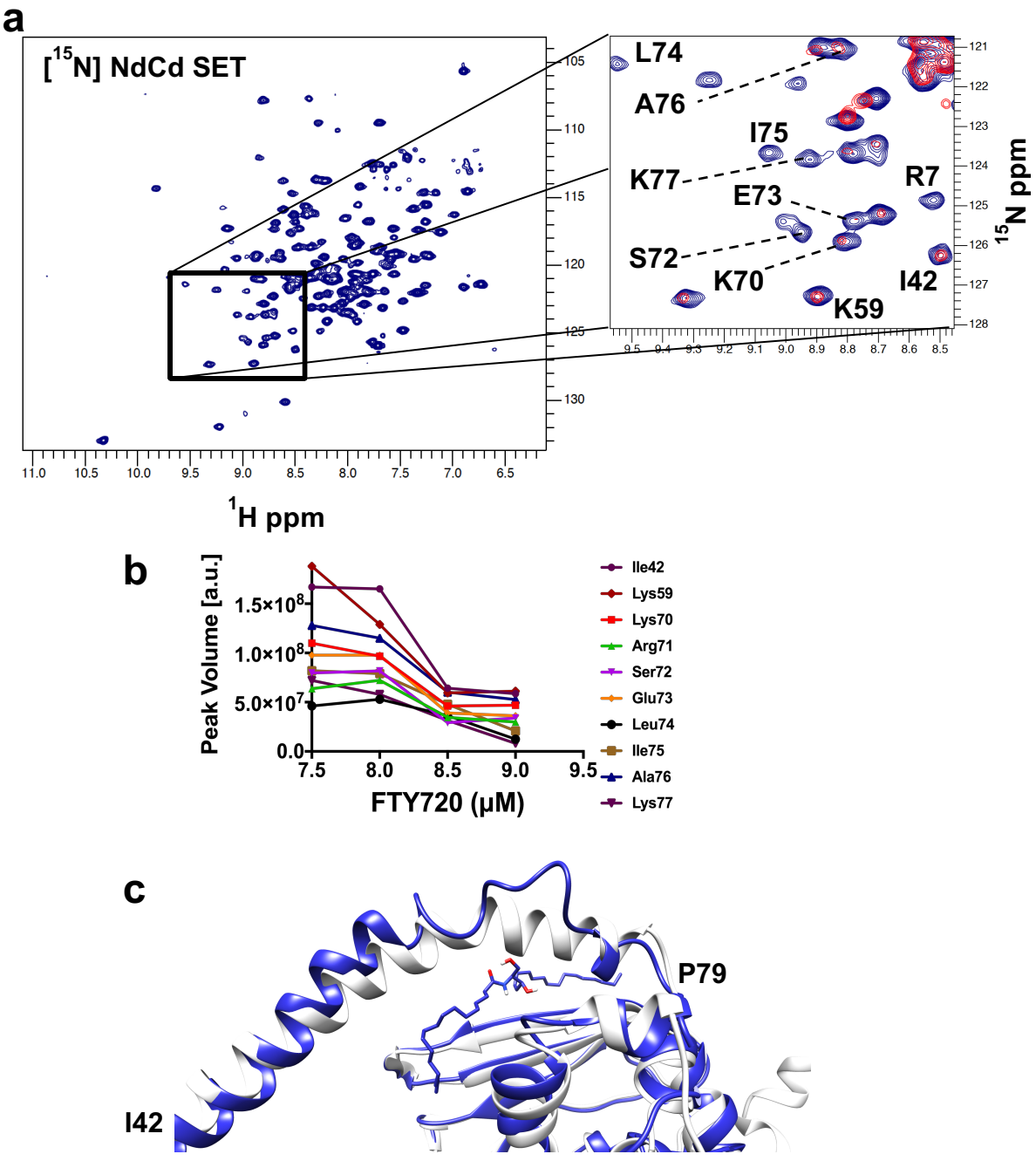

Figure 35| Lipid-Binding may alter SET dimerization domain to prevent oligomerization

(a) Spectrum of highlights peaks that undergo line broadening upon the addition of FTY720. These peaks correspond to residues in the dimerization domain of SET. Blowout highlights broadened peaks (red) at 10 μM FTY720. **(b)** Quantitation of the change in peak height of assigned residues in the dimerization domain. Data are means n=3 experiments. **(c)** Comparison of NdCd SET^{WT} models in the absence (white) and presence (blue) of D-e-C18 ceramide illustrating predicted structural alterations in the N-terminal helix of SET.

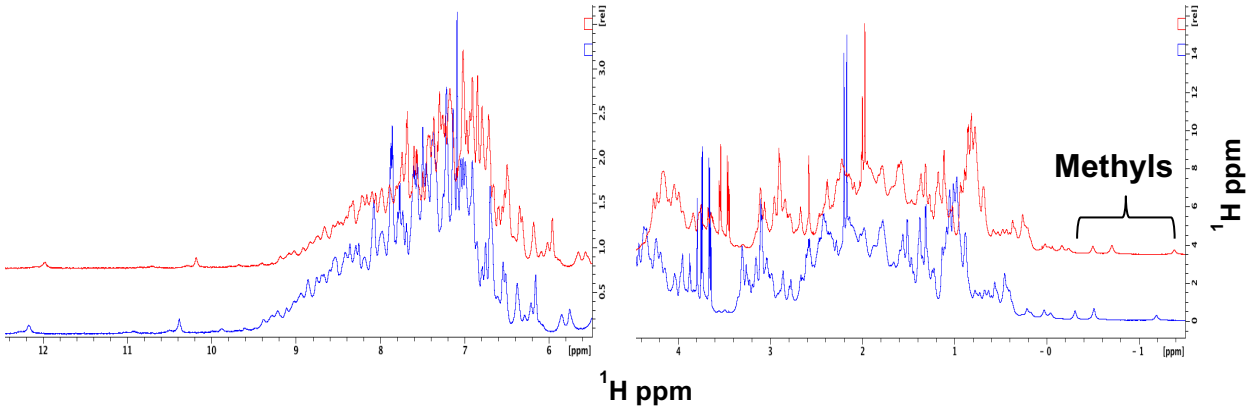

Figure 36| Line broadening is not related to protein degradation during NMR titrations.

Overlaid [^{1}H-^{1}H] 1D spectra of NdCd SET ± 10 μM FTY720 (red and blue, respectively) showing no protein degradation. Area between 4.5 ppm and 5.5 ppm excluded due to distortion from water signal.

The motion of molecules in solution is dependent on physical parameters such as size and shape of the molecule, temperature, and viscosity. A diffusion profile is measured by signal attenuation as a function of linearly increasing field gradient. A molecule can be spatially labeled in the sample tube and its motion/diffusion tracked. A diffusion coefficient, $\boldsymbol{D}$, can be calculated using the Stokes-Einstein equation.

$$\boldsymbol{D = \frac{\kappa T}{6\pi\eta r_s}}$$

The rate of diffusion is inversely related to molecular weight (i.e. a small diffusion coefficient = a large molecule). Pulsed field NMR experiments can be collected in 30 minutes or less with high resolution. We believed this would be a quick, straightforward approach to determine if lipid-binding prevents SET dimerization.

Then, we performed Diffusion-Ordered Spectroscopy (DOSY)[250–252] on NdCd-SET, which contains Gln29-Lys77, with and without FTY720 (Fig. 37). We generated a standard curve of apparent molecular weight using typical low molecular weight marker proteins (Fig. 37a)[253] to calculate an apparent molecular weight of SET with and without FTY720. If lipid-binding prevents dimerization, it is expected to cause an increase in the diffusion coefficient, representing a decrease in apparent molecular weight. Simply stated, the rate of diffusion is inversely related to the weight/size of the molecule. The data showed that NdCd-SET alone exhibited a diffusion coefficient of $0.591/10^{-10} m^2 s^{-1}$ giving an apparent molecular weight of 49.1 kDa, representing a dimer (Fig. 37b, upper panel). However, NdCd-SET with 10 μM FTY720 binding had a diffusion coefficient of $1.057/10^{-10} m^2 s^{-1}$, giving an apparent molecular weight of 22.3 kDa, representing a monomeric state (Fig. 37b, lower panel). Intriguingly, the sample with FTY720 exhibited a much broader diffusion peak. This could be due to the presence of species of SET as it

transitions from oligomers (in lower abundance) to monomers, causing a broadening of signal, but still resulting in an overall larger diffusion coefficient.

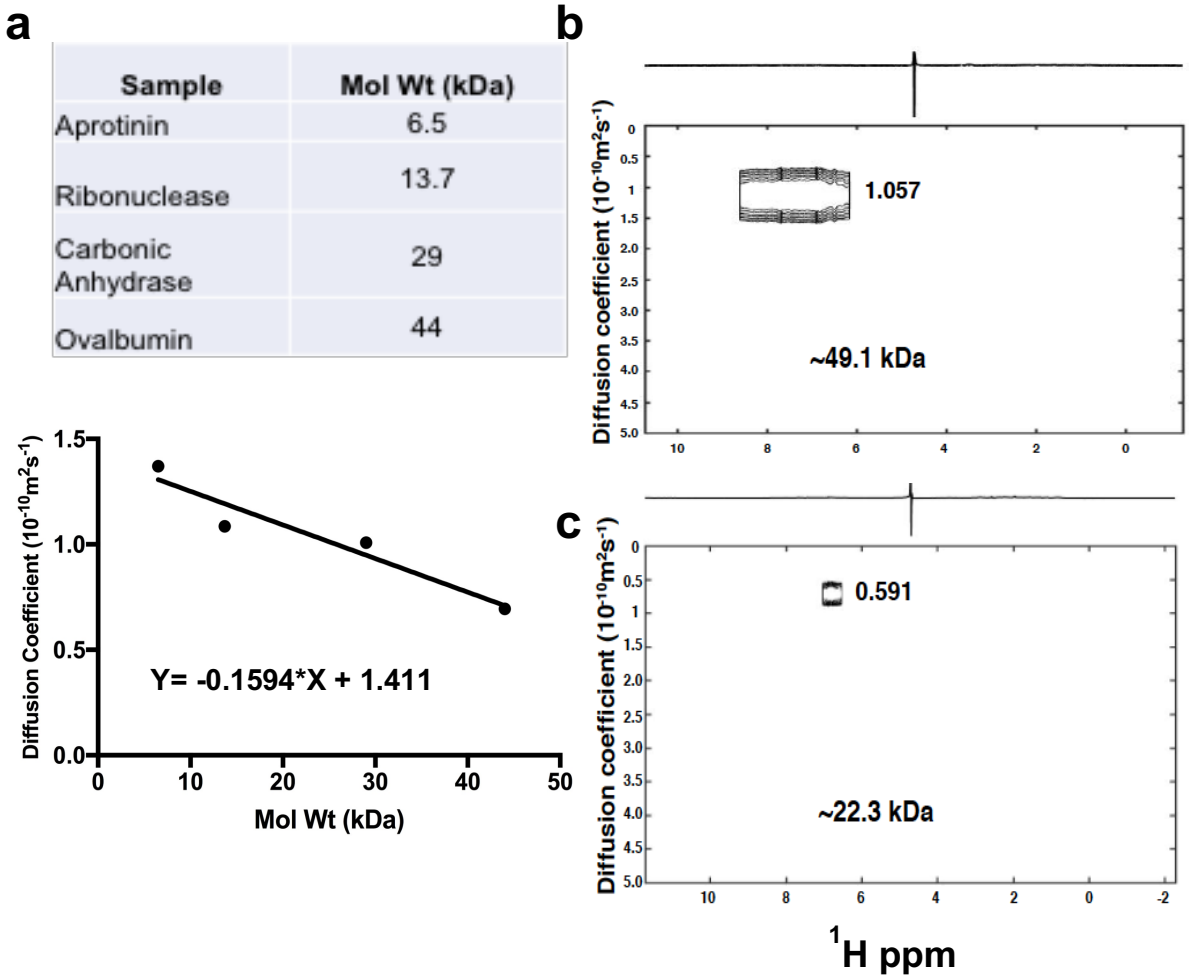

Figure 37| Exposure to FTY720 lowers apparent molecular weight of NdCd SET.

(a) DOSY spectra and diffusion coefficients ±10 μM FTY720 were analyzed with DOSYToolBox 2.7 [253]. **(b)** list of proteins used to make standard curve and their molecular weights. **(c)** standard curve of apparent molecular weights of proteins generated by diffusion ordered spectroscopy (DOSY).

To determine if the prevention of SET dimer/oligomer formation could occur in cells, A549 cells were treated with FTY720, D-*e*-C18, and L-*e*-C18 ceramides for 3 h, and SET oligomerization was analyzed by Western blotting after chemical crosslinking of proteins using glutaraldehyde. Data showed that SET exists primarily as a dimer and tetramer (oligomers) with low monomeric protein abundance in A549 cells, as expected (Fig. 38a). When treated with FTY720 (Fig. 38c-d) and D-*e*-C18 ceramide there was a sharp reduction in SET oligomer formation. L-*e*-C18 ceramide had no effect on reduction of SET oligomers (Fig. 38c-d). These data were also confirmed using the mutants of SET with reduced FTY720 binding, which remained as oligomers with/without FTY720 (Fig. 38e-f). Taken together, these data suggest that lipid-binding causes structural changes in the dimerization domain, preventing SET from forming oligomers both *in vitro* and in A549 cells.

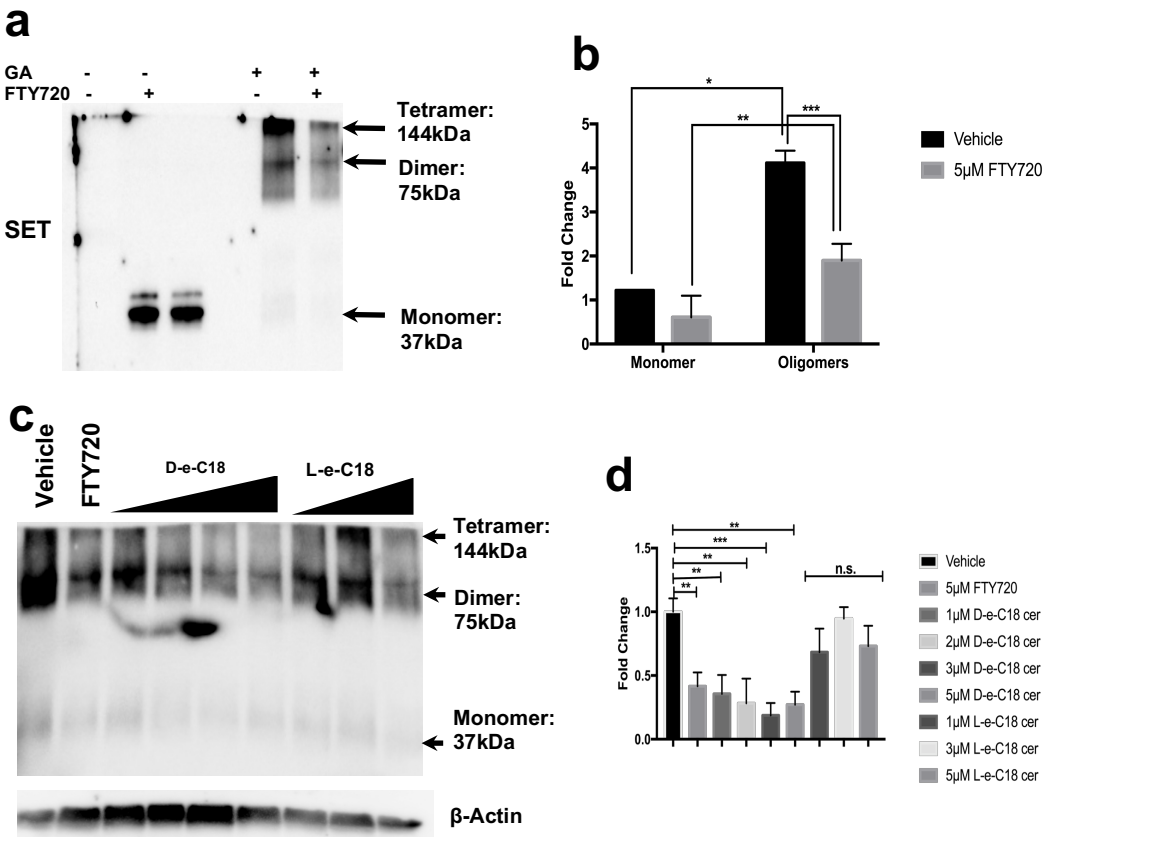
a
GA - - + +
FTY720 - + - +
Tetramer: 144kDa
Dimer: 75kDa
SET
Monomer: 37kDa
b
Fold Change
Monomer
Oligomers
Vehicle
5μM FTY720
c
Vehicle
FTY720
D-e-C18
L-e-C18
Tetramer: 144kDa
Dimer: 75kDa
Monomer: 37kDa
β-Actin
d
Fold Change
n.s.
Vehicle
5μM FTY720
1μM D-e-C18 cer
2μM D-e-C18 cer
3μM D-e-C18 cer
5μM D-e-C18 cer
1μM L-e-C18 cer
3μM L-e-C18 cer
5μM L-e-C18 cer
e
Vector
WT SET
R71A SET
E111A SET
FTY720
Blot: Flag
Tetramer: 144kDa
Dimer: 75kDa
Monomer: 37kDa
f
Fold Change
WT-SET
R71A-SET
E111A-SET
Vehicle
5μM FTY720

Figure 38| SET exists primarily as a dimer and tetramers (oligomers) with low monomeric protein abundance.

(a) representative blot for glutaraldehyde (GA) crosslinking of endogenous SET oligomers ± 5 μM FTY720 and 0.01% GA. **(b)** quantitation of crosslinking experiment. Representative blot of n= 3 individual experiments. Blots were quantified with ImageJ. Data are means normalized to actin ± S.D. and analyzed by two-way ANOVA with Tukey's post hoc test (*p < 0.0001, **p < 0.0001, ***p < 0.0001). **(c)** glutaraldehyde (GA) crosslinking of SET oligomers in response to 3 hrs. treatment with 1-5 μM D-*e*-C18 or L-*e*-C18-ceramides. Representative blot of n= 3 individual experiments. **(d)** Model showing prevention of SET oligomerization due to binding with FTY720 (*p< 0.05, **p< 0.01, ***p<0.00 and ****p< 0.0001). Data were analyzed by student's t-test. **(e)** representative blot for glutaraldehyde (GA) crosslinking of SET^{WT}, SET^{R71A}, and SET^{E111A} oligomers ± 5 μM FTY720 and 0.01% GA. **(f)** quantitation of GA crosslinking. Representative blot of n= 3 individual experiments. Blots were quantified with ImageJ. Data are means normalized to actin ± S.D. and analyzed by two-way ANOVA with Tukey's post hoc test (*p< 0.05, **p< 0.01, and ****p< 0.0001).

Summary

The work of this chapter proposes a possible mechanism to how ceramide or FTY720 interact with SET, leading to PP2A activation. Our data are consistent with previous findings that showed the N-terminal region (36-124) is essential for PP2A inhibition[180]. We show residues (R71 and E111) that may be essential for lipid-binding. Furthermore, we were able to show that ceramide is stabilized into the an 'extended' conformation upon binding to SET. In addition, the helical structure within the dimerization domain of SET is disrupted upon binding to FTY720 or ceramide, preventing oligomerization. Analysis of SET after crosslinking with GA shows a clear reduction in oligomerization. Therefore, we propose that SET oligomerization is essential for PP2A inhibition, since SET exists primarily as a dimer and tetramer within cells[182,242]. The fate of lipid-bound SET is unknown. It is important to note that the reduction in SET oligomers is not followed by a concomitant increase in monomeric SET (Fig. 38a). Still, the mechanism of PP2A activation through SET reaches beyond the realm of cancer biology into ceramide/SET/PP2A- mediated mechanisms of insulin resistance and vascular dysfunction in metabolic disease[193,254–256]. In both instances, increased levels of ceramide activate PP2A, through SET, leading to antagonistic insulin signaling through the AKT pathway or eNOS related vascular contractility problems, respectively. Contrary to cancer biology, the therapeutic goal would be to inhibit PP2A activity in metabolic disease.

Chapter 5: Examination of SET/PP2A Interaction

When examining the association of SET^{R71A} and SET^{E111A} with PP2A in the presence and absence of FTY720 we noted that endogenous SET and PP2AC have a very limited interaction (Fig. 34a-b). SET is thought to inhibit PP2A directly by binding the C-subunit *in vivo*, but the specific interactions between SET and PP2A have not yet been described. PP2A is expressed in the cell ubiquitously, while SET is predominantly nuclear (Fig. 39a). Given the information available and common assumptions in the PP2A field, we thought that the cells would be saturated with PLA signal. However, closer examination by proximity ligation assay between endogenous SET and PP2AC in A549 cells show a very limited interaction (Fig. 39b). This was very interesting because it intimated that SET possibly had a specificity for a unique heterotrimeric PP2A complex, and that this interaction may not be directly governed or limited to the catalytic subunit of PP2A. Both of these possibilities are dogmatic shifts in the PP2A field. To that end, we want to determine what unique heterotrimeric PP2A complex is activated by FTY720 or ceramide, possible downstream target(s), and if that complex is targeted by SET for inhibition.

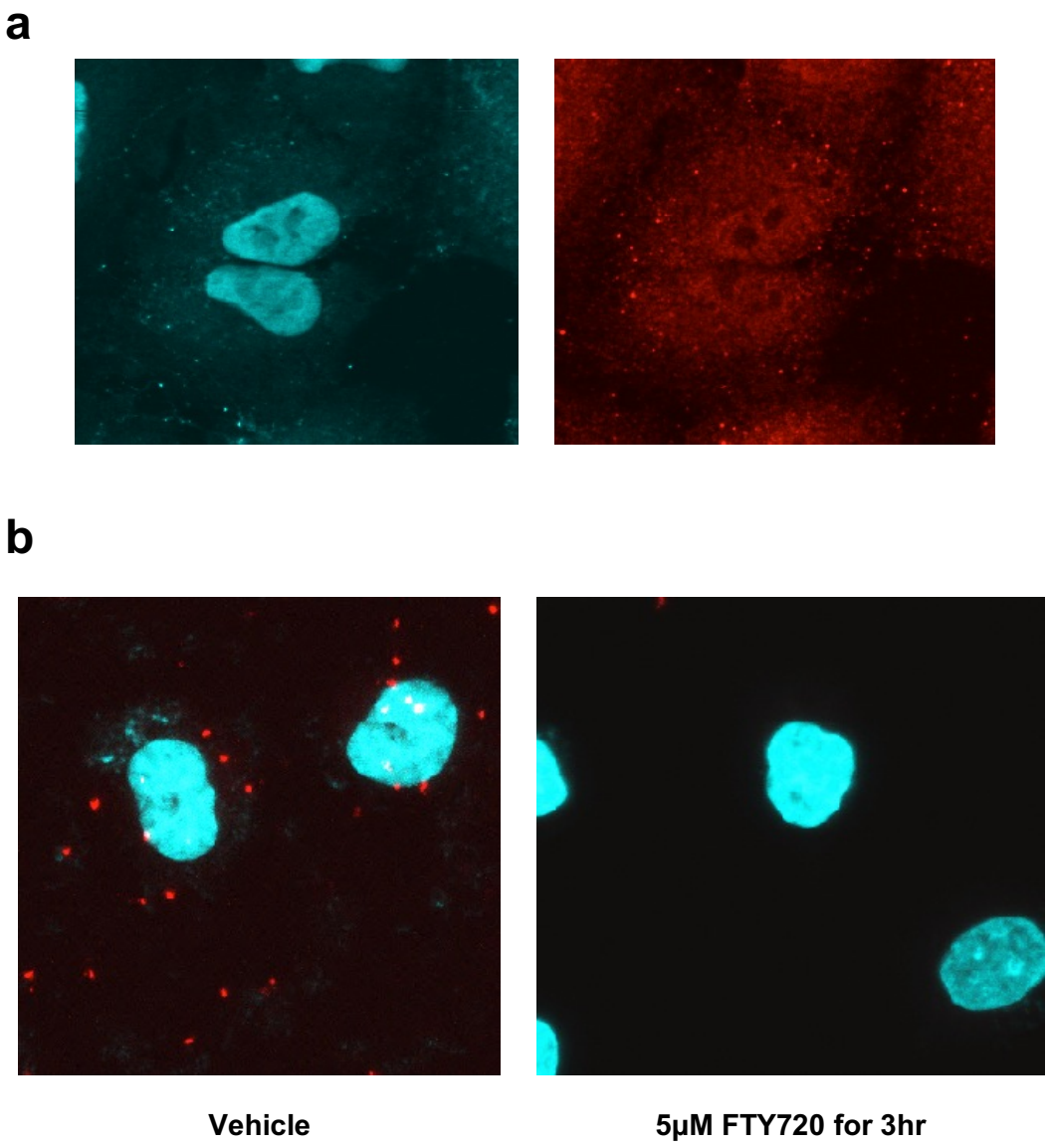

Figure 39| Endogenous SET and PP2A have minimal specific association within the cell.

(a) Immune fluorescence microscopy demonstrating subcellular localization and relative expression of SET (cyan) and PP2AC (red). **(b)** association between endogenous SET and PP2AC monitored in A549 cells with and without 5 μM FTY720 treatment for 3 hours by PLA using antibodies against SET and PP2AC.

FTY-720-SET interaction selectively activates a specific PP2A holoenzyme

To determine downstream protein targets of PP2A in response to its activation by FTY720 upon SET binding and inactivation, we performed stable isotope labeling of cells in culture (SILAC) analysis by mass spectrometry. A549 cells stably overexpressing HA-tagged PP2ACα were grown in heavy (^{15}N-arginine labeled) and light (normal) DMEM media. After three weeks of growing cells, the 'heavy cells' were treated with a high dose (20 μM) of FTY720 for 2 hours, washed, collected, and lysed. PP2ACα was immuno-precipitated by the HA-tag in both treated and control cells. The elution of control and treated samples were mixed and run on SDS-PAGE. The gel was then Coomassie stained for analysis by mass spectrometry. The ratio of ^{15}N:^{14}N was analyzed for changes in protein levels as result of exposure to FTY720.

Table 4: SILAC Results of PP2A-related subunits

Name	Normalized H/L Ratio
PPP2AAα	0.566766
PP2ACα;PP2ACβ	0.539531
B56δ;B56γ1	0.463518
PP2AAβ	0.0790197
B55α	0.0219061

The SILAC analysis resulted in over 130 possible proteins that increase or decrease association with PP2AC in response to FTY720 treatment. These proteins represented a wide array of cellular functions (Fig. 40). Interestingly, SET was not among the list, suggesting that FTY720 binding relieves SET from PP2AC, as we expected (Appendix II: Table 6). Several PP2A subunits were increased after FTY20 treatment, including PP2AAβ and PP2A-B56γ (Table 5). These data suggested that FTY720-mediated activation of PP2A might require a selective PP2A holoenzyme with specific A, B and C

subunits. To test this hypothesis, we generated stable shRNA-dependent knockdown of each PP2A subunit identified by SILAC analysis in A549 cells (*see Fig. 53 in Appendix II for blots of knockdowns and shRNA sequences). We then assessed whether the loss of the subunits perturbed by SET-FTY720 association affected SET-PP2A interaction by PLA (Fig. 41a-c). We further hypothesized that loss of SET-PP2A association (loss of PLA signal) in a particular knockdown cell line would indicate that an individual subunit was important for SET-PP2A interaction. The data showed that shRNA-mediated knockdown of PP2AA α or β, PP2A-B56γ, and PP2ACα subunits decreased SET association, compared to Scr-shRNA, or shRNAs against PP2AAα, PP2A-B56*δ*, or PP2ACβ (Fig. 41a-c). Furthermore, we assessed PP2A activation in shScr, shPP2ACα, shB56γ, and shB56*δ* stable cell lines in response to FTY720 by blotting for PP2A-phospho-Tyr^{307}. Phospho-Tyr^{307} is a marker of PP2A activity, where a decrease in phosphorylation correlates with an increase in PP2A activity. Exposure to FTY720 increases PP2A activity (decreased p-Tyr^{307}) in both the shScr and shB56*δ* cells, but not the shB56γ cells, suggesting PP2A containing the B56γ subunit are responsive to activation by FTY720 (Fig. 41d-e). Thus, these data suggest that FTY720-SET binding results in the selective activation of PP2A holoenzyme containing PP2A-Aβ, PP2A-B56γ, and PP2ACα subunit (Fig. 41a-c). These data are consistent with tumor suppressor functions of B56γ subunit of PP2A, whose various mutations or changes in expression are known to disrupt its tumor suppressor function[129–131].

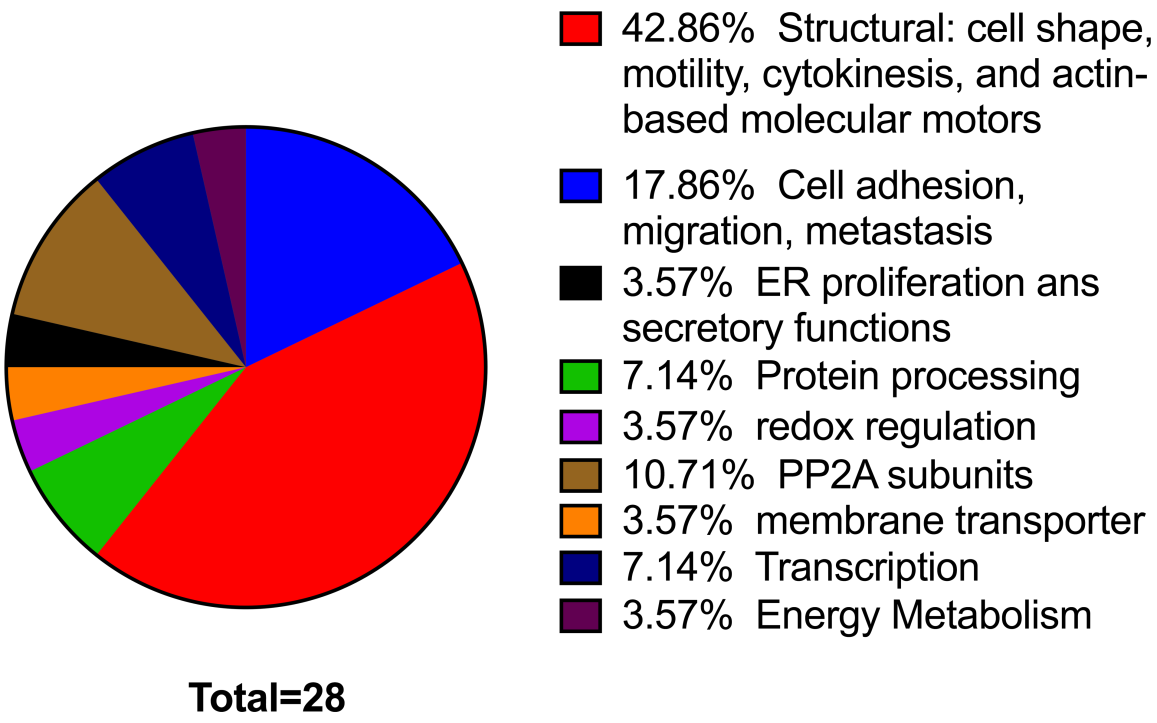

Figure 40| SILAC results divided by cellular function.

Treatment with FTY720 causes increased associated between PP2ACα and many proteins. The largest group of proteins had structural and motility functions. Proteins implicated in metastasis and cell migration were next, followed by various PP2A subunits.

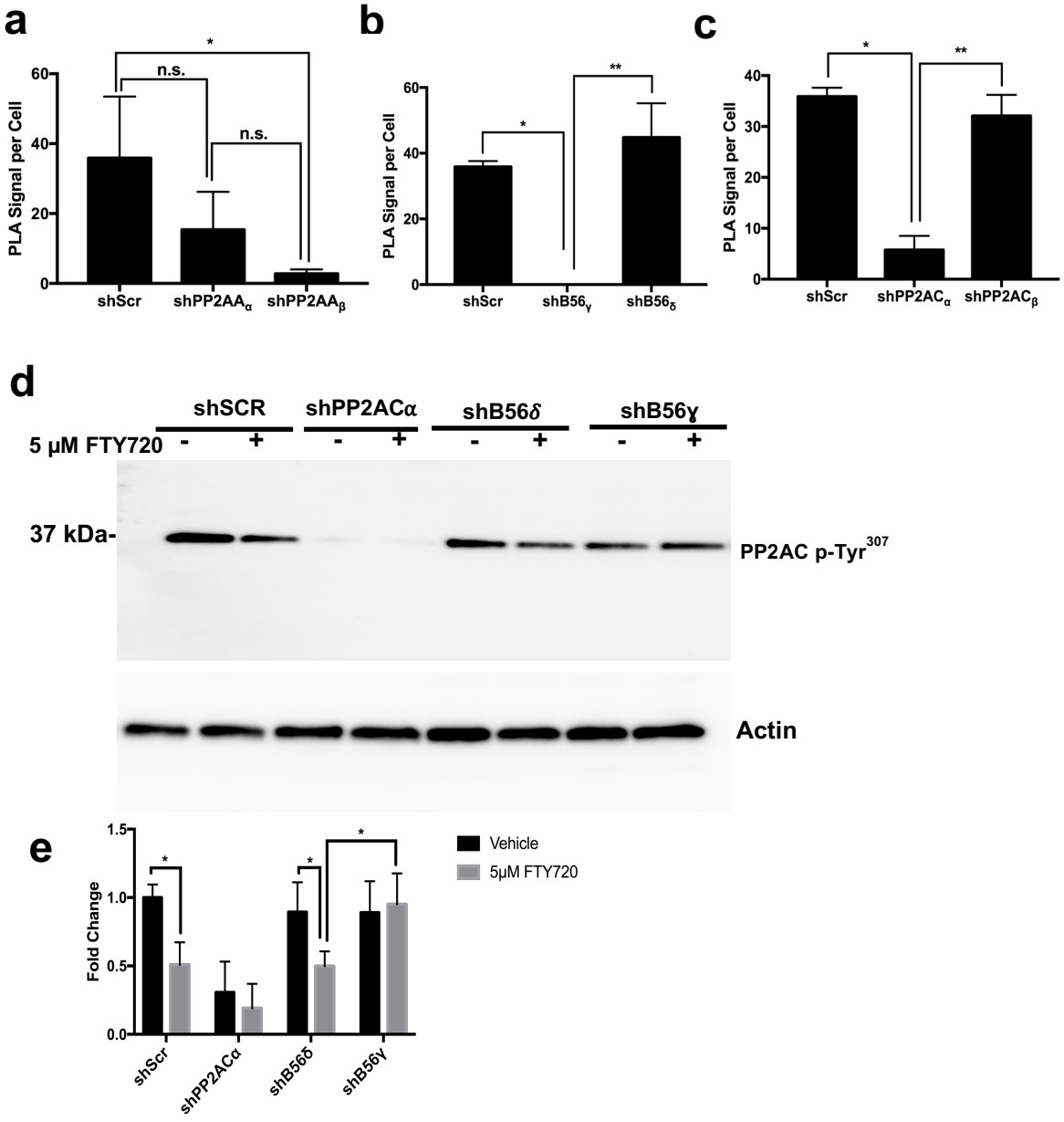

Figure 41| SET targets a specific heterotrimeric PP2A

(a) Association between endogenous SET and PP2AC in shPP2AAα and shPP2AAβ knockdown cells was analyzed by PLA. Data are means ± S.E.M. of n = 3 independent experiments, analyzed by student's t-test (*p = 0.0388). **(b)** Association between endogenous SET and PP2AC in shB56γ and shB56*δ* knockdown cells was examined by PLA. Data are means ± S.E.M. of n = 3 independent experiments, analyzed by student's t-test (*p = 0.0001, **p = 0.0147) **(c)** association between endogenous SET and PP2AC in shPP2ACα and shPP2ACβ knockdown cells was assessed by PLA. Data are means ± S.E.M. of n = 3 independent experiments, analyzed by student's t-test (*p = 0.0008, **p = 0.0114). **(d)** Western blot of PP2AC phosphor-Tyr^{307} as a marker for PP2A activity. **(e)** quantitation of p-Tyr^{307} blots. Representative blot of n= 3 individual experiments. Blots were quantified with ImageJ. Data are means normalized to actin ± S.D. and analyzed by two-way ANOVA with Tukey's post hoc test (*p < 0.0001, **p < 0.0001, ***p < 0.0001).

Moreover, exogenous expression of HA-PP2ACα, but not HA-PP2ACβ, in shPP2ACα-transfected cells restored SET-PP2ACα interaction, which was then inhibited by FTY720 (Fig. 42a-b). Similarly, expression of exogenous B56γ-V5, and not B56*δ*-V5 (Fig. 42c), in shB56γ-transfected cells restored SET-PP2ACα association, which was also inhibited by FTY20 (Fig. 42d). Thus, these data reveal that SET preferentially associates with a PP2A holoenzyme composed of PP2AAβ, B56γ, and PP2ACα subunits in A549 cells.

Remarkably, SET remained in complex with PP2A-B56γ with or without FTY720 or C18-ceramide (Fig. 43a-b). As a control, we used a peptide inhibitor of SET, OP449[208] with an unknown mechanism of SET inhibition for measuring its effects on SET-PP2A-B56γ association. Data showed that OP449 had significant reduction in the interaction between SET and PP2A-B56γ while also decreasing SET-PP2ACα association (Fig. 43a-c). The data suggests that SET is not a universal inhibitor of all PP2A holoenzymes, and that it targets, as a dimer/tetramer, a specific PP2A hetero-trimer through interacting with PP2A-B56γ and PP2ACα.

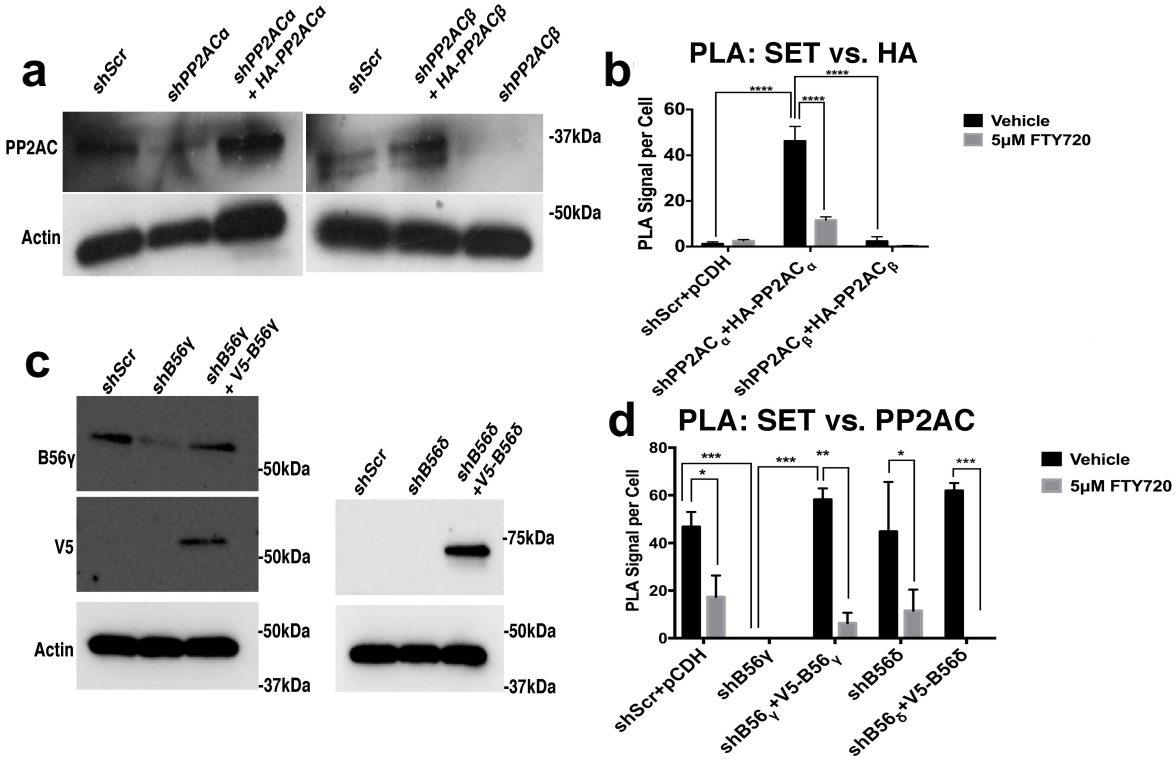

Figure 42| Reconstitution of PP2ACα and B56γ expression restores SET/PP2A association

(a) Western blot showing successful reconstitution of expression for HA-PP2ACα and HA-PP2ACβ. **(b)** association between endogenous SET and HA-tagged PP2AC in shPP2ACα and shPP2ACβ stable knockdown cells with rescued expression (shPP2ACα + HA-PP2ACα and shPP2ACβ + HA-PP2Acβ) was assessed by PLA using antibodies against SET and HA epitope. Quantitation of PLA. Data are means ± S.E.M. of n = 3 independent experiments, analyzed by student's t-test (****p<0.0001). **(c)** Western blot showing successful reconstitution of expression for V5-B56γ and V5-B56δ. **(d)** association between endogenous SET and PP2AC in shB56γ and shB56δ stable knockdown cells with rescued expression (V5-B56γ and V5-B56δ) was assessed by PLA using antibodies against SET and PP2AC. Quantitation of PLA. Data are means ± S.E.M. of n = 3 independent experiments, analyzed by student's t-test (*p< 0.05, **p< 0.01, ***p<0.001).

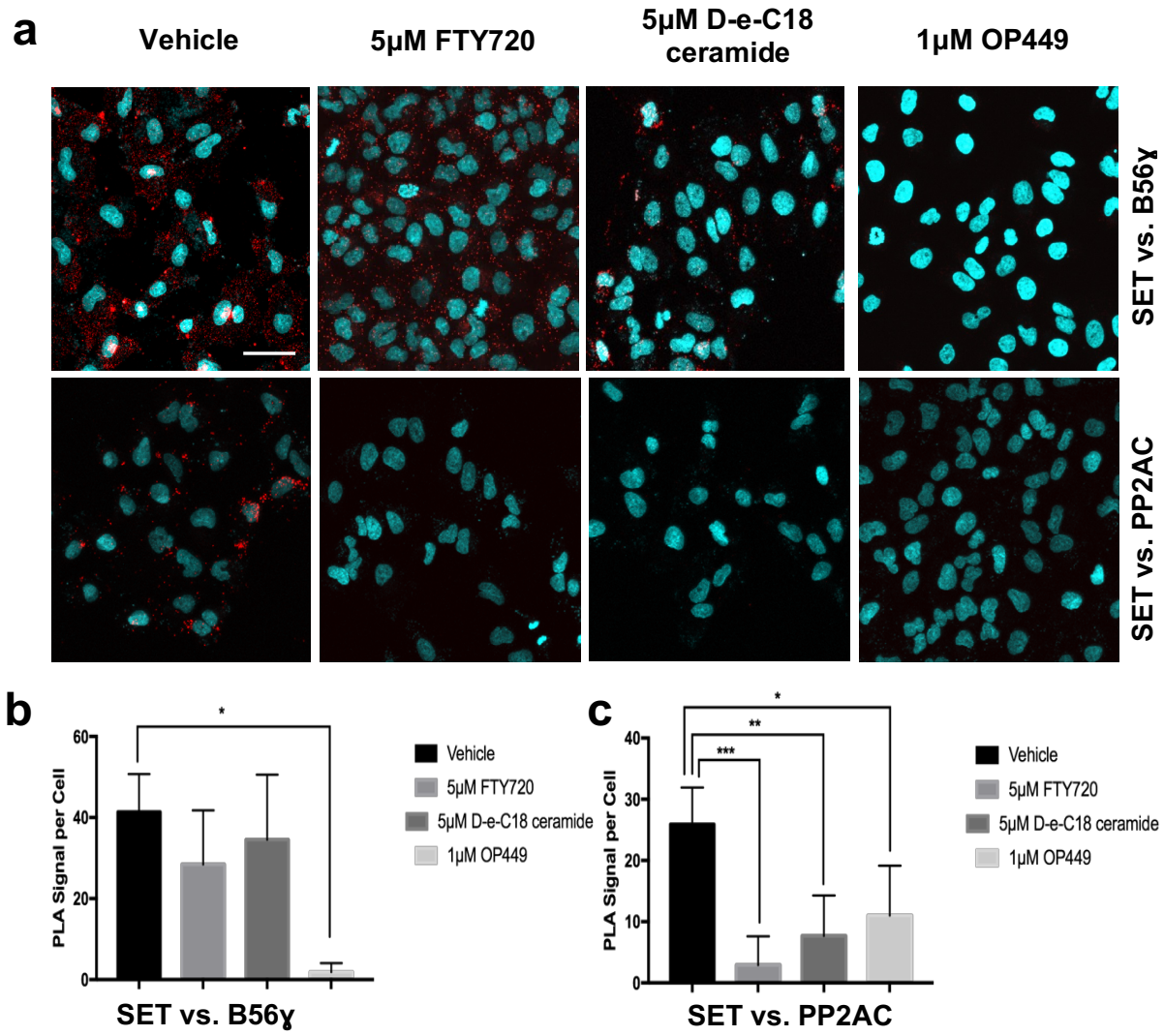

Figure 43| SET remains in complex with PP2A-B56γ after exposure to FTY720 or D-*erythro*-C18 ceramide

(a) association between endogenous SET/PP2AC and SET/B56ɣ ± 5 μM FTY720, 5 μM D-e-C18 ceramide, or 1 μM OP449 treatment for 3 h assessed by PLA using antibodies against SET, PP2AC, and B56ɣ. Representative images of n ≥ 3 independent experiments per group. Scale bars represent 100 μm. **(b, c)** quantitation of PLA experiments. Error bars are SEM of n ≥ 3 independent experiments per group Data are means ± S.E.M. of n ≥ 3 independent experiments per group, analyzed by two-way ANOVA with Tukey's post hoc test (*p< 0.05, **p< 0.01, ***p<0.00 and ****p< 0.0001).

To further validate these data, we performed GST pulldown assays using various recombinant PP2A subunits and WT-SET with/without FTY720 in vitro. These studies demonstrated that SET preferentially associates with PP2AAβ-GST, and not with PP2AAα-GST in vitro (Fig. 44a). This interaction between SET and PP2AAβ-GST is reduced in response to FTY720 (50 μM) (Fig. 44b). The pull-down assays also showed that FTY720 at 25, 50 and 100 μM reduced the interaction of SET with the in vitro assembled PP2A holoenzyme containing PP2AAβ-GST, PP2AB'γ1, and PP2ACα (Fig. 44c). However, FTY720 (12.5-50 μM) had no effect on the interaction between SET and PP2AB'γ1-GST (Fig. 44d). These data revealed that while FTY720 inhibits the interaction between SET and PP2AAβ-GST, SET remains bound to PP2AB'γ1 with/without FTY720 in vitro, consistent with data obtained in A549 cells.

Taken together, these data suggest that SET might not be a universal inhibitor of all PP2A holoenzymes, and that it targets, as a dimer/tetramer, a specific PP2A holoenzyme composed of PP2AAβ, B56γ, and PP2ACα subunits. These data also suggest that although FTY720 inhibits the interaction between SET- PP2AAβ-PP2ACα complex, SET stays associated with B56γ with or without FTY720 in A549 cells (or with PP2AB'γ1 *in vitro*) (Fig. 45).

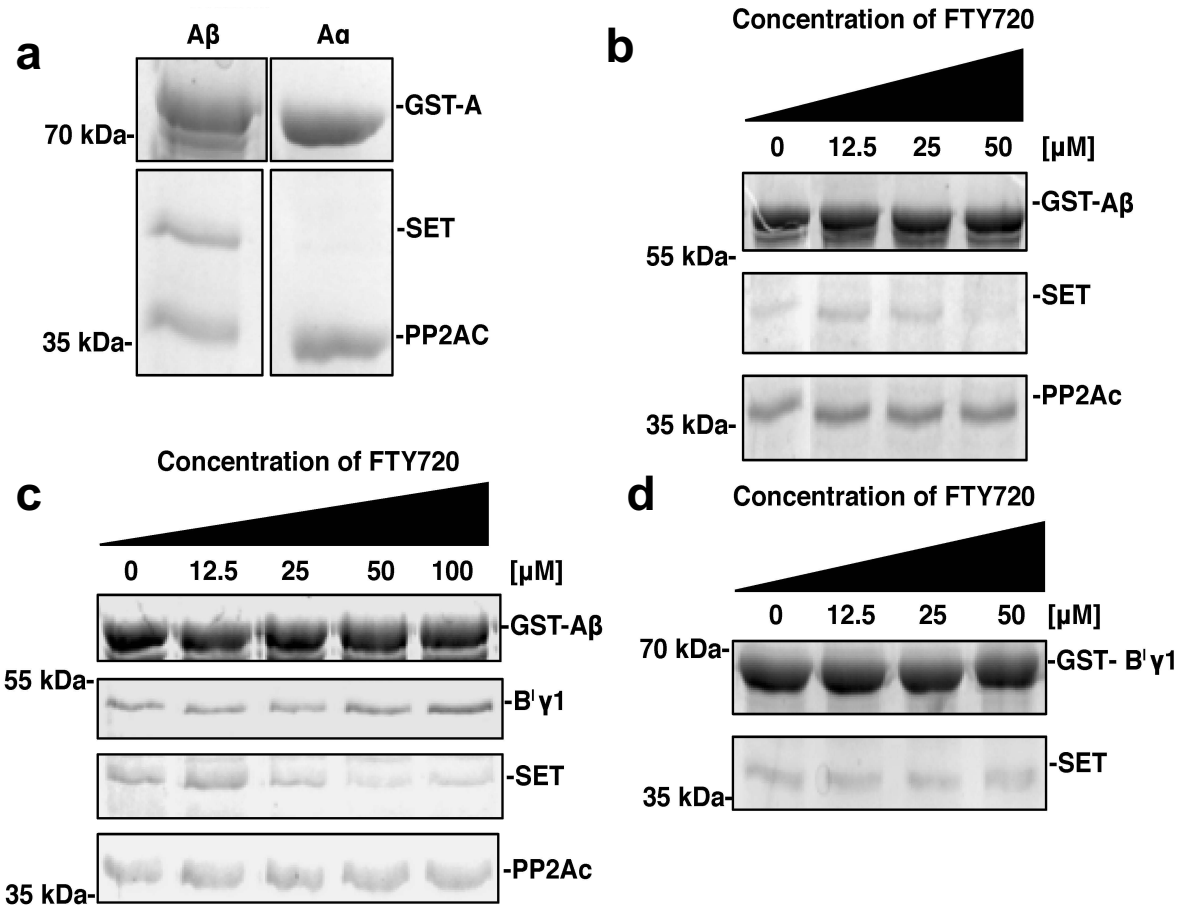

Figure 44| *In vitro* pull-down assays corroborate SET interaction with a specific PP2A holoenzyme

(a) Pull-down assay with either GST-tagged PP2A core enzyme (AβCα or AαCα) and SET. **(b)** Pull-down assay with either GST-tagged PP2A core enzyme (AβCα) and SET with increasing (0-50 μM) FTY720. **(c)** Pull-down assay with either GST-tagged PP2A holoenzyme (AβCαBγ1) and SET with increasing (0-100 μM) FTY720. **(d)** Pull-down assay with either GST-tagged Bγ1and SET with increasing (0-50 μM) FTY720.

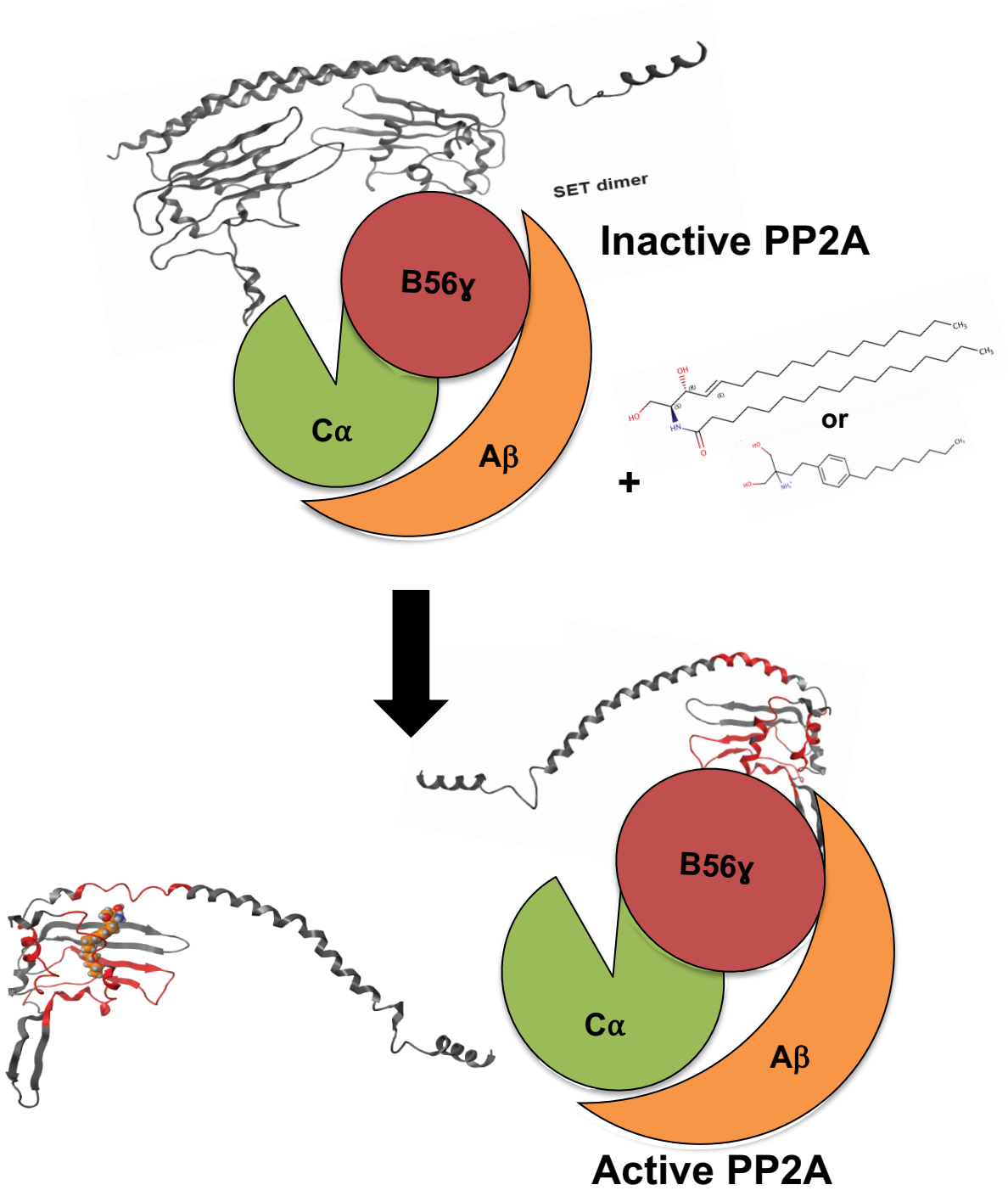

Figure 45| Model of SET/PP2A complex and mode of activation with ligand.

SET oligomerization is essential for PP2A inhibition. Lipid-binding prevents SET oligomerization resulting in active PP2A. Additionally, SET remains with FTY720-activated PP2A by maintaining contact with the B56γ subunit, as a possible regulatory mechanism.

Myosin IIa is targeted by FTY720-activated PP2A

Because our data revealed that PP2A-B56γ plays a key role in the activation of PP2A by FTY720 upon SET binding/inactivation, and it is important for substrate selectivity of the PP2A holoenzyme, we then assessed whether tumor suppressor non-muscle myosin IIa (MYH9) , identified as one of the highly PP2A-associated proteins after FTY720 activation in SILAC (Appendix II, Table 7), is targeted by activated PP2A holoenzyme containing PP2AA, PP2A-B56γ, and PP2ACα. To test this, we performed PLA between PP2AC and myosin IIa in sh-SCR and sh-PP2A-B56γ stable knockdown cell lines with and without treatment of 5 μM FTY720 for 3 h. We detected an increase in association of PP2AC and Myosin IIa in shSCR cells after treatment with FTY720. However, when we knocked down PP2A-B56γ, the association between PP2AC and myosin IIa was completely abrogated with/without FTY720 (Fig. 46a-b). Additionally, when we used non-muscle myosin IIa isolated from rabbit as a substrate for partially purified PP2AC *in vitro*, the data showed increased PP2A activity after treatment with FTY720 in shSCR transfected cells against purified myosin IIa, but not in cells transfected with shB56γ (Fig. 47a-b). Overexpressing SET^{R71A} or SET^{E111A}, both of which showed decreased FTY720 response, also resulted in decreased PP2A activity (Fig. 48a-b). Thus, these data suggest that the activation of a specific PP2A holoenzyme in response to FTY720-SET binding, containing PP2AA, PP2A-B56γ, and PP2ACα subunits selectively targets various downstream proteins, such as tumor suppressor non-muscle myosin IIa (MYH9).

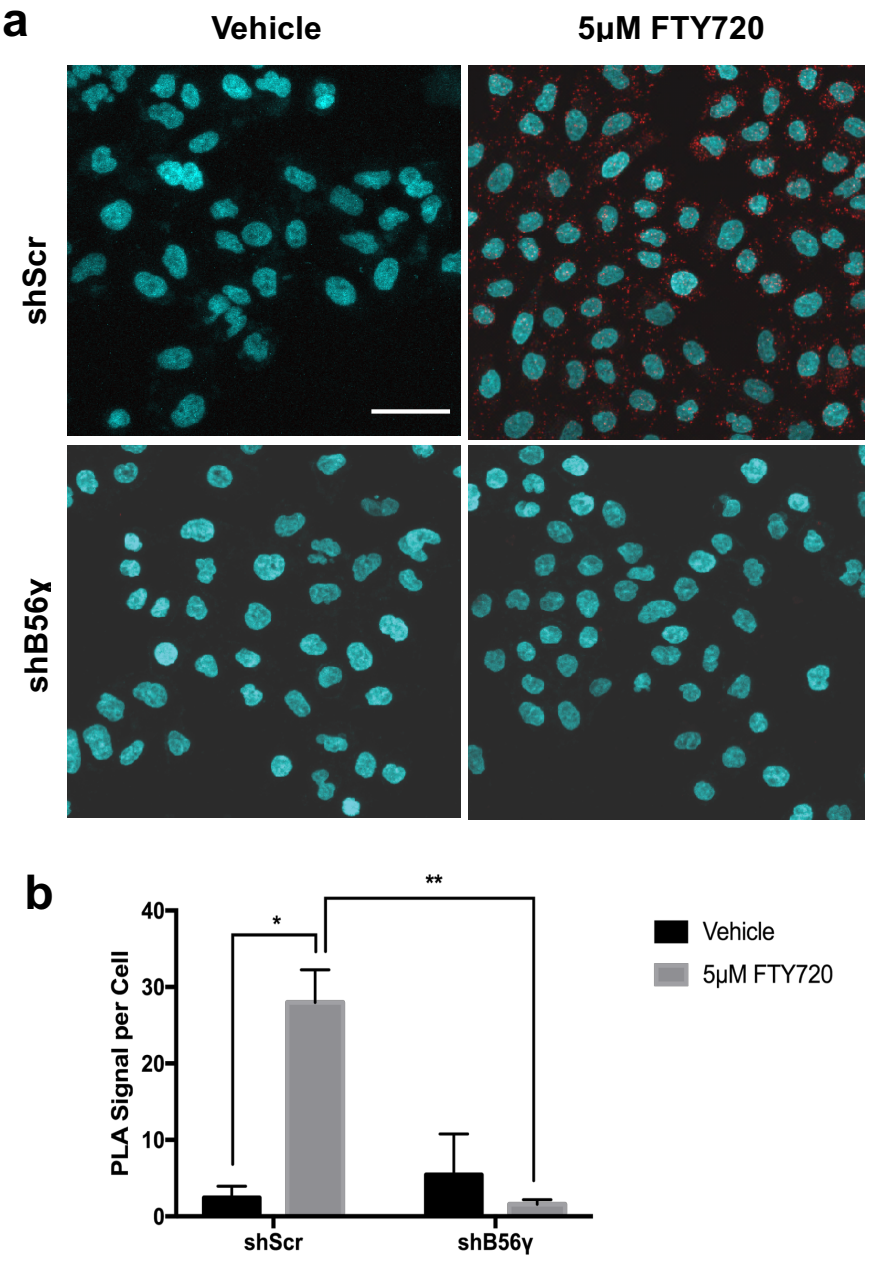

Figure 46| Myosin IIa is targeted by FTY720-activated PP2A.

(a) validation of PP2AC/Myosin IIa association observed in SILAC data. association between PP2AC and Myosin IIa in shSCR and shB56ɣ stable knockdown cell lines ± treatment of 5 μM FTY720 for 3 hrs by PLA using antibodies against PP2AC and myosin IIa. Representative images of n = 3 independent experiments. Scale bars represent 100 μm. **(b)** quantitation of PLA experiments. Data are means ± S.E.M. of n = 3 independent experiments, analyzed by two-way ANOVA with Tukey's post hoc test (*p = 0.0122, **p = 0.0049).

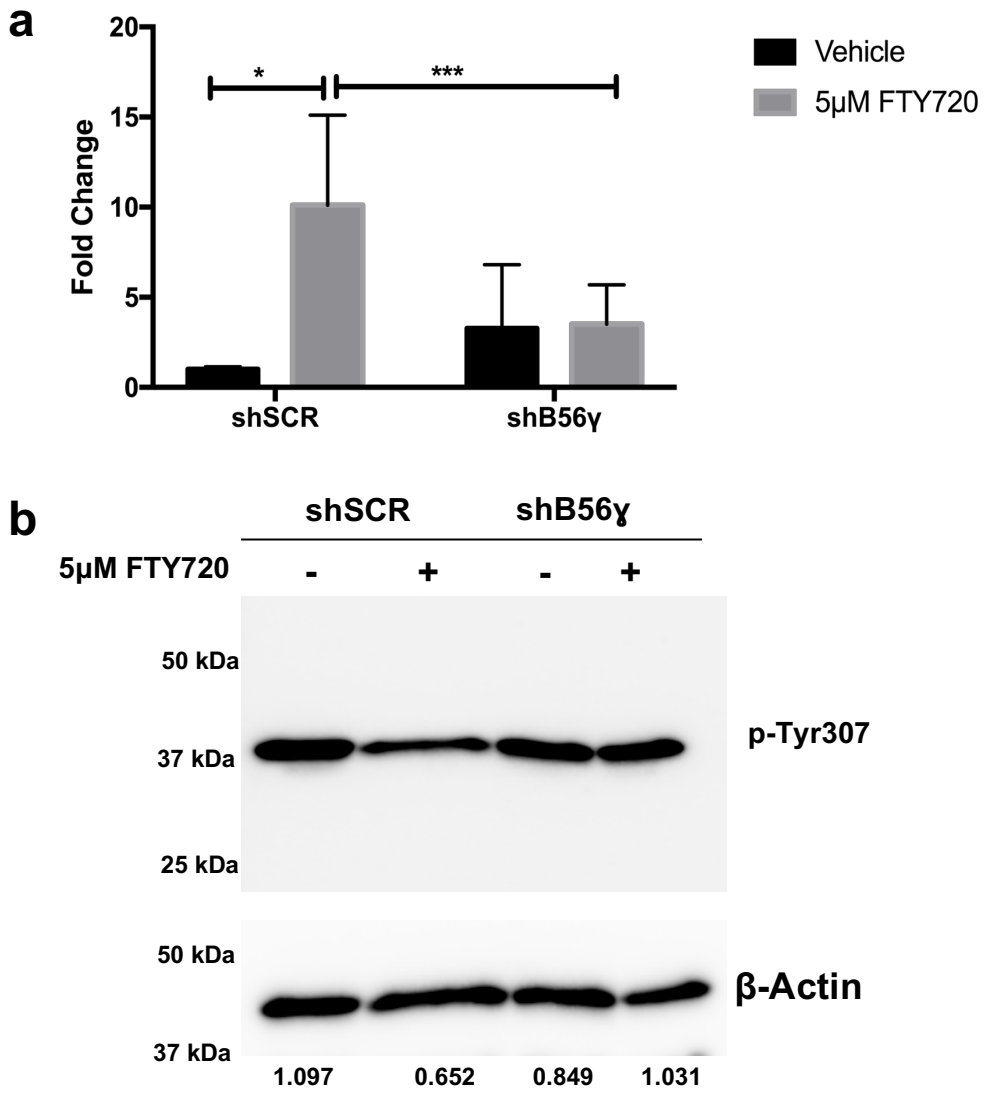

Figure 47| Myosin IIa is a potential substrate for FTY720-activated PP2A.

(a) PP2A activity assay in shSCR and shB56γ stable knockdown cell lines ± treatment of 5μM FTY720 for 16 h using purified rabbit non-muscle Myosin IIa as a substrate. Data are means ± S.D. of n = 3 independent experiments analyzed by two-way ANOVA with Tukey's post hoc test (*p = 0.0096, **p = 0.0224). **(b)** Western blot of p-Tyr307 on PP2AC, normalized to β-Actin.

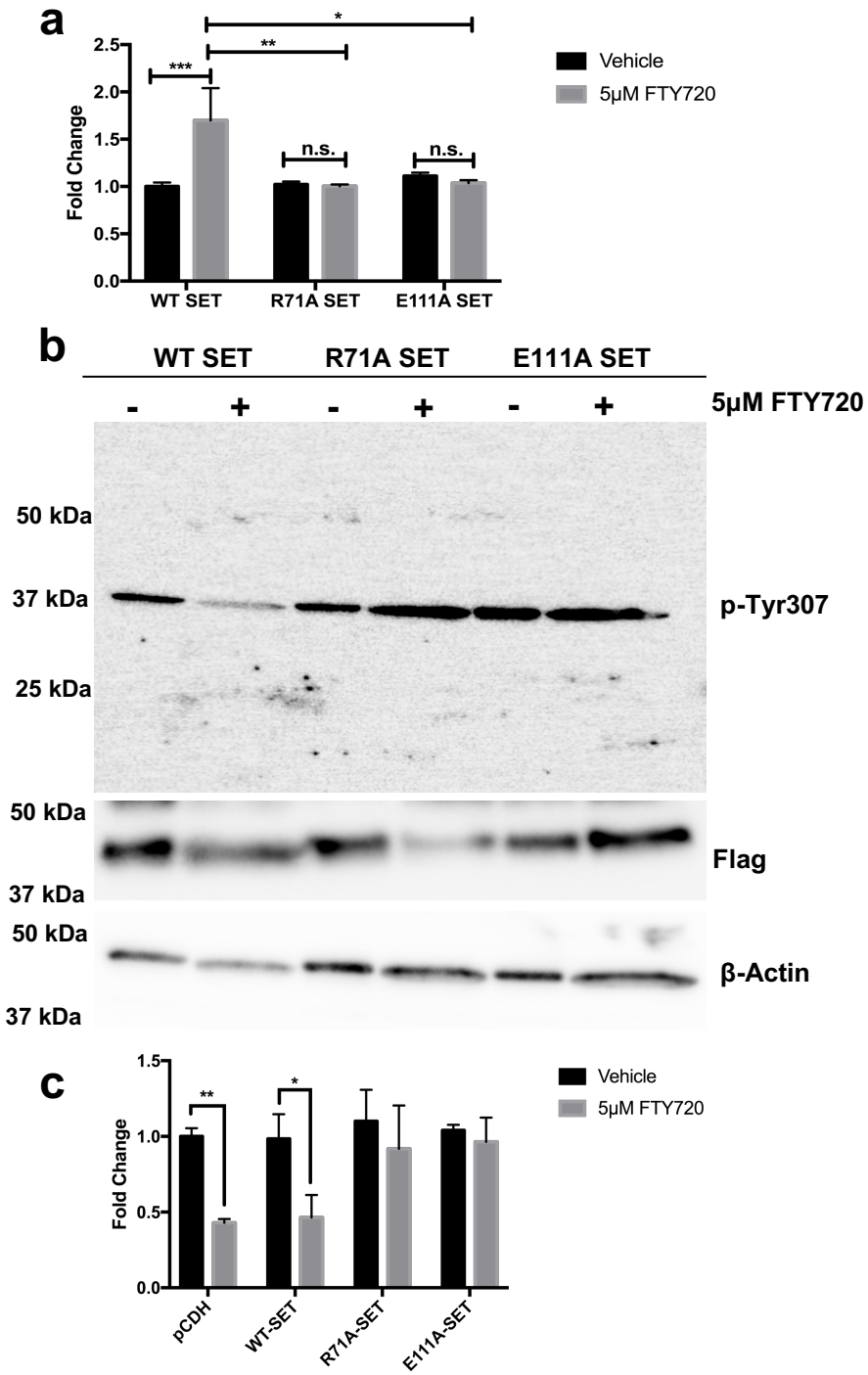

Figure 48| SET^{R71A} and SET^{E111A} mutants reduce PP2A activation in response to FTY720.

(a) PP2A activity assay in A549 cells transiently overexpressing WT, R71A, or E111A Flag SET ± treatment of 5 μM FTY720 for 16 h. using purified rabbit non-muscle Myosin IIa as a substrate. Data are means ± S.D. of n = 3 independent experiments analyzed by two-way ANOVA with Tukey's post hoc test (*p = 0.0011, **p = 0.0007, ***p = 0.0007). **(b)** Western blot of p-Tyr307 on PP2AC, normalized to β-Actin and Flag. **(c)** quantitation of p-Tyr^{307} blots. Representative blot of n= 3 individual

experiments. Blots were quantified with ImageJ. Data are means normalized to actin ± S.D. and analyzed by two-way ANOVA with Tukey's post hoc test (*$p < 0.0001$, **$p < 0.0001$, ***$p < 0.0001$).

Phosphorylation of SET influences PP2A activity

It is known that SET phosphorylation can increase or decrease its inhibitory function on PP2A in a site-dependent manner[98,184–187]. To examine whether SET-PP2A association controlled by FTY720 is also regulated by the phosphorylation status of SET in cells, we generated phospho-mimetic and non-phosphorylatable FLAG-tagged SET mutants of all known relevant sites, including S9E, S9A, S24E, S24A, S93E, S93A, Y133E, Y133F, Y133A, S171E, and S171A (Fig. 49a-b). Then, effects of these mutations on FLAG-SET-PP2A-B56γ association and FLAG-SET-PP2ACα association were measured using PLA in A549 cells with shRNA-mediated stable knockdown of endogenous SET. Data showed that phosphorylation of only the S171 residue of SET plays a role in PP2A association in response to FTY720 (Fig. 49c).

The SET^{S171A} mutant showed significantly increased association with PP2A, while SET^{S171E} showed a reduction in association when compared to SET^{WT} (Fig. 49c, 50a-b). The SET^{S171A} mutation showed resistance to FTY720-induced disruption of association with PP2ACα (Fig. 50a-b). Both SET^{S171A} and SET^{S171E} showed association with B56γ comparable with SET^{WT} with and without FTY720 treatment. These data also showed that SET^{S171A} association with B56γ was elevated compared to SET^{WT} and SET^{S171E} (Fig 51a-b) with/without FTY720, which is consistent with the effects of SET^{S171A} on resistance to decreased oligomerization by FTY720 (Fig. 52), resulting in resistance to PP2A activation in response to FTY720 (Fig 53a-b). These data support that dephosphorylation of SET at Ser171 plays a role in resistance to FTY720-mediated PP2A activation in A549 cells, and that both phosphorylated and non-phosphorylatable SET mutants at Ser171 stay associated with B56γ in the absence or presence of FTY720.

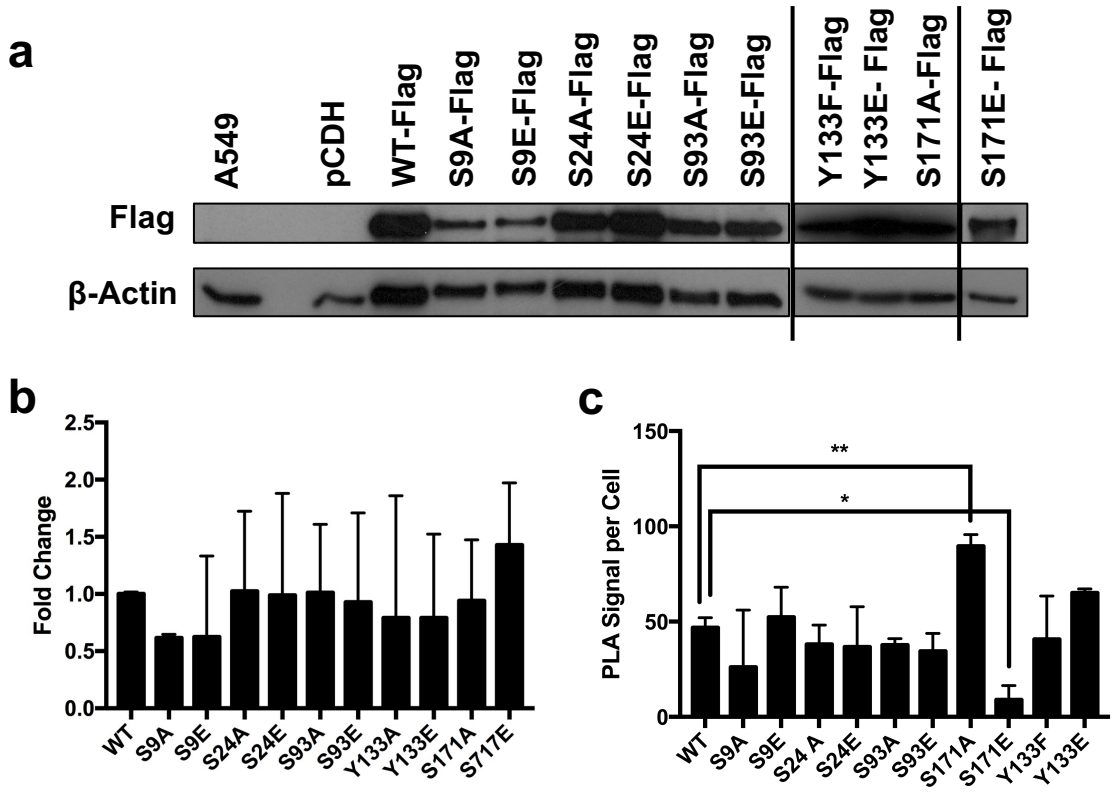

Figure 49| Expression of phospho-mimetic and non-phosphorylatable SET mutants.

(a) Western blot for Flag-tag on phospho-mimetic and non-phosphorylatable SET mutants. **(b)** Quantitation of mutant Flag-tagged SET expression normalized to actin. **(c)** Association between Flag-SET mutants and PP2AC ± 5 μM FTY720 was measured by PLA using antibodies against Flag and PP2AC. Data are means ± S.E.M. of at least 3 independent experiments, analyzed by Student's t test (*p= 0.0229, **p = 0.0061).

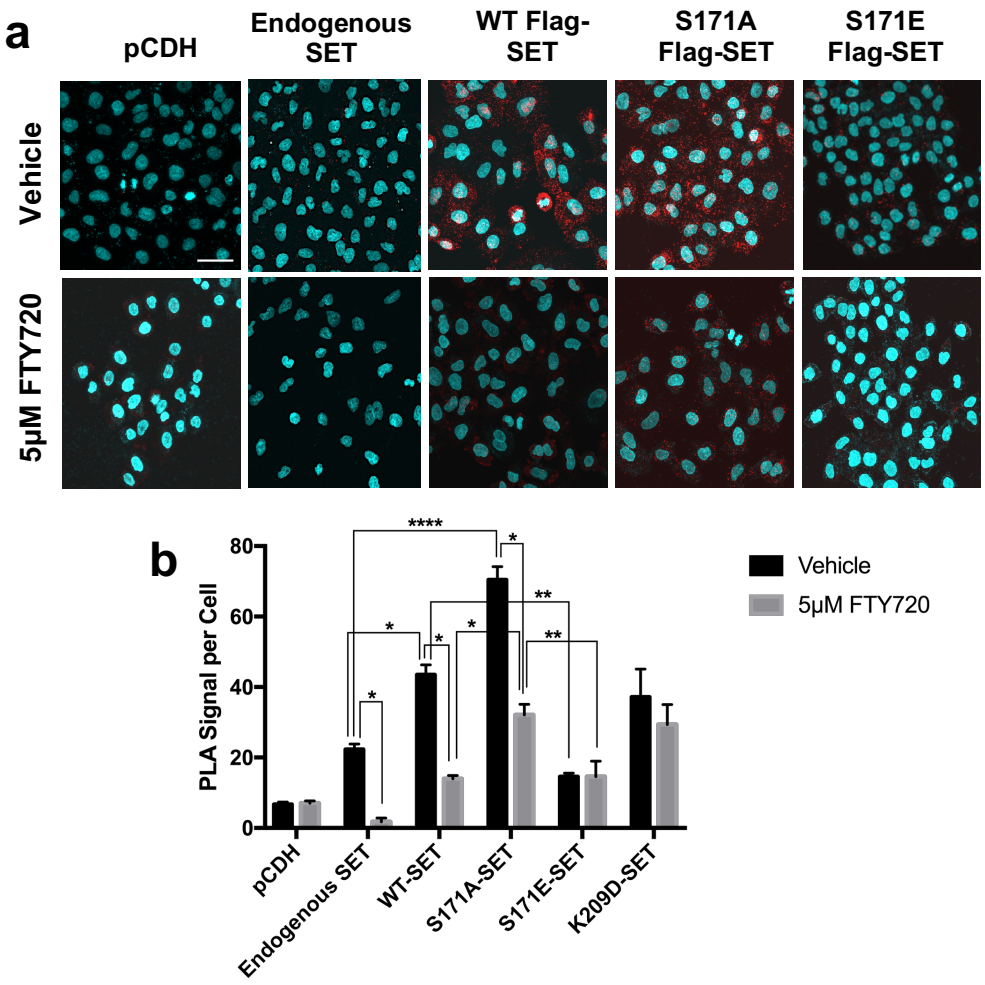

Figure 50| Phosphorylation at Serine^{171} influences SET/PP2A association.

(a) representative images of PLA between endogenous SET, S171, and K209D Flag-SET mutants and PP2AC ± 5 μM FTY720 (n=3 independent experiments per group). Scale bars represent 100 μm. **(b)** association between endogenous SET, Flag-SET^{WT}, Flag-SET^{S171A}, Flag-SET^{S171E}, and Flag-SET^{K209D} mutants and PP2AC ± 5 μM FTY720 with a pCDH empty vector control measured by PLA using antibodies against SET, Flag, and PP2AC. Data are means ± S.E.M. of n = 3 independent experiments, analyzed by two-way ANOVA with Tukey's post hoc test (*p< 0.05, **p< 0.01, ***p<0.00 and ****p< 0.0001).

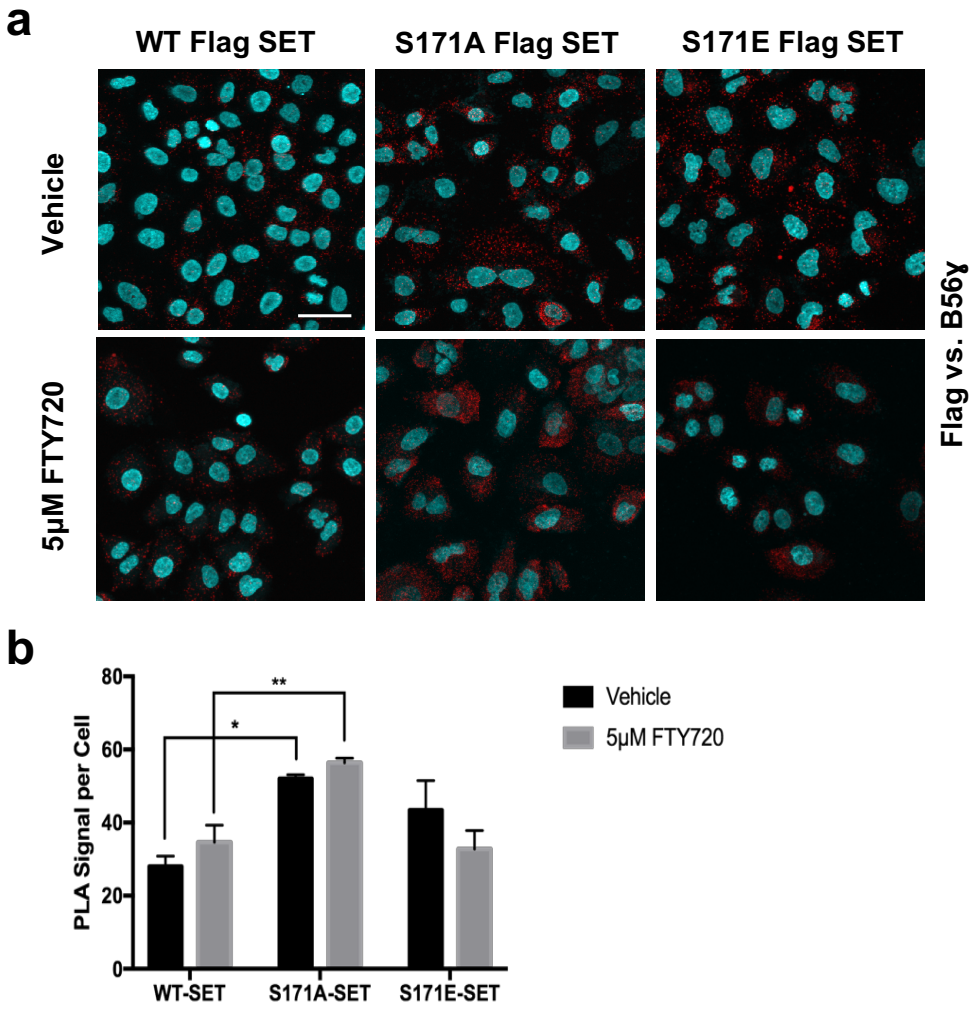

Figure 51| SET Ser^{171} mutants remain in contact with B56γ in the presence or absence of FTY720.

(a) representative images of PLA between S171A and S171E Flag-SET and B56γ ± 5 μM FTY720 (n=3 independent experiments per group). Scale bars represent 100 μm. **(b)** association between Flag-SET^{S171A} and Flag-SET^{S171E} and PP2A-B56γ ± 5 μM FTY720 assessed by PLA using antibodies against Flag and B56γ. Data are means ± S.E.M. of n = 3 independent experiments analyzed by two-way ANOVA with Tukey's post hoc test (*p = 0.0243, **p = 0.0439).

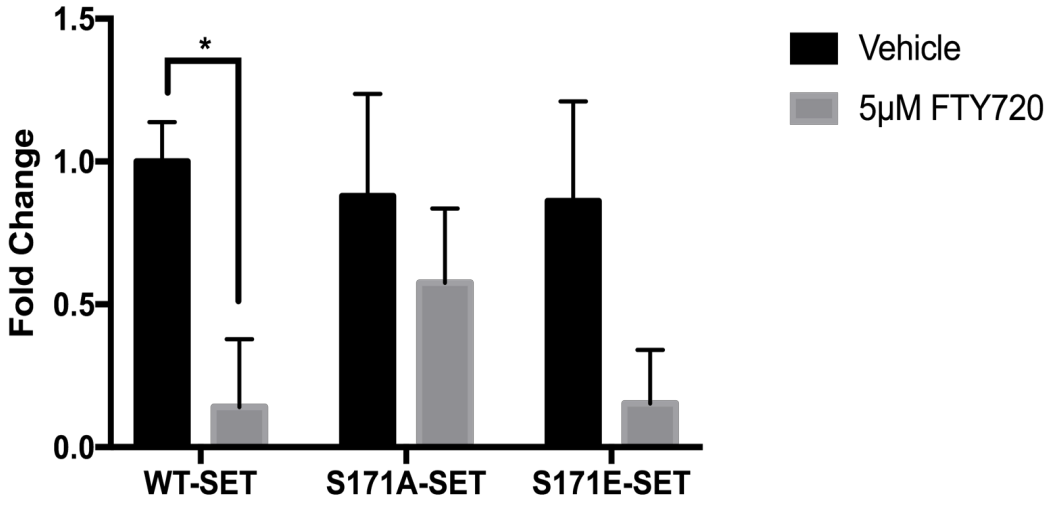

Figure 52| SET^{S171A} retains oligomeric state in the presence of FTY720.

Quantitation of glutaraldehyde (GA) crosslinking of Flag-SET^{WT}, Flag-SET^{S171A}, and Flag-SET^{S171E} oligomers in response to 3 h treatment with 5 μM FTY720. Data are means ± S.D. of n = 3 independent experiments analyzed by two-way ANOVA with Tukey's post hoc test (*p = 0.0321). Data are represented as a fold change compared to the vehicle treated SET^{WT} samples.

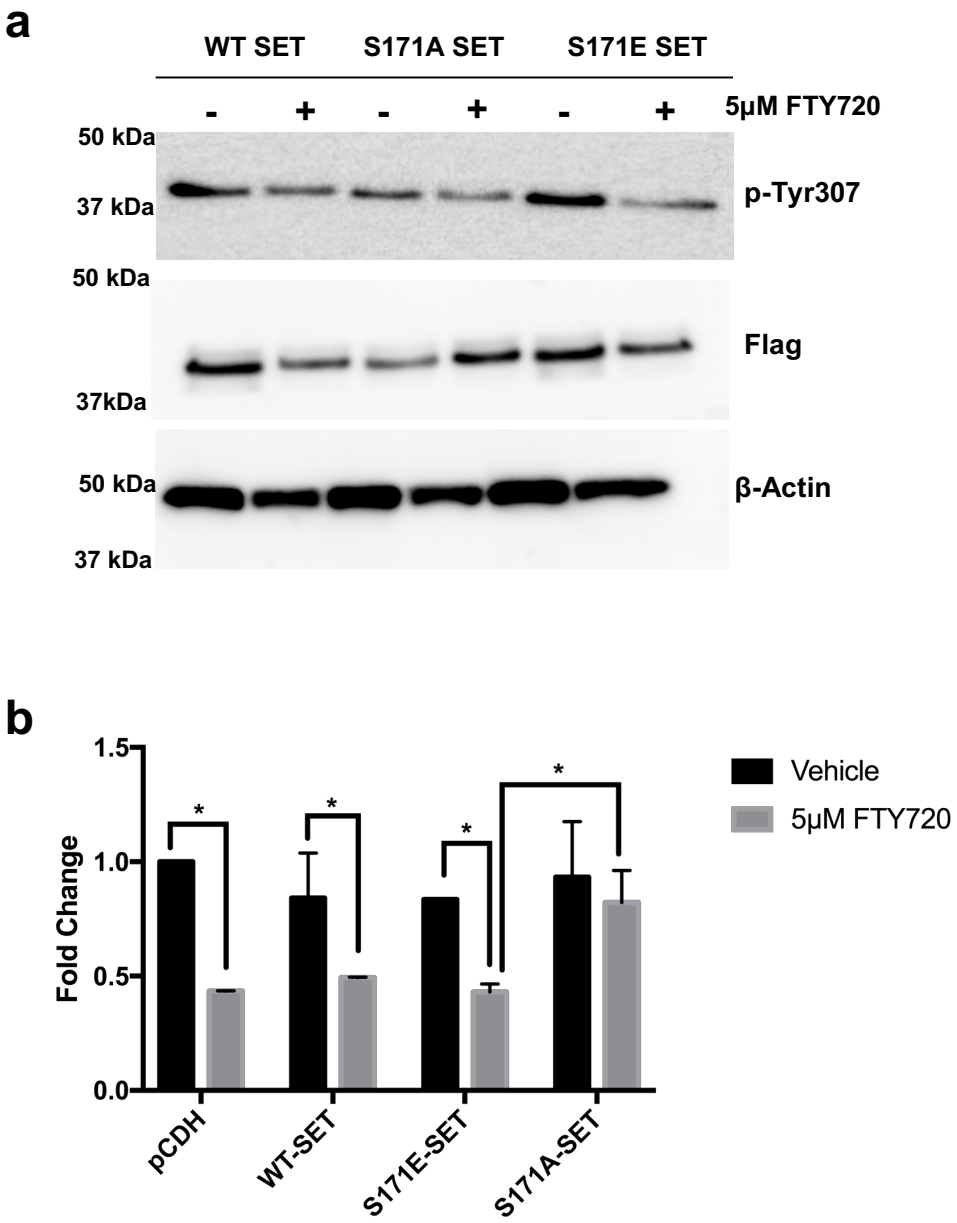

Figure 53| Expression of SETS171A reduces activation of PP2A.

(a) Western blot of p-Tyr307 of PP2AC as a marker of activity normalized to β-Actin and Flag expression. **(b)** quantitation of p-Tyr^{307} blots. Representative blot of n= 3 individual experiments. Blots were quantified with ImageJ. Data are means normalized to actin and Flag ± S.D. and analyzed by two-way ANOVA with Tukey's post hoc test (*$p < 0.0001$, **$p < 0.0001$, ***$p < 0.0001$).

The SET/PP2A Complex may assemble and originate in the Endoplasmic Reticulum

A persistent question in the SET/PP2A field is the source of the ceramide that bind SET. The simplest answer would be the source of ceramide with the cell; the ER. To this end, we examined if this specific SET/PP2A complex, containing PP2AA, PP2A-B56γ, and PP2ACα, is localized in the ER prior to activation with FTY720. We monitored the subcellular localization of PP2A via the B56γ subunit in response to FTY720 by immune fluorescence microscopy. Interestingly, we noted colocalization between B56γ and Protein Disulfide Isomerase A2 (PDI), a rough ER marker (Fig. 54a). Upon treatment with FTY720, B56γ shifted to the smooth ER (11β-HSD1 colocalization) (Fig. 54b). Eventually there was also formation of B56γ puncta colocalized with GM130, a Golgi marker (Fic. 54c). The data suggested that FTY720-activated PP2A originates in the ER; therefore, we isolated the ER to look for both SET and PP2A. As SET is predominantly a nuclear protein, PP2A was immune-precipitated after purification of ER by ultra-centrifugation (Fig. 55) to enrich for both proteins and increase chances of detection. There is a reduction in SET/PP2A association with exposure to FTY720 (Fig. 55). Furthermore, there is a reduction in both B56γ and SET after treatment with FTY720 (Fig. 55, right panel).

To further confirm the ER localization of SET and PP2A, we engineered a GFP-tagged SET to be retained in the ER (Fig. 56a-b). Ectopic expression of both SET^{WT}-GFP and SET^{ER}-GFP showed that retention of SET in the ER increased association with PP2A (Fig. 56c). Together, these data support our proposed mechanism of PP2A activation via FTY720 or ceramide preventing SET oligomerization. It also suggests that the SET/PP2A complex originates in the ER. It is, therefore, likely that modulation of ceramide, which is

generated in the ER, influences SET oligomerization, PP2A activation, and subsequent egress from the ER to execute its tumor suppressive functions.

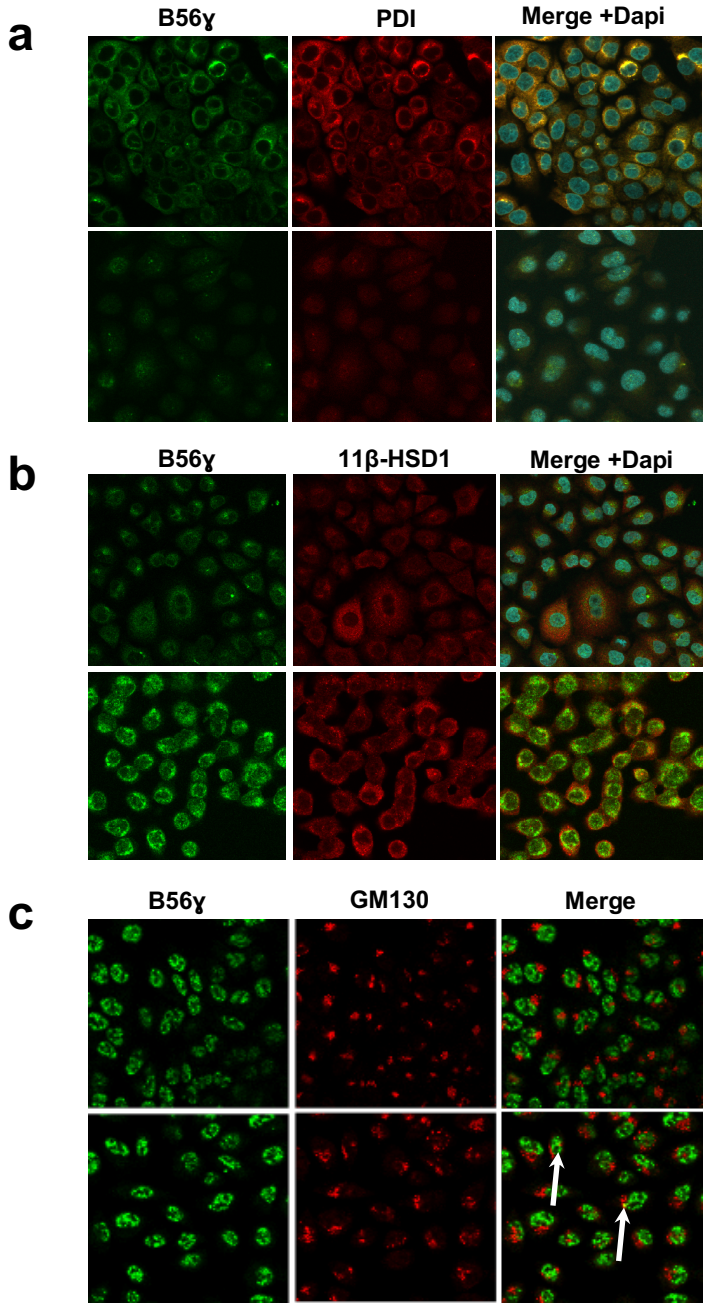

Figure 54| B56γ-containing PP2A translocate from the rough ER to Golgi after exposure to FTY720.

(a) observation of subcellular co-localization of B56γ with PDI ± 5 μM FTY720 for 3hr by immune fluorescence microscopy. **(b)** observation of subcellular co-localization of B56γ with 11β-HSD1 ± 5 μM FTY720 for 3hr by immune fluorescence microscopy. **(c)** observation of subcellular co-localization of B56γ with GM130 ± 5 μM FTY720 for 3hr by immune fluorescence microscopy.

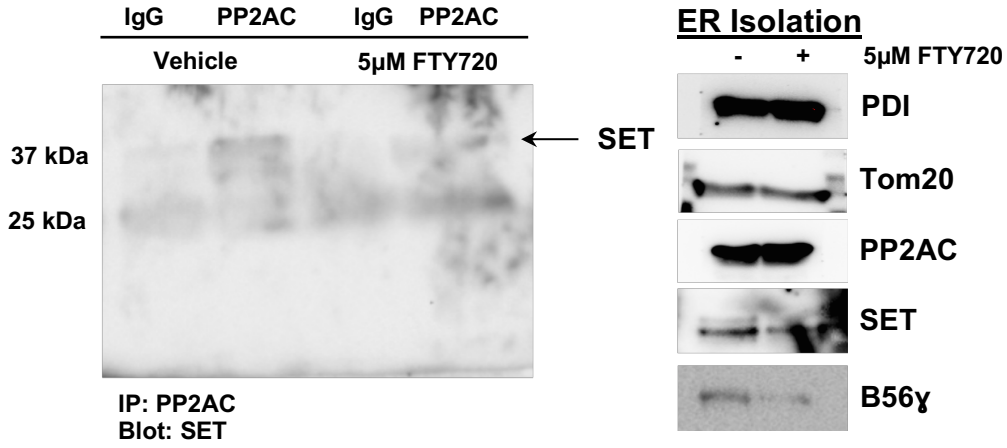

Figure 55| The SET/PP2A complex is detected in the endoplasmic reticulum.

(a) co-immune precipitation of PP2AC and SET from purified ER after exposure to 5 μM FTY720 for 3hr. PDI is an ER marker and TOM20 is a mitochondrial marker. ER was isolated by differential ultra-centrifugation.

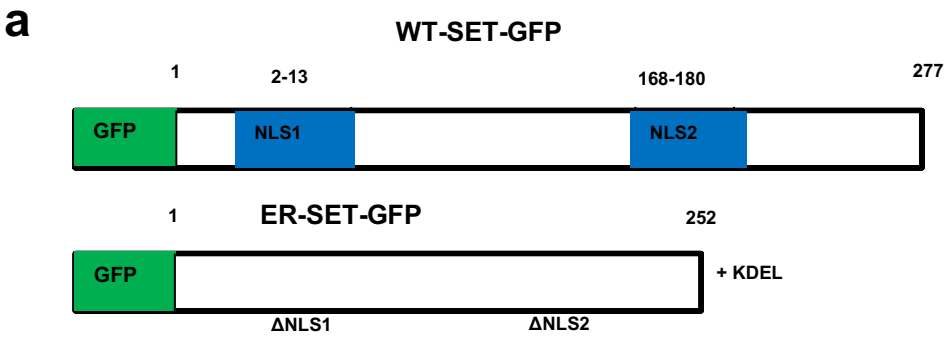
a
WT-SET-GFP
1
2-13
168-180
277
GFP
NLS1
NLS2
1
ER-SET-GFP
252
GFP
+ KDEL
ΔNLS1
ΔNLS2

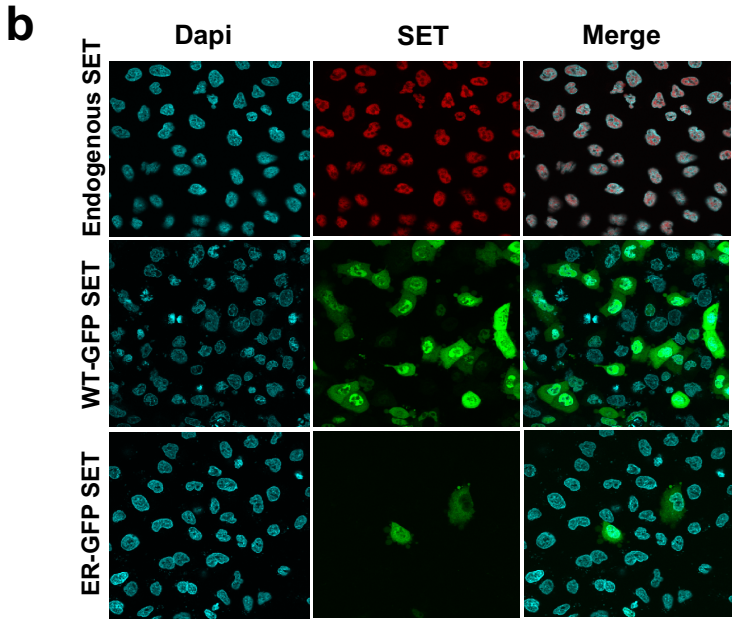
b
Dapi
SET
Merge
Endogenous SET
WT-GFP SET
ER-GFP SET

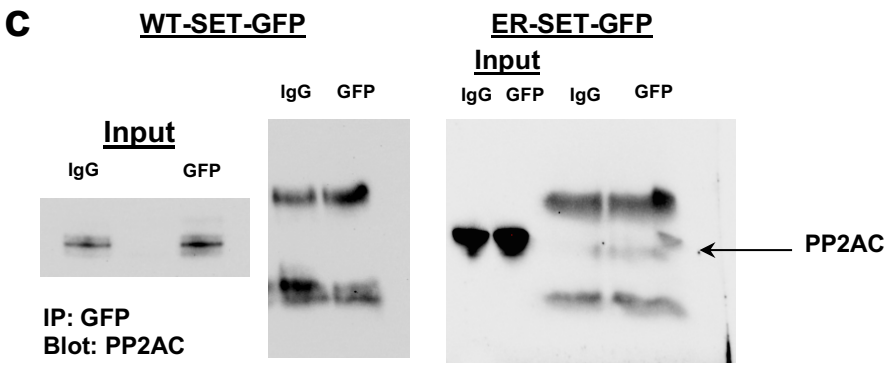
c
WT-SET-GFP
ER-SET-GFP
Input
IgG
GFP
Input
IgG
GFP
IgG
GFP
IgG
GFP
PP2AC
IP: GFP
Blot: PP2AC

Figure 56| Manipulation of SET subcellular localization enhances interaction with PP2A.

(a) diagram comparing features of SET^{WT} and SET^{ER}-GFP constructs. Both nuclear localization signals were removed and a KDEL ER-recycling sequence was added to the C-terminus. **(b)** Immune fluorescence microscopy comparing subcellular localization of ectopically expressed SET^{WT} and SET^{ER}-GFP. SET^{WT}-GFP localized heavily to the nucleus while SET^{ER}-GFP remains more cytoplasmic. **(c)** Co-immune precipitation of SET^{WT} and SET^{ER}-GFP with magnetic GFP-conjugated beads (Abcam). Detection of PP2AC by Western blot.

Summary

Data presented in this chapter show that the loss of specific PP2A subunits will disrupt SET-PP2A association, suggesting that SET inhibits a particular PP2A consisting of PP2AAβ, B56γ, and PP2ACα subunits. This suggests that the interaction may be more specific and that SET may not be a universal inhibitor of PP2A, as is widely believed. Moreover, at least a monomer of SET remains with FTY720-activated PP2A by maintaining contact with the B56γ subunit. The phosphorylation status of SET at S171 also plays a key role in determining SET-PP2A association. This is most likely due to manipulation of subcellular localization. Serine 171 falls within one of SET's nuclear localization signals. Literature suggests that dephosphorylation at this site increases the cytosolic abundance of SET by slowing its nuclear localization[186]. In this study, we also show data that suggest the SET/PP2A complex is loaded in ER and can egress to the Golgi upon stimulus with FTY720 or DeC18.

Chapter 6: Discussion and Future Directions

SET overexpression is involved in many cancers, where it functions as an inhibitor of PP2A. Reactivation of PP2A by targeting SET is known to be a potent avenue of tumor suppression; however, the specific interactions between SET and PP2A, as well as the interaction between SET and FTY720 or ceramide, have been largely unknown.

Here are described the first molecular details of sphingolipid-protein interaction by NMR spectroscopy. The structural work of this study proposes a possible mechanism as to how ceramide or FTY720 interacts with SET, leading to PP2A activation. The data reaches beyond the realm of cancer biology into ceramide/SET/PP2A-mediated mechanisms of insulin resistance and vascular dysfunction in metabolic disease[193,254–256]. In both instances, increased levels of ceramide activate PP2A, through SET, leading to antagonistic insulin signaling through the AKT pathway and eNOS-related vascular contractility problems. Contrary to cancer biology, the therapeutic goal would be to inhibit PP2A activity in metabolic disease. Overall, our data are consistent with previous findings that showed the N-terminal region (36-124) of SET to be essential for PP2A inhibition[180].

We show key residues (R71 and E111) that are essential for lipid-binding. Similar to D-*e*-C18-ceramide, the perturbations resulted in confined binding clusters with increasing amounts of FTY720 (0.5-10 μM). The shifts obtained with FTY720 also showed similar interaction sites as C18-ceramide along the interface between the helix of the dimerization domain and beta sheets in the globular region. The polar head groups of both compounds appear to anchor the binding along the interface between the helix of the dimerization domain and beta sheets in the globular region. E111 appeared to be

important in stabilizing the head group amine of FTY720, similar to ceramide binding. Data also showed that FTY720 engages with R71, while D-*e*-C18 ceramide did not show any significant association with R71. This interaction between FTY720 and R71 of SET appeared to be driven by an electrostatic cation/π-arene mechanism. The model also suggested that FTY720 is more buried in the cleft created by two anti-parallel beta sheet stabilized loops and an alpha helix than ceramide. Its lower molecular weight may allow it to better intercalate the protein. Overall, both FTY720 and ceramide are occupying the same region in SET, but in a different manner due to their divergent chemical structures.

In addition, the helical structure within the dimerization domain of SET may be disrupted upon binding to FTY720 or ceramide, preventing oligomerization. Analysis of SET after crosslinking with glutaraldehyde shows a clear reduction in oligomerization. It is thermodynamically more plausible that oligomers are prevented from forming by a small molecule as opposed to disrupting oligomers. Moreover, loss of the entire N-terminal region (Met1-Gly97) completely ablates lipid binding. Therefore, we propose that SET oligomerization is essential for PP2A inhibition, since SET exists primarily as a dimer and tetramer within cells[182,242]. Interestingly the SET^{R71A} mutant showed an increased propensity towards the monomer state compared to SET^{WT} and SET^{E111A}. The side chain of Arg71 is perfectly situated to extend down into the globular domain of SET. In that position it is able to participate in electrostatic and hydrogen bonding interactions with Glu111 and Thr113. It is possible that this acts as a stabilization mechanism for the helical structure of the dimerization domain. Evidence for this can be found in Figure 30, where CD data of SET^{R71A} shows that the charge loss causes SET to transition to a state with greater percentages of random coil and β-strands. This change, when localized to the

dimerization domain, could cause the R71A mutant to be more monomeric. The CD data further supports our proposed mechanism of a site-specific conformation transition centered in the dimerization domain of SET when FTY720 and C18-ceramide engage R71 and E111, respectively. Lipid-binding disrupts any electrostatic and hydrogen bonding interaction between Arg71 and Glu111 and/or Thr113. Collectively, these intriguing data further point to the importance of an intact N-terminal helix and dimerization domain for lipid-binding.

It is important to note that the reduction in SET oligomers is not followed by a concomitant increase in monomeric SET. The fate of lipid-bound SET is unknown. Treatment with the proteasome inhibitor MG132 did not rescue monomeric SET levels following FTY720 exposure, suggesting the monomeric SET is not subject to increased proteasomal degradation. Lysosomal degradation, or autophagy, is an established mechanism of sphingolipid metabolism. Rare genetic mutations (Gaucher's and Farber Diseases) can cause inborn errors of metabolism resulting in the accumulation of various sphingolipids, including ceramide[258–261]. Accounting for our data suggesting the SET/PP2A complex may originate in the ER, it is possible that lipid-bound SET undergoes lysosomal degradation. Pretreatment or co-treatment of cells with Bafilomycin A1, a vacuolar proton ATPase inhibitor, with FTY720 may inhibit lysosomal[262] degradation and possibly restore monomeric SET. If lipid-bound SET transitions to a state more similar to random coil, it is possible that the UPR pathway is responsible for clearing the protein in order to avoid ER stress. SET dimerization has been shown to influence inhibitor of histone acetyltransferases (INHAT) function[151,235], it is also possible that SET regulates its own transcription through an epigenetic mechanism.

In this study, we used a pyridinium ceramide as a molecular probe to test our 'extended' ceramide structure hypothesis[97]. NMR data showed that a particular proton on the pyridine ring had weak NOEs with both the alpha hydroxyl and aliphatic chain of the sphingosine base. This is indicative of transient proximity caused by rotation around the amide bond. Upon binding to SET, that rotation is stabilized into the 'extended' conformation, allowing protons on the pyridine ring to undergo efficient magnetization transfer when monitored by STD-NMR. If the ceramide were 'compact', magnetization transfer would be inefficient or non-existent due to steric hindrance caused by the sphingosine backbone. TOCSY analysis of FTY720 showed that the amine group, followed by the aromatic ring, initiates binding to SET. We were also able to gain insight into the stereochemical specificity that SET displays. When the chirality at carbons 2 and 3 on the sphingosine backbone are changed from 2S,3R (D-*erythro*) to 2R,3S (L-*threo*) the sphingosine backbone is not able to align in parallel with the N-terminal helix. Instead, the sphingosine backbone shifts perpendicular to the N-terminal helix, and possibly interferes with the polar head group's ability to engage the binding pocket (data not shown). Additionally, the 'handedness' of the N-terminal helix creates charge distribution through spin polarization, providing enantioselectivity[263].

It is interesting to note that despite both SET and PP2A being in high abundance in cells, there is only a limited interaction between the two proteins, as evidenced by PLA. This suggests that the interaction may be more specific and that SET may not be a universal inhibitor of PP2A, as is widely believed. Our data show that the loss of specific PP2A subunits will disrupt SET-PP2A association, proposing that SET inhibits a particular PP2A consisting of PP2AA, B56γ, and PP2ACα subunits. Literature indicates

that this PP2A, containing the B56γ regulatory subunit, is important for tumor suppression in many types of malignancies[130]. Its dysregulation, either by mutation or over expression, ablates PP2A's anti-tumor capabilities[129,131,133,264]. Based on our data, at least a monomer of SET remains with FTY720-activated PP2A by maintaining contact with the B56γ subunit. This apparent complex may be a mode of regulation, where PP2A can be turned off by SET oligomerization. Further studies are needed to describe the molecular details of the SET/ B56γ interaction.

This study relies on proximity ligation assays to look at protein-protein association in cells. While more precise than traditional immune fluorescence due to the necessity of targets to be within 40nm of each other, there are some weaknesses in the technique that need to be addressed. Foremost, the strength of the assay is lies in the quality/specificity of the primary antibodies being used. It is necessary to test via Western blot and immune-precipitation prior to use in PLA. If the antibody is not specific, then the results collected by PLA are not reliable. Another limitation is that this technique is semi-quantitative. The analysis software relies on manually set thresholds and puncta sizes. This sometimes results in either an over or under estimating of signal number.

Alternatively, a bioluminescence resonance energy transfer (BRET) or fluorescence resonance energy transfer (FRET) system could be used to look at protein-protein interactions. These systems are labor intensive due to the amount of cloning needed to construct the various combinations of fusion proteins. They are also very difficult to optimize because of the necessity to test combinations of N-terminal or C-terminal fusion proteins. A concern specific to SET and PP2A is the paucity of overall interaction. The resonance transfer may not result in consistently detectable signals. That

leaves us with *in vitro* binding assays. This requires the purification of all relevant PP2A subunits, the PP2AA, B56γ, and PP2ACα subunits, some of which require insect cell lines for expression. Moreover, a leucine carboxyl methyltransferase (LCMT) needs to be purified so that the C-terminal lysine of PP2ACα can be primed before assembly of the holoenzyme[140,141]. Traditional techniques such as surface plasmon resonance (SPR) and isothermal titration calorimetry (ITC). Both techniques require large amounts of protein that are quickly exhausted. Ultimately, PLA in combination with these in vitro assays would provide very strong evidence for SET being an inhibitor of a specific PP2A holoenzyme.

The data also show that the knockdown of B56γ completely ablates PP2A activity after exposure to FTY720, shown by monitoring total PP2A p-Tyr^{307} levels. This is very interesting and unexpected. Not only does it point to the specificity of SET; it may suggest that this particular PP2A plays a more important role in the overall regulation of the various PP2A species in the cell. The idea of a 'master-regulator PP2A' is very intriguing and deserves further investigation.

Interestingly, the phosphorylation status of SET at Ser171 also plays key roles in determining SET-PP2A association. In fact, while S171E had no effect on FTY720-mediated PP2A activation, S171A-SET was resistant to FTY720-mediated PP2A activation, which stayed associated with both PP2ACα and PP2A-B56γ subunits as an oligomeric protein with/without FTY720 in A549 cells. These data further support the idea that the oligomerization state of SET determines its association with PP2A, and that inhibition of SET- PP2ACα results in PP2A activation against specific downstream target proteins.

To this end, we determined that Myosin IIa, identified via SILAC mass spectrometry analysis, as a potential target of B56γ-containing PP2A. Myosin IIa has been identified as a tumor suppressor in squamous cell carcinoma[257]. There is evidence that PP2A-dependent dephosphorylation of myosin IIa exerts some influence over filament assembly[265]. However, the molecular details of how PP2A affects myosin IIa to drive tumor suppression are unknown and warrant further investigation.

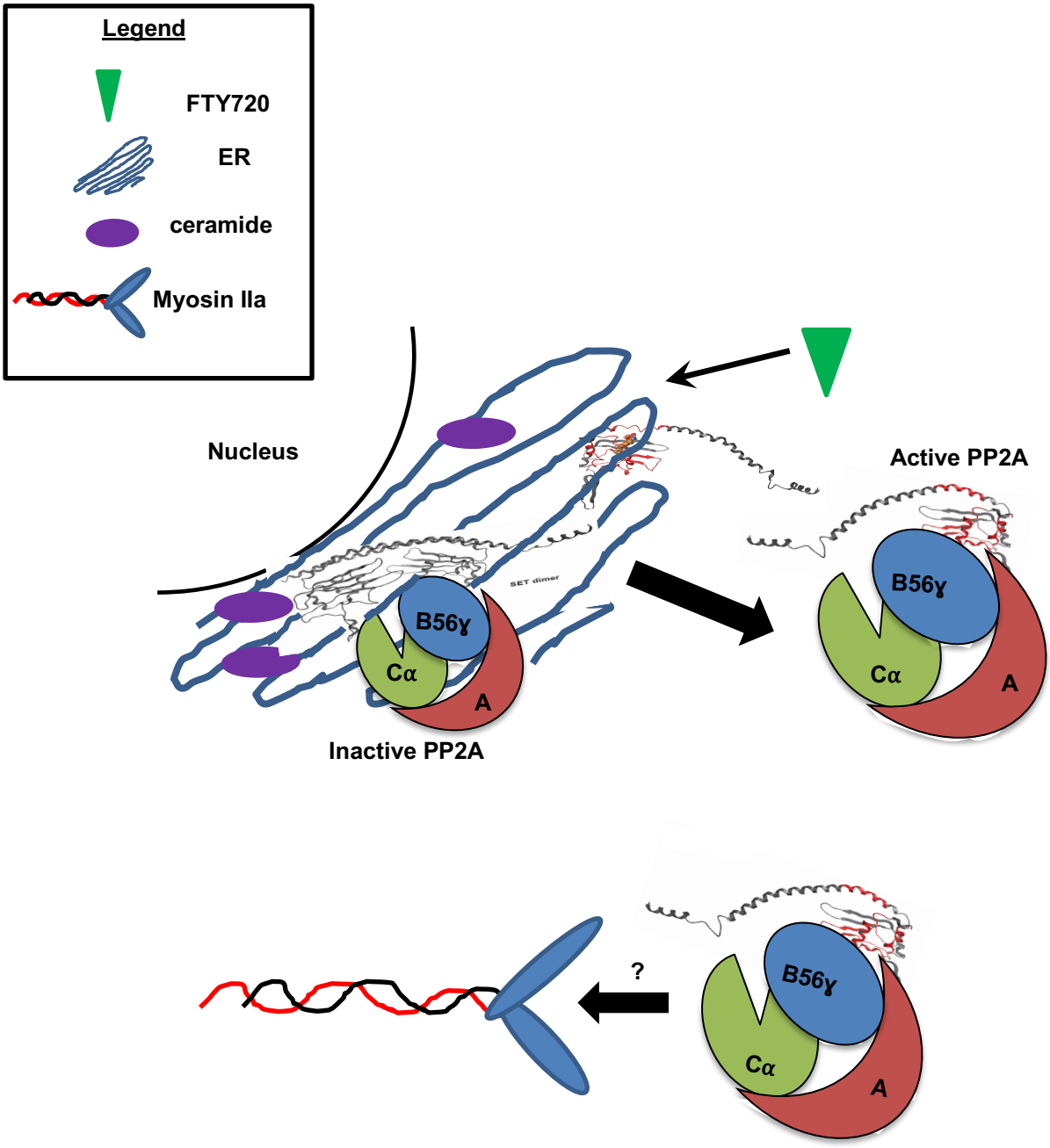

Figure 57| Working model of SET-dependent PP2A activation

The SET/ PP2A complex assembles in the endoplasmic reticulum. PP2A is inhibited by oligomeric SET. Increase in intracellular ceramide or exogenous exposure to FTY720 causes SET to become ligand-bound. Ligand-bound SET undergoes a site-specific conformational change from α-helix to random coil in the N-terminal dimerization domain. This prevents SET oligomerization, resulting in the activation of PP2A. The monomer-SET/PP2A complex then transitions from the ER to the Golgi when it targets non-muscle myosin IIa to induce cancer cell death.

Future Directions

Drug Discovery

SET overexpression has been identified in many cancer types. The therapeutic value of targeting SET, genetically or pharmacologically, to reactivate tumor suppressor PP2A has been shown in many cancer models. Nevertheless, there are no commercially available SET-targeting therapeutics due in large part to a lack of knowledge regarding SET/PP2A interaction and SET/ceramide interaction. Since FTY720 and its myriad derivatives are heavily patented by Novartis, the information obtained from this study will provide the foundation for the development of FTY720/ceramide mimetics as novel SET inhibitors to reactivate tumor suppressor PP2A.

We are using the NMR-guided models to drive the discovery/development of novel SET-targeting therapeutics. To begin, we ran over 300,000 simulations using an in-house chemical library of over 100,000 compounds. The compounds were ranked by Escore2, and the top 1,200 were re-docked with a higher stringency. This resulted in 125 significant compounds, which were further pruned based on compound chemistry. The compounds then need to be validated for binding and functionality. In this case, we can use ligand-observed NMR to look for binding events with SET. Chemical shifts and line broadening of the test compound's 1D are monitored. As a functional assay, we plan to use both PLA and a PP2A assay. Both can be adapted to achieve reasonably high throughput. We would look for an increase in PP2A activity to coincide with a loss of PLA signal when monitoring the association of endogenous SET and PP2AC. Lead

compounds would then be subjected to more vigorous biophysical analyses, such as SPR or ITC testing protein-ligand interaction.

An additional avenue of drug discovery is fragment-based screening. This method entails testing chemical moieties against protein while collecting 2D NMR data. Chemical shifts or monitored, much like for the studies outlined in Chapter 4. This method allows for the identification of weak binders that other biophysical analyses might otherwise miss. Fragment screening also allows one to access a greater fraction of chemical diversity, with a relatively small screening library. Typically, multi-site binding occurs for each functional group[266]. From there, the functional groups can be modeled into the protein based on their CSP fingerprint and a compound can then be built by chemically 'connecting' them. This results in a novel compound with the bare minimum structure needed to hit the target. The major drawback to this method is it requires a lot of protein to screen hundreds or thousands of fragments. The lack of a Sample Jet also limits feasibility because automation of the process allows for 24 hour data collection. For these reasons, we decided that a compound-based approach would be the best avenue of drug discovery. This study is in the very early stages and ongoing.

Since SET is found to be overexpressed in many cancers, a SET-targeted therapy could be widely used. SET overexpression could easily be tested for through biopsy and immunohistochemistry or Western blot comparing cancerous tissue to normal tissue. If SET is elevated in the cancer, then the individual would be a candidate for a SET-targeted therapy.

Define How PP2AC targets Myosin IIa

We determined that Myosin IIa, identified via SILAC mass spectrometry analysis, is a potential target of FTY720-activated, B56γ-containing PP2A. Myosin IIa has been identified as a tumor suppressor in squamous cell carcinoma[257]. Specifically, the disruption of ER to Golgi vesicular trafficking caused by the loss of myosin IIa was tumor suppressive[257]. It was recently shown that RAB 6 and 6a recruit myosin IIa to stimulate fission of vesicles budding from the trans-Golgi network[267]. There is also evidence that PP2A-dependent dephosphorylation of myosin IIa exerts some influence over myosin IIa filament assembly[265]. However, the molecular details of how PP2A affects myosin IIa to drive tumor suppression are unknown and warrant further investigation.

Since there is very little literature on PP2A and myosin IIa, finding the phosphorylation site on myosin IIa would be imperative to describing their interaction. A mass spectrometry (MS) based approach would be the best route of analysis. Immune precipitation of myosin IIa in vehicle and FTY720 treated cells, followed by MS analysis of each sample may identify differentially phosphorylated serine or threonine. We would expect reduced phosphorylation on serines or threonines targeted by FTY720-activated PP2A. Conversely, one could treat cells with the PP2A inhibitor, okadaic acid, and look for higher levels of phosphorylation compared to vehicle controls. All potential target residues would need to be mutated, and the experiment repeat for each myosin IIa mutant to confirm the residue(s) as a PP2A site.

Unpublished data from the lab shows that treatment of cancer cells with FTY720 causes D-*e*-C16 ceramide to be transported to the plasma membrane. Importantly,

brefeldin A, an inhibitor of ER to Golgi vesicular trafficking, abrogates FTY720-induced ceramide transport. Additionally, the knockdown of myosin IIa in cancer cells completely disrupts FTY720-induced D-*e*-C16 ceramide transport. Conceivably, the SET/PP2A complex could play a role in the transport of C16 ceramide to the plasma membrane by regulating Rab6/myosin IIa function.

Perhaps PP2A targets Rab6 directly and not myosin IIa. In a yeast model, serine phosphorylation of Rab 6 ortholog, Sec4p, negatively regulates activity necessary for cell viability[268]. Furthermore, evidence suggests that the phosphorylation status of Sec4p is governed by an unknown PP2A holoenzyme[268]. There are multiple reports of Rab family proteins being regulated by phosphorylation[268–273]; however, the opposing phosphatase(s) remains undescribed. Some literature also suggests that PP2A can target other GTPases RalA and Rac1[116,274], the latter of which facilitates the migration of a SET/PP2A complex to the plasma membrane.

Characterize and examine the possibility of the SET/PP2A complex assembling in the endoplasmic reticulum

The question always lingering around the SET/PP2A field is where does SET find ceramide? The simplest answer would be the ER, the main source of ceramide within cells. Ceramide levels can be regulated to rapidly increase or decrease in order to regulate the activity of tumor suppressive PP2A. Increased ceramide levels would inhibit SET oligomerization, and activate PP2A, while decreased ceramide levels would promote SET oligomerization which results in inhibition of PP2A activity. This is an efficient mechanism to regulate a very important enzyme in the cell. In this study, we show data

that suggest the SET/PP2A complex is localized in ER and can egress to the Golgi upon stimulus with FTY720 or DeC18. The ER localization of the SET/PP2A complex is plausible if it plays a role in the transport of C16 ceramide to the plasma membrane by regulating Rab6/myosin IIa function discussed in the previous section.

CERS6/C16-ceramide expression protects against ER stress by activating the ATF6/CHOP unfolded protein response pathway[45]. If lipid-bound SET transitions to a state more similar to random coil, it is possible that the UPR pathway is responsible for clearing the protein in order to avoid ER stress. Perhaps the mobilization of C16 ceramide has a twofold affect: disruption of plasma membrane integrity causing cell rupture and initiation of the UPR pathway to dispose of lipid-bound SET. In this case, brefeldin A could be used to induce the UPR pathway in conjunction with FTY720 after pre-treatment of cells with cycloheximide. The ER could be isolated by differential centrifugation to examine potential SET accumulation.

It is possible that the SET-PP2A complex/Rab6/myosin IIa/C16 ceramide axis is meant to maintain membrane fluidity under homeostatic physiological condition by transporting long chain ceramides[275,276]. However, overabundance of SET or exogenous cell stress (FTY720) can manipulate this pathway to support pro-survival or tumor suppressive roles.

Describe How SET interacts with the B56γ subunit of PP2A

Unexpectedly, we noted that at least a monomer of SET remains with FTY720-activated PP2A by maintaining contact with the B56γ subunit. This apparent complex may be a mode of regulation, where PP2A can be turned off by SET oligomerization.

X-ray crystallography would be the best way to examine the interaction between SET and B56γ. Crystallization of the SET/B56γ complex and SET/PP2A holoenzyme (consisting of PP2AA, B56γ, and PP2ACα subunits) in the presence and absence of FTY720 or DeC18 ceramide would provide details for this study. This study would require the purification of all relevant PP2A subunits, PP2AA, B56γ, and PP2ACα subunits, some of which require insect cell lines for expression. Moreover, a lysine methyltransferase (LMT) needs to be purified so that the C-terminal lysine of PP2ACα can be primed before assembly of the holoenzyme. In addition to setting crystal screens for the afore mentioned complexes, one could also try to crystalize the SET/PP2A holoenzyme complex in conditions previously published for the holoenzyme alone[115]. Literature suggests that multi-wavelength anomalous diffraction (MAD) would be required to resolve the phase problem along with molecular replacement to generate a structure due to the size of the SET/PP2A complex[115,141,277,278].

The molecular replacement method is a common tool to overcome the phase problem in X-ray crystallography. The phase problem is the ability to only measure the amplitude of a wave and not its origin after diffraction. The origin determines where wave maxima occur and does not influence the amplitude of a wave. This means phase can make waves constructive, giving strong diffraction, or destructive, the latter resulting in weak diffraction and lost information pertaining to electron density (structure). If the structure of a homologous protein has already been solved, the phase information from that protein can be superimposed onto collected diffraction data to generate an initial phase and electron density for the unknown structure[279]. This method requires high

homology between proteins to avoid introducing bias when generating a structure. If structure factors (F-values are representations of reflection phases and amplitudes) are too different, then the method can fail to produce an initial electron density[280].

Multi wavelength anomalous diffraction (MAD) with selenomethionine replacement of methionine can also resolve the phase problem. Heavy atoms (selenium) have a delayed emission of certain wavelength X-rays, which causes phase shifts in all reflections[281]. The analysis of these phase shifts at varying wavelengths can resolve the phase problem and provide an initial phase for the entire protein. Heavy atoms scatter X rays more strongly, so the wave amplitude changes. Comparison of the native protein and heavy protein structure factors are then used to geometrically solve the phase based on constructive or destructive diffraction[279]. If crystallography proves unfruitful, high resolution cryo-electron microscopy would be a potential alternative to obtain structure of the SET/PP2A holoenzyme.

Once structures are solved, point mutations need to be made at contact points between SET and B56γ. These mutations need to be validated structurally, and then introduced to cell systems for functional bioassays. PLA could be used to examine the effect the mutations have mon association between SET and PP2AC and SET and B56γ. These studies could be coupled with PP2A activity assays. The structural details gained from this study would identify the interface of SET and B56γ interaction. Drug discovery studies could then be undertaken to target this region, leading to the inability of SET to interact with PP2A and subsequent PP2A activation. The combinatorial approach of structural and molecular biology would not only enhance knowledge in the PP2A field,

but also be used to design a novel SET-targeting drug to reactivate PP2A through a completely different mechanism.

Further investigate how lipid-binding affects SET oligomerization

Some additional work could be done to further describe how lipid binding effects SET oligomerization. Triple resonance NMR experiments can be performed in the absence and presence of FTY720. Backbone chemical shifts can be processed to calculate a random coil index (RCI). RCI calculates protein flexibility by computing an inverse weighted average of backbone secondary chemical shifts and predicting values of model-free order parameters as well as per-residue RMSD of NMR datasets[282]. The expected result would be that the addition of FTY720 causes N-terminal residues in the dimerization domain to index more similarly with random coil than α-helix. If the SET^{R71A} mutant is able to be crystalized, the structure may support the mechanism proposed earlier in the chapter. BRET studies of SET^{WT} and SET^{R71A} could potentially be used in cells to support the biological relevance of Arg71 and its role in SET oligomerization. In SET knockdown cells various combinations of N-terminal or C-terminal GFP^2 fusion SET could be tested in the absence and presence of FTY720 or DeC18 ceramide. We would be looking a loss of GFP signal during exposure to FTY720 or DeC18 ceramide. These data from proposed experiments combined with the data presented here would add valuable information to the understanding of SET regulation of PP2A activity.

Overall, there are important implications of the data reported here with regards to understanding PP2A regulation and tumor suppression[283] by providing the molecular details of interactions between SET and PP2A, or SET-ceramide/FTY720. The structural information obtained concerning the lipid-binding pocket of SET will provide the foundation for the development of FTY720/ceramide analogs as novel SET inhibitors to reactivate tumor suppressor PP2A with improved specificity and anti-cancer function, without immune suppression and other deleterious toxicities.

Appendix I

Protocols for the Purification of Recombinant SET Constructs

Purification of Nd-SET

Nd-SET was cloned into a pET-22b (+) vector after PCR amplification with the following primers:

Forward: 5' CAGTAGCA**CATATG**ACCTCAGAAAAAGAACAGCAAGAAG 3'

Reverse: 5' GTC**CTCGAG**TTAGTCATCTTCTCCTTCATCCTCCTC 3'

BL21 (DE3) pLys cells were transformed and grown in Luria-Bertani (LB) media at 37°C with 100μg/ml ampicillin. Protein expression was induced with 0.03 mM IPTG overnight at 18˚C, with shaking at 190rpm. The cells were collected and resuspended in 10mM Na phosphate pH 8.0, 500mM NaCl, 20mM imidazole, 2% glycerol, 0.1% triton-X 100, and 0.5mM PMSF. Cells were lysed by sonication, and the lysate was then clarified by centrifugation at 15,000 rpm for 75 minutes at 4˚C. The clarified cell lysates were then filtered through 0.22μm membrane.

The protein was loaded onto a sepharose Fast Flow HisTrap column (GE Healthcare) and eluted using a linear gradient ending at 500mM imidazole (Fig. 44). The pooled fractions were then dialyzed overnight at 4°C into phosphate buffer (10 mM phosphate buffer, 50 mM NaCl pH 8.0).

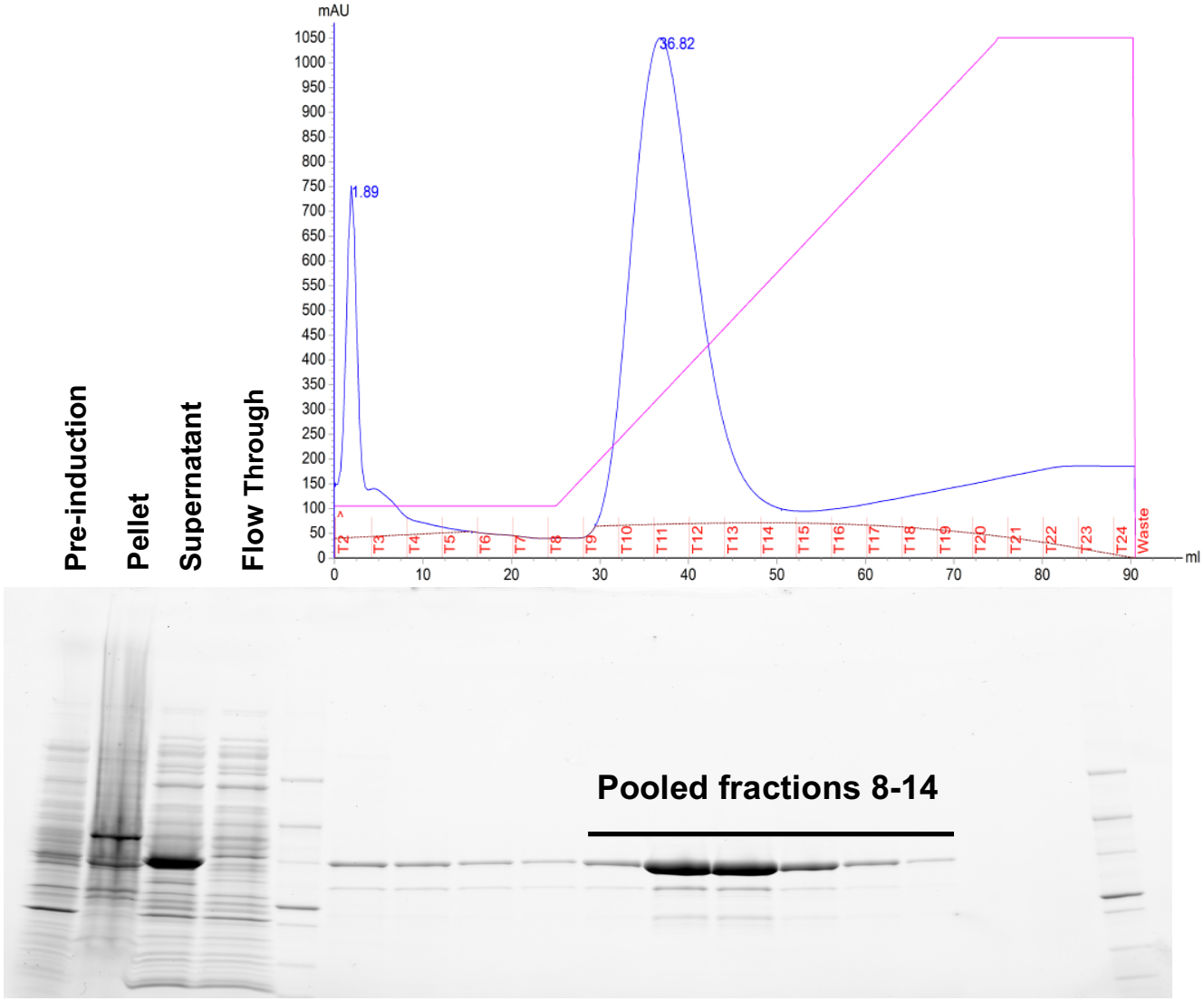

Figure 58| Elution of Nd SET from nickel affinity column.

The imidazole gradient runs from 50mM to 500mM. Nd-SET elutes from the column at approximately 200mM imidazole. Protein purity is estimated at ~95% by Coomassie stained SDS-PAGE.

Purification of NdCd-SET

NdCd-SET was cloned into a pET28b (+) vector after PCR amplification with the following primers:

Forward: 5' CGCGTGGTTCCCATATGGAAAACCTGTACTTCCAATCACCTCAGAAAAAGAACA 3'

Reverse: 5' GATCCTTACTACATATCACATATCGGGAACCAAGTA 3'

BL21 (DE3) pLys cells were transformed and grown in Luria-Bertani (LB) media at 37°C with 100µg/ml kanamycin. Protein expression was induced with 0.03 mM IPTG overnight at 18˚C, with shaking at 190rpm. The cells were collected and resuspended in 10mM Na phosphate pH 8.0, 500mM NaCl, 20mM imidazole, 2% glycerol, 0.1% triton-X 100, and 0.5mM PMSF. Cells were lysed by sonication, and the lysate was then clarified by centrifugation at 15,000 rpm for 75 minutes at 4˚C. The clarified cell lysates were then filtered through 0.22µm membrane.

The protein was loaded onto a sepharose Fast Flow HisTrap column (GE Healthcare) and eluted using a linear gradient ending at 500mM imidazole (Fig. 45a). The pooled fractions were incubated overnight at 4˚C with Thrombin to cleave the 6X-Histidine tag (Fig. 45b). The cleaved protein was then injected onto a HiLoad 26/60 200 prep grade column pre-equilibrated with phosphate buffer (10 mM phosphate buffer, 50 mM NaCl pH 8.0) for a final polishing step (Fig. 46).

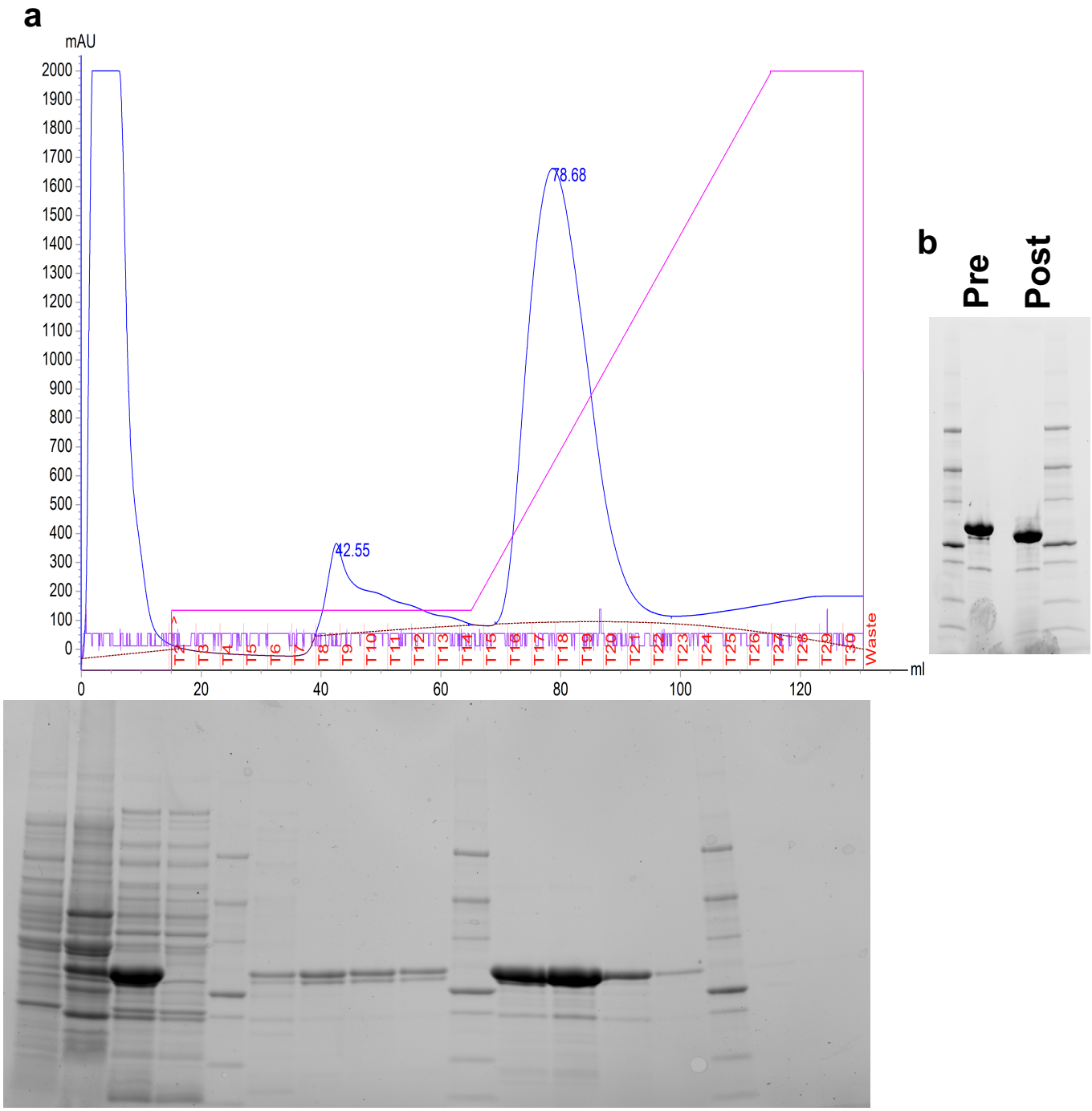

Figure 59| Elution of NdCd SET from nickel affinity column.

a, The imidazole gradient runs from 50mM to 500mM. NdCd-SET elutes from the column at approximately 200mM imidazole. **b,** Pooled fractions of NdCd-SET pre-and post-overnight thrombin cleavage at 4˚C.

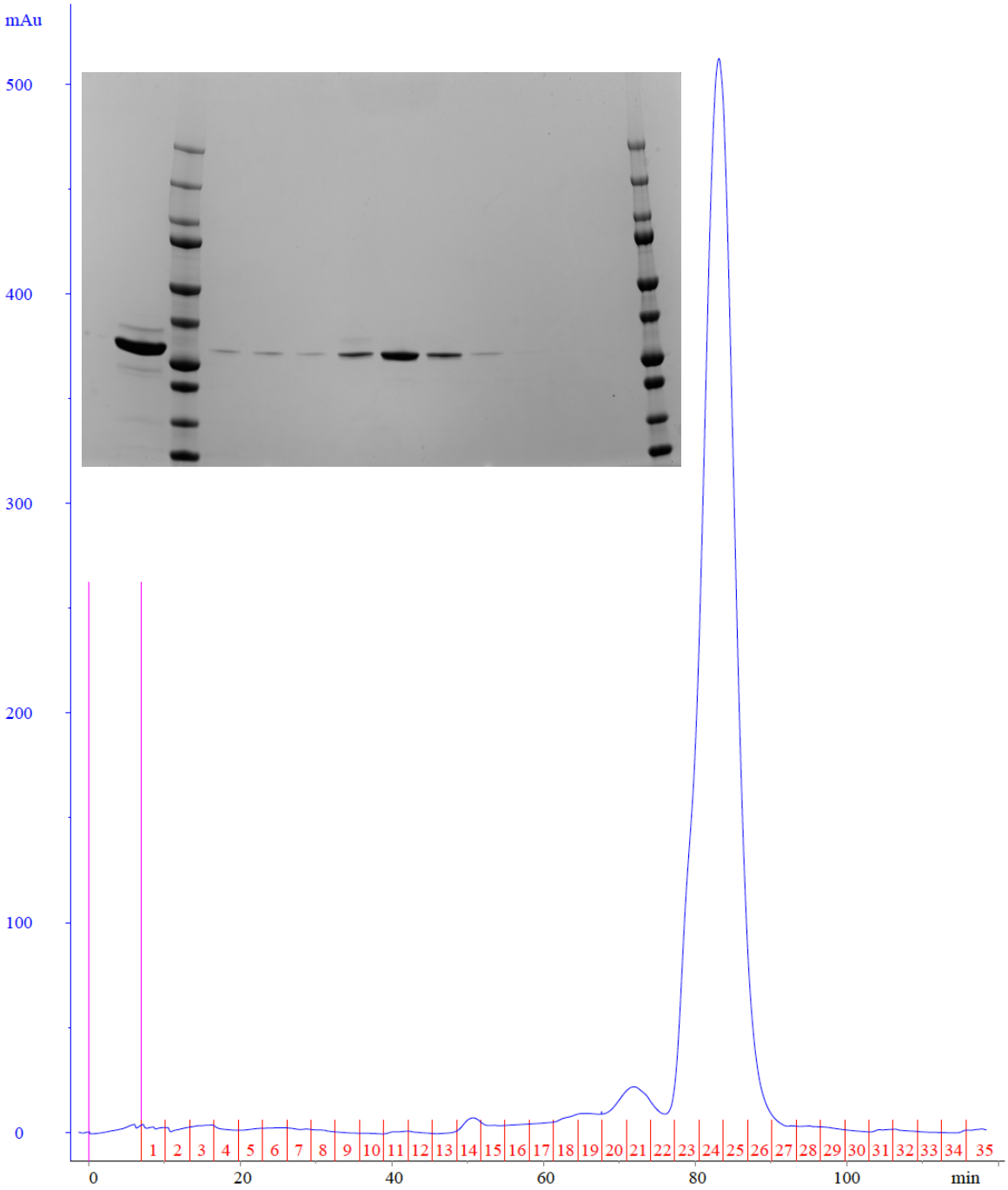

Figure 60| Elution of NdCd SET from gel filtration column.

Thrombin-cleaved NdCd-SET loaded onto and eluted from a HiLoad 26/60 200 prep grade column. Protein purity is estimated at >95% by Coomassie stained SDS-PAGE.

Purification of TRUNC SET 1

TRUNC SET 1 was cloned into a pHGK vector using the following primers:

FORWARD: 5' CGCGTGGTTCCCATATGGAAAACCTGTACTTCCAATCACCTCAGAAAAAGAACAGCAAGA 3'

REVERSE: 5' GATCCTTACTACATATCAGTAAGGATTTTCATCAAAATAAAAATCTATTCTGTAACCTG 3'

BL21 (DE3) pLys cells were transformed and grown in ^{15}N-labeled M9 minimal media at 37°C with 100μg/ml kanamycin. The cells were grown to high density OD_{600} = 0.8 before protein expression was induced with 0.03 mM IPTG overnight at 18˚C, with shaking at 190rpm. The cells were collected and resuspended in 10mM Na phosphate pH 8.0, 500mM NaCl, 20mM imidazole, 2% glycerol, 0.1% triton-X 100, and 0.5mM PMSF. Cells were lysed by sonication, and the lysate was then clarified by centrifugation at 15,000 rpm for 75 minutes at 4˚C. The clarified cell lysates were then filtered through 0.22μm membrane.

The protein was loaded onto a sepharose Fast Flow HisTrap column (GE Healthcare) and eluted using a three step gradient beginning at 50mM imidazole, primary elution at 250mM imidazole, and ending at 500mM imidazole (Fig. 47). The pooled fractions were incubated overnight at 4˚C with TEV protease with 1 mM DTT to cleave the 6X-Histidine tagged-GB1 (Fig. 48). TRUNC SET 1 precipitates over a 24-hour period, speeding up upon cleavage of GB1 (Fig. 48). The addition of L-arginine or L-glutamine to stabilize charges did not prevent precipitation. Adjusting the pH (either more acidic or basic) had no effect.

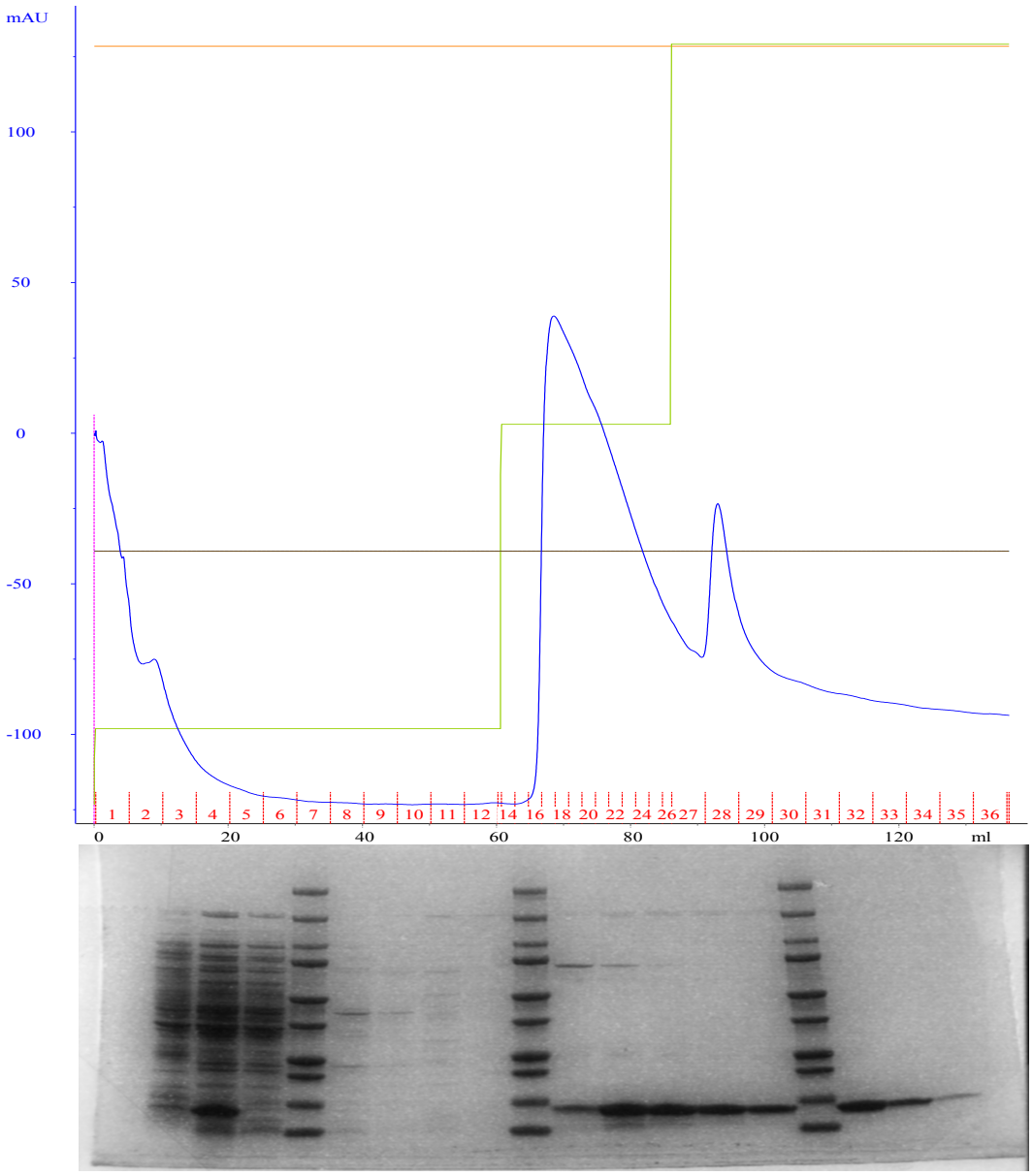

Figure 61| Elution of GB1-TRUNC SET 1 fusion protein from nickel affinity column.

The primary elution of protein occurs at 250mM imidazole between fractions 16-26, with a secondary elution from fraction 28 at 500mM imidazole. Fractions 16-28 were pooled for overnight TEV protease cleavage.

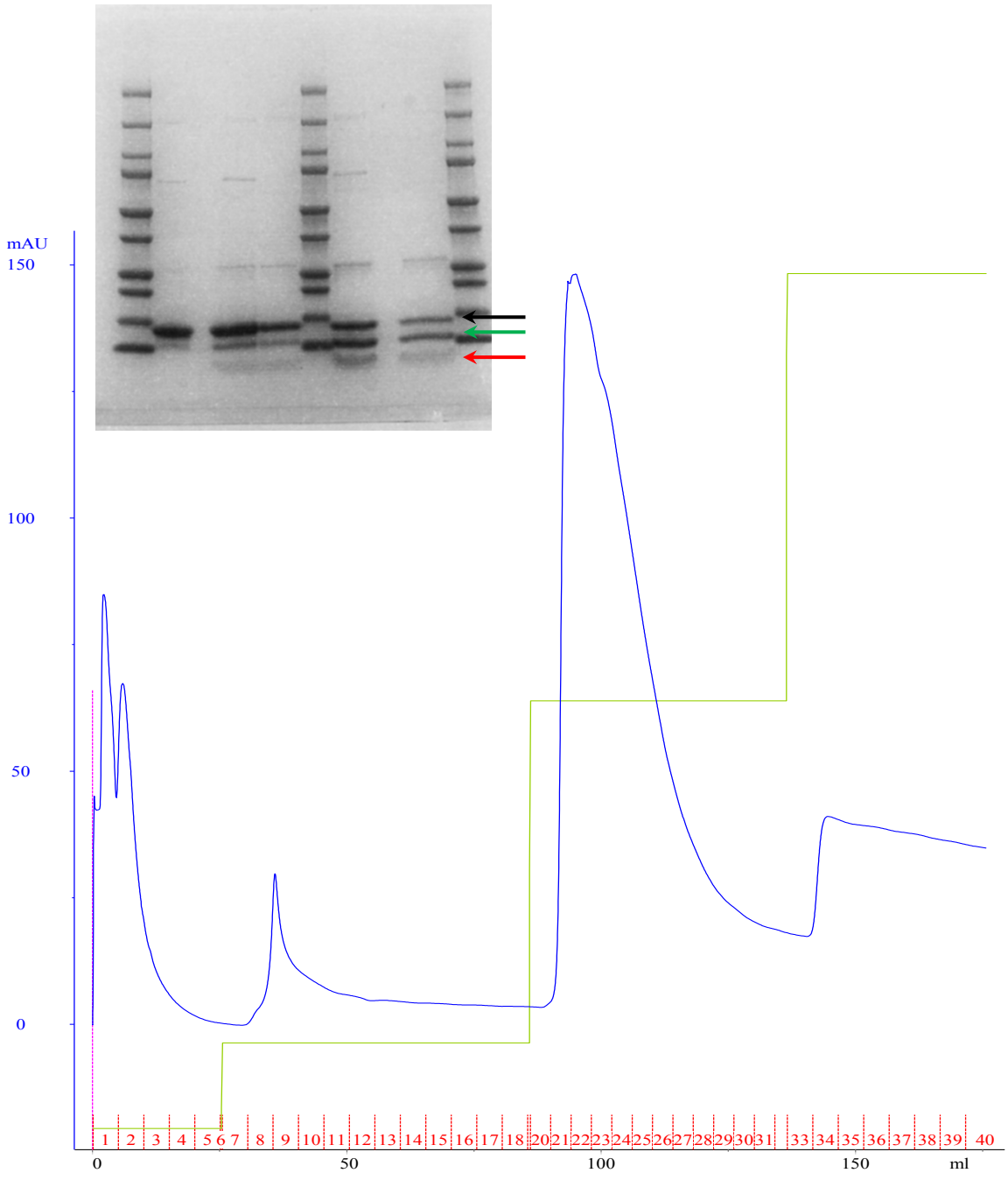

Figure 62| Elution of cleaved GB1 from nickel affinity column.

The gel image shows products that result from TEV cleavage. The black arrow points to uncleaved GB1-TRUNC SET 1 fusion protein. The green arrow points to GB1. The red arrow indicates precipitated TRUNC SET 1. Precipitated TRUNC SET 1 was removed and the remaining sample was loaded onto the column. GB1 was the primary eluent at 250mM imidazole.

Purification of TRUNC SET 2

TRUNC SET 2 was cloned into a pHGK vector using the following primers:

Forward: 5' CGCGTGGTTCCCATATGGAAAACCTGGTACTTCCAATCAGGGGAGGAAGATGAAGAGGCAC 3'

Reverse: 5' GATCCTTACTACATATCATCCTTCATCATCCATATC 3'

BL21 (DE3) pLys cells were transformed and grown in ^{13}C-^{15}N labeled M9 minimal media at 37°C with 100µg/ml kanamycin. The cells were grown to high density OD_{600} = 0.8 before protein expression was induced with 0.03 mM IPTG overnight at 18˚C, with shaking at 190rpm. The cells were collected and resuspended in 10mM Na phosphate pH 8.0, 500mM NaCl, 20mM imidazole, 2% glycerol, 0.1% triton-X 100, and 0.5mM PMSF. Cells were lysed by sonication, and the lysate was then clarified by centrifugation at 15,000 rpm for 75 minutes at 4˚C. The clarified cell lysates were then filtered through 0.22µm membrane.

The protein was loaded onto a sepharose Fast Flow HisTrap column (GE Healthcare) and eluted using a three step gradient beginning at 50mM imidazole, primary elution at 250mM imidazole, gradient ending at 500mM imidazole (Fig. 49). The pooled fractions were incubated overnight at 4˚C with TEV protease with 1 mM DTT to cleave the 6X-Histidine tagged-GB1 (Fig. 50). Cleaved protein was again passed through a sepharose Fast Flow HisTrap column (GE Healthcare) to remove GB1 and TEV. The flow through was collected as the final purification product. The cleaved TRUNC SET 2 was then dialyzed overnight at 4˚C in phosphate buffer (10 mM phosphate buffer, 50 mM NaCl pH 8.0).

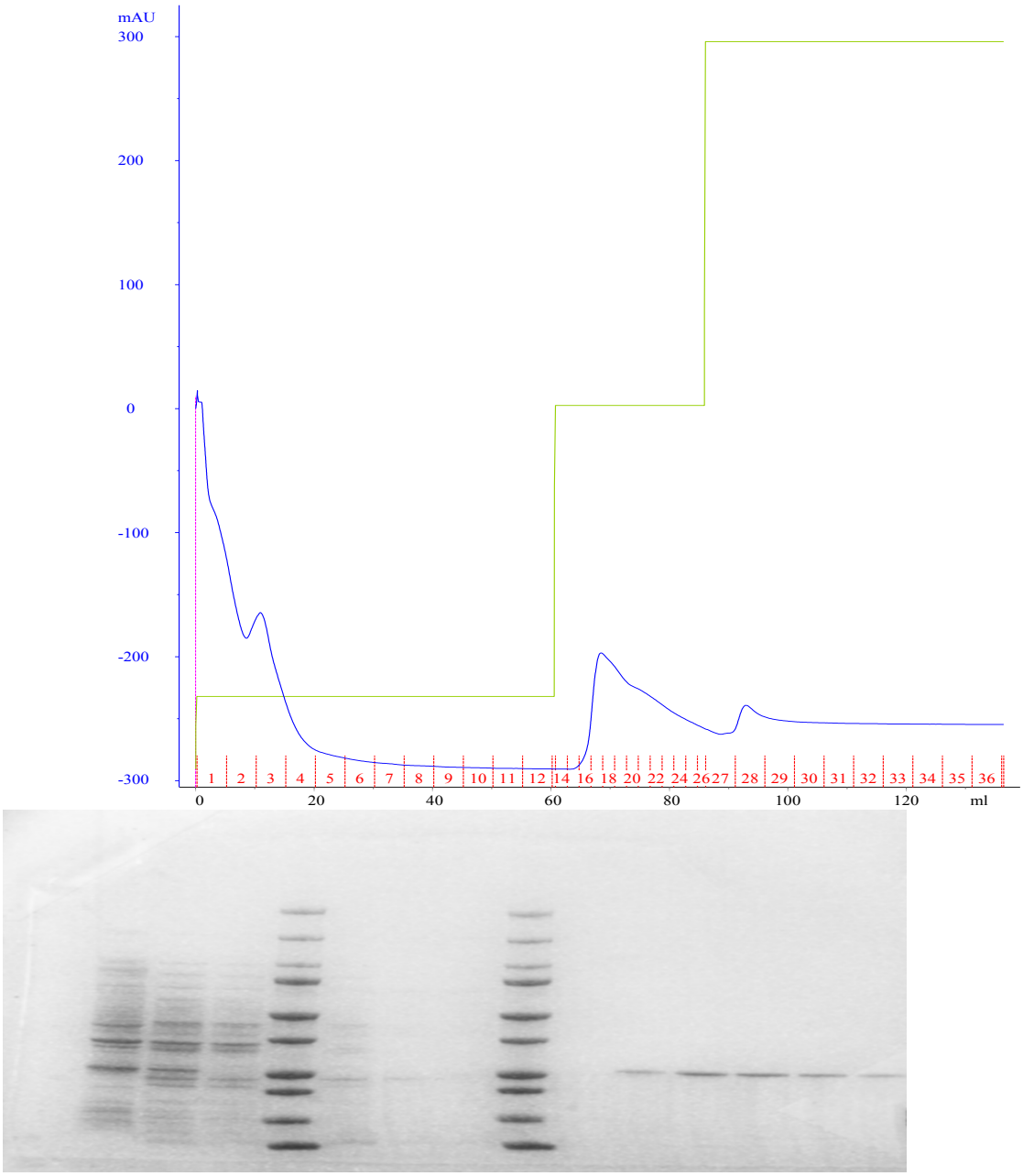

Figure 63| Elution of GB1-TRUNC SET 2 fusion protein from nickel affinity column.

The primary elution of protein occurs at 250mM imidazole between fractions 16-26, with a secondary elution from fraction 28 at 500mM imidazole. Fractions 16-28 were pooled for overnight TEV protease cleavage.

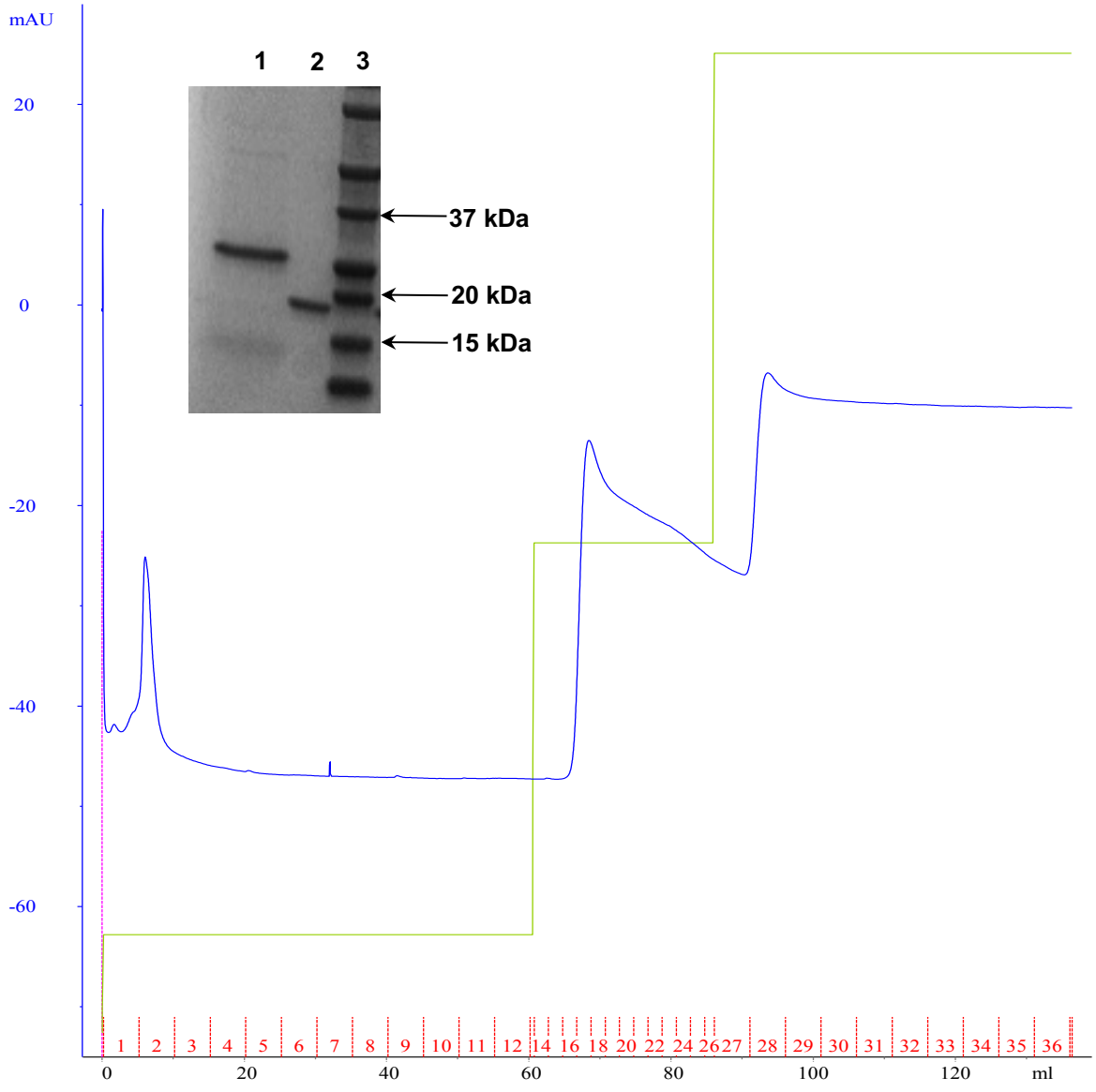

Figure 64| Elution of cleaved GB1 from nickel affinity column.

Cleaved TRUNC SET 2 was collected in the flow through following TEV cleavage and loading the nickel affinity column. GB1 was the primary eluent at 250mM imidazole.

Purification of TRUNC SET 3

TRUNC SET 3 was cloned into a pHGK vector using the following primers:

Forward: 5' CGCGTGGTTCCCATATGGAAAACCTGTACTTCCAATCAGGTGCTGATGAGTTAGGA 3'

Reverse: 5' GATCCTTACTACATATCAGTCATCTTCTCCTTCATCCTCCTC 3'

BL21 (DE3) pLys cells were transformed and grown in ^{13}C-^{15}N labeled M9 minimal media at 37°C with 100µg/ml kanamycin. The cells were grown to high density OD_{600} = 0.8 before protein expression was induced with 0.03 mM IPTG overnight at 18˚C, with shaking at 190rpm. The cells were collected and resuspended in 10mM Na phosphate pH 8.0, 500mM NaCl, 20mM imidazole, 2% glycerol, 0.1% triton-X 100, and 0.5mM PMSF. Cells were lysed by sonication, and the lysate was then clarified by centrifugation at 15,000 rpm for 75 minutes at 4˚C. The clarified cell lysates were then filtered through 0.22µm membrane.

The protein was loaded onto a sepharose Fast Flow HisTrap column (GE Healthcare) and eluted using a three step gradient beginning at 50mM imidazole, primary elution at 250mM imidazole, gradient ending at 500mM imidazole (Fig. 51). The pooled fractions were incubated overnight at 4˚C with TEV protease with 1 mM DTT to cleave the 6X-Histidine tagged-GB1 (Fig. 52). Cleaved protein was again passed through a sepharose Fast Flow HisTrap column (GE Healthcare) to remove GB1 and TEV. The flow through was collected as the final purification product. Cleaved TRUNC SET 3 was then dialyzed overnight at 4 ˚C into phosphate buffer (10 mM phosphate buffer, 50 mM NaCl pH 8.0).

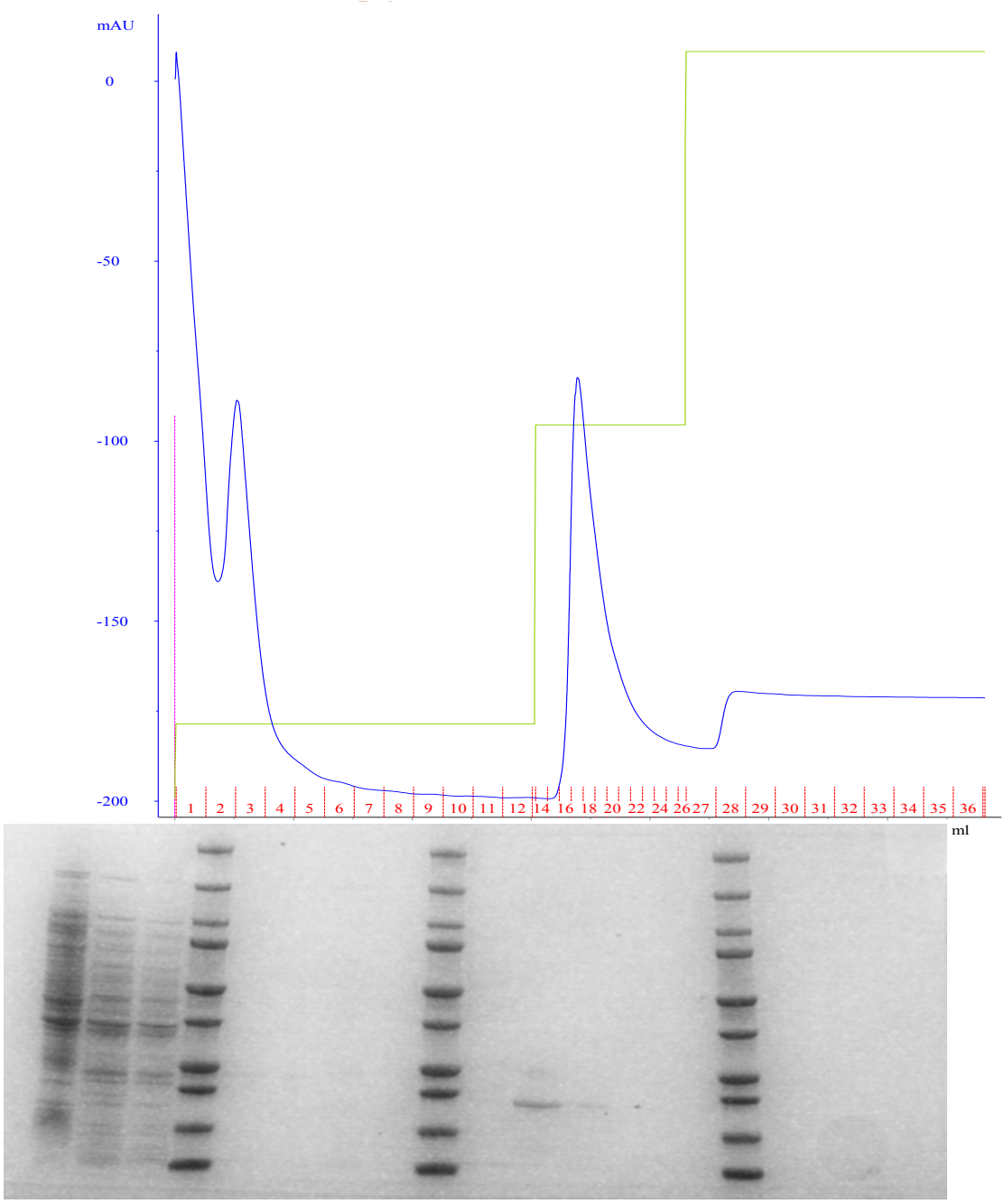

Figure 65| Elution of GB1-TRUNC SET 3 fusion protein from nickel affinity column.

The primary elution of protein occurs at 250mM imidazole between fractions 16-22. Fractions 16-21 were pooled for overnight TEV protease cleavage.

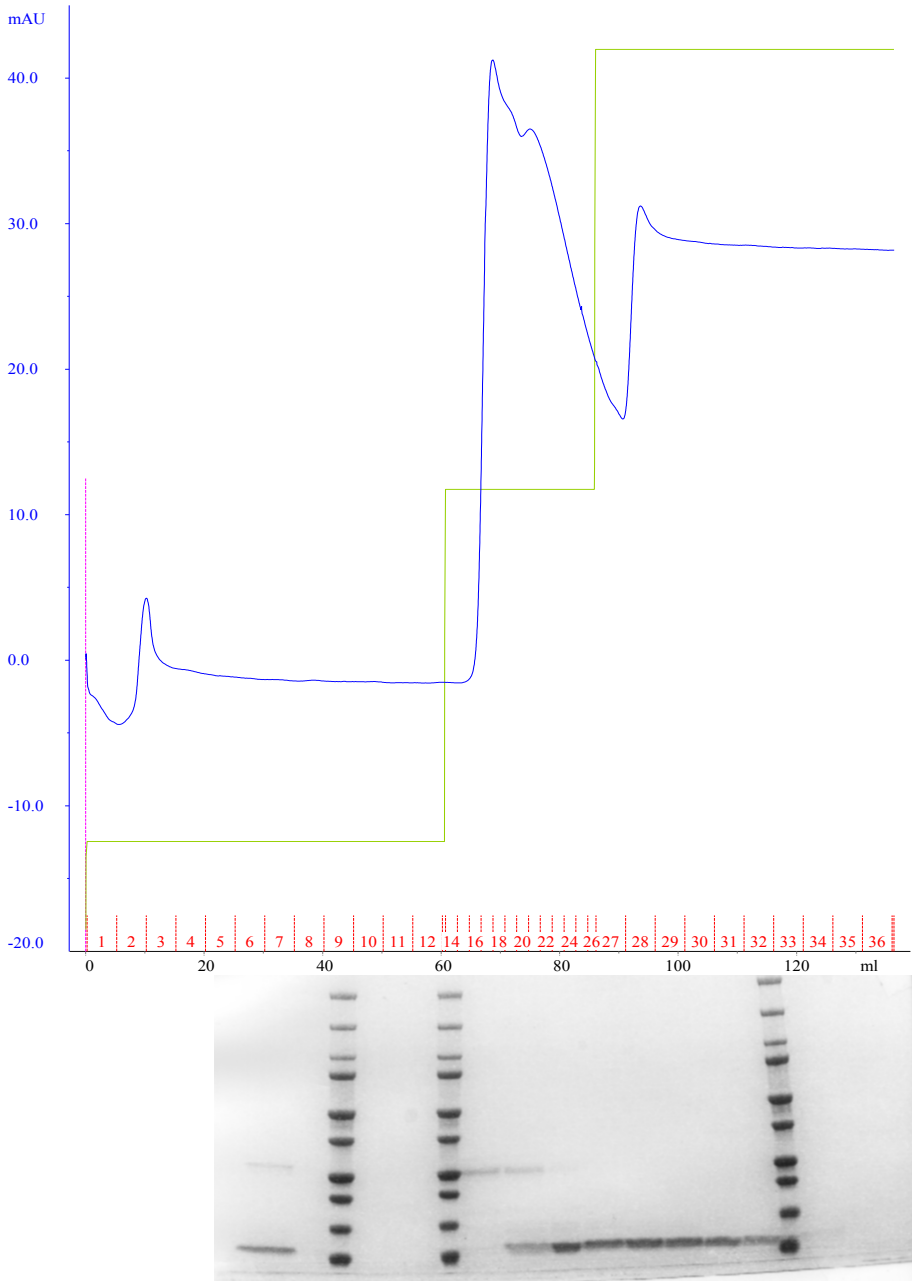

Figure 66| Elution of cleaved GB1 from nickel affinity column.

Cleaved TRUNC SET 1 was collected in the flow through following TEV cleavage and loading the nickel affinity column. GB1 was the primary eluent at 250mM imidazole. GB1 and TRUNC SET 3 run at the same molecular weight marker (first lane compared to other lanes).

Recipe for M9 Minimal Media to Make Isotopically Labeled Protein

Solution A (autoclave sterilize)

Na_2HPO_4 (anhydrous)	14.6g	
KH_2PO_4 (anhydrous)	5.4g	
NH_4Cl	1.0g	**^{15}N labeled Ammonium Chloride**
dH_2O	975ml	

pH 7.2

Solution B

Glucose	4.0g	*(2.0g if **^{13}C-glucose**)
$MgSO_4$	240mg	
Thiamine hydrochloride	20mg	

The following are made up as stock solutions and will last years:

5g/l $MnSO_4$	0.5ml
37.5g/l $CaCl_2$	0.5ml
1g/l $FeCl_2$	0.5ml

Antibiotic of choice

Dissolved in 25ml dH_2O and filter sterilized into sterilized solution A.

Conditioning and Growth Protocol for Bacterial Cultures in Deuterium Oxide (D_2O) M9 Minimal Media (^{2}H-M9)

All glassware must be autoclaved, rinsed with 95% D_2O, and dried with Nitrogen gas to retain hygroscopic conditions and not dilute the deuterons. Media preparation is the same as traditional M9 media outlined on the previous page except all stocks are made in 99.99% D_2O.

- Day 1 (evening): Grow cells overnight from a glycerol stock in LB at 37°C
- Day 2 (morning): Add 200 μL of LB culture to 1.8 mL 35% D_2O ^{2}H-M9 for 25% final concentration of D_2O. Grow cells overnight at 37°C.
- Day 3 (morning): Add 200 μL of 25% ^{2}H-M9 culture to 1.8 mL 80% D_2O ^{2}H-M9 for 75% final concentration of D_2O. Grow cells overnight at 37°C.
- Day 4 (morning): Add 200 μL 75% ^{2}H-M9 culture to 7mL of 100% ^{2}H-M9. Grow cells for 8+ hours at 37°C.
- Day 4 (evening): Add 5mL of the 99% ^{2}H-M9 culture to 50mL 100% ^{2}H-M9 culture with labeled isotopes. Grow cells to high density overnight at 37°C.
- Day 5 (morning): Add 25 mL of 99.9% ^{2}H-M9 culture to each 2L flask. Grow at 37°C until OD_{600} reaches 0.8.
- Day 5 (evening): Induce expression with 0.03 mM IPTG overnight at 18˚C, with shaking at 190rpm.

Appendix II

TABLE 5: SILAC Identified Interactions with PP2ACα after treatment with FTY720

Decreased	Moderate Increase	Larger Increase	No detectable change

SILAC Results	
Gene Name	**Ratio H/L Normalized**
AHNAK	-3.20556
PLEC;PLEC1	-2.41419
INTS1;DKFZP586J0619	-1.57824
PCM1	-1.47237
SOGA1	-1.45024
SOGA2	-1.3968
EIF5B	-1.32261
MYOF	-1.30326
TCOF1	-1.28824
ITPR3	-1.26164
RAB11FIP5;GAF1;DKFZp434H018	-1.17332
NHSL1	-1.16278
CEP350	-1.1373
CAD	-1.00651
SNRNP200	-0.930463
PRR14L	-0.822631
CDK12	-0.784707
TLN1	-0.696471
SSFA2	-0.680452
RP11-632C17__A.1-001;RPL29	-0.678464
MAP1B	-0.592854
PRKDC	-0.499483
FASN	-0.488532
RPS3	-0.480317
GCN1L1;PRIC295	-0.462555
MYO5C	-0.376789
MYO10;DKFZp762A083	-0.355904
DYNC1H1	-0.257804
SF3A1	-0.248965
DLG5	-0.219925
SEC16A	-0.205281
PRRC2C	**-0.195418**
SVIL	-0.190125
ANXA2;ANXA2P2	-0.117913

VIM;PRPH	-0.031680
FLNA	-0.007623
RNF213	-0.002273
DKFZp686A1195;TJP1;DKFZp686M05161	0.0129261
MYO5A	0.0167816
PPP2R2A	**0.0219061**
IQGAP1	0.0612924
PPP2R1B	**0.0790197**
TNKS1BP1	0.0798389
TSR1	0.0831112
MACF1	0.0836559
ANKLE2	0.0915306
ARHGAP21	0.119821
DST	0.131589
GAPD;GAPDH	0.146134
MPRIP	0.180275
FLNB;DKFZp686A1668	0.267476
ZFHX3	0.316609
CKAP5	0.401412
HSP90AA1;EL52	0.408277
PPP2R5D;PPP2R5C	**0.463518**
SAP30BP;DKFZp586L2022	0.490878
PPP2CB;PPP2CA	**0.539531**
PPP2R1A	**0.566766**
RRBP1	0.605305
SLC3A2	0.613437
PRDX6	0.662752
SPTAN1	0.796515
MYO18A	0.841571
TUBB;XTP3TPATP1;TUBB2C;TUBB4B;TUBB2B;TUBB2A;DKFZp566F223;TUBB3	0.842456
SPTBN1	0.842858
DNAJC13	0.863304
MYLK	0.871607
SIPA1L3	0.972178
MYH14	1.03393
ACTG1	1.09255
MYO1B	1.22836
MYO1C	1.39726
MYH9	**1.56086**
LAMA5	2.219
STRN3	NaN
EVPL	NaN
LTF;GIG12	NaN

UBB;UBC;UBA52;RPS27A;UBBP4;DKFZp434K0435;UbC	NaN
TFRC	NaN
PPP4R1	NaN
CACNA1I;CACNA1H;CACNA1G	NaN
SRRM1	NaN
MTOR;FRAP1	NaN
LYZ	NaN
RPL6	NaN
MYO9A	NaN
EIF4G1;EIF4G3;EIF4G1 variant protein	NaN
MYH10	NaN
UBR5	NaN
LGALS3BP	NaN
DDX41	NaN
LIMA1	NaN
CAPRIN1	NaN
SYT7	NaN
HSP90AB1;HSP90AA2;HSP90AB2P	NaN
ERCC5	NaN
CTNNA1	NaN
WBP11	NaN
CKB	NaN
DKFZp686P18130;FECH	NaN
DDX3Y;DDX3X	NaN
CDK11B;CDK11A;CDC2L1;CDC2L2	NaN
	NaN
PPP2R5E;PPP2R5B	NaN
HEATR5B	NaN
ARID2	NaN
RPS24	NaN
ANKHD1;FLJ00246	NaN
RPL8	NaN
HSPA8	NaN
	NaN
SBF1;DKFZp761D0422	NaN
RPS3A;LOC402287	NaN
RBBP6	NaN
ATP2A2	NaN
MPRIP	NaN
MSH4	NaN
ACTN4	NaN
FNBP3;PRPF40A	NaN
IGKC;IGK@	NaN
IGHA1;SNC73;DKFZp686G21220;DKFZp686J11235;DKFZp686K18196	NaN

LAMC1	NaN
POLR2A	NaN
LCN1;LCN1P1	NaN
RPS8	NaN
RPS18	NaN
CLTC	NaN
DSG1	NaN
CCDC6	NaN
GBF1	NaN
	NaN
PPP2R5A	NaN
CALML5	NaN
ABCA13	NaN
ABCC2	NaN
CCDC124	NaN
DOCK7	NaN
ANAPC1	NaN
	NaN

Appendix III

List of shRNA Sequences Used in the Generation of Stable Cell Lines

PPP2R5C (B'_{gamma}): TRCN0000293411 CDS
CCGGTCCAGAAGTTACGTCAGTGTTCTCGAGAACACTGACGTAACTTCTGGAT
TTTTG

PPP2R5D (B'_{delta}): TRCN0000010715 CDS
CCGGCCAGCCAAACATAGCCAAGAACTCGAGTTCTTGGCTATGTTTGGCTGG
TTTTT

PPP2R2A (B_{alpha}): TRCN0000002493 CDS
CCGGGCAAGTGGCAAGCGAAAGAAACTCGAGTTTCTTTCGCTTGCCACTTGC
TTTTT

PPP2R4 (PTPA): TRCN0000001118 3'UTR
CCGGCCGTTTGATGAGAGGCTGTTTCTCGAGAAACAGCCTCTCATCAAACGG
TTTTT

PPP2R3B (B''_{delta}): TRCN0000011056 CDS
CCGGCCAAAGCATTCCGACCTTCTACTCGAGTAGAAGGTCGGAATGCTTTGG
TTTTT

PPP2R2B (B_{beta}): TRCN0000071492 CDS
CCGGCCACTGCAACACCTTCGTATACTCGAGTATACGAAGGTGTTGCAGTGG
TTTTTG

SET: TRCN0000077183 3'UTR
CCGGCCAACATGTATCTGTCTACTTCTCGAGAAGTAGACAGATACATGTTGGT
TTTTG

TRCN0000077187 CDS
CCGGGCAAGAAGCAATTGAACATATCTCGAGATATGTTCAATTGCTTCTTGCT
TTTTG

PPP2CA (PP2ACa): TRCN0000002483 CDS
CCGGTGGAACTTGACGATACTCTAACTCGAGTTAGAGTATCGTCAAGTTCCAT
TTTT

PPP2CB (PP2ACb): TRCN0000318551 CDS
CCGGAGCCGACAAATTACCCAAGTACTCGAGTACTTGGGTAATTTGTCGGCTT
TTTTG

PPP2R1A (PP2AAa): TRCN0000012624 CDS
CCGGGCACCGAATGACTACACTCTTCTCGAGAAGAGTGTAGTCATTCGGTGC
TTTTT

PPP2R1B (PP2AAb): TRCN0000341550 CDS
CCGGTGTCCCATTGTTCACGAATTTCTCGAGAAATTCGTGAACAATGGGACAT
TTTTG

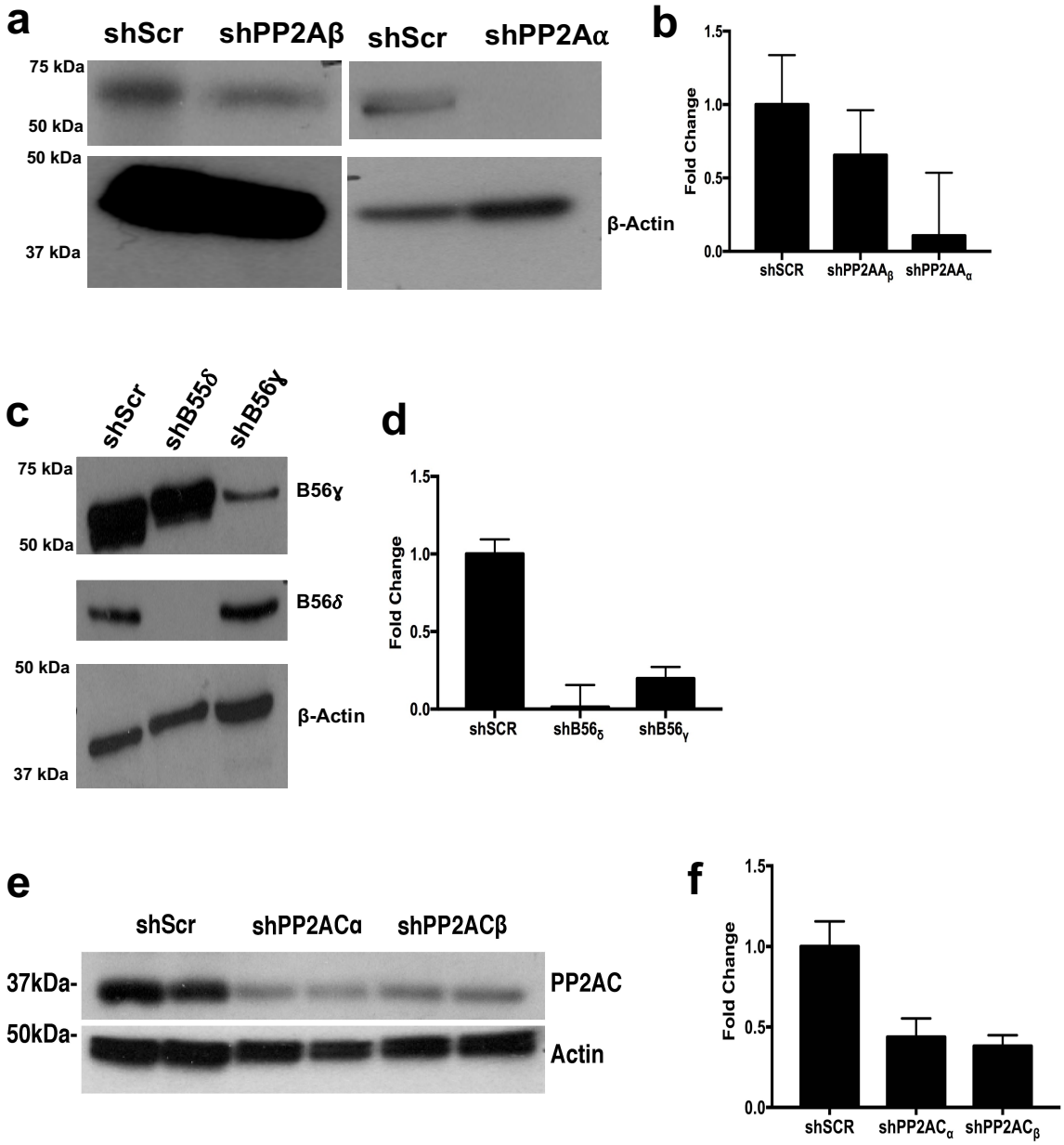

Figure 67| Knockdown efficiency of PP2A-related subunits.

(a) Western blot analysis of stable A subunit knockdown in shPP2AAα and shPP2Aβ A549 cells. **(b)** Quantitation of PP2AA knockdown normalized to actin. **(c)** Western blot analysis of stable B subunit knockdown in shB56ɣ and shB56*δ* A549 cells. **(d)** Quantitation of B56ɣ and B56*δ* knockdown. **(e)** Western blot analysis of stable PP2AC knockdown in shPP2ACα and shPP2ACβ A549 cells. **(g)** Quantitation of PP2AC knockdown efficiency normalized to actin.

References

1. Ogretmen B. Sphingolipid metabolism in cancer signalling and therapy. Nat Rev Cancer. 2017 Nov 17; PMID: 29147025

2. Ogretmen B, Hannun YA. Biologically active sphingolipids in cancer pathogenesis and treatment. Nat Rev Cancer. 2004 Aug;4(8):604–616. PMID: 15286740

3. Ponnusamy S, Meyers-Needham M, Senkal CE, Saddoughi SA, Sentelle D, Selvam SP, Salas A, Ogretmen B. Sphingolipids and cancer: ceramide and sphingosine-1-phosphate in the regulation of cell death and drug resistance. Future Oncol Lond Engl. 2010 Oct;6(10):1603–1624. PMCID: PMC3071292

4. Saddoughi SA, Ogretmen B. Diverse functions of ceramide in cancer cell death and proliferation. Adv Cancer Res. 2013;117:37–58. PMID: 23290776

5. Saddoughi SA, Song P, Ogretmen B. Roles of bioactive sphingolipids in cancer biology and therapeutics. Subcell Biochem. 2008;49:413–440. PMCID: PMC2636716

6. Hannun YA, Obeid LM. The Ceramide-centric universe of lipid-mediated cell regulation: stress encounters of the lipid kind. J Biol Chem. 2002 Jul 19;277(29):25847–25850. PMID: 12011103

7. Hannun YA. Functions of ceramide in coordinating cellular responses to stress. Science. 1996 Dec 13;274(5294):1855–1859. PMID: 8943189

8. Andrieu-Abadie N, Gouazé V, Salvayre R, Levade T. Ceramide in apoptosis signaling: relationship with oxidative stress. Free Radic Biol Med. 2001 Sep 15;31(6):717–728. PMID: 11557309

9. Pyne NJ, Pyne S. Sphingosine 1-phosphate and cancer. Nat Rev Cancer. 2010 Jul;10(7):489–503. PMID: 20555359

10. Oskouian B, Sooriyakumaran P, Borowsky AD, Crans A, Dillard-Telm L, Tam YY, Bandhuvula P, Saba JD. Sphingosine-1-phosphate lyase potentiates apoptosis via p53- and p38-dependent pathways and is down-regulated in colon cancer. Proc Natl Acad Sci U S A. 2006 Nov 14;103(46):17384–17389. PMCID: PMC1859938

11. Degagné E, Pandurangan A, Bandhuvula P, Kumar A, Eltanawy A, Zhang M, Yoshinaga Y, Nefedov M, de Jong PJ, Fong LG, Young SG, Bittman R, Ahmedi Y, Saba JD. Sphingosine-1-phosphate lyase downregulation promotes colon carcinogenesis through STAT3-activated microRNAs. J Clin Invest. 2014 Dec;124(12):5368–5384. PMCID: PMC4348973

12. Panneer Selvam S, De Palma RM, Oaks JJ, Oleinik N, Peterson YK, Stahelin RV, Skordalakes E, Ponnusamy S, Garrett-Mayer E, Smith CD, Ogretmen B. Binding of the sphingolipid S1P to hTERT stabilizes telomerase at the nuclear periphery by allosterically mimicking protein phosphorylation. Sci Signal. 2015;8(381):ra58. PMCID: PMC4492107

13. Hait NC, Allegood J, Maceyka M, Strub GM, Harikumar KB, Singh SK, Luo C, Marmorstein R, Kordula T, Milstien S, Spiegel S. Regulation of histone acetylation

in the nucleus by sphingosine-1-phosphate. Science. 2009 Sep 4;325(5945):1254–1257. PMCID: PMC2850596

14. Liu Y, Deng J, Wang L, Lee H, Armstrong B, Scuto A, Kowolik C, Weiss LM, Forman S, Yu H. S1PR1 is an effective target to block STAT3 signaling in activated B cell-like diffuse large B-cell lymphoma. Blood. 2012 Aug 16;120(7):1458–1465. PMCID: PMC3423784

15. Feng H, Stachura DL, White RM, Gutierrez A, Zhang L, Sanda T, Jette CA, Testa JR, Neuberg DS, Langenau DM, Kutok JL, Zon LI, Traver D, Fleming MD, Kanki JP, Look AT. T-lymphoblastic lymphoma cells express high levels of BCL2, S1P1, and ICAM1, leading to a blockade of tumor cell intravasation. Cancer Cell. 2010 Oct 19;18(4):353–366. PMCID: PMC3003429

16. Ponnusamy S, Selvam SP, Mehrotra S, Kawamori T, Snider AJ, Obeid LM, Shao Y, Sabbadini R, Ogretmen B. Communication between host organism and cancer cells is transduced by systemic sphingosine kinase 1/sphingosine 1-phosphate signalling to regulate tumour metastasis. EMBO Mol Med. 2012 Aug;4(8):761–775. PMCID: PMC3494075

17. Adada MM, Canals D, Jeong N, Kelkar AD, Hernandez-Corbacho M, Pulkoski-Gross MJ, Donaldson JC, Hannun YA, Obeid LM. Intracellular sphingosine kinase 2-derived sphingosine-1-phosphate mediates epidermal growth factor-induced ezrin-radixin-moesin phosphorylation and cancer cell invasion. FASEB J Off Publ Fed Am Soc Exp Biol. 2015 Nov;29(11):4654–4669. PMCID: PMC4608912

18. Powell JA, Lewis AC, Zhu W, Toubia J, Pitman MR, Wallington-Beddoe CT, Moretti PAB, Iarossi D, Samaraweera SE, Cummings N, Ramshaw HS, Thomas D, Wei AH, Lopez AF, D'Andrea RJ, Lewis ID, Pitson SM. Targeting sphingosine kinase 1 induces MCL1-dependent cell death in acute myeloid leukemia. Blood. 2017 09;129(6):771–782. PMID: 27956387

19. Liang J, Nagahashi M, Kim EY, Harikumar KB, Yamada A, Huang W-C, Hait NC, Allegood JC, Price MM, Avni D, Takabe K, Kordula T, Milstien S, Spiegel S. Sphingosine-1-Phosphate Links Persistent STAT3 Activation, Chronic Intestinal Inflammation, and Development of Colitis-Associated Cancer. Cancer Cell. 2012 Dec 22; PMID: 23273921

20. Visentin B, Vekich JA, Sibbald BJ, Cavalli AL, Moreno KM, Matteo RG, Garland WA, Lu Y, Yu S, Hall HS, Kundra V, Mills GB, Sabbadini RA. Validation of an anti-sphingosine-1-phosphate antibody as a potential therapeutic in reducing growth, invasion, and angiogenesis in multiple tumor lineages. Cancer Cell. 2006 Mar;9(3):225–238. PMID: 16530706

21. Brizuela L, Martin C, Jeannot P, Ader I, Gstalder C, Andrieu G, Bocquet M, Laffosse J-M, Gomez-Brouchet A, Malavaud B, Sabbadini RA, Cuvillier O. Osteoblast-derived sphingosine 1-phosphate to induce proliferation and confer resistance to therapeutics to bone metastasis-derived prostate cancer cells. Mol Oncol. 2014 Oct;8(7):1181–1195. PMCID: PMC5528572

22. Kumar A, Zamora-Pineda J, Degagné E, Saba JD. S1P Lyase Regulation of Thymic Egress and Oncogenic Inflammatory Signaling. Mediators Inflamm. 2017;2017:7685142. PMCID: PMC5733215

23. Zamora-Pineda J, Kumar A, Suh JH, Zhang M, Saba JD. Dendritic cell sphingosine-1-phosphate lyase regulates thymic egress. J Exp Med. 2016 14;213(12):2773–2791. PMCID: PMC5110016

24. Zhao J, Liu J, Lee J-F, Zhang W, Kandouz M, VanHecke GC, Chen S, Ahn Y-H, Lonardo F, Lee M-J. TGF-β/SMAD3 Pathway Stimulates Sphingosine-1 Phosphate Receptor 3 Expression: IMPLICATION OF SPHINGOSINE-1 PHOSPHATE RECEPTOR 3 IN LUNG ADENOCARCINOMA PROGRESSION. J Biol Chem. 2016 30;291(53):27343–27353. PMCID: PMC5207160

25. Ohotski J, Rosen H, Bittman R, Pyne S, Pyne NJ. Sphingosine kinase 2 prevents the nuclear translocation of sphingosine 1-phosphate receptor-2 and tyrosine 416 phosphorylated c-Src and increases estrogen receptor negative MDA-MB-231 breast cancer cell growth: The role of sphingosine 1-phosphate receptor-4. Cell Signal. 2014 May;26(5):1040–1047. PMID: 24486401

26. Ohotski J, Long JS, Orange C, Elsberger B, Mallon E, Doughty J, Pyne S, Pyne NJ, Edwards J. Expression of sphingosine 1-phosphate receptor 4 and sphingosine kinase 1 is associated with outcome in oestrogen receptor-negative breast cancer. Br J Cancer. 2012 Apr 10;106(8):1453–1459. PMCID: PMC3326679

27. Andrieu G, Ledoux A, Branka S, Bocquet M, Gilhodes J, Walzer T, Kasahara K, Inagaki M, Sabbadini RA, Cuvillier O, Hatzoglou A. Sphingosine 1-phosphate signaling through its receptor S1P5 promotes chromosome segregation and mitotic progression. Sci Signal. 2017 Mar 28;10(472). PMID: 28351953

28. Parham KA, Zebol JR, Tooley KL, Sun WY, Moldenhauer LM, Cockshell MP, Gliddon BL, Moretti PA, Tigyi G, Pitson SM, Bonder CS. Sphingosine 1-phosphate is a ligand for peroxisome proliferator-activated receptor-γ that regulates neoangiogenesis. FASEB J Off Publ Fed Am Soc Exp Biol. 2015 Sep;29(9):3638–3653. PMID: 25985799

29. Alvarez SE, Harikumar KB, Hait NC, Allegood J, Strub GM, Kim EY, Maceyka M, Jiang H, Luo C, Kordula T, Milstien S, Spiegel S. Sphingosine-1-phosphate is a missing cofactor for the E3 ubiquitin ligase TRAF2. Nature. 2010 Jun 24;465(7301):1084–1088. PMCID: PMC2946785

30. Etemadi N, Chopin M, Anderton H, Tanzer MC, Rickard JA, Abeysekera W, Hall C, Spall SK, Wang B, Xiong Y, Hla T, Pitson SM, Bonder CS, Wong WW-L, Ernst M, Smyth GK, Vaux DL, Nutt SL, Nachbur U, Silke J. TRAF2 regulates TNF and NF-κB signalling to suppress apoptosis and skin inflammation independently of Sphingosine kinase 1. eLife. 2015 Dec 23;4. PMCID: PMC4769158

31. Strub GM, Paillard M, Liang J, Gomez L, Allegood JC, Hait NC, Maceyka M, Price MM, Chen Q, Simpson DC, Kordula T, Milstien S, Lesnefsky EJ, Spiegel S. Sphingosine-1-phosphate produced by sphingosine kinase 2 in mitochondria

interacts with prohibitin 2 to regulate complex IV assembly and respiration. FASEB J Off Publ Fed Am Soc Exp Biol. 2011 Feb;25(2):600–612. PMCID: PMC3023391

32. Santana P, Peña LA, Haimovitz-Friedman A, Martin S, Green D, McLoughlin M, Cordon-Cardo C, Schuchman EH, Fuks Z, Kolesnick R. Acid sphingomyelinase-deficient human lymphoblasts and mice are defective in radiation-induced apoptosis. Cell. 1996 Jul 26;86(2):189–199. PMID: 8706124

33. Plo I, Ghandour S, Feutz AC, Clanet M, Laurent G, Bettaieb A. Involvement of de novo ceramide biosynthesis in lymphotoxin-induced oligodendrocyte death. Neuroreport. 1999 Aug 2;10(11):2373–2376. PMID: 10439466

34. Zhang P, Liu B, Jenkins GM, Hannun YA, Obeid LM. Expression of neutral sphingomyelinase identifies a distinct pool of sphingomyelin involved in apoptosis. J Biol Chem. 1997 Apr 11;272(15):9609–9612. PMID: 9092485

35. Siskind LJ, Mullen TD, Romero Rosales K, Clarke CJ, Hernandez-Corbacho MJ, Edinger AL, Obeid LM. The BCL-2 protein BAK is required for long-chain ceramide generation during apoptosis. J Biol Chem. 2010 Apr 16;285(16):11818–11826. PMCID: PMC2852918

36. Obeid LM, Linardic CM, Karolak LA, Hannun YA. Programmed cell death induced by ceramide. Science. 1993 Mar 19;259(5102):1769–1771. PMID: 8456305

37. Sentelle RD, Senkal CE, Jiang W, Ponnusamy S, Gencer S, Selvam SP, Ramshesh VK, Peterson YK, Lemasters JJ, Szulc ZM, Bielawski J, Ogretmen B. Ceramide

targets autophagosomes to mitochondria and induces lethal mitophagy. Nat Chem Biol. 2012 Oct;8(10):831–838. PMCID: PMC3689583

38. Dany M, Gencer S, Nganga R, Thomas RJ, Oleinik N, Baron KD, Szulc ZM, Ruvolo P, Kornblau S, Andreeff M, Ogretmen B. Targeting FLT3-ITD signaling mediates ceramide-dependent mitophagy and attenuates drug resistance in AML. Blood. 2016 Oct 13;128(15):1944–1958. PMCID: PMC5064718

39. Thomas RJ, Oleinik N, Panneer Selvam S, Vaena SG, Dany M, Nganga RN, Depalma R, Baron KD, Kim J, Szulc ZM, Ogretmen B. HPV/E7 induces chemotherapy-mediated tumor suppression by ceramide-dependent mitophagy. EMBO Mol Med. 2017 Jun 12; PMID: 28606997

40. Han G, Gupta SD, Gable K, Niranjanakumari S, Moitra P, Eichler F, Brown RH, Harmon JM, Dunn TM. Identification of small subunits of mammalian serine palmitoyltransferase that confer distinct acyl-CoA substrate specificities. Proc Natl Acad Sci U S A. 2009 May 19;106(20):8186–8191. PMCID: PMC2688822

41. Bode H, Bourquin F, Suriyanarayanan S, Wei Y, Alecu I, Othman A, Von Eckardstein A, Hornemann T. HSAN1 mutations in serine palmitoyltransferase reveal a close structure-function-phenotype relationship. Hum Mol Genet. 2016 Mar 1;25(5):853–865. PMID: 26681808

42. Kramer R, Bielawski J, Kistner-Griffin E, Othman A, Alecu I, Ernst D, Kornhauser D, Hornemann T, Spassieva S. Neurotoxic 1-deoxysphingolipids and paclitaxel-

induced peripheral neuropathy. FASEB J Off Publ Fed Am Soc Exp Biol. 2015 Nov;29(11):4461–4472. PMCID: PMC4608911

43. Meyers-Needham M, Ponnusamy S, Gencer S, Jiang W, Thomas RJ, Senkal CE, Ogretmen B. Concerted functions of HDAC1 and microRNA-574-5p repress alternatively spliced ceramide synthase 1 expression in human cancer cells. EMBO Mol Med. 2012 Feb;4(2):78–92. PMCID: PMC3376837

44. Koybasi S, Senkal CE, Sundararaj K, Spassieva S, Bielawski J, Osta W, Day TA, Jiang JC, Jazwinski SM, Hannun YA, Obeid LM, Ogretmen B. Defects in cell growth regulation by C18:0-ceramide and longevity assurance gene 1 in human head and neck squamous cell carcinomas. J Biol Chem. 2004 Oct 22;279(43):44311–44319. PMID: 15317812

45. Senkal CE, Ponnusamy S, Bielawski J, Hannun YA, Ogretmen B. Antiapoptotic roles of ceramide-synthase-6-generated C16-ceramide via selective regulation of the ATF6/CHOP arm of ER-stress-response pathways. FASEB J Off Publ Fed Am Soc Exp Biol. 2010 Jan;24(1):296–308. PMCID: PMC2797032

46. Senkal CE, Ponnusamy S, Manevich Y, Meyers-Needham M, Saddoughi SA, Mukhopadyay A, Dent P, Bielawski J, Ogretmen B. Alteration of ceramide synthase 6/C16-ceramide induces activating transcription factor 6-mediated endoplasmic reticulum (ER) stress and apoptosis via perturbation of cellular Ca2+ and ER/Golgi membrane network. J Biol Chem. 2011 Dec 9;286(49):42446–42458. PMCID: PMC3234959

47. Suzuki M, Cao K, Kato S, Komizu Y, Mizutani N, Tanaka K, Arima C, Tai MC, Yanagisawa K, Togawa N, Shiraishi T, Usami N, Taniguchi T, Fukui T, Yokoi K, Wakahara K, Hasegawa Y, Mizutani Y, Igarashi Y, Inokuchi J, Iwaki S, Fujii S, Satou A, Matsumoto Y, Ueoka R, Tamiya-Koizumi K, Murate T, Nakamura M, Kyogashima M, Takahashi T. Targeting ceramide synthase 6-dependent metastasis-prone phenotype in lung cancer cells. J Clin Invest. 2016 Jan;126(1):254–265. PMCID: PMC4701566

48. Schiffmann S, Sandner J, Birod K, Wobst I, Angioni C, Ruckhäberle E, Kaufmann M, Ackermann H, Lötsch J, Schmidt H, Geisslinger G, Grösch S. Ceramide synthases and ceramide levels are increased in breast cancer tissue. Carcinogenesis. 2009 May;30(5):745–752. PMID: 19279183

49. Fekry B, Jeffries KA, Esmaeilniakooshkghazi A, Ogretmen B, Krupenko SA, Krupenko NI. CerS6 Is a Novel Transcriptional Target of p53 Protein Activated by Non-genotoxic Stress. J Biol Chem. 2016 05;291(32):16586–16596. PMCID: PMC4974374

50. Jensen SA, Calvert AE, Volpert G, Kouri FM, Hurley LA, Luciano JP, Wu Y, Chalastanis A, Futerman AH, Stegh AH. Bcl2L13 is a ceramide synthase inhibitor in glioblastoma. Proc Natl Acad Sci U S A. 2014 Apr 15;111(15):5682–5687. PMCID: PMC3992626

51. White-Gilbertson S, Mullen T, Senkal C, Lu P, Ogretmen B, Obeid L, Voelkel-Johnson C. Ceramide synthase 6 modulates TRAIL sensitivity and nuclear

translocation of active caspase-3 in colon cancer cells. Oncogene. 2009 Feb 26;28(8):1132–1141. PMCID: PMC2648838

52. Rahmaniyan M, Curley RW, Obeid LM, Hannun YA, Kraveka JM. Identification of dihydroceramide desaturase as a direct in vitro target for fenretinide. J Biol Chem. 2011 Jul 15;286(28):24754–24764. PMCID: PMC3137051

53. Airola MV, Shanbhogue P, Shamseddine AA, Guja KE, Senkal CE, Maini R, Bartke N, Wu BX, Obeid LM, Garcia-Diaz M, Hannun YA. Structure of human nSMase2 reveals an interdomain allosteric activation mechanism for ceramide generation. Proc Natl Acad Sci U S A. 2017 11;114(28):E5549–E5558. PMCID: PMC5514751

54. Shamseddine AA, Clarke CJ, Carroll B, Airola MV, Mohammed S, Rella A, Obeid LM, Hannun YA. P53-dependent upregulation of neutral sphingomyelinase-2: role in doxorubicin-induced growth arrest. Cell Death Dis. 2015 Oct 29;6:e1947. PMCID: PMC4632297

55. Trajkovic K, Hsu C, Chiantia S, Rajendran L, Wenzel D, Wieland F, Schwille P, Brügger B, Simons M. Ceramide triggers budding of exosome vesicles into multivesicular endosomes. Science. 2008 Feb 29;319(5867):1244–1247. PMID: 18309083

56. Carpinteiro A, Becker KA, Japtok L, Hessler G, Keitsch S, Požgajovà M, Schmid KW, Adams C, Müller S, Kleuser B, Edwards MJ, Grassmé H, Helfrich I, Gulbins

E. Regulation of hematogenous tumor metastasis by acid sphingomyelinase. EMBO Mol Med. 2015 Jun;7(6):714–734. PMCID: PMC4459814

57. Gorelik A, Illes K, Heinz LX, Superti-Furga G, Nagar B. Crystal structure of mammalian acid sphingomyelinase. Nat Commun. 2016 Jul 20;7:12196. PMCID: PMC4961792

58. Kudo N, Kumagai K, Tomishige N, Yamaji T, Wakatsuki S, Nishijima M, Hanada K, Kato R. Structural basis for specific lipid recognition by CERT responsible for nonvesicular trafficking of ceramide. Proc Natl Acad Sci U S A. 2008 Jan 15;105(2):488–493. PMCID: PMC2206563

59. Kawano M, Kumagai K, Nishijima M, Hanada K. Efficient trafficking of ceramide from the endoplasmic reticulum to the Golgi apparatus requires a VAMP-associated protein-interacting FFAT motif of CERT. J Biol Chem. 2006 Oct 6;281(40):30279–30288. PMID: 16895911

60. Heering J, Weis N, Holeiter M, Neugart F, Staebler A, Fehm TN, Bischoff A, Schiller J, Duss S, Schmid S, Korte T, Herrmann A, Olayioye MA. Loss of the ceramide transfer protein augments EGF receptor signaling in breast cancer. Cancer Res. 2012 Jun 1;72(11):2855–2866. PMID: 22472120

61. Lee AJX, Roylance R, Sander J, Gorman P, Endesfelder D, Kschischo M, Jones NP, East P, Nicke B, Spassieva S, Obeid LM, Birkbak NJ, Szallasi Z, McKnight NC, Rowan AJ, Speirs V, Hanby AM, Downward J, Tooze SA, Swanton C. CERT depletion predicts chemotherapy benefit and mediates cytotoxic and polyploid-

specific cancer cell death through autophagy induction. J Pathol. 2012 Feb;226(3):482–494. PMID: 21953249

62. Hullin-Matsuda F, Tomishige N, Sakai S, Ishitsuka R, Ishii K, Makino A, Greimel P, Abe M, Laviad EL, Lagarde M, Vidal H, Saito T, Osada H, Hanada K, Futerman AH, Kobayashi T. Limonoid compounds inhibit sphingomyelin biosynthesis by preventing CERT protein-dependent extraction of ceramides from the endoplasmic reticulum. J Biol Chem. 2012 Jul 13;287(29):24397–24411. PMCID: PMC3397866

63. Eliyahu E, Park J-H, Shtraizent N, He X, Schuchman EH. Acid ceramidase is a novel factor required for early embryo survival. FASEB J Off Publ Fed Am Soc Exp Biol. 2007 May;21(7):1403–1409. PMID: 17264167

64. Beckham TH, Cheng JC, Lu P, Shao Y, Troyer D, Lance R, Marrison ST, Norris JS, Liu X. Acid ceramidase induces sphingosine kinase 1/S1P receptor 2-mediated activation of oncogenic Akt signaling. Oncogenesis. 2013 Jun 3;2:e49. PMCID: PMC3740300

65. Cheng JC, Bai A, Beckham TH, Marrison ST, Yount CL, Young K, Lu P, Bartlett AM, Wu BX, Keane BJ, Armeson KE, Marshall DT, Keane TE, Smith MT, Jones EE, Drake RR, Bielawska A, Norris JS, Liu X. Radiation-induced acid ceramidase confers prostate cancer resistance and tumor relapse. J Clin Invest. 2013 Oct;123(10):4344–4358. PMCID: PMC3784522

66. Tirodkar TS, Lu P, Bai A, Scheffel MJ, Gencer S, Garrett-Mayer E, Bielawska A, Ogretmen B, Voelkel-Johnson C. Expression of Ceramide Synthase 6

Transcriptionally Activates Acid Ceramidase in a c-Jun N-terminal Kinase (JNK)-dependent Manner. J Biol Chem. 2015 May 22;290(21):13157–13167. PMCID: PMC4505570

67. Wijesinghe DS, Brentnall M, Mietla JA, Hoeferlin LA, Diegelmann RF, Boise LH, Chalfant CE. Ceramide kinase is required for a normal eicosanoid response and the subsequent orderly migration of fibroblasts. J Lipid Res. 2014 Jul;55(7):1298–1309. PMCID: PMC4076082

68. Pastukhov O, Schwalm S, Zangemeister-Wittke U, Fabbro D, Bornancin F, Japtok L, Kleuser B, Pfeilschifter J, Huwiler A. The ceramide kinase inhibitor NVP-231 inhibits breast and lung cancer cell proliferation by inducing M phase arrest and subsequent cell death. Br J Pharmacol. 2014 Dec;171(24):5829–5844. PMCID: PMC4290720

69. Payne AW, Pant DK, Pan T-C, Chodosh LA. Ceramide kinase promotes tumor cell survival and mammary tumor recurrence. Cancer Res. 2014 Nov 1;74(21):6352–6363. PMCID: PMC4285436

70. Kim JW, Park Y, Roh J-L, Cho K-J, Choi S-H, Nam SY, Kim SY. Prognostic value of glucosylceramide synthase and P-glycoprotein expression in oral cavity cancer. Int J Clin Oncol. 2016 Oct;21(5):883–889. PMID: 27000845

71. Stefanovic M, Tutusaus A, Martinez-Nieto GA, Bárcena C, de Gregorio E, Moutinho C, Barbero-Camps E, Villanueva A, Colell A, Marí M, García-Ruiz C, Fernandez-Checa JC, Morales A. Targeting glucosylceramide synthase upregulation

reverts sorafenib resistance in experimental hepatocellular carcinoma. Oncotarget. 2016 Feb 16;7(7):8253–8267. PMCID: PMC4884990

72. Roh J-L, Kim EH, Park JY, Kim JW. Inhibition of Glucosylceramide Synthase Sensitizes Head and Neck Cancer to Cisplatin. Mol Cancer Ther. 2015 Aug;14(8):1907–1915. PMID: 26063766

73. Liu Y-Y, Patwardhan GA, Bhinge K, Gupta V, Gu X, Jazwinski SM. Suppression of glucosylceramide synthase restores p53-dependent apoptosis in mutant p53 cancer cells. Cancer Res. 2011 Mar 15;71(6):2276–2285. PMCID: PMC3059346

74. Gupta V, Bhinge KN, Hosain SB, Xiong K, Gu X, Shi R, Ho M-Y, Khoo K-H, Li S-C, Li Y-T, Ambudkar SV, Jazwinski SM, Liu Y-Y. Ceramide glycosylation by glucosylceramide synthase selectively maintains the properties of breast cancer stem cells. J Biol Chem. 2012 Oct 26;287(44):37195–37205. PMCID: PMC3481319

75. Wooten-Blanks LG, Song P, Senkal CE, Ogretmen B. Mechanisms of ceramide-mediated repression of the human telomerase reverse transcriptase promoter via deacetylation of Sp3 by histone deacetylase 1. FASEB J Off Publ Fed Am Soc Exp Biol. 2007 Oct;21(12):3386–3397. PMID: 17548428

76. Sundararaj KP, Wood RE, Ponnusamy S, Salas AM, Szulc Z, Bielawska A, Obeid LM, Hannun YA, Ogretmen B. Rapid shortening of telomere length in response to ceramide involves the inhibition of telomere binding activity of nuclear glyceraldehyde-3-phosphate dehydrogenase. J Biol Chem. 2004 Feb 13;279(7):6152–6162. PMID: 14630908

77. Snook CF, Jones JA, Hannun YA. Sphingolipid-binding proteins. Biochim Biophys Acta. 2006 Aug;1761(8):927–946. PMID: 16901751

78. Huwiler A, Brunner J, Hummel R, Vervoordeldonk M, Stabel S, van den Bosch H, Pfeilschifter J. Ceramide-binding and activation defines protein kinase c-Raf as a ceramide-activated protein kinase. Proc Natl Acad Sci U S A. 1996 Jul 9;93(14):6959–6963. PMCID: PMC38916

79. Yin X, Zafrullah M, Lee H, Haimovitz-Friedman A, Fuks Z, Kolesnick R. A ceramide-binding C1 domain mediates kinase suppressor of ras membrane translocation. Cell Physiol Biochem Int J Exp Cell Physiol Biochem Pharmacol. 2009;24(3–4):219–230. PMCID: PMC2978518

80. Bourbon NA, Yun J, Kester M. Ceramide directly activates protein kinase C zeta to regulate a stress-activated protein kinase signaling complex. J Biol Chem. 2000 Nov 10;275(45):35617–35623. PMID: 10962008

81. Heinrich M, Wickel M, Schneider-Brachert W, Sandberg C, Gahr J, Schwandner R, Weber T, Saftig P, Peters C, Brunner J, Krönke M, Schütze S. Cathepsin D targeted by acid sphingomyelinase-derived ceramide. EMBO J. 1999 Oct 1;18(19):5252–5263. PMCID: PMC1171596

82. Novgorodov SA, Szulc ZM, Luberto C, Jones JA, Bielawski J, Bielawska A, Hannun YA, Obeid LM. Positively charged ceramide is a potent inducer of mitochondrial permeabilization. J Biol Chem. 2005 Apr 22;280(16):16096–16105. PMID: 15722351

83. Antoon JW, Liu J, Gestaut MM, Burow ME, Beckman BS, Foroozesh M. Design, synthesis, and biological activity of a family of novel ceramide analogues in chemoresistant breast cancer cells. J Med Chem. 2009 Sep 24;52(18):5748–5752. PMID: 19694470

84. Crawford KW, Bittman R, Chun J, Byun HS, Bowen WD. Novel ceramide analogues display selective cytotoxicity in drug-resistant breast tumor cell lines compared to normal breast epithelial cells. Cell Mol Biol Noisy--Gd Fr. 2003 Nov;49(7):1017–1023. PMID: 14682383

85. Liu X, Ryland L, Yang J, Liao A, Aliaga C, Watts R, Tan S-F, Kaiser J, Shanmugavelandy SS, Rogers A, Loughran K, Petersen B, Yuen J, Meng F, Baab KT, Jarbadan NR, Broeg K, Zhang R, Liao J, Sayers TJ, Kester M, Loughran TP. Targeting of survivin by nanoliposomal ceramide induces complete remission in a rat model of NK-LGL leukemia. Blood. 2010 Nov 18;116(20):4192–4201. PMCID: PMC2993625

86. Stover T, Kester M. Liposomal delivery enhances short-chain ceramide-induced apoptosis of breast cancer cells. J Pharmacol Exp Ther. 2003 Nov;307(2):468–475. PMID: 12975495

87. Stover TC, Sharma A, Robertson GP, Kester M. Systemic delivery of liposomal short-chain ceramide limits solid tumor growth in murine models of breast adenocarcinoma. Clin Cancer Res Off J Am Assoc Cancer Res. 2005 May 1;11(9):3465–3474. PMID: 15867249

88. van Vlerken LE, Duan Z, Seiden MV, Amiji MM. Modulation of intracellular ceramide using polymeric nanoparticles to overcome multidrug resistance in cancer. Cancer Res. 2007 May 15;67(10):4843–4850. PMID: 17510414

89. Kapitonov D, Allegood JC, Mitchell C, Hait NC, Almenara JA, Adams JK, Zipkin RE, Dent P, Kordula T, Milstien S, Spiegel S. Targeting sphingosine kinase 1 inhibits Akt signaling, induces apoptosis, and suppresses growth of human glioblastoma cells and xenografts. Cancer Res. 2009 Sep 1;69(17):6915–6923. PMCID: PMC2752891

90. Ju T, Gao D, Fang Z-Y. Targeting colorectal cancer cells by a novel sphingosine kinase 1 inhibitor PF-543. Biochem Biophys Res Commun. 2016 Feb 12;470(3):728–734. PMID: 26775841

91. Wang J, Knapp S, Pyne NJ, Pyne S, Elkins JM. Crystal Structure of Sphingosine Kinase 1 with PF-543. ACS Med Chem Lett. 2014 Dec 11;5(12):1329–1333. PMCID: PMC4265818

92. Schnute ME, McReynolds MD, Kasten T, Yates M, Jerome G, Rains JW, Hall T, Chrencik J, Kraus M, Cronin CN, Saabye M, Highkin MK, Broadus R, Ogawa S, Cukyne K, Zawadzke LE, Peterkin V, Iyanar K, Scholten JA, Wendling J, Fujiwara H, Nemirovskiy O, Wittwer AJ, Nagiec MM. Modulation of cellular S1P levels with a novel, potent and specific inhibitor of sphingosine kinase-1. Biochem J. 2012 May 15;444(1):79–88. PMID: 22397330

93. Venkata JK, An N, Stuart R, Costa LJ, Cai H, Coker W, Song JH, Gibbs K, Matson T, Garrett-Mayer E, Wan Z, Ogretmen B, Smith C, Kang Y. Inhibition of sphingosine kinase 2 downregulates the expression of c-Myc and Mcl-1 and induces apoptosis in multiple myeloma. Blood. 2014 Sep 18;124(12):1915–1925. PMCID: PMC4168346

94. Qin Z, Dai L, Trillo-Tinoco J, Senkal C, Wang W, Reske T, Bonstaff K, Del Valle L, Rodriguez P, Flemington E, Voelkel-Johnson C, Smith CD, Ogretmen B, Parsons C. Targeting sphingosine kinase induces apoptosis and tumor regression for KSHV-associated primary effusion lymphoma. Mol Cancer Ther. 2014 Jan;13(1):154–164. PMCID: PMC3918494

95. Senkal CE, Ponnusamy S, Rossi MJ, Sundararaj K, Szulc Z, Bielawski J, Bielawska A, Meyer M, Cobanoglu B, Koybasi S, Sinha D, Day TA, Obeid LM, Hannun YA, Ogretmen B. Potent Antitumor Activity of a Novel Cationic Pyridinium-Ceramide Alone or in Combination with Gemcitabine against Human Head and Neck Squamous Cell Carcinomas in Vitro and in Vivo. J Pharmacol Exp Ther. 2006 Jun 1;317(3):1188–1199. PMID: 16510697

96. Beckham TH, Lu P, Jones EE, Marrison T, Lewis CS, Cheng JC, Ramshesh VK, Beeson G, Beeson CC, Drake RR, Bielawska A, Bielawski J, Szulc ZM, Ogretmen B, Norris JS, Liu X. LCL124, a cationic analog of ceramide, selectively induces pancreatic cancer cell death by accumulating in mitochondria. J Pharmacol Exp Ther. 2013 Jan;344(1):167–178. PMCID: PMC3533418

97. Saddoughi SA, Gencer S, Peterson YK, Ward KE, Mukhopadhyay A, Oaks J, Bielawski J, Szulc ZM, Thomas RJ, Selvam SP, Senkal CE, Garrett-Mayer E, De Palma RM, Fedarovich D, Liu A, Habib AA, Stahelin RV, Perrotti D, Ogretmen B. Sphingosine analogue drug FTY720 targets I2PP2A/SET and mediates lung tumour suppression via activation of PP2A-RIPK1-dependent necroptosis. EMBO Mol Med. 2012 Nov 25; PMID: 23180565

98. Oaks JJ, Santhanam R, Walker CJ, Roof S, Harb JG, Ferenchak G, Eisfeld A-K, Van Brocklyn JR, Briesewitz R, Saddoughi SA, Nagata K, Bittman R, Caligiuri MA, Abdel-Wahab O, Levine R, Arlinghaus RB, Quintas-Cardama A, Goldman JM, Apperley J, Reid A, Milojkovic D, Ziolo MT, Marcucci G, Ogretmen B, Neviani P, Perrotti D. Antagonistic activities of the immunomodulator and PP2A-activating drug FTY720 (Fingolimod, Gilenya) in Jak2-driven hematologic malignancies. Blood. 2013 Sep 12;122(11):1923–1934. PMCID: PMC3772499

99. Cohen JA, Barkhof F, Comi G, Hartung H-P, Khatri BO, Montalban X, Pelletier J, Capra R, Gallo P, Izquierdo G, Tiel-Wilck K, de Vera A, Jin J, Stites T, Wu S, Aradhye S, Kappos L. Oral fingolimod or intramuscular interferon for relapsing multiple sclerosis. N Engl J Med. 2010 Feb 4;362(5):402–415. PMID: 20089954

100. Neviani P, Harb JG, Oaks JJ, Santhanam R, Walker CJ, Ellis JJ, Ferenchak G, Dorrance AM, Paisie CA, Eiring AM, Ma Y, Mao HC, Zhang B, Wunderlich M, May PC, Sun C, Saddoughi SA, Bielawski J, Blum W, Klisovic RB, Solt JA, Byrd JC, Volinia S, Cortes J, Huettner CS, Koschmieder S, Holyoake TL, Devine S, Caligiuri MA, Croce CM, Garzon R, Ogretmen B, Arlinghaus RB, Chen C-S,

Bittman R, Hokland P, Roy D-C, Milojkovic D, Apperley J, Goldman JM, Reid A, Mulloy JC, Bhatia R, Marcucci G, Perrotti D. PP2A-activating drugs selectively eradicate TKI-resistant chronic myeloid leukemic stem cells. J Clin Invest. 2013 Oct;123(10):4144–4157. PMCID: PMC3784537

101. Kappos L, Radue E-W, O'Connor P, Polman C, Hohlfeld R, Calabresi P, Selmaj K, Agoropoulou C, Leyk M, Zhang-Auberson L, Burtin P, FREEDOMS Study Group. A placebo-controlled trial of oral fingolimod in relapsing multiple sclerosis. N Engl J Med. 2010 Feb 4;362(5):387–401. PMID: 20089952

102. Li M-H, Swenson R, Harel M, Jana S, Stolarzewicz E, Hla T, Shapiro LH, Ferrer F. Antitumor Activity of a Novel Sphingosine-1-Phosphate 2 Antagonist, AB1, in Neuroblastoma. J Pharmacol Exp Ther. 2015 Sep;354(3):261–268. PMCID: PMC4538871

103. Kennedy PC, Zhu R, Huang T, Tomsig JL, Mathews TP, David M, Peyruchaud O, Macdonald TL, Lynch KR. Characterization of a sphingosine 1-phosphate receptor antagonist prodrug. J Pharmacol Exp Ther. 2011 Sep;338(3):879–889. PMCID: PMC3164350

104. Pal SK, Drabkin HA, Reeves JA, Hainsworth JD, Hazel SE, Paggiarino DA, Wojciak J, Woodnutt G, Bhatt RS. A phase 2 study of the sphingosine-1-phosphate antibody sonepcizumab in patients with metastatic renal cell carcinoma. Cancer. 2017 Feb 15;123(4):576–582. PMID: 27727447

105. Lewis CS, Voelkel-Johnson C, Smith CD. Suppression of c-Myc and RRM2 expression in pancreatic cancer cells by the sphingosine kinase-2 inhibitor ABC294640. Oncotarget. 2016 Sep 13;7(37):60181–60192. PMCID: PMC5312377

106. Venant H, Rahmaniyan M, Jones EE, Lu P, Lilly MB, Garrett-Mayer E, Drake RR, Kraveka JM, Smith CD, Voelkel-Johnson C. The Sphingosine Kinase 2 Inhibitor ABC294640 Reduces the Growth of Prostate Cancer Cells and Results in Accumulation of Dihydroceramides In Vitro and In Vivo. Mol Cancer Ther. 2015 Dec;14(12):2744–2752. PMCID: PMC4674301

107. Britten CD, Garrett-Mayer E, Chin SH, Shirai K, Ogretmen B, Bentz TA, Brisendine A, Anderton K, Cusack SL, Maines LW, Zhuang Y, Smith CD, Thomas MB. A Phase I Study of ABC294640, a First-in-Class Sphingosine Kinase-2 Inhibitor, in Patients with Advanced Solid Tumors. Clin Cancer Res Off J Am Assoc Cancer Res. 2017 Aug 15;23(16):4642–4650. PMCID: PMC5559328

108. A Phase II Study of ABC294640 as Second-Line Monotherapy in Patients With Advanced Hepatocellular Carcinoma - Full Text View - ClinicalTrials.gov [Internet]. [cited 2018 Jun 4]. Available from: https://clinicaltrials.gov/ct2/show/NCT02939807

109. ABC294640 in Refractory / Relapsed Multiple Myeloma - Full Text View - ClinicalTrials.gov [Internet]. [cited 2018 Jun 4]. Available from: https://clinicaltrials.gov/ct2/show/NCT02757326

110. Early Phase Evaluation of ABC294640 in Patients With Refractory/Relapsed Diffuse Large B-cell Lymphoma or Kaposi Sarcoma - Full Text View - ClinicalTrials.gov [Internet]. [cited 2018 Jun 4]. Available from: https://clinicaltrials.gov/ct2/show/NCT02229981

111. Janssens V, Goris J. Protein phosphatase 2A: a highly regulated family of serine/threonine phosphatases implicated in cell growth and signalling. Biochem J. 2001 Feb 1;353(Pt 3):417–439. PMCID: PMC1221586

112. Virshup DM. Protein phosphatase 2A: a panoply of enzymes. Curr Opin Cell Biol. 2000 Apr;12(2):180–185. PMID: 10712915

113. Schönthal AH. Role of serine/threonine protein phosphatase 2A in cancer. Cancer Lett. 2001 Sep 10;170(1):1–13. PMID: 11448528

114. Herzog F, Kahraman A, Boehringer D, Mak R, Bracher A, Walzthoeni T, Leitner A, Beck M, Hartl F-U, Ban N, Malmström L, Aebersold R. Structural Probing of a Protein Phosphatase 2A Network by Chemical Cross-Linking and Mass Spectrometry. Science. 2012 Sep 14;337(6100):1348–1352.

115. Cho US, Xu W. Crystal structure of a protein phosphatase 2A heterotrimeric holoenzyme. Nature. 2007 Jan 4;445(7123):53–57. PMID: 17086192

116. Sablina AA, Chen W, Arroyo JD, Corral L, Hector M, Bulmer SE, DeCaprio JA, Hahn WC. The tumor suppressor PP2A Abeta regulates the RalA GTPase. Cell. 2007 Jun 1;129(5):969–982. PMCID: PMC1945132

117. Chen W, Arroyo JD, Timmons JC, Possemato R, Hahn WC. Cancer-associated PP2A Aalpha subunits induce functional haploinsufficiency and tumorigenicity. Cancer Res. 2005 Sep 15;65(18):8183–8192. PMID: 16166293

118. Calin GA, di Iasio MG, Caprini E, Vorechovsky I, Natali PG, Sozzi G, Croce CM, Barbanti-Brodano G, Russo G, Negrini M. Low frequency of alterations of the alpha (PPP2R1A) and beta (PPP2R1B) isoforms of the subunit A of the serine-threonine phosphatase 2A in human neoplasms. Oncogene. 2000 Feb 24;19(9):1191–1195. PMID: 10713707

119. Ruediger R, Pham HT, Walter G. Disruption of protein phosphatase 2A subunit interaction in human cancers with mutations in the A alpha subunit gene. Oncogene. 2001 Jan 4;20(1):10–15. PMID: 11244497

120. Tamaki M, Goi T, Hirono Y, Katayama K, Yamaguchi A. PPP2R1B gene alterations inhibit interaction of PP2A-Abeta and PP2A-C proteins in colorectal cancers. Oncol Rep. 2004 Mar;11(3):655–659. PMID: 14767517

121. McCright B, Rivers AM, Audlin S, Virshup DM. The B56 family of protein phosphatase 2A (PP2A) regulatory subunits encodes differentiation-induced phosphoproteins that target PP2A to both nucleus and cytoplasm. J Biol Chem. 1996 Sep 6;271(36):22081–22089. PMID: 8703017

122. Sontag E. Protein phosphatase 2A: the Trojan Horse of cellular signaling. Cell Signal. 2001 Jan;13(1):7–16. PMID: 11257442

123. Schöls L, Amoiridis G, Büttner T, Przuntek H, Epplen JT, Riess O. Autosomal dominant cerebellar ataxia: phenotypic differences in genetically defined subtypes? Ann Neurol. 1997 Dec;42(6):924–932. PMID: 9403486

124. Hu P, Yu L, Zhang M, Zheng L, Zhao Y, Fu Q, Zhao S. Molecular cloning and mapping of the brain-abundant B1gamma subunit of protein phosphatase 2A, PPP2R2C, to human chromosome 4p16. Genomics. 2000 Jul 1;67(1):83–86. PMID: 10945473

125. Ruteshouser EC, Ashworth LK, Huff V. Absence of PPP2R1A mutations in Wilms tumor. Oncogene. 2001 Apr 12;20(16):2050–2054. PMID: 11360189

126. McCright B, Brothman AR, Virshup DM. Assignment of human protein phosphatase 2A regulatory subunit genes b56alpha, b56beta, b56gamma, b56delta, and b56epsilon (PPP2R5A-PPP2R5E), highly expressed in muscle and brain, to chromosome regions 1q41, 11q12, 3p21, 6p21.1, and 7p11.2 --> p12. Genomics. 1996 Aug 15;36(1):168–170. PMID: 8812429

127. Jones TA, Barker HM, da Cruz e Silva EF, Mayer-Jaekel RE, Hemmings BA, Spurr NK, Sheer D, Cohen PT. Localization of the genes encoding the catalytic subunits of protein phosphatase 2A to human chromosome bands 5q23-->q31 and 8p12-->p11.2, respectively. Cytogenet Cell Genet. 1993;63(1):35–41. PMID: 8383590

128. Seshacharyulu P, Pandey P, Datta K, Batra SK. Phosphatase: PP2A structural importance, regulation and its aberrant expression in cancer. Cancer Lett. 2013 Jul 10;335(1):9–18. PMCID: PMC3665613

129. Deichmann M, Polychronidis M, Wacker J, Thome M, Näher H. The protein phosphatase 2A subunit Bgamma gene is identified to be differentially expressed in malignant melanomas by subtractive suppression hybridization. Melanoma Res. 2001 Dec;11(6):577–585. PMID: 11725204

130. Nobumori Y, Shouse GP, Wu Y, Lee KJ, Shen B, Liu X. B56γ Tumor-Associated Mutations Provide New Mechanisms for B56γ-PP2A Tumor Suppressor Activity. Mol Cancer Res. 2013 Sep 1;11(9):995–1003. PMID: 23723076

131. Shouse GP, Nobumori Y, Liu X. A B56gamma mutation in lung cancer disrupts the p53-dependent tumor-suppressor function of protein phosphatase 2A. Oncogene. 2010 Jul 8;29(27):3933–3941. PMCID: PMC2900437

132. Moreno CS, Park S, Nelson K, Ashby D, Hubalek F, Lane WS, Pallas DC. WD40 repeat proteins striatin and S/G(2) nuclear autoantigen are members of a novel family of calmodulin-binding proteins that associate with protein phosphatase 2A. J Biol Chem. 2000 Feb 25;275(8):5257–5263. PMCID: PMC3505218

133. Chen W, Possemato R, Campbell KT, Plattner CA, Pallas DC, Hahn WC. Identification of specific PP2A complexes involved in human cell transformation. Cancer Cell. 2004 Feb;5(2):127–136. PMID: 14998489

134. Ito A, Kataoka TR, Watanabe M, Nishiyama K, Mazaki Y, Sabe H, Kitamura Y, Nojima H. A truncated isoform of the PP2A B56 subunit promotes cell motility through paxillin phosphorylation. EMBO J. 2000 Feb 15;19(4):562–571. PMCID: PMC305594

135. Voorhoeve PM, Hijmans EM, Bernards R. Functional interaction between a novel protein phosphatase 2A regulatory subunit, PR59, and the retinoblastoma-related p107 protein. Oncogene. 1999 Jan 14;18(2):515–524. PMID: 9927208

136. Janssens V, Longin S, Goris J. PP2A holoenzyme assembly: in cauda venenum (the sting is in the tail). Trends Biochem Sci. 2008 Mar;33(3):113–121. PMID: 18291659

137. Guo H, Reddy SA, Damuni Z. Purification and characterization of an autophosphorylation-activated protein serine threonine kinase that phosphorylates and inactivates protein phosphatase 2A. J Biol Chem. 1993 May 25;268(15):11193–11198. PMID: 8388387

138. Favre B, Zolnierowicz S, Turowski P, Hemmings BA. The catalytic subunit of protein phosphatase 2A is carboxyl-methylated in vivo. J Biol Chem. 1994 Jun 10;269(23):16311–16317. PMID: 8206937

139. Brautigan DL. Flicking the switches: phosphorylation of serine/threonine protein phosphatases. Semin Cancer Biol. 1995 Aug;6(4):211–217. PMID: 8541516

140. Stanevich V, Jiang L, Satyshur KA, Li Y, Jeffrey PD, Li Z, Menden P, Semmelhack MF, Xing Y. The structural basis for tight control of PP2A methylation and function by LCMT-1. Mol Cell. 2011 Feb 4;41(3):331–342. PMCID: PMC3060061

141. Stanevich V, Zheng A, Guo F, Jiang L, Wlodarchak N, Xing Y. Mechanisms of the scaffold subunit in facilitating protein phosphatase 2A methylation. PloS One. 2014;9(1):e86955. PMCID: PMC3900686

142. Dobrowsky RT, Kamibayashi C, Mumby MC, Hannun YA. Ceramide activates heterotrimeric protein phosphatase 2A. J Biol Chem. 1993 Jul 25;268(21):15523–15530. PMID: 8393446

143. Chalfant CE, Rathman K, Pinkerman RL, Wood RE, Obeid LM, Ogretmen B, Hannun YA. De novo ceramide regulates the alternative splicing of caspase 9 and Bcl-x in A549 lung adenocarcinoma cells. Dependence on protein phosphatase-1. J Biol Chem. 2002 Apr 12;277(15):12587–12595. PMID: 11801602

144. Lee JY, Bielawska AE, Obeid LM. Regulation of cyclin-dependent kinase 2 activity by ceramide. Exp Cell Res. 2000 Dec 15;261(2):303–311. PMID: 11112337

145. Nagahara Y, Matsuoka Y, Saito K, Ikekita M, Higuchi S, Shinomiya T. Coordinate involvement of cell cycle arrest and apoptosis strengthen the effect of FTY720. Jpn J Cancer Res Gann. 2001 Jun;92(6):680–687. PMID: 11429058

146. Brinkmann V, Billich A, Baumruker T, Heining P, Schmouder R, Francis G, Aradhye S, Burtin P. Fingolimod (FTY720): discovery and development of an oral drug to treat multiple sclerosis. Nat Rev Drug Discov. 2010 Nov;9(11):883–897. PMID: 21031003

147. David OJ, Kovarik JM, Schmouder RL. Clinical pharmacokinetics of fingolimod. Clin Pharmacokinet. 2012 Jan 1;51(1):15–28. PMID: 22149256

148. Mukhopadhyay A, Saddoughi SA, Song P, Sultan I, Ponnusamy S, Senkal CE, Snook CF, Arnold HK, Sears RC, Hannun YA, Ogretmen B. Direct interaction between the inhibitor 2 and ceramide via sphingolipid-protein binding is involved in

the regulation of protein phosphatase 2A activity and signaling. FASEB J Off Publ Fed Am Soc Exp Biol. 2009 Mar;23(3):751–763. PMID: 19028839

149. Chalfant CE, Kishikawa K, Mumby MC, Kamibayashi C, Bielawska A, Hannun YA. Long chain ceramides activate protein phosphatase-1 and protein phosphatase-2A. Activation is stereospecific and regulated by phosphatidic acid. J Biol Chem. 1999 Jul 16;274(29):20313–20317. PMID: 10400653

150. Chalfant CE, Szulc Z, Roddy P, Bielawska A, Hannun YA. The structural requirements for ceramide activation of serine-threonine protein phosphatases. J Lipid Res. 2004 Mar;45(3):496–506. PMID: 14657198

151. Seo SB, McNamara P, Heo S, Turner A, Lane WS, Chakravarti D. Regulation of histone acetylation and transcription by INHAT, a human cellular complex containing the set oncoprotein. Cell. 2001 Jan 12;104(1):119–130. PMID: 11163245

152. Habrukowich C, Han DK, Le A, Rezaul K, Pan W, Ghosh M, Li Z, Dodge-Kafka K, Jiang X, Bittman R, Hla T. Sphingosine interaction with acidic leucine-rich nuclear phosphoprotein-32A (ANP32A) regulates PP2A activity and cyclooxygenase (COX)-2 expression in human endothelial cells. J Biol Chem. 2010 Aug 27;285(35):26825–26831. PMCID: PMC2930681

153. Hayashi E, Kuramitsu Y, Okada F, Fujimoto M, Zhang X, Kobayashi M, Iizuka N, Ueyama Y, Nakamura K. Proteomic profiling for cancer progression: Differential display analysis for the expression of intracellular proteins between regressive and

progressive cancer cell lines. Proteomics. 2005 Mar;5(4):1024–1032. PMID: 15712240

154. Hoffarth S, Zitzer A, Wiewrodt R, Hähnel PS, Beyer V, Kreft A, Biesterfeld S, Schuler M. pp32/PHAPI determines the apoptosis response of non-small-cell lung cancer. Cell Death Differ. 2008 Jan;15(1):161–170. PMID: 17962813

155. Schafer ZT, Parrish AB, Wright KM, Margolis SS, Marks JR, Deshmukh M, Kornbluth S. Enhanced sensitivity to cytochrome c-induced apoptosis mediated by PHAPI in breast cancer cells. Cancer Res. 2006 Feb 15;66(4):2210–2218. PMID: 16489023

156. Bai J, Brody JR, Kadkol SS, Pasternack GR. Tumor suppression and potentiation by manipulation of pp32 expression. Oncogene. 2001 Apr 19;20(17):2153–2160. PMID: 11360199

157. Xie M, Ji Z, Bao Y, Zhu Y, Xu Y, Wang L, Gao S, Liu Z, Tian Z, Meng Q, Shi H, Yu R. PHAP1 promotes glioma cell proliferation by regulating the Akt/p27/stathmin pathway. J Cell Mol Med [Internet]. [cited 2018 Jun 1];0(0). Available from: https://onlinelibrary.wiley.com/doi/abs/10.1111/jcmm.13639

158. Kadkol SS, Brody JR, Epstein JI, Kuhajda FP, Pasternack GR. Novel nuclear phosphoprotein pp32 is highly expressed in intermediate- and high-grade prostate cancer. The Prostate. 1998 Feb 15;34(3):231–237. PMID: 9492852

159. Velmurugan BK, Yeh K-T, Lee C-H, Lin S-H, Chin M-C, Chiang S-L, Wang Z-H, Hua C-H, Tsai M-H, Chang J-G, Ko Y-C. Acidic leucine-rich nuclear

phosphoprotein-32A (ANP32A) association with lymph node metastasis predicts poor survival in oral squamous cell carcinoma patients. Oncotarget. 2016 Feb 24;7(10):10879–10890. PMCID: PMC4905446

160. Shi H, Hood KA, Hayes MT, Stubbs RS. Proteomic analysis of advanced colorectal cancer by laser capture microdissection and two-dimensional difference gel electrophoresis. J Proteomics. 2011 Dec 21;75(2):339–351. PMID: 21843667

161. Li C, Ruan H-Q, Liu Y-S, Xu M-J, Dai J, Sheng Q-H, Tan Y-X, Yao Z-Z, Wang H-Y, Wu J-R, Zeng R. Quantitative Proteomics Reveal up-regulated Protein Expression of the SET Complex Associated with Hepatocellular Carcinoma. J Proteome Res. 2012 Feb 3;11(2):871–885.

162. Yan W, Bai Z, Wang J, Li X, Chi B, Chen X. ANP32A modulates cell growth by regulating p38 and Akt activity in colorectal cancer. Oncol Rep. 2017 Sep 1;38(3):1605–1612.

163. Wang X, Blanchard J, Tung YC, Grundke-Iqbal I, Iqbal K. Inhibition of Protein Phosphatase-2A (PP2A) by I1PP2A Leads to Hyperphosphorylation of Tau, Neurodegeneration, and Cognitive Impairment in Rats. J Alzheimers Dis JAD. 2015;45(2):423–435. PMID: 25589718

164. Chen S, Li B, Grundke-Iqbal I, Iqbal K. I1PP2A affects tau phosphorylation via association with the catalytic subunit of protein phosphatase 2A. J Biol Chem. 2008 Apr 18;283(16):10513–10521. PMCID: PMC2447634

165. Kovacech B, Kontsekova E, Zilka N, Novak P, Skrabana R, Filipcik P, Iqbal K, Novak M. A novel monoclonal antibody DC63 reveals that inhibitor 1 of protein phosphatase 2A is preferentially nuclearly localised in human brain. FEBS Lett. 2007 Feb 20;581(4):617–622. PMID: 17266954

166. Yi F, Ni W, Liu W, Bai J, Li W. Expression and biological role of CIP2A in human astrocytoma. Mol Med Rep. 2013 May 1;7(5):1376–1380.

167. Zhai M, Cong L, Han Y, Tu G. CIP2A is overexpressed in osteosarcoma and regulates cell proliferation and invasion. Tumor Biol. 2014 Feb 1;35(2):1123–1128.

168. Haesen D, Sents W, Ivanova E, Lambrecht C, Janssens V. Cellular inhibitors of protein phosphatase PP2A in cancer. Biomed Res. 2012;23(SPEC. ISSUE):197–211.

169. Westermarck J, Hahn WC. Multiple pathways regulated by the tumor suppressor PP2A in transformation. Trends Mol Med. 2008 Apr;14(4):152–160. PMID: 18329957

170. Puustinen P, Jäättelä M. KIAA1524/CIP2A promotes cancer growth by coordinating the activities of MTORC1 and MYC. Autophagy. 2014 Jul 29;10(7):1352–1354. PMID: 24905455

171. Coenen EA, Zwaan CM, Meyer C, Marschalek R, Pieters R, van der Veken LT, Beverloo HB, van den Heuvel-Eibrink MM. KIAA1524: A novel MLL translocation partner in acute myeloid leukemia. Leuk Res. 2011 Jan;35(1):133–135. PMID: 20943269

172. Rincón R, Cristóbal I, Zazo S, Arpí O, Menéndez S, Manso R, Lluch A, Eroles P, Rovira A, Albanell J, García-Foncillas J, Madoz-Gúrpide J, Rojo F. PP2A inhibition determines poor outcome and doxorubicin resistance in early breast cancer and its activation shows promising therapeutic effects. Oncotarget. 2015 Feb 28;6(6):4299–4314. PMCID: PMC4414191

173. Laine A, Sihto H, Come C, Rosenfeldt MT, Zwolinska A, Niemelä M, Khanna A, Chan EK, Kähäri V-M, Kellokumpu-Lehtinen P-L, Sansom OJ, Evan GI, Junttila MR, Ryan KM, Marine J-C, Joensuu H, Westermarck J. Senescence Sensitivity of Breast Cancer Cells Is Defined by Positive Feedback Loop between CIP2A and E2F1. Cancer Discov. 2013 Feb 1;3(2):182–197. PMID: 23306062

174. Khanna A, Pimanda JE, Westermarck J. Cancerous Inhibitor of Protein Phosphatase 2A, an Emerging Human Oncoprotein and a Potential Cancer Therapy Target. Cancer Res. 2013 Nov 15;73(22):6548–6553. PMID: 24204027

175. Liu Z, Ma L, Wen Z-S, Hu Z, Wu F-Q, Li W, Liu J, Zhou G-B. Cancerous inhibitor of PP2A is targeted by natural compound celastrol for degradation in non-small-cell lung cancer. Carcinogenesis. 2014 Apr;35(4):905–914. PMCID: PMC4319067

176. Firestein R, Cui X, Huie P, Cleary ML. Set domain-dependent regulation of transcriptional silencing and growth control by SUV39H1, a mammalian ortholog of Drosophila Su(var)3-9. Mol Cell Biol. 2000 Jul;20(13):4900–4909. PMCID: PMC85941

177. Saito S, Miyaji-Yamaguchi M, Nagata K. Aberrant intracellular localization of SET-CAN fusion protein, associated with a leukemia, disorganizes nuclear export. Int J Cancer J Int Cancer. 2004 Sep 10;111(4):501–507. PMID: 15239126

178. von Lindern M, van Baal S, Wiegant J, Raap A, Hagemeijer A, Grosveld G. Can, a putative oncogene associated with myeloid leukemogenesis, may be activated by fusion of its 3' half to different genes: characterization of the set gene. Mol Cell Biol. 1992 Aug;12(8):3346–3355. PMCID: PMC364582

179. Fan Z, Beresford PJ, Oh DY, Zhang D, Lieberman J. Tumor suppressor NM23-H1 is a granzyme A-activated DNase during CTL-mediated apoptosis, and the nucleosome assembly protein SET is its inhibitor. Cell. 2003 Mar 7;112(5):659–672. PMID: 12628186

180. Saito S, Miyaji-Yamaguchi M, Shimoyama T, Nagata K. Functional domains of template-activating factor-I as a protein phosphatase 2A inhibitor. Biochem Biophys Res Commun. 1999 Jun 7;259(2):471–475. PMID: 10362532

181. Karetsou Z, Emmanouilidou A, Sanidas I, Liokatis S, Nikolakaki E, Politou AS, Papamarcaki T. Identification of distinct SET/TAF-Ibeta domains required for core histone binding and quantitative characterisation of the interaction. BMC Biochem. 2009;10:10. PMCID: PMC2676315

182. Miyaji-Yamaguchi M, Okuwaki M, Nagata K. Coiled-coil structure-mediated dimerization of template activating factor-I is critical for its chromatin remodeling activity. J Mol Biol. 1999 Jul 9;290(2):547–557. PMID: 10390352

183. Wang GG, Cai L, Pasillas MP, Kamps MP. NUP98-NSD1 links H3K36 methylation to Hox-A gene activation and leukaemogenesis. Nat Cell Biol. 2007 Jul;9(7):804–812. PMID: 17589499

184. Anazawa Y, Nakagawa H, Furihara M, Ashida S, Tamura K, Yoshioka H, Shuin T, Fujioka T, Katagiri T, Nakamura Y. PCOTH, a novel gene overexpressed in prostate cancers, promotes prostate cancer cell growth through phosphorylation of oncoprotein TAF-Ibeta/SET. Cancer Res. 2005 Jun 1;65(11):4578–4586. PMID: 15930275

185. Yu G, Yan T, Feng Y, Liu X, Xia Y, Luo H, Wang J-Z, Wang X. Ser9 phosphorylation causes cytoplasmic detention of I2PP2A/SET in Alzheimer disease. Neurobiol Aging. 2013 Jul;34(7):1748–1758. PMID: 23374587

186. Irie A, Harada K, Araki N, Nishimura Y. Phosphorylation of SET protein at Ser171 by protein kinase D2 diminishes its inhibitory effect on protein phosphatase 2A. PloS One. 2012;7(12):e51242. PMCID: PMC3522678

187. Vasudevan NT, Mohan ML, Gupta MK, Hussain AK, Naga Prasad SV. Inhibition of protein phosphatase 2A activity by PI3Kγ regulates β-adrenergic receptor function. Mol Cell. 2011 Mar 18;41(6):636–648. PMCID: PMC3063893

188. Neviani P, Santhanam R, Trotta R, Notari M, Blaser BW, Liu S, Mao H, Chang JS, Galietta A, Uttam A, Roy DC, Valtieri M, Bruner-Klisovic R, Caligiuri MA, Bloomfield CD, Marcucci G, Perrotti D. The tumor suppressor PP2A is functionally

inactivated in blast crisis CML through the inhibitory activity of the BCR/ABL-regulated SET protein. Cancer Cell. 2005 Nov;8(5):355–368. PMID: 16286244

189. Carlson SG, Eng E, Kim EG, Perlman EJ, Copeland TD, Ballermann BJ. Expression of SET, an inhibitor of protein phosphatase 2A, in renal development and Wilms' tumor. J Am Soc Nephrol JASN. 1998 Oct;9(10):1873–1880. PMID: 9773788

190. Ouellet V, Le Page C, Guyot M-C, Lussier C, Tonin PN, Provencher DM, Mes-Masson A-M. SET complex in serous epithelial ovarian cancer. Int J Cancer J Int Cancer. 2006 Nov 1;119(9):2119–2126. PMID: 16823850

191. Furuya H, Shimizu Y, Kawamori T. Sphingolipids in cancer. Cancer Metastasis Rev. 2011 Dec;30(3–4):567–576. PMID: 22005951

192. Mukhopadhyay A, Tabanor K, Chaguturu R, Aldrich JV. Targeting inhibitor 2 of protein phosphatase 2A as a therapeutic strategy for prostate cancer treatment. Cancer Biol Ther. 2013 Oct 1;14(10):962–972. PMCID: PMC3926893

193. Bharath LP, Ruan T, Li Y, Ravindran A, Wan X, Nhan JK, Walker ML, Deeter L, Goodrich R, Johnson E, Munday D, Mueller R, Kunz D, Jones D, Reese V, Summers SA, Babu PVA, Holland WL, Zhang Q-J, Abel ED, Symons JD. Ceramide initiated protein phosphatase 2A activation contributes to arterial dysfunction in vivo. Diabetes. 2015 Aug 7;db150244. PMID: 26253611

194. Saydam G, Aydin HH, Sahin F, Selvi N, Oktem G, Terzioglu E, Buyukkececi F, Omay SB. Involvement of protein phosphatase 2A in interferon-alpha-2b-induced

apoptosis in K562 human chronic myelogenous leukaemia cells. Leuk Res. 2003 Aug;27(8):709–717. PMID: 12801529

195. Bialojan C, Takai A. Inhibitory effect of a marine-sponge toxin, okadaic acid, on protein phosphatases. Specificity and kinetics. Biochem J. 1988 Nov 15;256(1):283–290. PMCID: PMC1135400

196. Suganuma M, Fujiki H, Suguri H, Yoshizawa S, Hirota M, Nakayasu M, Ojika M, Wakamatsu K, Yamada K, Sugimura T. Okadaic acid: an additional non-phorbol-12-tetradecanoate-13-acetate-type tumor promoter. Proc Natl Acad Sci U S A. 1988 Mar;85(6):1768–1771. PMCID: PMC279860

197. Roberts KG, Smith AM, McDougall F, Carpenter H, Horan M, Neviani P, Powell JA, Thomas D, Guthridge MA, Perrotti D, Sim ATR, Ashman LK, Verrills NM. Essential requirement for PP2A inhibition by the oncogenic receptor c-KIT suggests PP2A reactivation as a strategy to treat c-KIT+ cancers. Cancer Res. 2010 Jul 1;70(13):5438–5447. PMCID: PMC2933456

198. Cristóbal I, Garcia-Orti L, Cirauqui C, Cortes-Lavaud X, García-Sánchez MA, Calasanz MJ, Odero MD. Overexpression of SET is a recurrent event associated with poor outcome and contributes to protein phosphatase 2A inhibition in acute myeloid leukemia. Haematologica. 2012 Apr 1;97(4):543–550. PMID: 22133779

199. Chen L, Luo L-F, Lu J, Li L, Liu Y-F, Wang J, Liu H, Song H, Jiang H, Chen S-J, Luo C, Li KK. FTY720 Induces Apoptosis of M2 Subtype Acute Myeloid

Leukemia Cells by Targeting Sphingolipid Metabolism and Increasing Endogenous Ceramide Levels. PLoS ONE. 2014 Jul 22;9(7):e103033.

200. Ramaswamy K, Spitzer B, Kentsis A. Therapeutic Re-Activation of Protein Phosphatase 2A in Acute Myeloid Leukemia. Front Oncol. 2015;5:16. PMCID: PMC4313608

201. Agarwal A, MacKenzie RJ, Pippa R, Eide CA, Oddo J, Tyner JW, Sears R, Vitek MP, Odero MD, Christensen DJ, Druker BJ. Antagonism of SET using OP449 enhances the efficacy of tyrosine kinase inhibitors and overcomes drug resistance in myeloid leukemia. Clin Cancer Res Off J Am Assoc Cancer Res. 2014 Apr 15;20(8):2092–2103. PMCID: PMC3989420

202. Christensen DJ, Chen Y, Oddo J, Matta KM, Neil J, Davis ED, Volkheimer AD, Lanasa MC, Friedman DR, Goodman BK, Gockerman JP, Diehl LF, de Castro CM, Moore JO, Vitek MP, Weinberg JB. SET oncoprotein overexpression in B-cell chronic lymphocytic leukemia and non-Hodgkin lymphoma: a predictor of aggressive disease and a new treatment target. Blood. 2011 Oct 13;118(15):4150–4158. PMCID: PMC3204732

203. Farrell AS, Allen-Petersen B, Daniel CJ, Wang X, Wang Z, Rodriguez S, Impey S, Oddo J, Vitek MP, Lopez C, Christensen DJ, Sheppard B, Sears RC. Targeting Inhibitors of the Tumor Suppressor PP2A for the Treatment of Pancreatic Cancer. Mol Cancer Res [Internet]. 2014 Mar 25 [cited 2014 May 22]; Available from: http://mcr.aacrjournals.org/content/early/2014/05/19/1541-7786.MCR-13-0542 PMID: 24667985

204. Mody HR, Hung SW, Naidu K, Lee H, Gilbert CA, Hoang TT, Pathak RK, Manoharan R, Muruganandan S, Govindarajan R. SET contributes to the epithelial-mesenchymal transition of pancreatic cancer. Oncotarget. 2017 Sep 15;8(40):67966–67979. PMCID: PMC5620228

205. Cristóbal I, Torrejón B, Rojo F, García-Foncillas J. Potential contribution of SET and c-MYC deregulation to promote extracellular matrix remodelling in hepatocellular carcinoma. Br J Pharmacol. 2018;175(3):573–574. PMCID: PMC5773959

206. Janghorban M, Farrell AS, Allen-Petersen BL, Pelz C, Daniel CJ, Oddo J, Langer EM, Christensen DJ, Sears RC. Targeting c-MYC by antagonizing PP2A inhibitors in breast cancer. Proc Natl Acad Sci U S A. 2014 Jun 24;111(25):9157–9162. PMCID: PMC4078832

207. Cristóbal I, Rincón R, Manso R, Caramés C, Zazo S, Madoz-Gúrpide J, Rojo F, García-Foncillas J. Deregulation of the PP2A inhibitor SET shows promising therapeutic implications and determines poor clinical outcome in patients with metastatic colorectal cancer. Clin Cancer Res Off J Am Assoc Cancer Res. 2015 Jan 15;21(2):347–356. PMID: 25388166

208. Christensen DJ, Ohkubo N, Oddo J, Kanegan MJV, Neil J, Li F, Colton CA, Vitek MP. Apolipoprotein E and Peptide Mimetics Modulate Inflammation by Binding the SET Protein and Activating Protein Phosphatase 2A. J Immunol. 2011 Feb 15;186(4):2535–2542. PMID: 21289314

209. Neviani P, Perrotti D. SETting OP449 into the PP2A-Activating Drug Family. Clin Cancer Res. 2014 Apr 15;20(8):2026–2028. PMID: 24634375

210. Clubb RT, Thanabal V, Wagner G. A constant-time three-dimensional triple-resonance pulse scheme to correlate intraresidue 1HN, 15N, and 13C′ chemical shifts in 15N□13C-labelled proteins. J Magn Reson 1969. 1992 Mar 1;97(1):213–217.

211. Grzesiek S, Bax A. Improved 3D triple-resonance NMR techniques applied to a 31 kDa protein. J Magn Reson 1969. 1992 Feb 1;96(2):432–440.

212. Grzesiek S, Bax A. Amino acid type determination in the sequential assignment procedure of uniformly 13C/15N-enriched proteins. J Biomol NMR. 1993;3(2):185–204.

213. Kay LE, Xu GY, Yamazaki T. Enhanced-Sensitivity Triple-Resonance Spectroscopy with Minimal H2O Saturation. J Magn Reson A. 1994 Jul 1;109(1):129–133.

214. Muhandiram DR, Kay LE. Gradient-Enhanced Triple-Resonance Three-Dimensional NMR Experiments with Improved Sensitivity. J Magn Reson B. 1994 Mar 1;103(3):203–216.

215. Sattler M, Schleucher J, Griesinger C. Heteronuclear multidimensional NMR experiments for the structure determination of proteins in solution employing pulsed field gradients. Prog Nucl Magn Reson Spectrosc. 1999 Mar 19;34(2):93–158.

216. Schleucher J, Sattler M, Griesinger C. Coherence Selection by Gradients without Signal Attenuation: Application to the Three-Dimensional HNCO Experiment. Angew Chem Int Ed Engl. 1993 Oct 1;32(10):1489–1491.

217. Wittekind M, Mueller L. HNCACB, a High-Sensitivity 3D NMR Experiment to Correlate Amide-Proton and Nitrogen Resonances with the Alpha- and Beta-Carbon Resonances in Proteins. J Magn Reson B. 1993 Apr;101(2):201–205.

218. Vranken W, Boucher W, Stevens T, Fogh R, Pajon A, Llinas M, Ulrich E, Markley J, Ionides J, Laue E. The CCPN Data Model for NMR Spectroscopy: development of a software pipeline. Proteins. 2005 Jun 1;59:687–96.

219. Salzmann M, Pervushin K, Wider G, Senn H, Wüthrich K. TROSY in triple-resonance experiments: New perspectives for sequential NMR assignment of large proteins. Proc Natl Acad Sci. 1998 Nov 10;95(23):13585–13590. PMID: 9811843

220. Salzmann M, Wider G, Pervushin K, Senn H, Wüthrich K. TROSY-type Triple-Resonance Experiments for Sequential NMR Assignments of Large Proteins. J Am Chem Soc. 1999 Feb 1;121(4):844–848.

221. Salzmann M, Pervushin K, Wider G, Senn H, Wüthrich K. NMR Assignment and Secondary Structure Determination of an Octameric 110 kDa Protein Using TROSY in Triple Resonance Experiments. J Am Chem Soc. 2000 Aug 1;122(31):7543–7548.

222. Favier A, Brutscher B. Recovering lost magnetization: polarization enhancement in biomolecular NMR. J Biomol NMR. 2011 Jan 1;49(1):9–15.

223. Lescop E, Schanda P, Brutscher B. A set of BEST triple-resonance experiments for time-optimized protein resonance assignment. J Magn Reson. 2007 Jul 1;187(1):163–169.

224. Schulte-Herbrüggen T, Sørensen OW. Clean TROSY: Compensation for Relaxation-Induced Artifacts. J Magn Reson. 2000 May 1;144(1):123–128.

225. Williamson MP. Using chemical shift perturbation to characterise ligand binding. Prog Nucl Magn Reson Spectrosc. 2013 Aug 1;73:1–16.

226. Griesinger C, Sørensen OW, Ernst RR. Practical aspects of the E.COSY technique. Measurement of scalar spin-spin coupling constants in peptides. J Magn Reson 1969. 1987 Dec 1;75(3):474–492.

227. Boyer RD, Johnson R, Krishnamurthy K. Compensation of refocusing inefficiency with synchronized inversion sweep (CRISIS) in multiplicity-edited HSQC. J Magn Reson. 2003 Dec;165(2):253–259.

228. Cicero DO, Barbato G, Bazzo R. Sensitivity Enhancement of a Two-Dimensional Experiment for the Measurement of Heteronuclear Long-Range Coupling Constants, by a New Scheme of Coherence Selection by Gradients. J Magn Reson. 2001 Jan;148(1):209–213.

229. Wagner R, Berger S. Gradient-Selected NOESY—A Fourfold Reduction of the Measurement Time for the NOESY Experiment. J Magn Reson A. 1996 Nov;123(1):119–121.

230. Hwang TL, Shaka AJ. Water Suppression That Works. Excitation Sculpting Using Arbitrary Wave-Forms and Pulsed-Field Gradients. J Magn Reson A. 1995 Feb;112(2):275–279.

231. Mayer M, Meyer B. Characterization of ligand binding by saturation transfer difference NMR spectroscopy. Angew Chem - Int Ed. 1999;38(12):1784–1788.

232. Mayer M, Meyer B. Charakterisierung von Ligandenbindung durch Sättigungstransfer-Differenz-NMR-Spektroskopie. Angew Chem. 1999 Jun 14;111(12):1902–1906.

233. Wüthrich K. NMR in biological research: peptides and proteins. Amsterdam; New York: North-Holland Pub. Co. ; Sole distributors for the U.S.A. and Canada, American Elsevier Pub. Co.; 1976.

234. Mayer M, Meyer B. Group Epitope Mapping by Saturation Transfer Difference NMR To Identify Segments of a Ligand in Direct Contact with a Protein Receptor. J Am Chem Soc. 2001 Jun 1;123(25):6108–6117.

235. Muto S, Senda M, Akai Y, Sato L, Suzuki T, Nagai R, Senda T, Horikoshi M. Relationship between the structure of SET/TAF-Ibeta/INHAT and its histone chaperone activity. Proc Natl Acad Sci U S A. 2007 Mar 13;104(11):4285–4290. PMCID: PMC1810507

236. Xing Y, Xu Y, Chen Y, Jeffrey PD, Chao Y, Lin Z, Li Z, Strack S, Stock JB, Shi Y. Structure of protein phosphatase 2A core enzyme bound to tumor-inducing toxins. Cell. 2006 Oct 20;127(2):341–353. PMID: 17055435

237. Xu Y, Xing Y, Chen Y, Chao Y, Lin Z, Fan E, Yu JW, Strack S, Jeffrey PD, Shi Y. Structure of the protein phosphatase 2A holoenzyme. Cell. 2006 Dec 15;127(6):1239–1251. PMID: 17174897

238. LeMaster DM. Deuterium labelling in NMR structural analysis of larger proteins. Q Rev Biophys. 1990 May;23(2):133–174.

239. Keeler J. Understanding NMR Spectroscopy. 2013 Jan 1;

240. Friebolin H. Basic one- and two-dimensional NMR spectroscopy /. 4th completely rev. and updated ed. Weinheim ; WILEY-VCH,; c2005.

241. Xu Z, Yang W, Shi N, Gao Y, Teng M, Niu L. Cloning, purification, crystallization and preliminary X-ray crystallographic analysis of SET/TAF-Iβ ΔN from Homo sapiens. Acta Crystallograph Sect F Struct Biol Cryst Commun. 2010 Jul 29;66(8):926–928.

242. Nagata K, Kawase H, Handa H, Yano K, Yamasaki M, Ishimi Y, Okuda A, Kikuchi A, Matsumoto K. Replication factor encoded by a putative oncogene, set, associated with myeloid leukemogenesis. Proc Natl Acad Sci. 1995 May 9;92(10):4279–4283.

243. Angulo J, Nieto PM. STD-NMR: application to transient interactions between biomolecules-a quantitative approach. Eur Biophys J EBJ. 2011 Dec;40(12):1357–1369. PMID: 21947507

244. Angulo J, Enríquez-Navas PM, Nieto PM. Ligand–Receptor Binding Affinities from Saturation Transfer Difference (STD) NMR Spectroscopy: The Binding Isotherm of STD Initial Growth Rates. Chem – Eur J. 2010 Jul 12;16(26):7803–7812.

245. Krishnan VV, Murali N, Kumar A. A diffusion equation approach to spin diffusion in biomolecules. J Magn Reson 1969. 1989 Sep;84(2):255–267.

246. R H McMENAMY JLO. The Specific Binding of L-Tryptophan to Serum Albumin. J Biol Chem. 1959;233(6):1436–47.

247. Soga S, Shirai H, Kobori M, Hirayama N. Use of Amino Acid Composition to Predict Ligand-Binding Sites. J Chem Inf Model. 2007 Mar 1;47(2):400–406.

248. Trager RE, Giblock P, Soltani S, Upadhyay AA, Rekapalli B, Peterson YK. Docking optimization, variance and promiscuity for large-scale drug-like chemical space using high performance computing architectures. Drug Discov Today. 2016 Oct 1;21(10):1672–1680.

249. Muto S, Senda M, Adachi N, Suzuki T, Nagai R, Senda T, Horikoshi M. Purification, crystallization and preliminary X-ray diffraction analysis of human oncoprotein SET/TAF-1beta. Acta Crystallogr D Biol Crystallogr. 2004 Apr;60(Pt 4):712–714. PMID: 15039562

250. Wu DH, Chen AD, Johnson CS. An Improved Diffusion-Ordered Spectroscopy Experiment Incorporating Bipolar-Gradient Pulses. J Magn Reson A. 1995 Aug 1;115(2):260–264.

251. Stejskal EO, Tanner JE. Spin Diffusion Measurements: Spin Echoes in the Presence of a Time-Dependent Field Gradient. J Chem Phys. 1965 Jan 1;42(1):288–292.

252. Johnson CS. Diffusion ordered nuclear magnetic resonance spectroscopy: principles and applications. Prog Nucl Magn Reson Spectrosc. 1999 May 20;34(3):203–256.

253. Nilsson M. The DOSY Toolbox: A new tool for processing PFG NMR diffusion data. J Magn Reson. 2009 Oct 1;200(2):296–302.

254. Adams JM 2nd, Pratipanawatr T, Berria R, Wang E, DeFronzo RA, Sullards MC, Mandarino LJ. Ceramide content is increased in skeletal muscle from obese insulin-resistant humans. Diabetes. 2004 Jan;53(1):25–31. PMID: 14693694

255. Amati F, Dubé JJ, Alvarez-Carnero E, Edreira MM, Chomentowski P, Coen PM, Switzer GE, Bickel PE, Stefanovic-Racic M, Toledo FGS, Goodpaster BH. Skeletal Muscle Triglycerides, Diacylglycerols, and Ceramides in Insulin Resistance Another Paradox in Endurance-Trained Athletes? Diabetes. 2011 Oct 1;60(10):2588–2597. PMID: 21873552

256. Chavez JA, Knotts TA, Wang L-P, Li G, Dobrowsky RT, Florant GL, Summers SA. A Role for Ceramide, but Not Diacylglycerol, in the Antagonism of Insulin Signal Transduction by Saturated Fatty Acids. J Biol Chem. 2003 Mar 21;278(12):10297–10303. PMID: 12525490

257. Schramek D, Sendoel A, Segal JP, Beronja S, Heller E, Oristian D, Reva B, Fuchs E. Direct in Vivo RNAi Screen Unveils Myosin IIa as a Tumor Suppressor of

Squamous Cell Carcinomas. Science. 2014 Jan 17;343(6168):309–313. PMID: 24436421

258. Alayoubi AM, Wang JCM, Au BCY, Carpentier S, Garcia V, Dworski S, El-Ghamrasni S, Kirouac KN, Exertier MJ, Xiong ZJ, Privé GG, Simonaro CM, Casas J, Fabrias G, Schuchman EH, Turner PV, Hakem R, Levade T, Medin JA. Systemic ceramide accumulation leads to severe and varied pathological consequences. EMBO Mol Med. 2013 Jun;5(6):827–842. PMCID: PMC3779446

259. Levade T, Tempesta MC, Salvayre R. The in situ degradation of ceramide, a potential lipid mediator, is not completely impaired in Farber disease. FEBS Lett. 1993 Aug 30;329(3):306–312. PMID: 8365472

260. van Echten-Deckert G, Klein A, Linke T, Heinemann T, Weisgerber J, Sandhoff K. Turnover of endogenous ceramide in cultured normal and Farber fibroblasts. J Lipid Res. 1997 Dec;38(12):2569–2579. PMID: 9458280

261. Wei BL, Denton PW, O'Neill E, Luo T, Foster JL, Garcia JV. Inhibition of Lysosome and Proteasome Function Enhances Human Immunodeficiency Virus Type 1 Infection. J Virol. 2005 May;79(9):5705–5712. PMCID: PMC1082736

262. Bayer N, Schober D, Prchla E, Murphy RF, Blaas D, Fuchs R. Effect of bafilomycin A1 and nocodazole on endocytic transport in HeLa cells: implications for viral uncoating and infection. J Virol. 1998 Dec;72(12):9645–9655. PMCID: PMC110474

263. Kumar A, Capua E, Kesharwani MK, Martin JML, Sitbon E, Waldeck DH, Naaman R. Chirality-induced spin polarization places symmetry constraints on biomolecular interactions. Proc Natl Acad Sci. 2017 Mar 7;114(10):2474–2478. PMID: 28228525

264. Li H-H, Cai X, Shouse GP, Piluso LG, Liu X. A specific PP2A regulatory subunit, B56gamma, mediates DNA damage-induced dephosphorylation of p53 at Thr55. EMBO J. 2007 Jan 24;26(2):402–411. PMCID: PMC1783465

265. Rai V, Egelhoff TT. Role of B regulatory subunits of protein phosphatase type 2A in myosin II assembly control in Dictyostelium discoideum. Eukaryot Cell. 2011 Apr;10(4):604–610. PMCID: PMC3127641

266. Hajduk PJ, Greer J. A decade of fragment-based drug design: strategic advances and lessons learned. Nat Rev Drug Discov. 2007 Mar;6(3):211–219. PMID: 17290284

267. Miserey-Lenkei S, Bousquet H, Pylypenko O, Bardin S, Dimitrov A, Bressanelli G, Bonifay R, Fraisier V, Guillou C, Bougeret C, Houdusse A, Echard A, Goud B. Coupling fission and exit of RAB6 vesicles at Golgi hotspots through kinesin-myosin interactions. Nat Commun. 2017 Nov 1;8(1):1254. PMCID: PMC5665954

268. Heger CD, Wrann CD, Collins RN. Phosphorylation Provides a Negative Mode of Regulation for the Yeast Rab GTPase Sec4p. PLoS ONE [Internet]. 2011 Sep 12 [cited 2018 Aug 15];6(9). Available from: https://www.ncbi.nlm.nih.gov/pmc/articles/PMC3171412/ PMCID: PMC3171412

269. Bailly E, McCaffrey M, Touchot N, Zahraoui A, Goud B, Bornens M. Phosphorylation of two small GTP-binding proteins of the Rab family by p34cdc2. Nature. 1991 Apr 25;350(6320):715–718. PMID: 1902553

270. Chiariello M, Bruni CB, Bucci C. The small GTPases Rab5a, Rab5b and Rab5c are differentially phosphorylated in vitro. FEBS Lett. 1999 Jun 18;453(1–2):20–24. PMID: 10403367

271. Karniguian A, Zahraoui A, Tavitian A. Identification of small GTP-binding rab proteins in human platelets: thrombin-induced phosphorylation of rab3B, rab6, and rab8 proteins. Proc Natl Acad Sci U S A. 1993 Aug 15;90(16):7647–7651. PMCID: PMC47199

272. van der Sluijs P, Hull M, Huber LA, Mâle P, Goud B, Mellman I. Reversible phosphorylation--dephosphorylation determines the localization of rab4 during the cell cycle. EMBO J. 1992 Dec;11(12):4379–4389. PMCID: PMC557012

273. Ayad N, Hull M, Mellman I. Mitotic phosphorylation of rab4 prevents binding to a specific receptor on endosome membranes. EMBO J. 1997 Aug 1;16(15):4497–4507. PMCID: PMC1170076

274. ten Klooster JP, Leeuwen I v, Scheres N, Anthony EC, Hordijk PL. Rac1-induced cell migration requires membrane recruitment of the nuclear oncogene SET. EMBO J. 2007 Jan 24;26(2):336–345. PMCID: PMC1783461

275. Catapano ER, Natale P, Monroy F, López-Montero I. The enzymatic sphingomyelin to ceramide conversion increases the shear membrane viscosity at the air-water interface. Adv Colloid Interface Sci. 2017 Sep 1;247:555–560.

276. Wanner R, Peiser M, Wittig B. Keratinocytes rapidly readjust ceramide-sphingomyelin homeostasis and contain a phosphatidylcholine-sphingomyelin transacylase. J Invest Dermatol. 2004 Mar;122(3):773–782. PMID: 15086565

277. Wlodarchak N, Guo F, Satyshur KA, Jiang L, Jeffrey PD, Sun T, Stanevich V, Mumby MC, Xing Y. Structure of the Ca2+-dependent PP2A heterotrimer and insights into Cdc6 dephosphorylation. Cell Res. 2013 Jul;23(7):931–946. PMCID: PMC3698643

278. Jiang L, Stanevich V, Satyshur KA, Kong M, Watkins GR, Wadzinski BE, Sengupta R, Xing Y. Structural basis of protein phosphatase 2A stable latency. Nat Commun. 2013 Apr 16;4:1699.

279. Cowtan K. Phase Problem in X-ray Crystallography, and Its Solution. eLS [Internet]. John Wiley & Sons, Ltd; 2001 [cited 2015 Sep 11]. Available from: http://onlinelibrary.wiley.com/doi/10.1038/npg.els.0002722/abstract

280. Wlodawer A, Minor W, Dauter Z, Jaskolski M. Protein crystallography for non-crystallographers, or how to get the best (but not more) from published macromolecular structures. FEBS J. 2008 Jan 1;275(1):1–21.

281. Ealick SE. Advances in multiple wavelength anomalous diffraction crystallography. Curr Opin Chem Biol. 2000 Oct;4(5):495–499. PMID: 11006535

282. Berjanskii MV, Wishart DS. A simple method to predict protein flexibility using secondary chemical shifts. J Am Chem Soc. 2005 Nov 2;127(43):14970–14971. PMID: 16248604

283. Garner EF, Williams AP, Stafman LL, Aye JM, Mroczek-Musulman E, Moore BP, Stewart JE, Friedman GK, Beierle EA. FTY720 Decreases Tumorigenesis in Group 3 Medulloblastoma Patient-Derived Xenografts. Sci Rep. 2018 May 2;8(1):6913.